

# **Functionalisation of Carbon Supports for PtNi Nanoparticles as Fuel Cell Catalysts**

an der Universität Hamburg eingereichte Dissertation

zur Erlangung des Doktorgrades (Dr. rer. nat.)

an der Fakultät für Mathematik, Informatik und

Naturwissenschaften

Fachbereich Chemie

Institut für Physikalische Chemie

Universität Hamburg

Vorgelegt von:

**Elena Felgenhauer**

Hamburg

2024

# Dissertation

<b>Titel:</b>	Functionalisation of Carbon Supports for PtNi Nanoparticles as Fuel Cell Catalysts
<b>Titel (deu.):</b>	Funktionalisierung von Kohlenstoffträgern für PtNi-Nanopartikel als Brennstoffzellenkatalysator
<b>Eingereicht von:</b>	Elena Felgenhauer
<b>Datum der Einreichung:</b>	19.12.2024
<b>Datum der Disputation:</b>	04.04.2025
<b>Datum der Druckfreigabe:</b>	18.04.2025
<b>Matr. Nr.:</b>	6654138
<b>Arbeitsgruppe:</b>	Prof. Dr. Horst Weller
<b>Institut:</b>	Institut für Physikalische Chemie
<b>Universität:</b>	Universität Hamburg
<b>Erstgutachter:</b>	Prof. Dr. Horst Weller
<b>Zweitgutachter</b>	Prof. Dr. Alf Mews
<b>Prüfungskommission:</b>	Prof. Dr. Horst Weller (Vorsitz) Prof. Dr. Jakob Albert Prof. Dr. Mehtap Özaslan

Die Arbeiten zur vorgelegten Dissertation wurden an der Universität Hamburg im Zeitraum zwischen September 2020 und Juni 2024 in der Arbeitsgruppe von Prof. Dr. Horst Weller am Institut für Physikalische Chemie durchgeführt.

# I. List of Publications

- I.      **10/2022: Increasing the life-time of fuel cells: Development of nanoparticle-support-materials as electrocatalyst with decreased degradation**  
*Poster contribution at: NANOHYBRID - Hamburg Conference on Complex Nanostructures*
  
- II.     **04/2024: The Role of Dioleamide Formation during the Synthesis of Core@Shell@Shell Pt@NiPt@Pt Nanoparticles**  
V. Gutknecht, J. Rüter, E. Felgenhauer, H. Heller, H. Weller  
*Chemistry of Materials*, **2024**, 36, 3628–3642.
  
- III.    **07/2024: Increasing Fuel Cell Catalyst Stability by Support Functionalisation**  
*Poster contribution at: NANODRAGON - Symposium*

## II. Table of Contents

I.	List of Publications.....	3
II.	Table of Contents .....	4
III.	List of Abbreviations.....	5
IV.	List of Symbols.....	7
1.	Zusammenfassung.....	1
2.	Abstract .....	3
3.	Introduction.....	5
4.	Theory.....	7
	4.1. Fuel Cells .....	7
	4.2. Fuel Cell Catalysts .....	15
	4.3. Half-cell measurements .....	44
5.	Objective.....	58
6.	Results and discussion .....	59
	6.1. Functionalisation of Carbon Black .....	59
	6.2. Synthesis and Investigation of Nanoparticle-Support Catalysts.....	83
7.	Outlook .....	119
8.	Experimental part.....	120
	8.1 Chemicals .....	120
	8.2 Synthesis .....	121
	8.3 Characterisation.....	126
9.	Literature .....	139
10.	Appendix.....	1
11.	Danksagung .....	21
12.	Eidesstattliche Versicherung .....	23

### III. List of Abbreviations

AFC	–	Alkaline fuel cell
AST	–	Accelerated stress test
ATR	–	Attenuated total reflection
BDT	–	Butanedithiol
BET	–	Brunauer-Emmett-Teller (Theory)
BHT	–	Butylated hydroxytoluene
CB	–	Carbon Black
CV	–	Cyclic voltammetry
CCV	–	Closed-circuit voltage
DFT	–	Density functional theory
DMFC	–	Direct methanol fuel cell
ECSA	–	Electrochemical active surface area
EDA	–	Ethylenediamine
EDX	–	Energy-dispersive X-ray spectroscopy
EIS	–	Electrochemical impedance spectroscopy
FCCJ	–	Fuel Cell Commercialization Conference of Japan
FT-IR	–	Fourier-transform infrared spectroscopy
HER	–	Hydrogen evolution reaction
HOR	–	Hydrogen oxidation reaction
MCFC	–	Molten Carbonate Fuel Cell
MWCO	–	Molecular weight cut-off
NHE	–	Normal hydrogen electrode
NP	–	Nanoparticle
NPMC	–	Non-precious metal catalyst
OCV	–	Open cell voltage or open-circuit voltage
OER	–	Oxygen evolution reaction
ORR	–	Oxygen reduction reaction
PAFC	–	Phosphoric acid fuel cell
PBI	–	Polybenzimidazole
PDA	–	Phenylenediamine

PEMFC	–	Polymer electrolyte membrane fuel cell; proton exchange membrane fuel cell
PTFE	–	Polytetrafluoroethylene
RHE	–	Reversible hydrogen electrode
SCE	–	Saturated calomel electrode
SEM	–	Scanning electron microscopy
SHE	–	Standard hydrogen electrode
SOFC	–	Solid Oxide Fuel Cell
TEM	–	Transmission electron microscopy
TETA	–	Triethylenetetramine
THF	–	Tetrahydrofuran
TPD	–	Temperature programmed desorption
XPS	–	X-ray photoelectron spectroscopy

## IV. List of Symbols

$a_i$	–	Activity of reactants $i$
$C_d$		Double layer capacitance
$d$	–	Diameter
$E$	–	Electric potential
$\Delta E^0$	–	Standard potential
$E_C$	–	Cell voltage
$E_N$	–	Nernst voltage
$\Delta E_{th}^0$	–	Thermoneutral voltage
$E_{OCV}$	–	Open cell voltage, open-circuit voltage, reversible voltage
$F$	–	Faraday constant
$\Delta G$	–	Gibbs free energy
$\Delta_R G_m^0$	–	Molar Gibbs free energy at standard pressure
$\Delta H_m$	–	Molar reaction enthalpy
$\Delta_R H^0$	–	Standard reaction Enthalpy
$i$	–	Current
$I_k$	–	Diffusion-limited current
$I_{lim}$	–	Diffusion-limited current
$I_m$	–	Mass-specific ORR activity
$I_s$		Surface area-specific ORR activity
$j$	–	Charge density
$j_{cap}$		Capacitive current
$\eta_A$	–	Activation overvoltage
$\eta_C$	–	Cell efficiency
$\eta_D$	–	Diffusion overvoltage
$\eta_O$	–	Ohmic or resistance overvoltage
$\eta_R$	–	Reaction overvoltage
$\eta_T$	–	Theoretical efficiency
$m_{Pt}$	–	Mass of platinum
$P_{el}$	–	Electrical power

$Q_{\text{H,theo}}$		Theoretical charge of a monolayer of H atoms on a polycrystalline Pt surface
$Q_{\text{H,ad}}$		Hydrogen adsorption charge
$r$	–	Radius
$R_m$	–	Molar gas constant
$S$	–	Entropy
$T$	–	Temperature
$T\Delta S$	–	Reversible heat
$z$	–	Charge number

# 1. Zusammenfassung

Um die Effizienz zu steigern, werden in Brennstoffzellen Katalysatoren eingesetzt, die die Anoden- und Kathodenreaktionen erleichtern. Der am häufigsten verwendete Katalysator besteht aus platinbasierten Nanopartikeln, die auf einem *carbon black* (CB) Trägermaterial verteilt sind. Dieser Kompositkatalysator degradiert während des Betriebs, was zu einer graduellen Abnahme der Leistung der Brennstoffzelle führt. Daher war das Ziel dieser Arbeit, die Degradation des Katalysators zu verringern, indem die Wechselwirkung zwischen Partikeln und Träger durch Modifikation der Oberfläche des *carbon blacks* mit funktionellen Gruppen erhöht wird. Die Funktionalisierung des *carbon blacks Vulcan XC72R* erfolgte in zwei Schritten: einer chemischen Oxidation, gefolgt von einer Kondensationsreaktion der erzeugten COOH-Gruppen mit Diaminen (Ethylendiamin (EDA), Triethylenetetramin (TETA), Phenylendiamin (PDA)) oder einem Dithiol (Butandithiol (BDT)).

Die chemische Oxidation wurde mit einer Drei-zu-Eins-Mischung aus konzentrierter Schwefelsäure und Salpetersäure über unterschiedliche Zeiträume durchgeführt. Der Erfolg der Oxidation wurde durch einen Anstieg des O- und H-Gehalts angezeigt, wobei etwa ein Drittel des O-Gehalts von COOH-Gruppen stammte und der Rest verschiedenen Oxidgruppen zugeordnet werden konnte. Der Grad der Oxidation nahm mit längeren Oxidationszeiten zu, einhergehend mit einer Reduktion der BET-Oberfläche. Kürzere Oxidationszeiten (1-4 Stunden) lieferten eine ausreichende Menge an COOH-Gruppen, während eine große Oberfläche erhalten blieb.

Die Amin- und Thiolgruppen wurden entweder durch direkte Behandlung eines oxidierten Kohlenstoffs mit einem Diamin, oder über einen Carbonsäurechlorid-basierten Zwischenschritt, gefolgt von der Behandlung mit einem Diamin/Dithiol, eingeführt. Letztere Syntheseroute wies höhere Umwandlungsraten auf, war jedoch mit einer erhöhten Schwefelverunreinigung verbunden. Die Funktionalisierungen mit EDA und TETA waren die erfolgreichsten, wobei EDA hauptsächlich monofunktionale und TETA überwiegend verbrückende Funktionalisierungen zeigte.

Um die Nanopartikel-Träger-Katalysatoren zu erhalten, wurden vorab synthetisierte kolloidale PtNi- oder Pt-Nanopartikel mittels eines Fällungsverfahrens auf den modifizierten Kohlenstoff abgeschieden, angepasst an die sich ändernde Polarität der Substrate und Nanopartikel. Die katalytische Aktivität wurde mithilfe elektrochemischer Halbzellenmessungen von Arbeitselektroden, die mit einem Katalysator-Dünnschicht beschichtet wurden, untersucht. Die Morphologie des Dünnschicht, die durch das Trocknen einer Katalysatorsuspension (Tinte) auf der Arbeitselektrode erzeugt wird, wird durch die Trocknungsbedingungen beeinflusst. Stationäres

Trocknen führte zur Bildung eines „Kaffeeinges“. Eine flussbeschränkte Trocknung in einem Behälter mit einem kleinen Loch ermöglichte die Produktion gleichmäßigerer Dünnschichten. Der Einfluss der Dünnschicht-Morphologie war jedoch vernachlässigbar in Bezug auf die elektrochemisch aktive Oberfläche (ECSA).

Die ECSA wurde verwendet, um die katalytische Aktivität der synthetisierten Katalysatoren vor und nach einem beschleunigten Stresstest (AST) zu quantifizieren, um die Degradationsrate zu beurteilen. Die untersuchten Proben umfassten entweder PtNi- oder Pt-Nanopartikel, die auf einem der folgenden CB-Träger verteilt waren: unfunktionalisiertes Vulcan XC72R, oxidiertes CB, EDA-funktionalisiertes CB und TETA-funktionalisiertes CB. Zum Vergleich wurden die synthetisierten Katalysatoren mit dem kommerziellen Katalysator (Pt auf CB) verglichen.

Von den hergestellten Katalysatoren wiesen die PtNi-Katalysatoren eine höhere katalytische Aktivität als die Pt-Katalysatoren auf. Für beide Partikeltypen zeigten die auf Vulcan XC72R geträgerten Katalysatoren die höchsten ECSAs und den höchsten Grad an Degradation. Die geringste Degradation wurde für PtNi mit dem EDA-funktionalisierten Träger und für Pt mit dem TETA-funktionalisierten Träger erzielt, die ebenfalls anfängliche ECSAs aufwiesen, die mit Vulcan XC72R vergleichbar waren. Dies könnte der bevorzugten Wechselwirkung der PtNi-Partikel mit primären Aminogruppen (EDA) und der Pt-Partikel mit sekundären Aminogruppen (verbrückende Funktionalisierung von TETA) zugeschrieben werden. Darüber hinaus kann die reduzierte relative Degradationsrate auf das Entfernen der feinen Kohlenstoffstrukturen im Oxidationsschritt zurückgeführt werden. Im Vergleich zu allen vorbereiteten Katalysatoren wies der kommerzielle Katalysator *HiSPEC 3000* eine höhere anfängliche ECSA, aber auch einen höheren Grad an Degradation auf.

Insgesamt wurde gezeigt, dass die Aminfunktionalisierung der Kohlenstoffträger für PtNi- und Pt-Nanopartikel erfolgreich die elektrochemische Stabilität der Katalysatoren verbesserte, während die ECSA-Werte mit dem unfunktionalisierten Kohlenstoffträger vergleichbar blieben.

## 2. Abstract

To enhance efficiency, catalysts are employed in fuel cells to facilitate the anode and cathode reactions. The most common catalyst is composed of platinum-based nanoparticles, distributed on a carbon black (CB) support. This composite catalyst degrades during usage, gradually lowering the fuel cell performance. Hence, the objective of this work was to decrease catalyst degradation by increasing the particle-support interaction through modification of the carbon black surface with functional groups. The functionalisation on the carbon black *Vulcan XC72R* was carried out in two steps: a chemical oxidation, followed by a condensation reaction of the produced COOH groups with diamines (ethylenediamine (EDA), triethylenetetramine (TETA), phenylenediamine (PDA)) or a dithiol (butanedithiol (BDT)).

The chemical oxidation was conducted with a three-to-one mixture of concentrated sulphuric and nitric acid for varying durations. The successful oxidation was indicated by an increase of the O and H content with roughly a third of the O content originating from COOH groups and the remainder attributed to a variety of oxide groups. The degree of oxidation increased with longer oxidation times, accompanied with a reduction of the BET surface area. Short oxidation times (1-4 hours) provided a sufficient amount of COOH groups while maintaining a large surface area.

The amine and thiol groups were introduced by either direct treatment of an oxidised carbon with a diamine, or *via* an acyl chloride intermediate step, followed by diamine/dithiol treatment. The latter synthesis route demonstrated higher conversion rates, but entailed increased sulphur impurities. The functionalisations with EDA and TETA were the most successful with EDA mainly displaying monofunctional and TETA displaying bridged functionalisations.

To obtain the nanoparticle-support catalysts, pre-synthesised colloidal PtNi or Pt nanoparticles were deposited on the modified carbon blacks *via* a precipitation method, adjusted according to the changing polarity of the substrates and nanoparticles. The catalytic activity was investigated using electrochemical half-cell measurements of a working electrode containing a catalyst thin-film. The thin-film morphology, produced by drying a catalyst suspension (ink) on the working electrode, is influenced by the drying conditions. Stationary drying resulted in the formation of a coffee-ring. Flow-restricted drying in a container with a small hole was able to produce more uniform thin-films. However, the influence of the thin-film morphology was negligible towards the electrochemical active surface area (ECSA).

The ECSA was employed to quantify the catalytic activity of the synthesised catalysts before and after an accelerated stress test (AST) to assess the degradation rate. The investigated samples

comprised either PtNi or Pt nanoparticles, supported one of the following CB supports: unfunctionalised *Vulcan XC72R*, oxidised CB, EDA-functionalised, TETA-functionalised. As a reference, the synthesised catalysts were compared with the commercial catalyst (Pt on CB).

Of the prepared catalysts, PtNi catalysts demonstrated higher catalytic activity than Pt catalysts. For both particle types, the *Vulcan XC72R*-supported catalysts displayed the highest ECSAs, and the highest degree of degradation. The lowest degradation was achieved for PtNi with the EDA-functionalised support and for Pt with the TETA-functionalised support, which also displayed initial ECSAs, comparable to *Vulcan XC72R*. This may be attributed the preferred interaction of the PtNi with primary amine groups (EDA) and of the Pt particles with secondary amine groups (bridged binding of TETA). Furthermore, the reduced relative degradation rate may be attributed to a removal of the carbon fine structures in the oxidation step. Compared to all prepared catalysts, the commercial catalyst *HiSPEC 3000* displayed a higher initial ECSA, but also a higher degree of degradation.

To conclude, the amine-functionalisation of the carbon supports for PtNi and Pt nanoparticles successfully improved the electrochemical stability of the catalysts while maintaining ECSA values comparable to the unfunctionalised carbon support.

### 3. Introduction

Hydrogen fuel cells are viewed as a key technology in achieving a carbon-neutral, zero-pollution energy sector.<sup>[1]</sup> Hydrogen can serve as a storage medium, produced through electrolysis of water using renewable energy sources such as wind or solar power – a concept known as ‘power-to-gas’.<sup>[2]</sup> Moreover, in the mobility sector, fuel cell vehicles can represent a valuable addition to battery electric vehicles, especially for long-range or heavy-duty vehicles.<sup>[3,4]</sup>

In the pursuit of achieving a widespread availability of fuel cells, it is imperative to increase power output while reducing production costs. One approach for realising this objective is the reduction of the precious metal platinum, which is only available in limited quantities, in the fuel cell catalyst<sup>[5,6]</sup> while maintaining a high performance and long-term stability. The catalysts are necessary to reduce the activation energy of the fuel oxidation and oxygen reduction reactions occurring at the anode and cathode, respectively.<sup>[7]</sup> The commonly employed catalyst in fuel cells consists of platinum-based nanoparticles, embedded on a high-surface carbon support material.<sup>[8,9]</sup> The utilisation of the fuel cell entails an electrochemical degradation of such nanoparticle-support composite catalyst.<sup>[10]</sup> This reduces the fuel cell performance over time and eventually leads to the fuel cell’s end-of-life. Hence, current fuel cell catalyst research focusses on the enhancement of the catalyst’s mass-specific catalytic activity in order to reduce the necessary platinum content, and secondly on the improvement of its electrocatalytic stability to prolong the life-time of the fuel cell.

Since the catalytic reactions are occurring on the metal surface, the high surface-to-volume ratio of the metal nanoparticles ensures the optimal surface utilisation per metal weight. One strategy for the platinum reduction comprises of the addition of a co-metal to form an alloy<sup>[11–14]</sup> or core-shell<sup>[15–17]</sup> nanocatalyst while also being able to improve the mass-specific activity<sup>[18]</sup> and stability.<sup>[15–17,19]</sup> Another approach features the improvement of the catalytic activity through modification of the nanoparticle’s shape. Examples for this are the highly catalytic active nanowires<sup>[20]</sup> or nanocages/frames/boxes<sup>[21–23]</sup>. Moreover, it was found<sup>[24]</sup> that distinct crystal facets exhibit varying degrees of catalytic efficacy, resulting in some crystal shapes, for example octahedrons, demonstrating greater activity than others.

The uniform distribution of the nanoparticles on a high-surface, conducting substrate further facilitates the accessibility of the particle surfaces. Hence, as strong interaction between the catalytic particles and their substrate is imperative for the catalytic performance. Moreover, the stronger interaction inhibits catalyst degradation originating from particle mobility. In the last six decades, various works were dedicated on the surface modification of carbon substrates in order to facilitate

an improved metal-support interaction. Firstly, influences of oxygen functionalisations, induced by gas-treatment<sup>[25]</sup> or chemical treatment<sup>[26,27]</sup> were examined, revealing contradictory results, with both enhancing<sup>[26–29]</sup> or inhibiting<sup>[30–32]</sup> effects concerning metal-support interaction. Further research investigated various types of surface-functionalizations on carbon blacks or other carbon substrates. Examples include functionalizations with fluorine,<sup>[33]</sup> thiol,<sup>[34]</sup> sulfonic acid<sup>[35,36]</sup> or amines,<sup>[37–39]</sup> surface-doping with nitrogen<sup>[40–42]</sup> or boron<sup>[43,44]</sup> that propose beneficial effects of surface modifications with respect to catalytic performance.

This work investigates the influence of different surface modifications of the carbon black *Vulcan XC72R* on the catalytic activities and stability of PtNi and Pt nanoparticle-support-composite catalysts. The synthesis route involved an oxidation prior to further functionalization through either amide linkage or thiol ester formation with a diamine or dithiol, respectively. The obtained oxide-, amine- or thiol-functionalised substrates were loaded with catalytic active colloidal nanoparticles *via* a precipitation approach to form the nanoparticle-support-composite catalysts. The catalytic performance was evaluated using electrochemical thin-film disc-electrode half-cell measurements. The electrochemical surface area (ECSA) was used as an indicator of catalytic activity, and its progression throughout the accelerated stress test (AST) was monitored to assess electrochemical degradation.

## 4. Theory

In 1894, three decades after the commercialisation of the combustion engine<sup>[7]</sup>, OSTWALD<sup>[45]</sup> criticised the steam engine as inefficient and polluting, and suggests to use the electrochemical conversion of fuels instead, to comfortably obtain energy without smoke, soot, or fire. Today, this criticism is as valid as ever, making it worthwhile to further investigate the improvement of fuel cells.

### 4.1. Fuel Cells

The principle of a fuel cell is based on the works of SCHOENBEIN<sup>[46]</sup> and GROVE<sup>[47]</sup> from 1839. After half a century of minimal progress,<sup>[7]</sup> research on fuel cells was revived by BACON<sup>[48]</sup> and since then, there has been a steady advancement in fuel cell technology.

Fuel cells are a type of galvanic cell, which are defined by their ability to generate current through a spontaneous redox reaction. The distinctive feature of the fuel cell is that its reactants are supplied externally. The basic reaction of a fuel cell consists of a combustion reaction – the oxidation of a fuel, entailing the release of energy. However, in a fuel cell, the two half-reactions of the fuel oxidation and oxygen reduction are separated, and the electric circuit is closed by an external conductor. The electrical energy, resulting from the difference in chemical potentials between the two half-reactions, can be harvested by an electrical load, integrated into the external circuit.<sup>[7,49,50]</sup>

Similar to a combustion engine, an externally provided fuel is required. Various compounds can be employed as fuels, for example hydrogen, methanol, methane, gasoline, ammonia or hydrazine.<sup>[51]</sup> The most prevalent fuel is hydrogen with its overall cell reaction presented in equation 4.1. Similar to hydrogen, other fuels are converted to their respective low-molecular waste products.



The fundamental structure of a hydrogen fuel cell is illustrated schematically in figure 4.1. The two electrodes, anode and cathode, are separated by an acidic or alkaline ion-conducting electrolyte while an external circuit connects both electrodes. The redox half-reactions take place at the interface between the electrode and the electrolyte. The oxidation reaction occurs at the negative anode, whereas the reduction reaction takes place at the positive cathode. The specific electrode reactions depend on the type of electrolyte as compared in figure 4.1. The type of electrolyte also determines whether a proton (acid fuel cell) or a hydroxyl ion (alkaline fuel cell) is transferred through the electrolyte to the opposing electrode.<sup>[7]</sup>

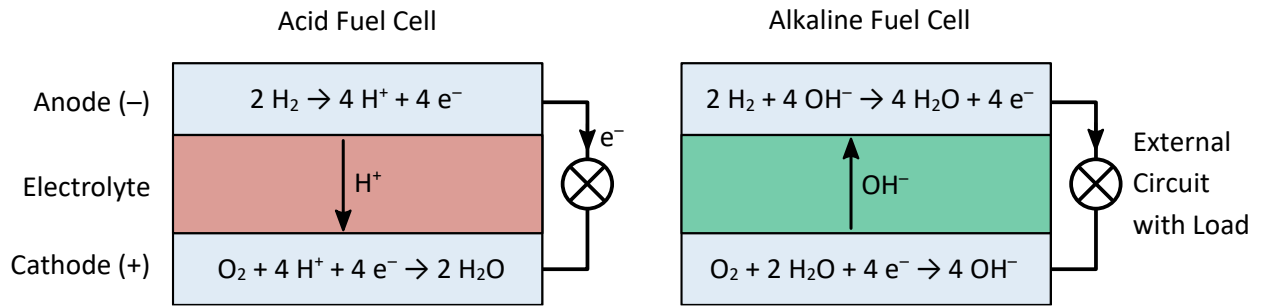


**Fig. 4.1:** Basic electrode reactions of acid and alkaline hydrogen fuel cells.

The voltage that can be generated by a single fuel cell is dependent on the standard potential  $E^0$  of the underlying cell reaction and a number of other detrimental factors, including activation energies, resistance or mass transport losses. The potential efficiency of a fuel cell is discussed further in the following chapter. As a consequence of these factors, the voltage of a single fuel cell is typically less than one volt, which is insufficient for most applications. Hence, usually several cells are combined to form a fuel cell stack. Here, several cells are connected using a bipolar plate between the anode of one cell and the cathode of the next, which allows the feed of reactant and waste gases through channels.<sup>[7]</sup>

#### 4.1.1. Fuel Cell Efficiency

The advantage of the fuel cell resides in its capacity for direct conversion of chemical energy into electrical energy, thereby obtaining high theoretical efficiencies. As shown in equation 4.2, the theoretical efficiency of a fuel cell  $\eta_T$  is dependent upon the ratio of the molar formation enthalpy  $\Delta H$  to the Gibbs free energy  $\Delta G$ . Consequently, different types of fuel lead to varying efficiencies. For a hydrogen fuel cell, the theoretical efficiency is 83 % at 25 °C.<sup>[7,49,52]</sup>

$$\eta_T = \frac{\Delta G}{\Delta H} = \frac{\Delta E^0}{\Delta E_{\text{th}}^0} \quad (4.2)$$

However, in a real fuel cell, the theoretical efficiency is not achieved for a variety of reasons. Figure 4.2, referred to as current-voltage curve or  $i$ - $V$  curve, summarises the various influences on the actually measurable cell voltage.

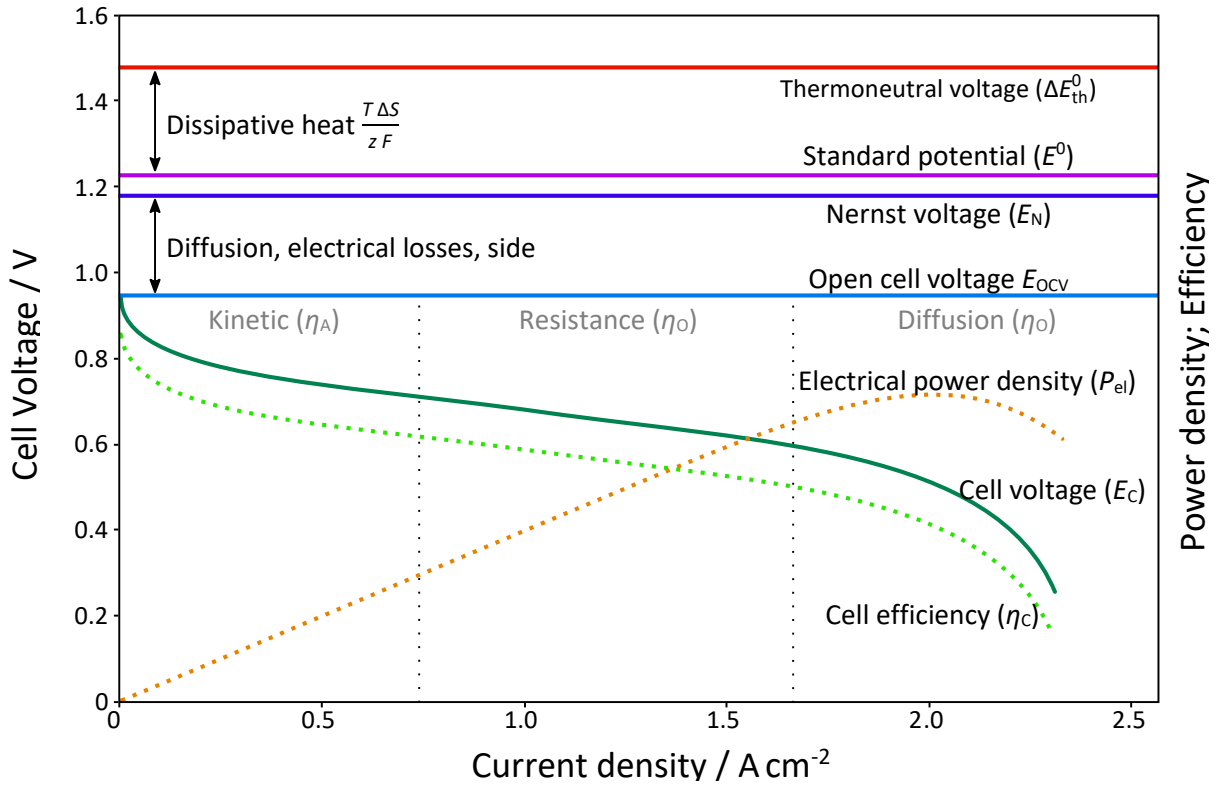


**Fig. 4.2:** Typical current-voltage ( $i$ - $V$ ) curve of a fuel cell. The dashed lines refer to the right-hand axis.

Another way to calculate the theoretical efficiency is by dividing the standard potential  $\Delta E^0$  by the thermoneutral voltage  $\Delta E_{th}^0$ , which is the theoretically achievable maximal voltage level under standard conditions. As described in equation 4.3, the thermoneutral voltage can be calculated using the standard reaction Enthalpy  $\Delta_R H^0$ , the charge number  $z$  and the Faraday constant  $F$ .<sup>[49]</sup>

$$\Delta E_H^0 = \frac{\Delta_R H^0}{z F} \quad (4.3)$$

The standard potential  $E^0$  is the potential at the thermodynamic equilibrium. It is calculated in equation 4.4, using the molar Gibbs free energy at standard pressure  $\Delta_R G_m^0$ . Compared to the thermoneutral voltage, the standard potential is lowered by the contributions of the dissipative heat, which can be interpreted as the increase of entropy. The standard potential of equation 4.1 is 1.229 V (for liquid water). Furthermore, the potential  $E$  is dependent on the temperature and the state of matter of the reactants.<sup>[7,49,52]</sup>

$$E^0 = \frac{\Delta_R G_m^0}{z F} \quad (4.4)$$

The Nernst voltage  $E_N$  in equation 4.5 with the molar gas constant  $R_m$  further considers the linear dependency on the temperature  $T$  and the logarithmic dependency on the activities  $a_i$  of the contributing reactants.<sup>[7,49]</sup>

$$E_N = E^0 - \frac{R_m T}{z F} \cdot \sum v_i \cdot \ln(a_i) \quad (4.5)$$

The open cell voltage  $E_{OCV}$  (or open-circuit voltage; reversible cell voltage) is the voltage that is measured in the absence of any load, which is considerably lower than the Nernst voltage due to side reactions, diffusion of hydrogen from the anode to the cathode, or electrical losses resulting from imperfect insulation, etc. The actually measurable cell voltage  $E_C$ , also referred to as closed-circuit voltage, is depending upon the load current. As visible in equation 4.6, the cell voltage is lowered from the open cell voltage by various types of overvoltages  $\eta$ .<sup>[49,51,52]</sup>

$$E_C(i) = E_{OCV} - \eta_A - \eta_O - \eta_D - \eta_R \quad (4.6)$$

As illustrated in figure 4.2, the predominant type of overvoltage is dependent upon the current density and can be divided into three areas. At low charge densities, the activation overvoltage  $\eta_A$  predominates. The activation overvoltage originates from the kinetic processes at the anode, and especially at the cathode, namely the finite charge transfer rate of electrons or ions across the phase boundary between the electrode and the electrolyte. At elevated charge densities, the ohmic (or resistance) overvoltage  $\eta_O$  becomes significant. The ohmic overvoltage derives from the internal resistance of the cell due to electron conduction and ion conduction resistances. At high charge densities, the diffusion rate of the reactants to the electrode is unable to keep pace with the reaction, wherefor the diffusion overvoltage  $\eta_D$  is predominant in this charge region. The final overvoltage, which plays a role in all three areas, is the reaction overvoltage  $\eta_R$ , that arises due to limited reaction rates in coupled reactions.<sup>[49,52]</sup>

The mentioned influences reduce the theoretical efficiency  $\eta_T$  to the cell efficiency  $\eta_C$ . The cell efficiency  $\eta_C$  is defined in equation 4.7 as the ratio of cell voltage  $E_C$  to the thermoneutral voltage, essentially the ratio of actual to ideal voltage.<sup>[49,52]</sup>

$$\eta_C = \frac{E_C(i)}{\Delta E_{th}^0} \quad (4.7)$$

The electrical power  $P_{el}$  can be calculated with equation 4.8. The power density curve in figure 4.2 can be obtained by multiplying the voltage and current density of each point in the current-voltage curve. It is apparent that the maximum power density of a fuel cell typically occurs at moderately

high current densities, despite the fact that the cell voltage decreases with increasing charge density.<sup>[49]</sup>

$$P_{el} = E \cdot i \quad (4.8)$$

#### 4.1.2. Types of Fuel Cells

Throughout the years, a variety of types of fuel cells have been developed. The fuel cells differ primarily in their type of fuel, operating temperature, and electrolyte composition. An overview of the most common types of fuel cells can be found in figure 4.3.<sup>[49,51,52]</sup>

As previously stated, different types of fuel can be employed in a fuel cell. In this regard, direct and indirect fuel cells can be distinguished. The former directly converts the fuel *via* the electrochemical reaction, as it is the case with a hydrogen fuel cell, a direct methanol fuel cell, or a high-temperature methane fuel cell. The latter, on the other hand, necessitates a preceding reforming step to hydrogen. An example for an indirect fuel cell is the low-temperature methane fuel cell.<sup>[51]</sup>

Consequently, whether a fuel can be used directly or indirectly is also dependent on the operating temperature. The fuel cells are categorised into three classes based on their operating temperature: low-temperature (50-150 °C), medium-temperature (~200 °C), and high-temperature (600-1000 °C).<sup>[51]</sup>

The operating temperature also influences the employable catalyst for the electrode reactions. While low operating temperatures often necessitate the use of platinum-based catalysts, it is possible to utilise a less expensive nickel catalyst at elevated temperatures.<sup>[52]</sup>

Furthermore, a variety of electrolytes can be employed. The classic fuel cell utilises an aqueous or concentrated acid or base as electrolyte. Additionally, at high operating temperatures, molten carbonates or ceramics may be applied as electrolytes in fuel cells. The most widely used electrolyte in commercial fuel cells is the polymer electrolyte membrane, which employs a solid, proton-conducting polymer as electrolyte. The advantage of such polymer electrolyte resides in the absence of any corrosive material that may potentially leak and the irrelevance of the fuel cell's orientation during operation.<sup>[51]</sup>

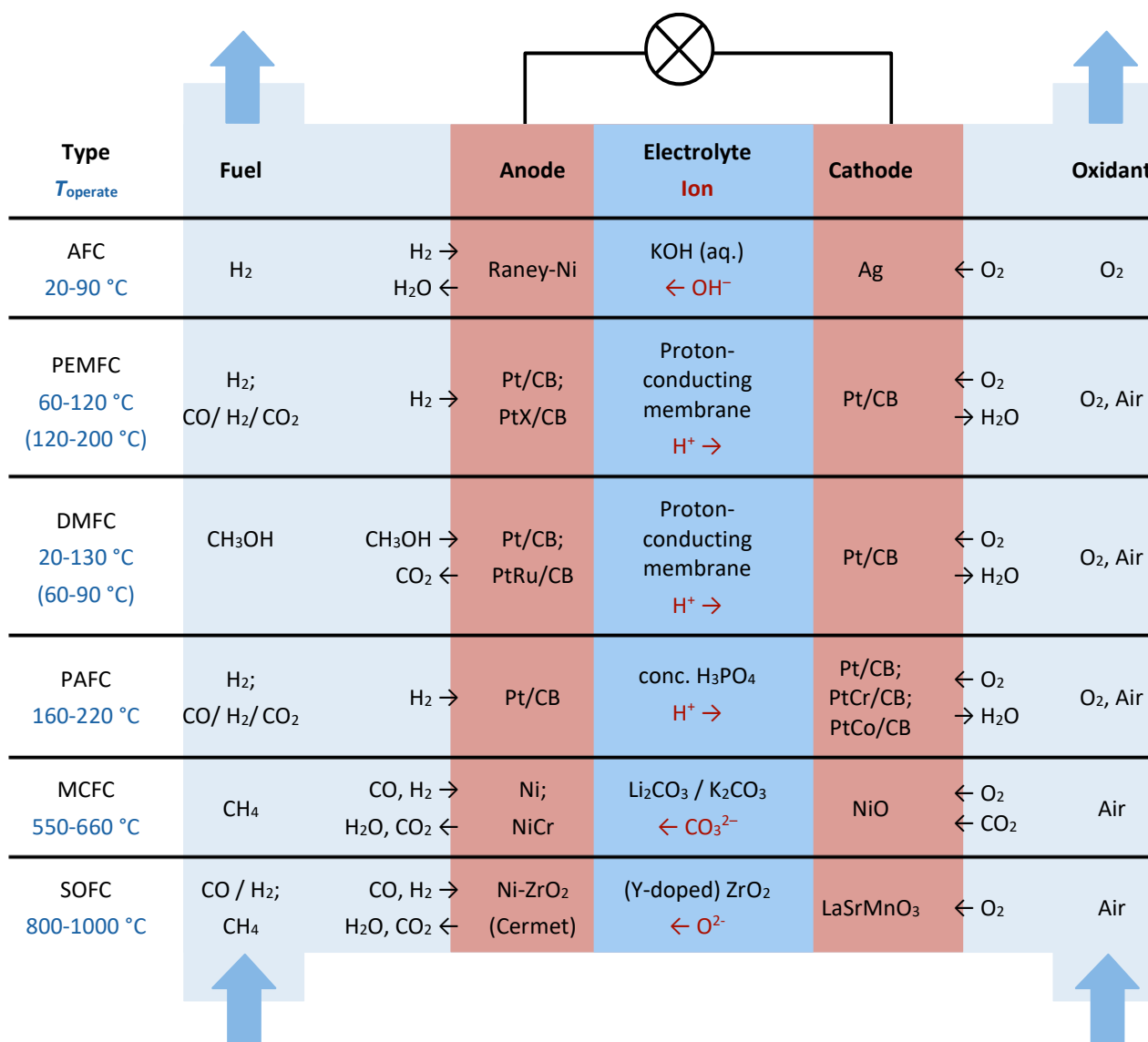


**Fig. 4.3:** Overview of the basic structure and reactions of Alkaline Fuel Cell (AFC), Polymer Electrolyte Membrane Fuel Cell (PEMFC), Direct Methanol Fuel Cell (DMFC), Phosphoric Acid Fuel Cell (PAFC), Molten Carbonate Fuel Cell (MCFC), Solid Oxide Fuel Cell (SOFC).

The standard polymer-electrolyte is the perfluorosulfonic acid perfluoroethylene copolymer, known under the trade name *Nafion*. The chemical structure is shown in figure 4.4. The backbone of *Nafion* is equivalent to polytetrafluoroethylene (PTFE, *Teflon*). However, *Nafion* additionally possesses side chains with a sodium sulfonate end group, which is why this type of polymer is also referred to as ionomer. The sulfonate groups are highly hydrophilic, which leaves *Nafion* with the capacity to adsorb up to 50% of its dry weight in water. When hydrated, water clusters around the side chains, resulting in separated water microdomains within the macromolecular structure. Within these water microdomains, protons can be conducted following the Grotthus mechanism, as verified by TSUSHIMA *et al.*<sup>[53]</sup> Here, the protons hop from one water molecule to another while forming

hydronium ions in the process. Due to this transport mechanism, the proton transfer rate is much higher compared to a vehicular mechanism, where the hydronium ion travels through the water domain as a whole. At a relative humidity of 100 %, the conductivity of *Nafion* ranges between 0.01 and 0.1 S cm<sup>-1</sup>.<sup>[7]</sup>

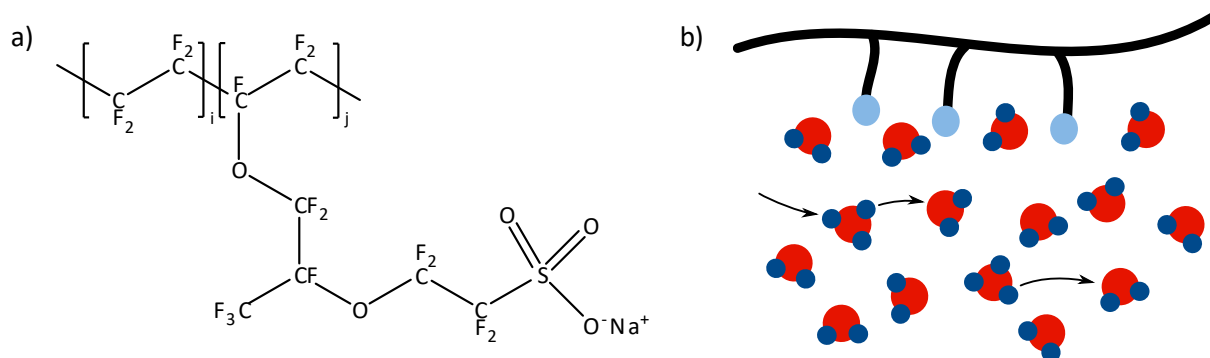


**Fig. 4.4:** a) Chemical structure of *Nafion*, a perfluorosulfonic acid perfluoroethylene copolymer. b) Schematic representation of the proton transportation process following the Grotthus mechanism.

Owing to the PTFE back-bone, *Nafion* possesses excellent mechanical and chemical stability, which enables the production of very thin membranes. For its excellent proton conductivity to function, the membrane has to be sufficiently hydrated at all times, which leads to some drawbacks. At low temperatures, the water in the membrane can freeze and at high temperatures, evaporate. Therefore, the operation temperature cannot exceed 80 °C at atmospheric pressure. At elevated pressure, higher operation temperatures can be maintained, however this may entail the breakthrough of gases. The increase of the operation temperature is also limited by the degradation of the sulfonate groups above 90 °C and the transition from the amorphous to glass phase of *Nafion* at 120-130 °C. Furthermore, the fluorination of the polymer is cost-intensive and entails environmental issues. Therefore, a multitude of other polymers has been investigated. The most promising, non-fluorinated polymer is polybenzimidazole (PBI), which possesses excellent heat-resistance. However, its low inherent proton conductivity has to be increased via doping with a strong acid, such as phosphoric acid. But it also renders the electrolyte water-free, thereby eliminating the need for water-management.<sup>[7,49,54]</sup>

Polymer conducting membranes such as *Nafion* are used in polymer electrolyte membrane fuel cells (PEMFC) or direct methanol fuel cells (DMFC). The PEMFC is the most widely used fuel cell type.<sup>[55]</sup> With a power-output of 0.1-500 kW, its applications focus on vehicles, but PEMFCs are also applied in aerospace. On the other hand, with a 0.01-1 kW power-output, the DMFC is mostly employed in small devices. Both types profit from the solid, non-volatile, *Nafion* electrolyte but also both have the same drawbacks of high-cost catalysts and electrolytes, and a limit of life-time. The DMFC has the advantage of a liquid fuel, which is accordingly easier to store. However, the direct

conversion of methanol suffers from slower reaction kinetics, and the polar fuel may lead to a methanol-crossover across the polymer membrane. Both factors entail a reduction in efficiency. Furthermore, DMFCs are not CO<sub>2</sub>-neutral, though their CO<sub>2</sub>-emission is still reduced compared to combustion engines. The utilisation of PBI as polymer electrolyte allowed the development of a high-temperature PEMFC that operates at elevated temperatures of 120-200 °C. The elevated operating temperature enables an increase of the tolerance towards CO, and the system efficiency can be enhanced if the process heat is further used, for example as water heating.<sup>[7,49,51]</sup>

Another often used type of fuel cell is the solid oxide fuel cell (SOFC). Due to its high operating temperature of 800-1000 °C and its high power-output of  $\leq 100000$  kW, this type of fuel cell is most appropriate for continuous, stationary applications such as power plants. SOFCs have a high efficiency and resulting from its high operating temperature, the cost-effective Ni can be employed as catalyst and hydrocarbons can be directly converted without hydrogen reformation step. Furthermore, it is tolerant towards impurities such as sulphur, has long life-times and the conducting ceramic oxide electrolyte does not require an electrolyte management. Disadvantageous for this type of fuel cell is its high fabrication cost and severe material constraints.<sup>[49,51]</sup>

Other, less prevalent types of fuel cells include the alkaline fuel cell (AFC), phosphoric acid fuel cell (PAFC), and molten carbonate fuel cell (MCFC). The AFC had its major application in the Apollo space missions, where the low weight, long application duration and water byproduct offered substantial benefits compared to a battery. The simple KOH electrolyte of the AFC is rechargeable, yet it suffers from low tolerance towards impurities. The PAFC, employed in small power plants, has a high efficiency, but the catalyst is prone to CO poisoning and the catalyst is cost-intensive. Lastly, the MCFC is also employed in power plants. It has a high efficiency and is able to convert hydrocarbons directly. Drawbacks include a low sulphur tolerance, and the low conductivity of the electrolyte.<sup>[49,51]</sup>

## 4.2. Fuel Cell Catalysts

A catalyst reduces the activation energy of a reaction by providing an alternative, faster reaction pathway. As a result, the reaction rate is accelerated at constant temperature without changing the chemical equilibrium of the reaction. By doing so, the catalyst itself is not consumed by the reaction and therefore does not appear in the overall reaction equation.<sup>[50,56]</sup>

Catalysts can be categorised into homogeneous and heterogeneous catalysts. In the case of homogeneous catalysts, both catalyst and reactants are present in the same phase; for instance, both may be solved. Conversely, a heterogeneous catalyst exists in a different phase from the reactants. This is the case for a solid catalyst reacting with gaseous reactants as it is employed in fuel cells.<sup>[50,56]</sup>

Heterogeneous catalysts have the advantage of being easily separable from the reaction mixture. However, their catalytic activity occurs solely at the interface between catalyst and reactant phase – for solid catalysts at the surface of the catalyst. Therefore, an often-employed strategy is the use of catalysts with an extended surface area, such as porous- or nano-structures.

In a fuel cell, the catalysed redox reaction takes place at the three-phase boundary between the solid (metal) catalyst, the reactant gas and the electrolyte, as depicted in figure 4.5. For the reaction to occur, all three phases need to intersect, as the electrolyte provides the proton transport, the gas phase provides the reactant, the catalytic reaction occurs on the surface of the catalyst and the latter also provides the electron transportation. Therefore, the electrolyte has to extend out to the catalyst particles and lightly cover them.<sup>[7,49]</sup>

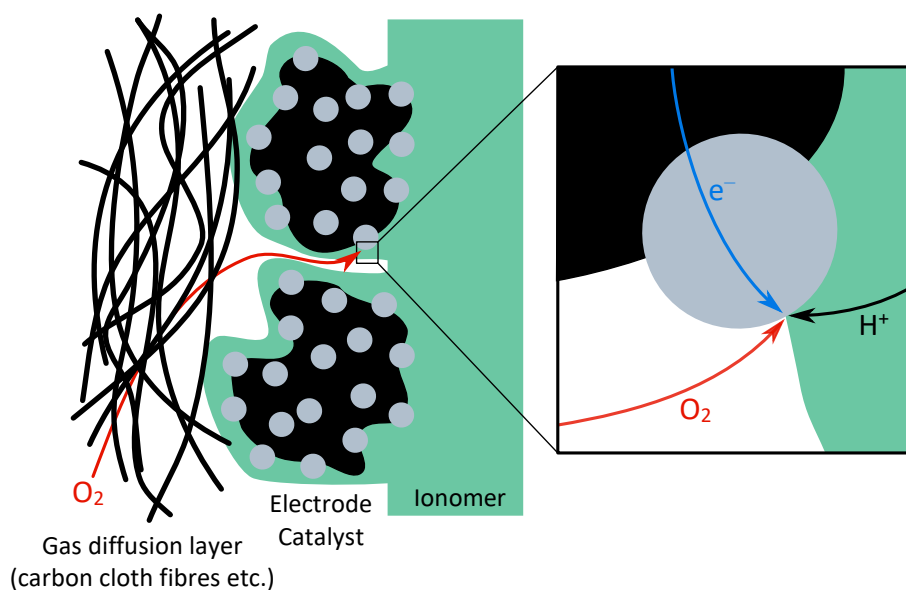


**Fig. 4.5:** Three-phase boundary between the catalyst (catalytic particles on porous support), the electrolyte (ionomer) and the reactant gas (here: O<sub>2</sub>) at the electrode of a polymer-electrolyte fuel cell.

The course of the catalytic reaction on the catalyst surface of the hydrogen oxidation at the anode is shown in figure 4.6. In the first step, the hydrogen molecule adsorbs to the catalyst surface while breaking the H-H bond. Subsequently, each adsorbed hydrogen atom loses one electron, and the proton desorbs from the surface. This hydrogen oxidation reaction (HOR) possesses very fast reaction kinetics leading to low voltage losses, even for low catalyst loadings.<sup>[57]</sup>

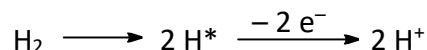


**Fig. 4.6:** Simplified reaction scheme of the hydrogen oxidation reaction (HOR) with \* denoting a surface site.

In contrast, the oxygen reduction reaction (ORR) at the cathode is a more complicated, multistep reaction involving multiple intermediate products such as  $\text{HO}_2^-$ ,  $\text{H}_2\text{O}_2$ ,  $\text{O}_2^{2-}$  and  $\text{HO}^-$  etc. The detailed reaction steps are still unclear and under investigation using rotating ring or disc electrode studies and scanning electron microscopy.<sup>[57,58]</sup>

Two distinct ORR mechanisms may occur in acidic media. The dissociative mechanism depicted in figure 4.7a is similar to the HOR. The oxygen bond is broken upon adsorbing to the catalyst surface and the adsorbed oxygen atoms are protonated and reduced in two consecutive steps, before the water molecule desorbs from the surface. In this reaction, four electrons are transferred, hence it is also called four-electron-pathway.<sup>[57,58]</sup>

The second mechanism is shown in figure 4.7b. In this associative mechanism, the O=O bond is not broken during the chemisorption. The chemisorbed  $\text{O}_2$ -molecule is protonated and reduced to form an  $\text{H}_2\text{O}_2$  intermediate, which can further react to split off  $\text{H}_2\text{O}$ . Alternatively,  $\text{H}_2\text{O}_2$  can desorb (and resorb) from the surface, which has been observed as a by-product. Since this mechanism involves the transfer of only two electrons, it is also known as two-electron-pathway.<sup>[57,58]</sup>

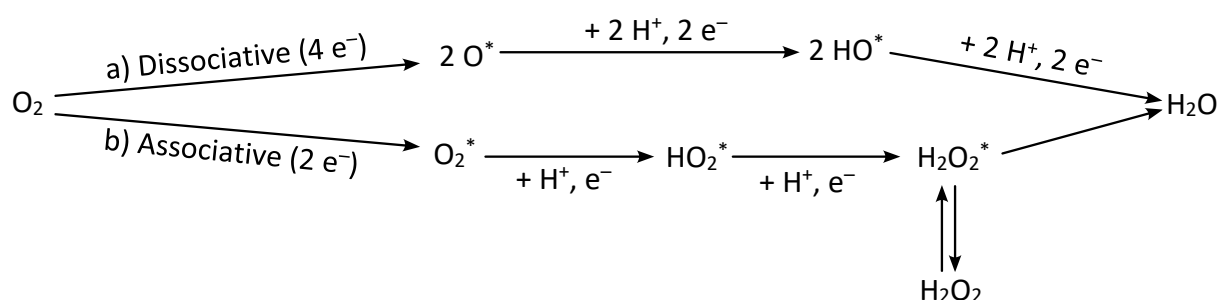


**Fig. 4.7:** Simplified reaction scheme of the a) dissociative reaction pathway and b) the associative reaction pathway of the oxygen reduction reaction (ORR) with \* denoting a surface site.

Compared to the HOR, The ORR has around five orders of magnitude slower reaction kinetics, necessitating higher catalyst loadings. Hence, the focus of hydrogen fuel cell catalyst research lies on

the improvement of the cathode catalyst. In general, a good catalyst is characterised by a high catalytic activity with a high selectivity, a high poison resistance and a high stability. In this context, a significant influence can be attributed to the nature of the interaction between the reactants and the catalyst's surface.<sup>[57–59]</sup>

The first step in a heterogenic catalytic reaction is the adsorption of the reactants to the catalyst's surface. The two adsorption types physisorption and chemisorption can be differentiated, as shown in figure 4.8.<sup>[50,58]</sup> In the case of physisorption, the adsorbate is bound to the surface via the weak, long-range van der Waals forces. The bond enthalpy  $H_P$  lies in the range of 10 to 40 kJ mol<sup>-1</sup> and the process is reversible. Chemisorption involves a stronger, usually covalent bond of the adsorbate to the surface with a bond enthalpy  $H_C$  of 80-400 kJ mol<sup>-1</sup>. It is often accompanied by a rupture or stretching of bonds and formation of new bonds.<sup>[50,60]</sup>

If a molecule approaches a surface, the potential energy will decrease, leading to the physisorption of the molecule. For the molecule to become chemisorbed, in most cases, it is necessary to overcome a potential barrier with the activation energy  $E_A$  due to the rupture or stretching of the chemical bonds. For instance, the chemisorption of hydrogen to a copper surface requires 20-40 kJ mol<sup>-1</sup>.<sup>[50]</sup>

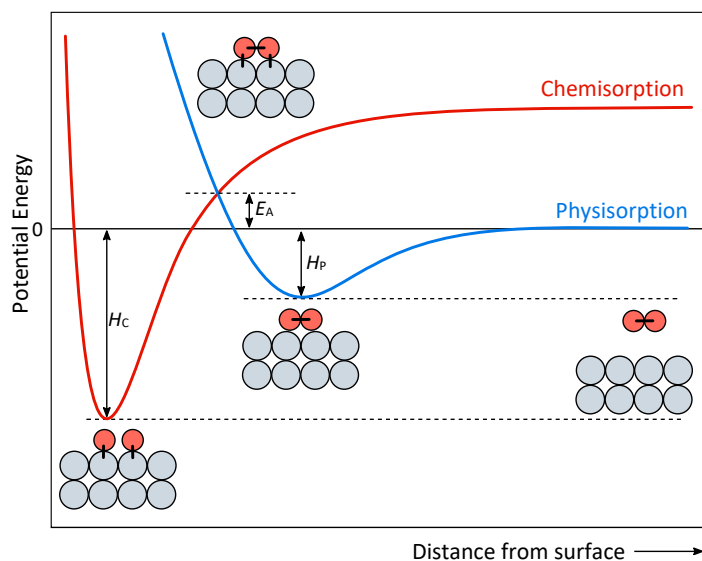


**Fig. 4.8:** Schematic course of the potential energy of an adsorbate molecule in the process of adsorbing to a surface in dependence of the distance from the surface.

For a catalyst-mediated reaction to be successful, it is imperative that the reactant molecules are bound to the catalyst surface strongly enough to break its chemical bond, but weakly enough to release the product molecules quickly from the surface. This is also known as the Sabatier principle.<sup>[57]</sup> Hence, the correct binding strength determines the catalytic activity of a catalyst to a specific reaction.

The binding strength  $E_{ad}$  is dependent on the position of the metal catalyst's  $d$ -band centre relative to the bonding orbital of the educt molecule. In contrast to the challenging determination of the adsorption energy, synchrotron-based high-resolution photoemission spectroscopy can be employed to easily assess the  $d$ -band energies. Figure 4.9 exemplary depicts the interaction between the  $2p$ -orbitals of oxygen with the  $d$  density states of Pt, relevant for the ORR. The coupling of the oxygen  $2p$  and platinum  $d$  states forms filled bonding and partly filled antibonding states. And the strength of the O-Pt interaction is determined by the filling of the antibonding states. The filling of the electronic states in the metal is dependent on their position relative to the Fermi level. If the electronic states shift to higher energies compared to the Fermi level, the antibonding states are shifted as well, which leads to a reduced filling of the antibonding states and thus to a stronger bond, and *vice versa*.<sup>[18]</sup>

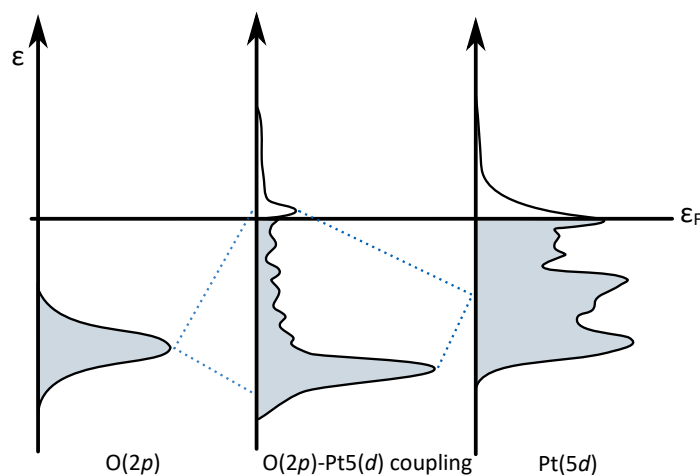


**Fig. 4.9:** Schematic representation of the interaction of the density of states (DFT calculated) of the  $2p$  orbital of oxygen(g) with the  $d$ -band of platinum(111). The energy density above the Fermi energy  $\epsilon_F$  can be allocated to antibonding states while the grey marked energy density below  $\epsilon_F$  can be allocated to bonding states.

To find the optimal catalyst among various transition metals, their catalytic activity as a function of their binding energy to the reactant can be utilised. This usually leads to a volcano-shaped plot – hence named volcano plot – as exemplary depicted in figure 4.10 for the ORR. Figure 4.10 clearly illustrates the Sabatier principle with the metals of the fitting binding energy demonstrating the highest catalytic activities. The pure transition metal with the highest catalytic activity for the ORR,<sup>[61]</sup> and also for the HOR,<sup>[62]</sup> is platinum. Notably, in both cases, platinum is not at the tip of the plot, suggesting the existence of an even more suitable material.

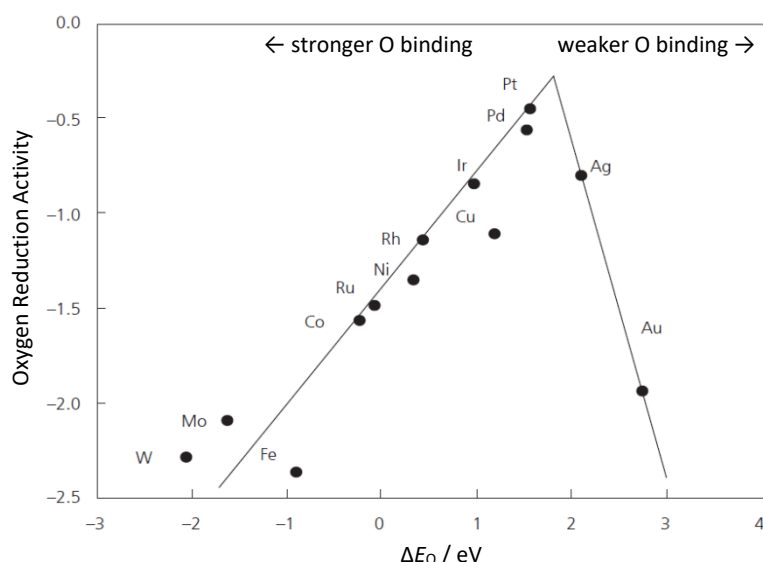


**Fig. 4.10:** Catalytic activity for the ORR of various transition metals as a function of oxygen binding energy  $\Delta E_O$ . (Reprinted with permission from [61]. Copyright 2004 American Chemical Society.)

For the ORR, platinum binds oxygen too strongly by about 0.2 eV. The catalytic activity of platinum can be tuned further by incorporating a second transition metal of the formula  $Pt_3X$ . DFT calculations predict the highest catalytic activity for the  $Pt_3Ni$  alloy.<sup>[18]</sup> But not only the chemical composition is crucial for catalytic activity. The geometry of the surface also plays a significant role with Pt(110) and  $Pt_3Ni(111)$  exhibiting the highest catalytic activity compared to the same material with other facets.<sup>[24]</sup>

The increase in catalytic activity can be explained by the ligand effect and the strain effect, which arise simultaneously in most ligand systems.<sup>[63]</sup> STAMENKOVIC *et al.*<sup>[24]</sup> showed that the outer shell of the  $Pt_3Ni$  alloy consisted of a pure platinum layer above a nickel-enriched second layer, followed by a slightly platinum-enriched third layer. This ligand effect induces an electronic charge transfer between the layers, which affects the electronic band structure.

The strain effect arises from the divergent lattice parameters of the Pt-enriched shell and the underlying alloy. A smaller alloy lattice results in a compression in the Pt shell, and *vice versa*, resulting in the modification of its *d*-band structure. While a compressive strain results in a weakening of the adsorption energy, an expansive strain strengthens the adsorption. The induced strain also remains preserved after the intentional dealloying of the less noble metal from the outer layers, thereby leveraging the advantages of dealloying for catalytic activity.<sup>[63,64]</sup>

One instance in which excessively strong bonding of an adsorbate to the surface of a metal catalyst plays a significant role is in the phenomenon of catalyst poisoning. For a platinum catalyst in a fuel

cell, CO, CO<sub>2</sub> and H<sub>2</sub>S impurities are the most relevant poisons, which adsorb to the surface and thus block the active sites for the reactants.<sup>[51]</sup> The efficacy of CO as a catalyst poison can be attributed to the manner in which it binds to the platinum surface. Alongside the electron donation of CO 5σ electrons to the platinum, the Pt 5d electrons also back-donate into the CO 2π\* orbital. This results in an especially strong multi-bond. The weakening of the multi-bond can be achieved by lowering of the *d*-band through alloying, which reduces the back-donation into the CO 2π\* orbital.<sup>[3,65]</sup>

The kind of reactant adsorption to the catalyst also influences the selectivity of a catalyst. In a catalytic reaction, a good catalyst only catalyses the desired reaction, and no side product or unwanted intermediate is produced. In a polymer electrolyte membrane fuel cell (PEMFC), a high selectivity for the dissociative four-electron ORR mechanism is desirable as the associative two-electron mechanism produces H<sub>2</sub>O<sub>2</sub> as an intermediate product. This is detrimental for an PEMFC, as the H<sub>2</sub>O<sub>2</sub> may diffuse to the membrane causing its radical oxidative degradation.<sup>[57]</sup>

One factor impacting which reaction pathway takes place is type of adsorption mode the oxygen embraces upon approaching the metal surface. Three distinct types can be differentiated as depicted in figure 4.11. The oxygen molecule can either adsorb *via* one metal atom as it is the case in the Griffith and Pauling mode, or *via* two metal atoms in the Bridge mode. If the oxygen molecule approaches the surface laterally, it adsorbs *via* the Griffith mode, or if the relative position is appropriate, the Bridge mode is used. Both Griffith and Bridge mode activate both oxygen atoms, favouring the dissociative adsorption of the oxygen molecule and thus leading to the desired four-electron pathway. In contrast, only one oxygen atom adsorbs to one metal atom in the Pauling mode. Here, only one oxygen atom is activated, the O=O bond stays intact and thus the two-electron pathway is favoured.<sup>[58]</sup>

On most transition metals, the associative pathway *via* the Pauling mode predominates, while the dissociative pathway *via* the Griffith mode is most likely on a clean platinum surface.<sup>[58]</sup> Furthermore, the choice of the reaction pathway is also dependent on the potential with lower potentials favouring the associative pathway.<sup>[66]</sup> RUVINSKIY *et al.*<sup>[67]</sup> determined a limit at 0.8 V for platinum nanoparticles under which the associative pathway predominates while the dissociative pathway predominates above this potential.

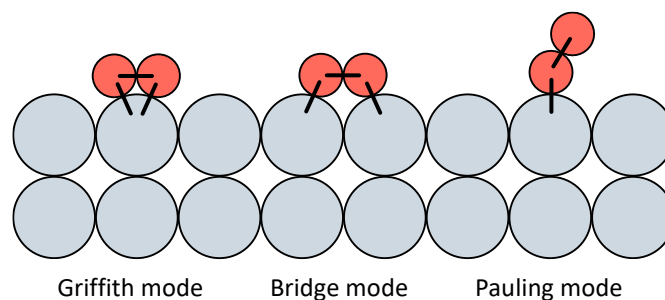


**Fig. 4.11:** Different types of oxygen adsorption modes to a metal surface.

Another important factor to consider for choosing an appropriate catalyst material is the catalyst's stability under fuel cell conditions. The catalyst material has to withstand harsh conditions of rapidly changing electrical potentials, a high pH, and a high temperature under the presence of impurities.<sup>[57,68]</sup> The thermodynamic stability dependent on electrical potential and pH can be discerned for various metals from its Pourbaix<sup>[69]</sup> diagram. Similar to a phase diagram, a Pourbaix diagram is divided into sections showing if the thermodynamical conditions for corrosion yielding a soluble or gaseous product are met, of if the metal is immune to corrosion or develops a passivating film. Figure 4.12a displays the Pourbaix diagram for platinum, demonstrating immunity over a wide range of pH values and potentials. At higher potentials, platinum is oxidised and forms an oxygen or hydroxy layer, which is also visible at potentials above 0.7-0.8 V vs. RHE in cyclic voltammograms, discussed in section 4.3.2. Compared to platinum, the Pourbaix diagram of nickel in figure 4.12b displays significant sections yielding soluble products.

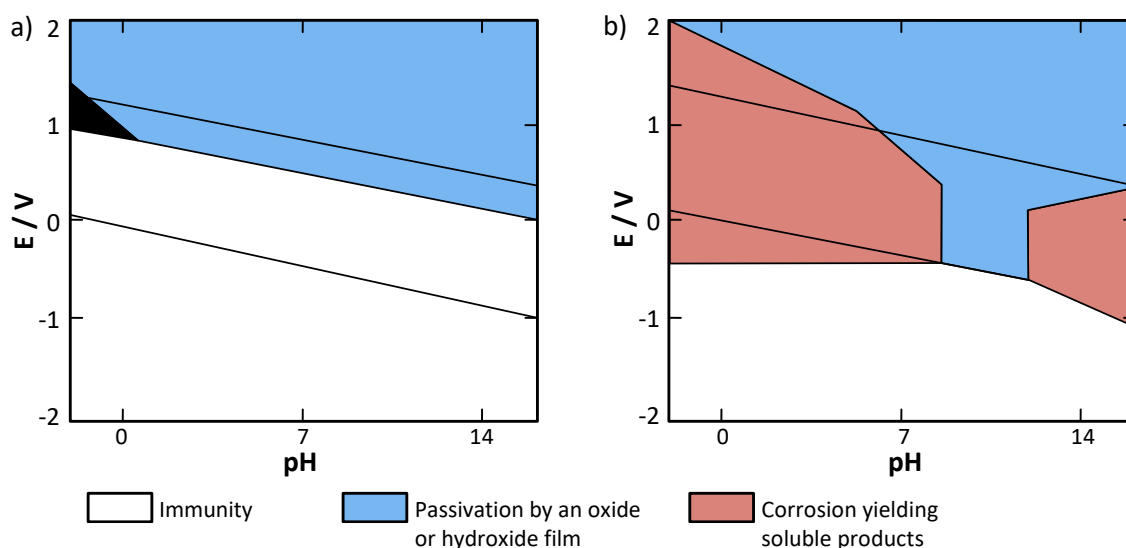


**Fig. 4.12:** Pourbaix diagram for a) platinum and b) nickel.

The previous considerations demonstrate that platinum and platinum alloy nanoparticles remain the most advanced catalytic materials to date. To fully exploit the potential of these materials, particular attention must be paid to the morphology of the catalyst. Since the catalytic reaction occurs on the surface of the catalyst, a high specific surface area is advantageous. Nanoparticles are especially suited for this purpose, as a decrease in radius results in an increased surface-to-volume ratio. Catalytic nanoparticles are further elucidated in section 4.2.1. To maximise accessibility of the reactants to the catalytic surface, these nanoparticles are embedded in a high-surface-area conductive substrate, as detailed in section 4.2.2. In this manner, a nanoparticle-support composite catalyst is formed. The industrial standard<sup>[8,9,59]</sup> for low-temperature fuel cells comprises of carbon black-supported platinum nanoparticles, also referred to as Pt/C. The synthesis of nanoparticle-support composite catalysts is described in section 4.2.3. The components of the composite catalyst function as a cohesive unit. Consequently, the properties of both the catalytic particles and the support material are vital for catalytic performance. Especially, the interaction between the catalytic particles significantly influences the catalysts performance, as elucidated in section 4.2.4. Furthermore, the material and morphology of both components also play a crucial role in regard to the durability of the catalyst. The catalyst degradation, which is an important factor for the commercialisation of a fuel cell, follows various mechanisms discussed further in section 4.2.5.

An alternative to Pt/C catalysts consists of non-precious metal catalysts (NPMC). They could give the potential benefit of significantly reduced material costs and are typically resistant towards common impurities. However, to date, their catalytic performance and durability have not yet reached the level necessary for commercialisation.<sup>[59]</sup> Examples for NPMCs comprise of nitrogen-coordinated iron or cobalt cations,<sup>[70]</sup> or carbon frameworks (CNT, graphene, etc.) doped by heteroatoms (N, B, S, P, Cl),<sup>[71,72]</sup> showing catalytic activity towards the ORR.

#### 4.2.1. Catalytic Nanoparticles

The catalytic materials with the most beneficial characteristics as catalysts for the HOR and ORR at ambient temperatures are platinum and platinum-alloys, as discussed in the previous section. Since the catalytic reaction occurs on the surface of the metal catalyst, an increase of the specific surface area leads to a more efficient utilisation of the precious metal. One approach is the application of metal nanocrystals as the surface-to-volume ratio is inversely proportional to the particle radius  $r$ .

Consequently, a reduction in particle size results in a higher electrochemical active surface area (ECSA), which is dependent on the specific surface area. However, this is not the case for the surface-

specific catalytic activity, which is constant above ca. 4 nm, but decreases with decreasing diameter below this threshold. This can be explained by geometric constraints that are linked to the reduction in particle size. While larger crystals develop distinct facets, the reduction in particle size results in crystals that contain a higher ratio of corner or edge atoms compared to crystal faces. The corner and edge atoms bind oxygen too strongly,<sup>[73]</sup> thereby reducing their catalytic activity. This phenomenon is known as ‘particle size effect’. The mass activity, which is dependent on both the specific surface area and the surface-specific catalytic activity, was reported<sup>[73–78]</sup> to have a maximum between 2 and 4 nm.

In addition to the material and the size of the catalytic particles, the particle shape also plays a significant role towards the catalytic activity. Therefore, current research investigates the synthesis of catalytic nanoparticles with controlled, elaborate structures. Figure 4.13 shows an overview of the recent development status of fuel cell catalyst nanoparticles.

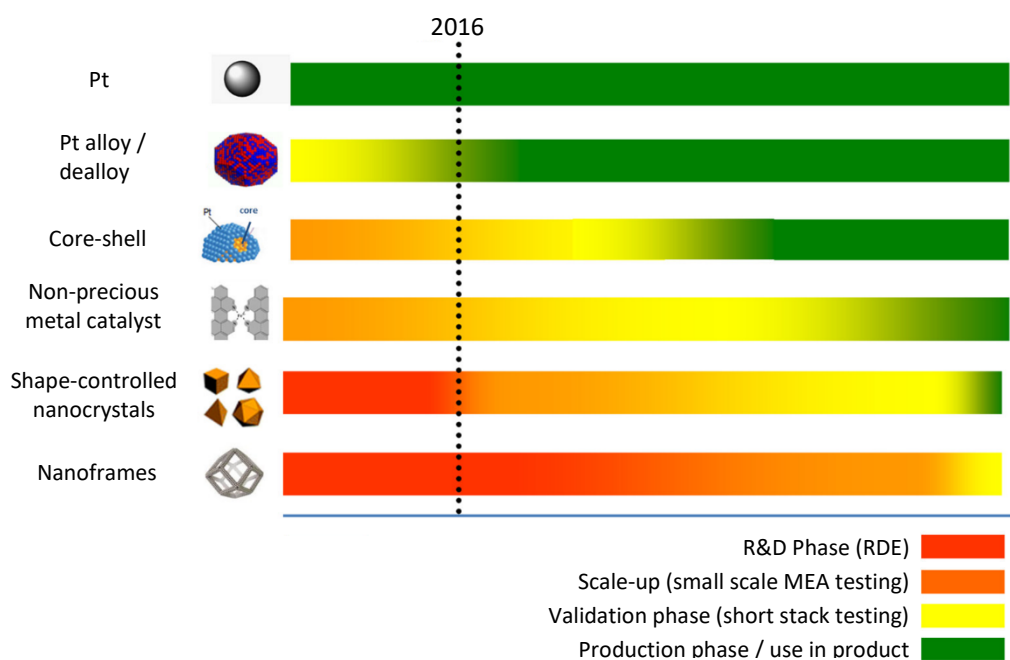


**Fig. 4.13:** Development status of catalysts employed in PEMFCs. (Reprinted with permission from [59]. Copyright 2017 American Chemical Society.)

The standard catalysts in commercial fuel cells consists of platinum nanoparticles supported on carbon substrates. However, the pure platinum particles are gradually replaced by platinum-alloy nanoparticles in commercial fuel cells since they display higher mass activities with similar or better durability. In 2015, PtCo nanocatalysts were already employed in commercially available fuel cell vehicles.<sup>[79,80]</sup> The platinum-alloy nanoparticles can be improved in regard to stability by de-alloying (pre-leaching). Here, the alloy metal is removed in a post-treatment using acid or heat, resulting in

the formation of a platinum-rich skin while maintaining the beneficial lattice strain correlated to the alloy. More elaborate structures include core-shell nanoparticles, shape-controlled nanoparticles and nanoframes.<sup>[59]</sup>

Core-shell nanoparticles consist of a platinum shell encasing a different metal such as palladium or nickel. The reduction of platinum may reduce costs while maintaining the catalytic activity. Furthermore, the core material may enhance the durability of the catalyst.<sup>[15,59]</sup>

Nanoparticles with tailored shape take advantage of the higher catalytic activity of some crystal facets relative to others, for example the (110) facet for Pt or the (111) facet for Pt<sub>3</sub>Ni.<sup>[24]</sup> The objective is to synthesise a crystal with a shape that only exposes the crystal facets with the highest activity, as this can result in very high mass-activities. Figure 4.14 shows exemplary shapes exposing only one type of crystal facet. However, the deviation from the thermodynamically most favourable form of a sphere may lead to a decreased durability.<sup>[59]</sup>

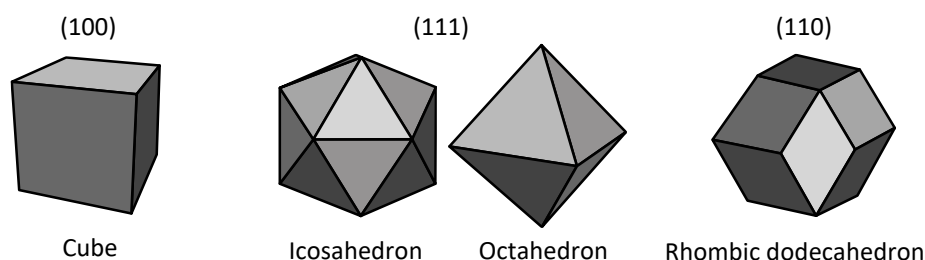


**Fig. 4.14:** Possible nanoparticle shapes exposing only one type of nanocrystal facet.

The most recently developed type of nanocatalyst is the nanoframe, which is a hollow structure, consisting of a <3 nm thin frame of a shaped nanocrystal. Nanoframes display exceptionally high mass activities due to their extended platinum surfaces. Due to thermal segregation, platinum alloy nanocages consisting of non-noble metal frameworks with a platinum skin can be produced. Furthermore, the particles are usually highly uniform and devoid of defects, resulting in an improved durability. One possible drawback may arise due to proton-conducting ionomer micelles being too big to penetrate the frame openings, leading to lower transport rates resulting in lower current densities.<sup>[59,81]</sup>

The production of the described elaborate nanoparticle sizes, shapes and compositions require a synthesis method with a very high degree of control. A chemical synthesis with such a high degree of control is the colloidal synthesis. The colloidal synthesis is a bottom-up approach involving a precursor and ligands.

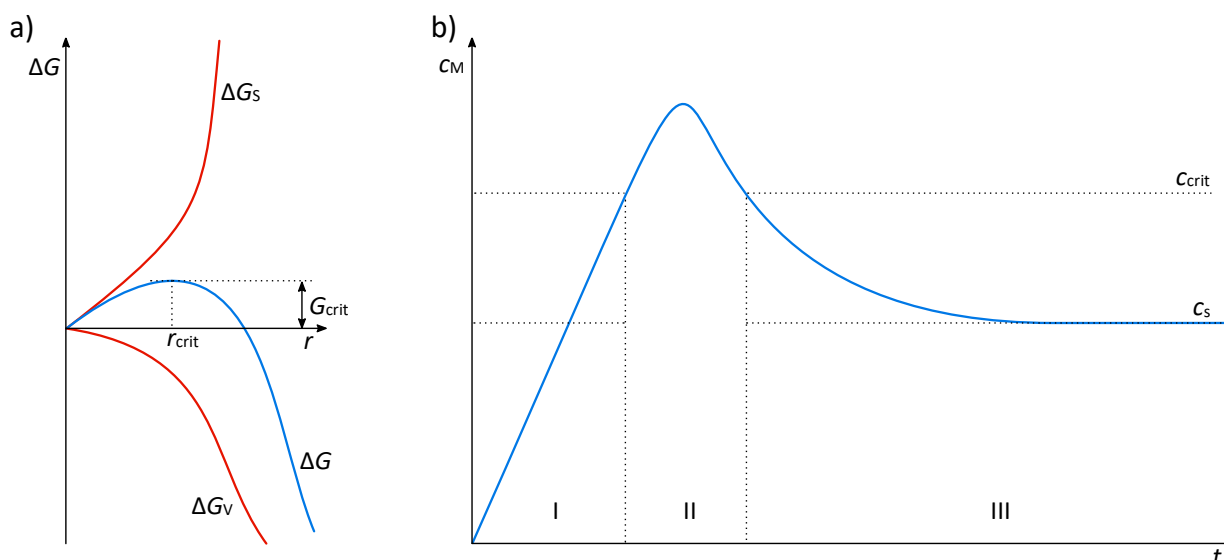
During the synthesis, the precursor is transformed by a reducing agent into a monomer, which is an active atomic or molecular species. For example, for the synthesis of platinum nanoparticles, a platinum salt is used as precursor that is reduced to the monomer  $\text{Pt}^0$ . Multiple monomers may form *nuclei*, which are stabilised in solution by ligands with a functional group coordinating to the monomer. Through the addition of more monomers, the *nuclei* may grow, or through the dissolution of the monomers, shrink. The surface of the evolved crystals is saturated by the ligands, which stabilise the particles as a dispersion and also prevent particle agglomeration. Herein, the adsorption of the ligands is a dynamic process with a constant attaching and detaching of the ligands, allowing the further growth or dissolution of the nanoparticles.<sup>[82]</sup>

Figure 4.15a and equation 4.9 illustrate the conditions necessary to form a stable crystal. The free enthalpy  $\Delta G$  is the interplay of the two opposing forces of free surface enthalpy  $\Delta G_S$  and free volume enthalpy  $\Delta G_V$ . While the free volume enthalpy, dependent on the volume of the crystal and the free energy of the bulk crystal  $\Delta G_V$ , is negative and thus beneficial for crystal growth, the positive free surface enthalpy, dependent on the surface of the crystal and the specific surface energy  $\gamma$ , favours the dissolution of the crystal. Since the volume of a crystal is proportional to  $r^3$  while the surface is proportional to only  $r^2$ , the free volume enthalpy predominates at a radius larger than  $r_{\text{crit}}$ , leading to the formation of a stable crystal. Up to that point, the energy barrier  $G_{\text{crit}}$  must be surmounted. The critical radius and critical enthalpy can be calculated with equation 4.10 and 4.11 by employing the molar volume of bulk crystal  $V_m$  and the supersaturation  $s$ .<sup>[83,84]</sup>

$$\Delta G = \Delta G_S + \Delta G_V = 4 \pi r^2 \gamma + \frac{4}{3} \pi r^3 \Delta G_V \quad (4.9)$$

$$\Delta r_{\text{crit}} = \frac{-2 \gamma}{\Delta G_V} = \frac{2 \gamma V_m}{R T \ln s} \quad (4.10)$$

$$\Delta G_{\text{crit}} = \frac{16 \pi \gamma^3 V_m^2}{3 (R T \ln s)^2} \quad (4.11)$$



**Fig. 4.15:** a) Origin of the critical radius  $r_{crit}$ . The free surface enthalpy  $\Delta G_s$  and the free volume enthalpy  $\Delta G_v$  form the free enthalpy  $\Delta G$  in dependence of the particle radius  $r$ . b) LaMer model showing the temporal progression of the monomer concentration  $c_M$  during nanoparticle nucleation and growth with the critical concentration  $c_{crit}$  and the saturation concentration  $c_s$ .

To obtain uniform particles, it is paramount to separate nucleation and growth. The nucleation has to occur during a very short timeframe before ceasing completely. Otherwise, later formed nuclei will have a shorter growth time resulting in smaller particles. The LaMer model<sup>[85]</sup> shown in figure 4.15 describes the course of the monomer concentration during particle nucleation and growth. The model is divided into three phases. Phase I shows the pre-nucleation phase. Here, the monomer concentration increases continuously due to the reduction of the precursor. Although the monomer concentration exceeds the saturation concentration in this phase, the energy is not sufficient to overcome the activation barrier. Phase II begins once the critical concentration is exceeded, and a supersaturation is attained. This results in a burst nucleation which in turn lowers the monomer concentration again below the critical concentration, thereby ceasing nucleation. Henceforth in phase III, solely particle growth occurs, reducing the monomer concentration, until the saturation concentration is reached.<sup>[83,84]</sup>

One way to achieve the separation of nucleation and growth is the hot injection<sup>[86]</sup> method. During this synthesis method, the monomer or the reducing agent is injected rapidly into the hot reaction mixture facilitating a burst nucleation. The nucleation depletes the monomer to an extent which prevents further nucleation. The reaction temperature can even be lowered during the growth period to reduce the chances of a secondary nucleation.

A phenomenon referred to as Ostwald ripening must be considered during the later stage of nanoparticle growth. According to equation 4.10, the critical radius is inversely proportional to the monomer supersaturation and temperature, leading to an increased  $r_{\text{crit}}$  at a decreasing supersaturation and temperature. Therefore, smaller particles become unstable and dissolve, resulting in the deposition of monomers onto larger nanoparticles, which in turn, grow. This leads to a defocusing of the size distribution with typical size distributions of 15 to 20 %.<sup>[83,84]</sup>

Under certain reaction conditions, the inverse process to the Ostwald ripening may occur, named digestive ripening. Here, a dispersion of polycrystalline nanocrystals, capped with weak ligands, which exhibits a large size distribution, is removed from the reaction solution and transferred to a new solvent under aid of strong ligands. The nanoparticles are refluxed with an excess of the strong ligands, which attack the nanocrystals at their crystal defects that exhibit lower lattice stabilisation energy and hence higher chemical reactivity. Subsequently, smaller clusters, stabilised by the ligands, react with the remaining crystals until an equilibrium between etching and redeposition process is established and all crystals have reached an optimal size. This process leads to the formation of single-crystal nanoparticles with a size distribution below 5 %.<sup>[87]</sup>

In most cases, the sphere is the thermodynamic equilibrium shape for the nanoparticles since the overall surface is minimised. Nanocrystals with other shapes can be obtained through a shape-controlled synthesis. Here, the different chemical potentials of the distinct crystal facets can be utilised to facilitate an anisotropic, kinetic growth. Since facets with higher chemical potential grow faster, the low-energy facets will subsequently present a larger surface area in relation to the high-energy facets. To facilitate the kinetic growth, a low growth temperature and high monomer concentration is advantageous. Additionally, organic ligands or inorganic stabilisers that selectively adsorb stronger to specific crystal facets may aid in the kinetic growth.<sup>[88]</sup>

An alternative synthesis approach to the classical colloidal synthesis is the electrochemical nanoparticle synthesis. Here, the nanoparticles are grown on an electrode or conductive substrate in a growth solution devoid of a reducing agent. Instead, a reductive current is employed. The electrochemical synthesis may be conducted without ligands, hence producing surfactant-free surfaces beneficial for heterogeneous catalysis. Anisotropic growth can be induced using oxidative etching followed by regrowth, application of a weak oxidising current which adds shape-directing oxygen-adsorbates, or through addition of shape-directing ligands.<sup>[89,90]</sup>

#### 4.2.2. Nanoparticle Support Materials

In fuel cells, especially in low temperature fuel cells, the catalyst typically consists of two parts: the catalytic active nanoparticles and the support material on which the nanoparticles are distributed. The even distribution of the nanoparticles on the support material increases the accessible nanoparticle surface and thus the catalytically active surface area while also decreasing degradation. As such, the requirements for the support material are a high specific surface area, good electrical conductivity, high stability under fuel cell usage conditions, and a suitable porosity that allows for good reactant flux. Since a high catalytic performance and catalyst durability is not only dependent on the catalytic nanoparticle, but also depends on the support material, the improvement of nanoparticle support materials has been subject of research for many groups.<sup>[8,9]</sup>

The most widely used support material for low-temperature fuel cells are carbon blacks, which are amorphous carbons<sup>[91]</sup> synthesised by pyrolysis of hydrocarbons<sup>[8,9,92]</sup>. Due to the manufacturing process, carbon blacks are very cheap and highly available,<sup>[8]</sup> but also suffer from sulphur impurities.<sup>[9,92]</sup> They are characterised by a medium to high electric conductivity<sup>[93]</sup> and specific surface area<sup>[9]</sup>. Though if the high specific surface area stems from micropores, it hinders the accessibility of reactants and *Nafion* micelles.<sup>[8,9]</sup> Another drawback of carbon blacks is their comparable low thermochemical<sup>[8,9]</sup> and electrochemical<sup>[94–96]</sup> stability leading to catalyst degradation. A more detailed description of carbon blacks is given in section 4.2.2.1.

Carbon blacks can be physically or chemically activated in pursuit of property enhancement. Physical activation refers to a thermal treatment with the objective of removing surface impurities. It is carried out in inert atmospheres at 800-1100 °C or under air/steam at 400-500 °C.<sup>[8]</sup> Chemical treatment on the other hand refers to the introduction of surface functional groups by oxidation.<sup>[8]</sup> The oxidation can be undertaken by various oxidants, such as acids, oxygen or other oxidants and usually, a variety of oxide groups is formed including carboxylic acid, phenolic groups or carbonyl groups.<sup>[92]</sup> They can serve as anchor groups for metal nanoparticles or precursor ions increasing the metal loading and nanoparticle dispersion.<sup>[27,97]</sup> Furthermore, the oxide groups increase hydrophilicity<sup>[27,92,98]</sup> and wettability<sup>[99]</sup> of the support material. Unfortunately, the presence of surface oxide groups will lower the carbon corrosion resistance even further.<sup>[100]</sup> However, as suitable surface functionalisation may enhance the interaction of catalytic nanoparticles with their support material<sup>[34–39]</sup>, the introduction of various groups such as  $-\text{NH}_2$ <sup>[39,101,102]</sup>,  $-\text{SH}$ <sup>[34]</sup>,  $-\text{SO}_3\text{H}$ ,<sup>[35,36]</sup>  $-\text{CF}_3$ ,<sup>[33]</sup> are being investigated. Oxidised carbon blacks are further described in section 4.2.2.2 and an overview over differently functionalised carbon blacks is given in section 4.2.2.3.

In order to improve properties as support materials in catalysts, various types of carbon materials are being explored. To improve reactant flux, the pore structures are adjusted to contain mainly mesopores (2-50 nm). Such materials include ordered mesoporous carbons and carbon gels.<sup>[8,9]</sup>

Ordered mesoporous carbons are synthesised by using a silica or triblock copolymer template. The templates are filled with a suitable carbon precursor, which is carbonised before removing the template. This synthesis method is deemed simple and relative cost-effective. The ordered mesoporous<sup>[8]</sup> carbons are characterised by a high specific surface area of 400-1800 m<sup>2</sup> g<sup>-1</sup>, but exhibit a rather low conductivity of 0.003-1.4 S cm<sup>-1</sup>. Furthermore, their surface can also contain oxide groups that may facilitate metal dispersion.<sup>[8,9]</sup>

Carbon gels are obtained by carbonisation of organic sol-gels. For this, suitable organic precursors such as resorcinol and formaldehyde are employed. After their polycondensation, the gel is dried and carbonised by pyrolysis in an inert atmosphere. Different kind of gels are distinguished by their drying method. Aerogels are evaporated normally, xerogels are dried supercritically and cryogels are freeze-dried. Because of the easy tunability of synthesis and processing conditions, a wide range of pore and surface properties can be obtained. Specific surface areas are in the range of 400-900 m<sup>2</sup>g<sup>-1</sup> and the conductivities<sup>[8]</sup> are approximately >1 S cm<sup>-1</sup>.<sup>[8]</sup>

Similarly to carbon blacks, mesoporous carbons also exhibit a low corrosion resistance. On the other hand, carbon materials with higher grade of graphitisation, exhibit a higher corrosion resistance. One method is thus to graphitise the carbon material *via* heat-treatment in an inert atmosphere of 2500-3000 °C. Though, this can be accompanied by a significant reduction in surface area. An alternative approach is the use of high surface area graphite, which is obtained through a special grinding process, which achieves high surface areas of around 300 m<sup>2</sup> g<sup>-1</sup>. Furthermore, materials of higher graphitic nature like graphene, carbon nanotubes or carbon nanofibres are being investigated as nanoparticle support materials.<sup>[8,103]</sup>

A relatively newly developed material<sup>[104]</sup> is the basic structural element of many carbon materials: graphene. Graphene is a single carbon sheet that is composed of sp<sup>2</sup> hybridised carbon, arranged in a hexagonal lattice, as illustrated in figure 4.16a.<sup>[9,105-107]</sup> It can be synthesised through chemical vapor deposition, arc-discharge, chemical exfoliation or reduction of graphene oxide. Graphene is characterised by a high mechanical stability and high corrosion resistance<sup>[104,105]</sup>. The rippled, but planar structure bears a very high theoretical surface area of ca. 2600 m<sup>2</sup> g<sup>-1</sup>.<sup>[9,104,108]</sup> The conductivity of a single graphene sheet is about 1000 S cm<sup>-1</sup>, but the charge transfer between graphene flakes usually reduces the conductivity on a macromolecular scale.<sup>[109]</sup> Graphene also exhibits a high

electron transfer rate, which is believed to facilitate the oxygen reduction reaction rate. Moreover, the strong interaction of platinum particles with the graphene's  $\pi$ -system may induce a positive effect on the platinum's electronic structure. On the other hand, the strong  $\pi$ - $\pi$  interactions between the individual graphene sheets and their high surface area can easily lead to aggregation between the sheets. To tackle this problem, the graphene-carbon-black composite materials have been investigated as catalyst support materials.<sup>[9,105,106]</sup>

Similar to other carbon materials, the oxidation of the inert graphene surface may enhance hydrophilicity and introduce anchor groups improving metal dispersion. Yet, with increasing oxidation grade, the conductivity decreases by usually 2-3 orders of magnitude. Another promising form of graphene modification is the doping with nitrogen. Here, the nitrogen atoms enter the carbon lattice with covalent bonds, forming pentagons and heptagons, which results in an increased conductivity of the neighbouring carbon atoms. Therefore, the doping results in a higher catalytic activity. Furthermore, the introduced defects can act as anchoring sites for metal particles and the catalyst's durability has also been found to be improved.<sup>[9,105,106]</sup>

Graphene sheets that are rolled into a seamless cylinder are known as carbon nanotubes (CNT).<sup>[107,110]</sup> Synthesis methods include arc discharge, laser ablation, chemical vapour deposition, and plasma enhanced chemical vapour deposition. Carbon nanotubes exist as single-wall (SWCNT) or multi-wall (MWCNT) carbon nanotubes, as depicted in figure 4.16. The latter consists of multiple carbon tubes stacked in one another with a spacing of typically 0.34 nm. The outer diameter typically measures 10-50 nm and the inner diameter 3-15 nm with a length of 10-50  $\mu\text{m}$ . The nanotubes are distinguished by their tube's helicity and diameter resulting in different properties. Among other things, the structure is responsible for the level of conductivity, and whether the tube has metallic or a semiconductor properties.<sup>[110,111]</sup> In general, due to their high crystallinity, CNTs exhibit a level of conductivity by several orders of magnitude higher compared to other carbon materials with  $10^2$ - $10^6 \text{ S cm}^{-1}$  for SWCNTs and  $10^3$ - $10^5 \text{ S cm}^{-1}$  for MWCNTs.<sup>[112]</sup> The porosity of MWCNTs can be attributed firstly to microporous inner cavities and secondly to mesopores that form between aggregated tubes, achieving surface areas of 200-400  $\text{m}^2 \text{ g}^{-1}$ . SWCNTs, on the other hand, mostly exhibit micropores, leading to higher specific surface areas of 400 to 900  $\text{m}^2 \text{ g}^{-1}$ . The CNT's graphitic character leads to thermal and electrochemical<sup>[113]</sup> stability that is higher compared to amorphous carbon. Moreover, CNTs have a positive effect on the platinum structure which is advantageous for the catalytic activity. However, one disadvantage concerning the commercialisation of carbon nanotubes as catalyst support material are their high manufacturing costs.<sup>[8,110]</sup>

Due to their inert surface, carbon nanotubes suffer from a lack of suitable particle anchor sites leading to poor particle dispersion, especially at high metal loadings.<sup>[8]</sup> Similar to previously mentioned carbon materials, the carbon nanotube surface can be oxidised or otherwise functionalised to render the surface more hydrophilic and improve particle support interaction.<sup>[8,9]</sup> Unfortunately, this is accompanied with a decrease in conductance by several orders of magnitude.<sup>[114]</sup>

A material similar to carbon nanotubes is the carbon nanofibre, also known as graphite nanofibre. They are synthesised by decomposition of gases containing a carbon precursor over a metal surface (chemical vapour deposition). Carbon nanotubes and nanofibres differ in the orientation of the graphene sheets. The latter consist of small graphene sheets that are stacked parallel to form long fibres.<sup>[8]</sup> According to their structure, they are categorised as platelet, ribbon, herring-bone or spiral types.<sup>[8,115]</sup> (The first three types are depicted in figure 4.16.) Accordingly, only the edge regions of carbon nanofibres are exposed which results in a sufficient amount of anchor groups negating the necessity of a functionalisation pre-treatment. Moreover, carbon nanofibres have no or only a thin hollow cavity, and compared to carbon nanotubes, they are much larger, exhibiting diameters of up to 500 nm and lengths up to a few millimetres. Carbon nanofibres exhibit conductivity, comparable to CNTs of  $10^2$ - $10^4$  S cm<sup>-1</sup> and medium specific surface areas of 10-300 m<sup>2</sup> g<sup>-1</sup>.<sup>[8,9]</sup>

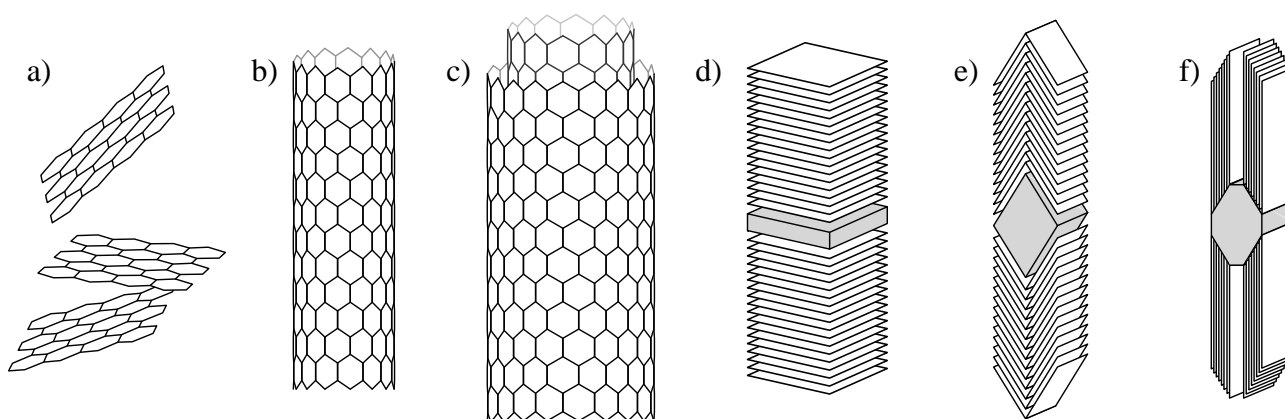


**Fig. 4.16:** Schematic illustration of different types of carbon support materials. a) Graphene. b) Single-walled carbon nanotubes. c) Multi-walled carbon nanotubes. d) Platelet-type carbon nanofibres. e) Herring-bone-type carbon nanofibres. f) Ribbon-type carbon nanofibres.

Despite the improvement in corrosion resistance associated with materials that exhibit a high degree of graphitisation, carbon corrosion is only reduced and continues to persist to a certain degree in all carbon materials. Therefore, non-carbon materials have been investigated as a potential alternative.<sup>[9,116]</sup>

In particular, conductive ceramics are regarded as promising candidates for fuel cell. Examples include many metal oxides like titania, zirconia, tin oxide, and tungsten oxide, which are often doped

or used in their sub-stoichiometric form to overcome the inherent low conductivity of many metal oxides at low temperatures. Non-oxide compounds include titanium nitride, titanium diboride, and tungsten carbide.<sup>[9,116]</sup>

These materials are valued due to their high corrosion stability within the fuel cell environment and the high electrochemical stability of ceramics supported nanoparticle catalysts. The electric conductivities span from  $0.1 \text{ S cm}^{-1}$  to values as high as  $10^5 \text{ S cm}^{-1}$ . Furthermore, many materials demonstrate enhanced CO tolerance or promote the catalytic reaction. Some metal oxides are known to interact with the supported particles, altering their catalytic activity, thus giving the potential to serve as a co-catalyst rather than just a mechanical support. An additional benefit exhibited by some materials, such as sulphated zirconia or hydrous ruthenium oxide, are their proton-conducting properties. This could reduce the necessary amount of ionomer, which may improve gas diffusion and water transportation.<sup>[9,116]</sup>

One challenge in the development of such support materials lies in achieving a sufficiently high specific surface area and appropriate porosity. Many ceramic support materials suffer from specific surface areas below  $100 \text{ m}^2 \text{ g}^{-1}$ , which significantly restricts the attainable catalytic active surface area and the possibility of high metal loadings.<sup>[9,116]</sup> HUANG *et al.* achieved mesoporous  $\text{TiO}_2$  supports through a template assisted method with a specific surface area of  $266 \text{ m}^2 \text{ g}^{-1}$ , which is comparable with *Vulcan XC72R*.<sup>[117]</sup>

Overall, a variety of fuel cell catalyst support materials has been developed. Starting with the classic carbon black, different carbon materials are being investigated, as well as non-carbon ceramic materials. All materials exhibit advantages and limitations, which have to be carefully evaluated, while also keeping in mind production costs that are an important factor for the economic feasibility. Therefore, research is ongoing as the optimal support material has yet to be found. A more detailed description of materials used in this work can be found in the following chapters.

#### 4.2.2.1. Carbon Blacks

The most commonly used support material for platinum or platinum alloy nanoparticles in commercial low-temperature fuel cells are high surface area carbon blacks.<sup>[8,9,118]</sup> Carbon blacks are amorphous carbons<sup>[91]</sup> that are synthesised *via* pyrolysis of hydrocarbons<sup>[8,9,92]</sup> with a limited supply of air at ca.  $1400 \text{ }^\circ\text{C}$ .<sup>[8]</sup> Through variation in starting material and pyrolysis conditions, carbon blacks with different morphologies and particle size distributions can be obtained.<sup>[9,92,118]</sup> Due to the manufacturing process, carbon blacks often contain small impurities of sulphur, hydrogen, and

oxygen.<sup>[9,92]</sup> The oxygen impurities can give the carbon black either acidic or basic properties, depending on the functional oxide group.<sup>[92]</sup>

The base structure of carbon black resembles that of graphite: The carbon atoms form layers with a honeycomb structure of six-membered carbon rings,<sup>[91]</sup> often saturated with hydrogen at the edge which is a remnant from the production using hydrocarbons.<sup>[92]</sup> These layers form crystallites with a diameter of ca. 0.3 nm and a height of ca. 0.2 nm,<sup>[119]</sup> that are held together by attractive Van-der-Waals forces. Though in contrast to graphite, the layers do not possess the mutual three-dimensional orientation.<sup>[91]</sup> They are not completely parallel and sometimes bent.<sup>[120,121]</sup> Also, the inter layer distance is variable, and with around 0.344-0.395 nm, higher than that of graphite (0.3354 nm).<sup>[91]</sup> Instead, the layers form a spherical shell structure, that can be attributed to the manufacturing process, where the layers are wrapped around a disordered nucleus with a preferred orientation parallel to the particle surface as shown in figure 4.17. These spherical particles have, depending on the type of carbon black, a diameter of 10 to 400 nm. Furthermore, the spheres typically build larger agglomerates, often chainlike, which contain meso- and macropores. Micropores on the other hand are thought to originate from the primary particles.<sup>[120,122]</sup>

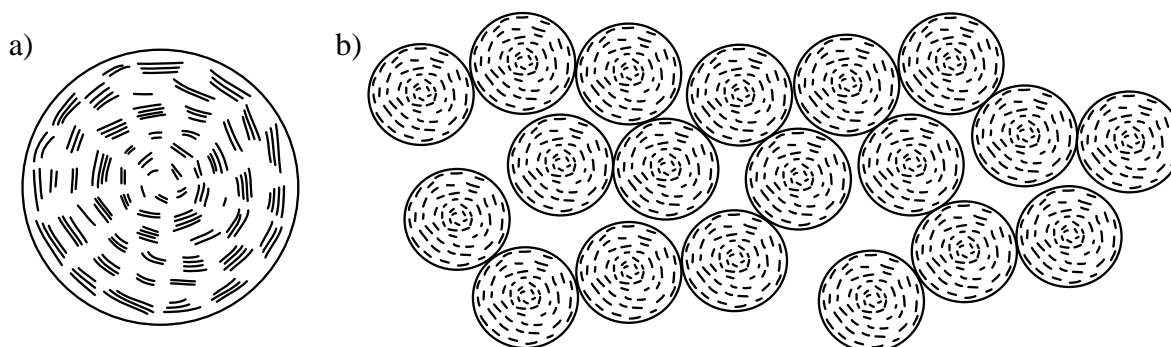


**Fig. 4.17:** Schematic visualisation of a section through a carbon black particle. **a)** Primary particle with graphene layers wrapped around a disordered nucleus. **b)** Agglomerates forming meso- and macropores.

The pore size distribution of the carbon blacks plays a big role for the application in fuel cells. While the pores contribute largely to the high specific surface area, smaller pores bear the problem of inaccessibility. Catalytic nanoparticles inside micro- and mesopores with a diameter below that of the micelle diameter of *Nafion* (>40 nm) cannot take part in the catalytic reaction.<sup>[8,9]</sup>

**Tab. 4.1:** Selection of carbon blacks used as support material in fuel cells.<sup>[9]</sup>

Carbon Black	Manufacturer	Specific surface area / m <sup>2</sup> g <sup>-1</sup>
<i>Vulcan XC72R</i>	<i>Cabot</i>	250
<i>Black Pearl 2000</i>	<i>Cabot</i>	1500
<i>Shawinigan</i>	<i>Chevron</i>	80
<i>Ketjen Black EC600J</i>	<i>Ketjen</i>	800
<i>Ketjen Black EC600JD</i>	<i>Ketjen</i>	1270
<i>Denka Black</i>	<i>Denka</i>	65

A table listing commonly used carbon blacks is provided in table 4.1. The carbon black *Vulcan XC72R* from *Cabot* used in this work is one of the most widely used support materials due to its low manufacturing costs, high electric conductivity of 4.0 S cm<sup>-1</sup><sup>[93]</sup> and high specific surface area of around 250 m<sup>2</sup>/g.<sup>[8,9,123]</sup> It consists of polydisperse particles with an average diameter of 30 nm,<sup>[8,124]</sup> which combine to form larger aggregates,<sup>[122]</sup> as seen in Figure 2.18a. It is a low structure carbon black, where the inter-particle pores dominate the pore structure.<sup>[35]</sup> (In contrast to high structure carbon blacks with dominating intra-particle pores.) The pore size distribution in Figure 4.18b reveals that *Vulcan XC72R* contains mainly larger pores with a macropore percentage of 54 %<sup>[123]</sup> and only a low amount of micropores.<sup>[122]</sup>

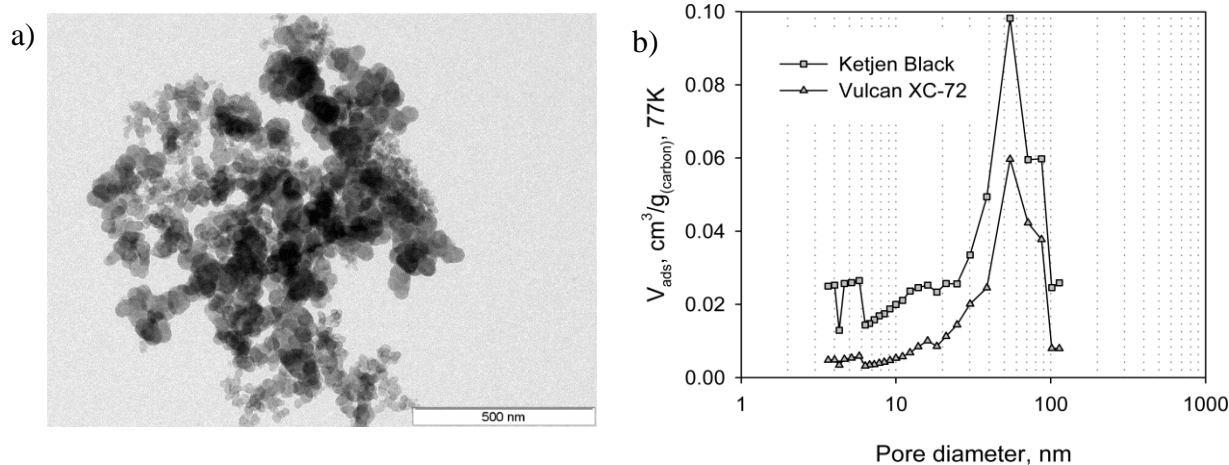


**Fig. 4.18:** a) TEM image of *Vulcan XC72R* von *Cabot*. b) Pore size distribution curves for *Ketjen Black* and *Vulcan XC-72*. (Reprinted with permission from [122]. Copyright 2010 American Chemical Society.)

#### 4.2.2.2. Oxidised Carbon Blacks

One method being explored to improve the properties as a fuel cell support material, is the oxidation of carbon blacks, which is also referred to as chemical activation.<sup>[8]</sup> The oxidative treatment can be carried out using oxidising agents such as NaOCl, KMnO<sub>4</sub> or (NH<sub>4</sub>)<sub>2</sub>S<sub>2</sub>O<sub>8</sub>, acids such as HNO<sub>3</sub>, H<sub>2</sub>O<sub>2</sub>

or citric acid, or by exposure to air, oxygen, oxygen plasma, or ozone. While the former, wet treatments can be carried out more easily and with standard equipment, it is difficult to control the oxidation reaction and to purify the oxidised carbon from residual oxidants.<sup>[8,91,92,125]</sup>

The base structure of the oxidised carbon blacks is composed of small layer stacks that are less regularly organised as in plain carbon black. The layers are curved and cross-linked with various oxide groups at the edges. The position of the oxide groups can be explained by the manufacturing process, where the oxidising agents primarily attack the edges and defect sides.<sup>[92]</sup> However, it is possible for strong acids, such as sulphuric acid, nitric acid, or a mixture of both, to disrupt the aromatic ring system of carbon nanotubes<sup>[126,127]</sup> and thus potentially attack the side of the graphene layers.

Another often observed side effect of the oxidative treatment is a reduction in specific surface area and micropore volume.<sup>[100,128–132]</sup> The decrease occurs to a greater extent with increasing severity of oxidation.<sup>[100,128–130]</sup> One explanation could be the blockage of micropores by the introduced functional groups.<sup>[132,133]</sup>

Due to the unspecific oxidation process, a variety of oxide groups such as carboxyl groups or carbonyl groups can be found. These groups cannot be viewed as discrete organic functional groups, but as a diverse combination of functional groups in numerous mesomeric forms located on the same amorphous polyaromatic frame. Because of the proximity to the aromatic carbon sheets, hydroxyl groups would have phenolic character while an ether group would have xanthene character. A selection of possible surface oxide groups is shown in figure 4.19.<sup>[92,134]</sup>

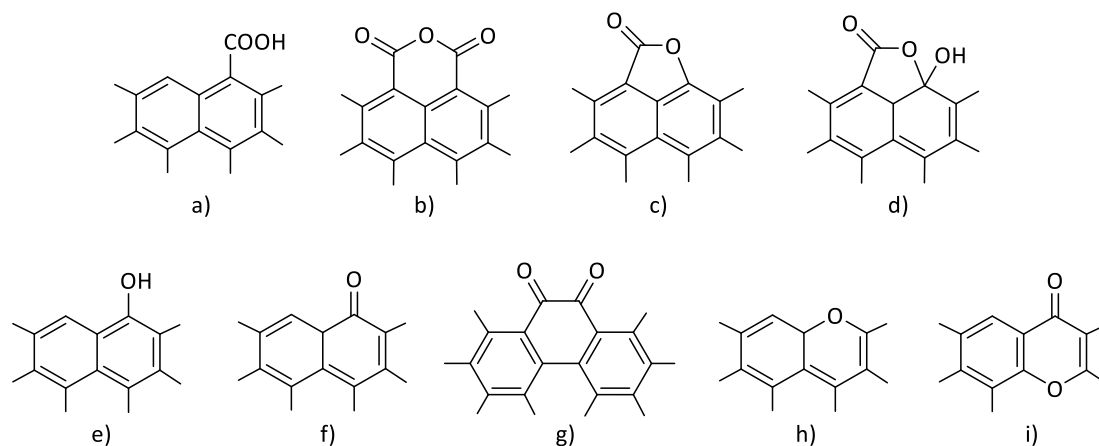


**Fig. 4.19:** Possible structures of surface oxygen groups in oxidised carbon blacks. a) carboxyl group b) carboxylic anhydride group c) lactone group d) lactol group e) hydroxyl group (phenolic character) f) carbonyl group g) quinone group h) ether group (xanthene character) i) pyrone.

The interplay of the individual group's dissociation constants determine the acid/base properties of the oxidised carbon black and its ion exchange properties including its isoelectric point.<sup>[92,135,136]</sup> The groups can be categorized according to their dissociation constants as high acidity (carboxylic groups), low acidity (anhydride and phenol groups), neutral or mild acidity (ketone groups), low basicity (aliphatic hydroxyl, quinone, lactone groups) or high basicity (pyrone groups, C- $\pi$  donor sites).<sup>[137]</sup> Although the latter is not an oxide group, it can be assumed that C- $\pi$  donor sites of the carbon black's aromatic sheets are also present in oxidized carbon blacks.<sup>[92,137]</sup>

Due to the inhomogeneous character of the oxidised carbon black with differently sized graphene sheets and randomly arranged oxide groups, the individual groups show a wide spread of dissociation constants. However, the acidity constants of groups differ several orders of magnitude and cluster around discrete values. Therefore, they can be differentiated by titration experiments.<sup>[92]</sup>

Direct titration methods are not very effective because of the slow adjustment of the ion exchange equilibrium of the functional groups, especially at high pH values.<sup>[98,138,139]</sup> A more convenient way is to perform a neutralisation adsorption titration experiment. This method includes an initial neutralisation step using an appropriate reactant such as 0.05 M NaHCO<sub>3</sub> for the determination of carboxyl groups. The neutralisation agent is added in excess and is separated from the oxidised carbon after a sufficient equilibration time. Next, an excess of HCl is added to an aliquot of the solution to neutralise the remaining NaHCO<sub>3</sub>. The CO<sub>2</sub>, that is generated by the reaction of NaHCO<sub>3</sub> with HCl, is removed by boiling. Lastly, the solution is back-titrated with NaOH to determine the amount of free HCl. Other functional groups can be detected with suitable reactants. For example, lactone rings can be opened with Na<sub>2</sub>CO<sub>3</sub> and NaOH, whereas a weak base like NaHCO<sub>3</sub> cannot open the ring. Phenolic hydroxyl groups are weakly acidic and require stronger bases like NaOH. As an even stronger base than NaOH, NaOEt reacts with carbonyl groups to hemiacetals, and it can open carboxylic anhydrides to form the ester plus the carboxylate. However, an oxidised carbon sample usually contains more oxygen than detectable by titration, which is often attributed to ether-type groups.<sup>[92]</sup> The titration experiments can be impractical when dealing with small sample sizes.<sup>[140]</sup> Other methods to investigate the type of surface oxygen groups include spectroscopy.

Infrared (IR) spectroscopy can be used to identify surface functional groups. However, the interpretation of the IR spectra can be challenging due to the inhomogeneous character of the material with a variety of non-isolated groups.<sup>[134,140,141]</sup> Broad absorption bands are expected due to the wide range of electronic environments of the functional groups<sup>[128,142]</sup> and multiple groups may contribute to one absorption band.<sup>[140]</sup> Additionally, the strong IR absorption of carbon can pose a hindrance.<sup>[92]</sup>

Especially with mildly oxidised carbons the intensity of the absorption bands is often not sufficient.<sup>[140]</sup>

Another method for the investigation of the surface oxygen groups is temperature-programmed desorption (TPD), also known as thermo desorption spectroscopy (TDS). In this method, the oxidised carbon is heated in an inert atmosphere, and the released gases are monitored.<sup>[27]</sup> The different functional groups decompose to CO and CO<sub>2</sub> at different temperatures.<sup>[140]</sup> While carboxyl and lactone groups decompose to CO<sub>2</sub>, phenol, ether, carbonyl, and quinone groups decompose to CO. Carboxylic anhydrides on the other hand show both a CO<sub>2</sub> and CO peak.<sup>[140]</sup> One issue that may arise, especially in micropores, is the occurrence of secondary reactions. At higher temperatures, the released CO<sub>2</sub> can react with the carbon surface to produce CO, while at lower temperatures, CO can react with surface oxygen groups to form CO<sub>2</sub>.<sup>[92]</sup>

X-ray photoelectron spectroscopy (XPS) is a surface-sensitive technique that reveals the chemical composition of the first few atomic layers.<sup>[140]</sup> The amount and type of surface oxygen groups can be determined by studying the O<sub>1s</sub> and C<sub>1s</sub> peaks.<sup>[60,143]</sup> XPS can also be used to determine the grade of graphitisation of the carbon sample using the area of the  $\pi$ - $\pi^*$  peak.<sup>[144]</sup>

#### 4.2.2.3. Further Functionalised Carbons

In addition to oxidised carbon blacks, alternative surface modifications have been employed in the pursuit of novel fuel cell support materials with enhanced properties. Suitable functional surface groups may enhance the support-nanoparticle interaction leading to improved stability and catalytic activity.<sup>[34–39]</sup> Carbon surface modifications have been studied on various types of carbon materials, such as carbon blacks<sup>[145–147]</sup>, carbon nanotubes<sup>[148–151]</sup> (CNTs), fullerenes<sup>[152–154]</sup>, and graphene<sup>[155]</sup>, etc. for a broad range of applications such as solubility of CNTs,<sup>[149]</sup> biofunctionalisation<sup>[156,157]</sup>, chemical force microscopy<sup>[158]</sup>, coupling of quantum dots to CNTs<sup>[148]</sup> and many more.

Depending on the functional group to be introduced to the carbon surface and the nature of the carbon surface, many synthesis routes have been applied. Fundamentally, for covalent functionalisations, direct (or in-situ generated additives) and multi-step synthesis method can be distinguished. Examples for direct functionalisation routes include the [2+1] cycloaddition of carbenes<sup>[153,154]</sup> or nitrenes<sup>[159]</sup>, the 1,3-dipolar cycloaddition of azomethine ylides<sup>[152,160,161]</sup>, radical addition<sup>[159,162–164]</sup> and halogenation<sup>[145,165]</sup>. The multi-step synthesis procedures require a primary introduction of functional groups through oxidation or halogenation. Examples are the exchange of previously added surface chlorine groups with cyanide groups<sup>[145]</sup> or the urethane linkage with hydroxyl groups<sup>[146]</sup>.

A commonly employed multi-step synthesis route in literature is the formation of carboxylic acid groups through oxidation, followed by amide linkage. This can be achieved by a number of different synthesis routes, which are summarised in figure 4.20. The easiest approach to achieve an amide linkage is the direct reaction of the carboxylic acid group with an amine. Though, it is still debated whether the amide<sup>[38,166]</sup> is formed, or the ammonium-carboxylate zwitterion<sup>[167,168]</sup>. Alternatively, the carboxylic acid group can be converted into a more reactive compound as an intermediate step. Commonly, thionyl chloride is used to obtain the highly electrophilic acyl chloride group which subsequently forms an amide linkage with an amine.<sup>[149,169]</sup> This approach comes with the disadvantage of harsh reaction conditions.<sup>[170]</sup> Another approach with milder reaction conditions is the esterification of the carboxylic acid group with an alcohol in acidic conditions and the subsequent reaction of the ester group with an amine to form the amide bond.<sup>[170]</sup> Also, a carbodiimide coupling can be undertaken by reacting the carboxylic acid group with a carbodiimide to form an O-acylisourea intermediate which can react further with an amine to form an amide.<sup>[148,156,171]</sup> To avoid the many possible side reactions here, additives such as N-hydroxysulfosuccinimide or N-hydroxysulfosuccinimide ought to be used.<sup>[171]</sup>

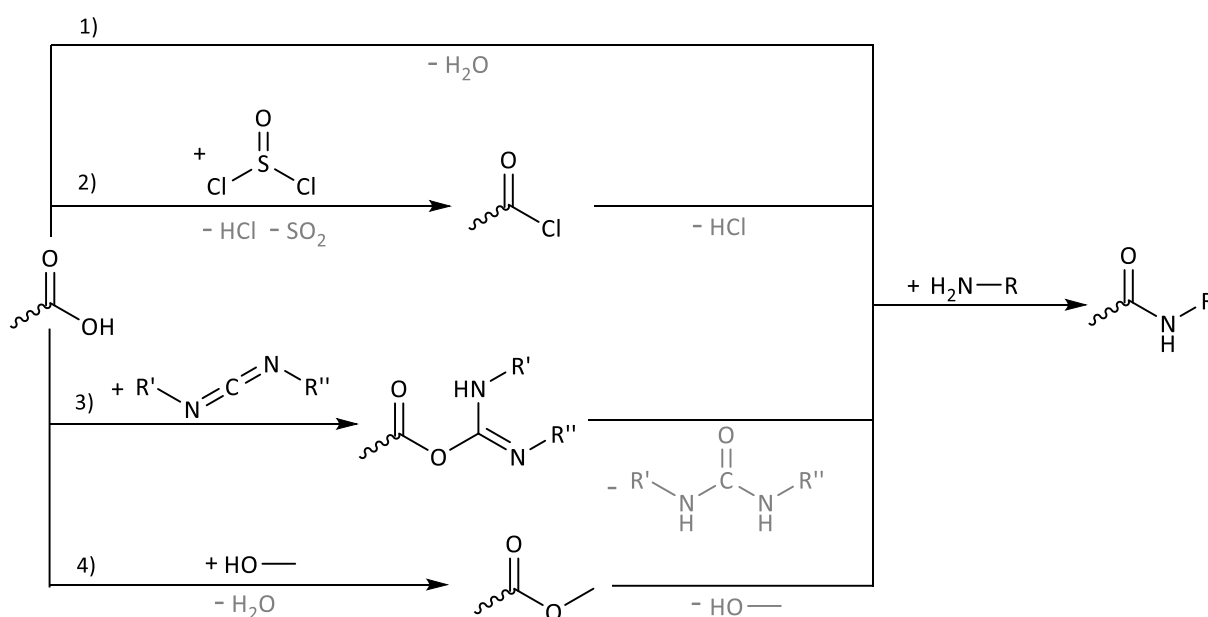


**Fig. 4.20:** Overview over different synthesis route for the carbon surface modification using oxidation, followed by amide linkage. (1) Direct synthesis route with amine. (2) Route using acyl chloride intermediate step. (3) Carbodiimide coupling. (4) Intermediate esterification route.

### 4.2.3. Nanoparticle-Support Composite Synthesis

To create a nanoparticle-support composite catalyst commonly employed in low-temperature fuel cells, one of two distinct synthesis approaches is typically employed.

The first synthesis approach, which is more prevalent in industry, is the impregnation method. In this approach, the formation of the catalytic nanoparticles is conducted directly on the carbon support material. For this, the carbon support is mixed with a solution of platinum salt, followed by the removal of the solvent in a drying step. Subsequently, the impregnated carbon support is reduced (e.g. with hydrogen or  $\text{NaBH}_4$ ) and/or heat treated to decompose the platinum salt to form platinum nanoparticles. The formation of an alloy catalyst can be achieved by employing a metal salt mixture or by subsequent impregnation step. The impregnation synthesis approach is a simple, cost-effective, one-step method. However, controlling the crystal size, size distribution, shape, and composition using this method is challenging. Furthermore, the surface chemistry and morphology of the support significantly influence the nanoparticle synthesis. One contributing factor is the presence of micropores in the substrate. Due to capillary forces, the platinum nanoparticles are preferentially formed within the micro pores, thereby reducing accessibility to the catalytic surface.<sup>[172,173]</sup>

The second synthesis approach involves the nanoparticle synthesis separated from the support material, and their subsequent deposition on the support. The separate nanoparticle synthesis can improve control over the nanoparticle morphology. Furthermore, the particles preferably deposit on the exterior surface of the support, thereby improving the catalyst surface accessibility. The particle deposition can be carried out for instance by mixing the particles and the support in a solvent and removing the solvent by evaporation. One synthesis method well suited for this purpose is the colloidal synthesis approach described in section 4.2.1. This method allows for excellent control over particle composition and morphology including size, size distribution and can even realise complex nanoparticle structures. However, the colloidal synthesis involves the application of surface-stabilising ligands, which may block the catalytic surface during fuel cell operation which is detrimental to the catalytic activity. Therefore, surfactant-free nanoparticle synthesis approaches are being investigated.<sup>[172-174]</sup>

### 4.2.4. Nanoparticle-Support Interaction

The catalytic performance and stability of a composite catalyst consisting of supported metal particles significantly depends on the interaction between the particles and the support. A strong interaction improves particle stability and accelerates the electron transfer at the electrode-electrolyte interface.

Conversely, a weak interaction may facilitate particle movement leading to agglomeration. Furthermore, during catalyst synthesis via the impregnation method, a strong interaction between the metal ion precursor and the support enhances particle dispersion.<sup>[8,9,173]</sup>

The interaction between platinum nanoparticles and its carbon substrate is attributed to the differing Fermi levels in Pt and C, which are equalised as a result of this interaction. This interaction is linked to a charge transfer from platinum to carbon, with a more substantial charge transfer associated with a stronger bond. The charge transfer can be observed using X-ray photoelectron spectroscopy (XPS). Here, the XPS of Pt 4f shifts to higher energies after the platinum nanoparticles are supported on the carbon substrate, with a greater shift indicating a stronger bond.<sup>[173]</sup>

The particle-support interaction is significantly influenced by the surface chemistry of the support. For pure carbon supports, such as the predominantly used carbon blacks, as well as CNTs or CNFs, etc. (described in Section 4.2.2), two types of interactions can be differentiated. The graphite structure consists of basal and edge planes. On the basal planes, the carbon interacts with the platinum particles via its  $\pi$ -electrons. On the other hand, a Pt-C bond is formed at the edge planes. Areas, where only one type is present are regarded as a homogeneous surface and a mixture is considered a heterogeneous surface. It has been noted that a heterogeneous surface featuring numerous inter-crystalline boundaries is more effective at stabilising metal particles in a highly dispersed state.<sup>[9]</sup>

In the case of oxidised carbon supports, the type of surface oxygen groups is critical for their interaction with the metal nanoparticles. Various oxygen groups can be categorised according to their acidity, as described in more detail in section 4.2.2.2. The surface comprises acidic carboxylic acid groups, mildly acidic anhydrides and phenolic groups, mildly basic quinones and lactones, and basic pyrone groups. Additionally, the graphene C- $\pi$  donor site also present on the oxidised surface are regarded basic as well.<sup>[137]</sup> It was observed after the synthesis via the impregnation method that mildly acidic oxygen groups and C- $\pi$  donor sites facilitate the platinum particle dispersion on the support while stronger acidic groups and basic groups are detrimental. It can be concluded that mildly acidic groups such as anhydrides and phenolic groups act as anchor sites for platinum precursor ions.<sup>[26,137]</sup>

Sintering experiments of platinum particles supported on differently oxidised carbon supports also showed improved particle stability under the presence of mildly acidic surface groups.<sup>[27]</sup> This suggests that these oxygen groups may also facilitate a good interaction with platinum particles.

Aside from oxygen functionalisation, other types of surface functional groups, such as sulfonic or phosphonic acid groups, were demonstrated to be beneficial towards interaction with platinum particles.<sup>[173]</sup> The amine-functionalised carbon substrates prepared by EGUIZABAL *et al.*<sup>[39]</sup> displayed

a higher shift of the XPS Pt 4f peaks towards higher energies compared to unfunctionalised carbon. This indicates a stronger charge transfer and thus an improved particle-support interaction.

#### 4.2.5. Degradation of Nanoparticle-Support Catalysts

Throughout the lifecycle of a fuel cell, its operation is accompanied with a decline of the cell voltage, leading eventually to its end-of-life. The origin of the voltage loss is predominantly caused by structural changes in the electrodes.<sup>[10,49]</sup>

During fuel cell operation, the catalyst has to withstand very harsh conditions, such as elevated temperature, low pH, impurities and high electrode potentials.<sup>[68]</sup> This particularly pertains to the cathode, which is generally operated at a higher electrical potential,<sup>[58]</sup> and may additionally reach high potentials up to 1.5 V during startup and shutdown phases, while the fuel cell normally operates at a rather steady potential below 1.0 V.<sup>[68,175]</sup>

The composite catalyst employed in a PEMFC typically consists of platinum-based nanoparticles, supported on a carbon black substrate. Both components of the composite, the catalytic particles and the carbon substrate, are subjected to degradation processes. The key factor in lowering the efficiency of the catalyst is the reduction of its catalytic surface area. This reduction can either arise through the loss of the catalytically active material, the growth of the catalytic nanoparticle leading to a lower surface-to-volume ratio, or the coverage of the catalytic surface. Accordingly, various degradation mechanisms can be differentiated, as represented in figure 4.21.

The degradation mechanisms are influenced by a variety of factors. Primarily, the structure of the catalyst, encompassing particle size, shape, composition, spatial distribution, type of support material and the interaction between the particles and the support material, affect the degradation process. With regard to the electrode potentials, higher potentials and potential fluctuations facilitate a significantly more severe degradation compared to lower, static potentials. However, under practical conditions, all mechanisms occur simultaneously complicating the task of distinguishing between individual processes.<sup>[68,176]</sup>

The first two degradation mechanisms encompass the dissolution of platinum. The dissolved platinum ions may either migrate from the catalyst and can be found in the ionomer membrane or the discharge water, or the ions may be redeposited on other nanoparticles. The process of platinum dissolution and redeposition follows a mechanism similar to the Ostwald ripening described in section 4.2.1. Usually, smaller particles with higher chemical potential dissolve and the redeposition on larger particles leads to a further growth. Hence it is referred to as electrochemical Ostwald ripening.<sup>[68]</sup>

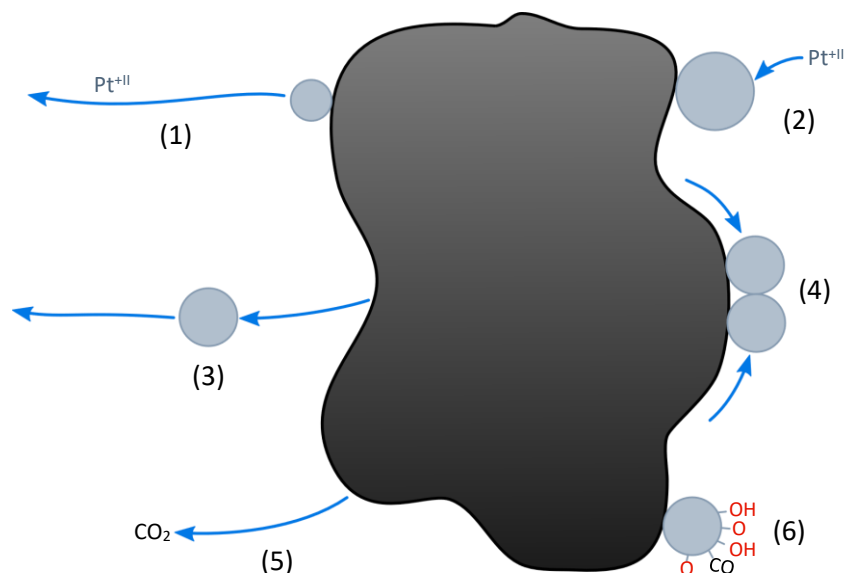


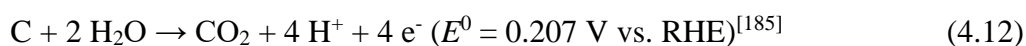
**Fig. 4.21:** Overview over the six types of degradation mechanisms of carbon supported platinum nanoparticle catalysts occurring during fuel cell operations. (1) Platinum dissolution and removal. (2) Platinum dissolution and redeposition (electrochemical Ostwald ripening). (3) Particle detachment and removal. (4) Particle migration and agglomeration. (5) Carbon corrosion. (6) Platinum surface oxidation.

Generally, due to the higher chemical potential, the dissolution of platinum alloys is favoured by smaller particle sizes,<sup>[177]</sup> anisotropic shapes, or rather Pt atoms with lower coordination numbers such as edges or kinks,<sup>[16]</sup> and less noble metal components in alloys.<sup>[178]</sup> NAGAI *et al.*<sup>[179]</sup> showed the low durability of highly catalytic active PtNi nanooctahedrons due to nickel leaching leading to spherical catalytic particles with reduced nickel content. Furthermore, platinum particles that are oxidised on their surface are more susceptible to dissolution.<sup>[175,175,180]</sup> Another contributing factor is the oxidation of the carbon support material. The electron-withdrawing carbon surface groups interacting with the platinum particles may facilitate the platinum dissolution.<sup>[181]</sup>

The third and fourth degradation mechanisms are associated with particle movement as a whole. This includes the detachment of the particles and their migration along the surface. A particle detachment without a subsequential re-adhesion to the support results in a loss of catalytic material. The migration of the particles typically promotes the agglomeration of multiple particles upon contact, leading to the formation of a larger particle with a reduced specific surface area. Particle mobility is facilitated by a low particle-support interaction, and, in the case of the agglomeration, also by a high spatial particle density.<sup>[68,176]</sup>

In addition to the degradation of catalytic nanoparticles, the carbon support material also undergoes degradation during fuel cell operation. The suggested carbon corrosion mechanism involves the reaction of carbon with water under the formation of carbon dioxide according to equation 4.12. This

carbon gasification has a thermodynamic equilibrium potential of 0.207 V; however, it is kinetically hindered. Nonetheless, the harsh operational conditions of the fuel cell, characterised by elevated temperatures, high potentials, and substantial oxygen concentrations at the cathode, render the reaction possible.<sup>[68,182,183]</sup> For commercial carbon black supports, carbon corrosion typically occurs at potentials exceeding 0.8-0.9 V<sup>[35,64]</sup> with potential fluctuations resulting in a more severe carbon corrosion than static potentials.<sup>[176,182]</sup> However, the catalytic metal, particularly platinum, catalyses the gasification of carbon.<sup>[182,184]</sup> Therefore, the electrical potential necessary for carbon corrosion is lowered to 0.6-0.8 V.<sup>[184]</sup>



The corrosion of the carbon support results in a reduction in its size, which facilitates the agglomeration or detachment of the supported nanoparticles, subsequently diminishing catalytic performance.<sup>[68,116,176,182]</sup> Furthermore, the reduction in the carbon structure may result in the destruction of the pore network essential for reactant transport, leading to mass transport losses.<sup>[68]</sup> Additionally, this shrinkage can reduce the contact between the catalyst and the current collector of the fuel cell, resulting in increased electrical resistance.<sup>[182]</sup> The carbon oxidation may also produce CO as an intermediate oxidation step,<sup>[184]</sup> which, known as a catalyst poison, may block the catalytic surface.

The degradation is presumed to start from defects in the graphite lattice of the carbon support.<sup>[182]</sup> Moreover, the type of carbon support is essential for its durability, with carbon supports of a higher degree of graphitisation exhibiting greater resistance to carbon corrosion.<sup>[35,94,95,113,182]</sup> It has been indicated that the surface oxidation of the carbon support may facilitate carbon corrosion. Additionally, the increased hydrophilicity of the oxidised carbon may assist in this process, as it leads to a higher presence of water to react with carbon (eq. 4.12).<sup>[100]</sup>

The previously described mechanisms pertained to irreversible catalyst degradation processes. Moreover, reversible catalyst degradation processes are also observed, derived from the surface coverage of the catalyst with oxides, hydroxides, or carbon monoxide. The resulting inhibition of catalytic active sites leads to a reduction in catalytic performance. Yet, the catalyst surface can be refreshed by applying a reductive potential.<sup>[176]</sup>

### 4.3. Half-cell measurements

The development of novel fuel cell catalysts typically begins on a laboratory scale. The catalysts are synthesised in small quantities and their properties are first tested separate from other fuel cell components. A suitable characterisation method for the determination of the catalytic performance are thin-film half-cell measurements as it is a fast screening method requiring only a small sample quantity.<sup>[186]</sup>

The measurement set-up, depicted in figure 4.22, typically consists of three electrodes (working electrode, counter electrode, reference electrode), immersed in an electrolyte filling the electrochemical cell. The three electrodes are connected *via* a potentiostat to control the voltage and measure the current.<sup>[7]</sup>

The sample to be examined is coated on a working electrode as a thin-film. The application of the catalyst sample to the working electrode is described in detail in section 4.3.4. The glassy carbon disc electrode is a commonly employed working electrode due to its chemical inertness and low permeability to gases and liquids.<sup>[187]</sup> A possible surface oxide layer or impurities are commonly removed from the glassy carbon electrode by polishing with a 0.05  $\mu\text{m}$   $\text{Al}_2\text{O}_3$ -particle suspension.<sup>[186]</sup>

To close the electric circuit, a counter electrode is employed. The counter electrode needs to have a sufficient area and usually consists of the same material as the material being investigated in order to prevent the dissolution of components from the counter electrode to deposit on the working electrode.<sup>[7]</sup>

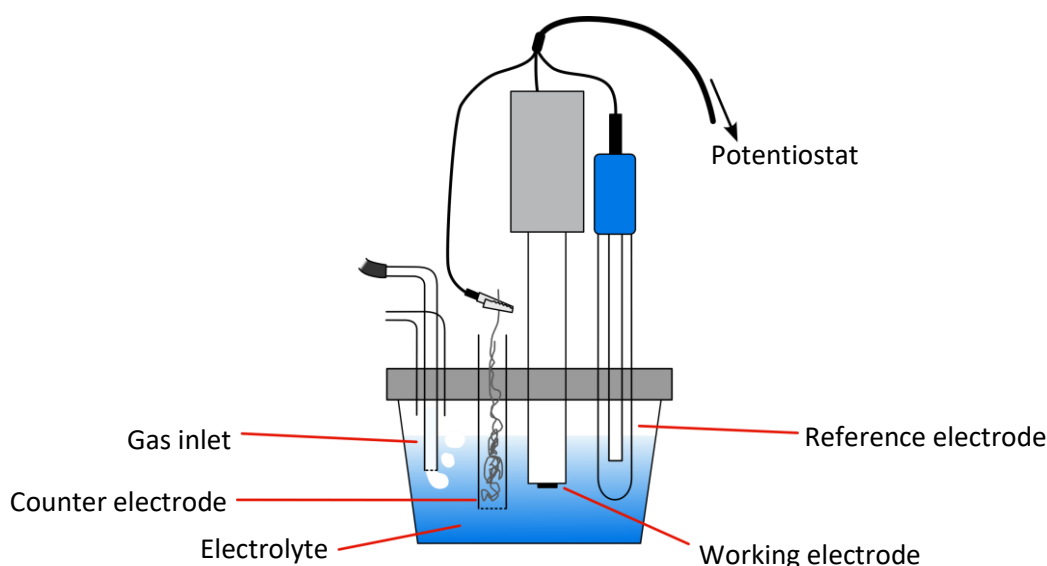


**Fig. 4.22:** Typical three-electrode set-up employed in half-cell measurements.

The third electrode is the reference electrode, which is necessary to assess the potential at the working electrode. The potential cannot be measured against the counter electrode because current flows through both. To avoid overpotential at the reference electrode, the current flowing through is kept as small as possible, using a high-resistance. The absolute potential of an electrode is dependent on the temperature, the pressure, the pH, and electrolyte composition and concentration.<sup>[188]</sup>

Electrode potentials are usually reported relative to the hydrogen electrode equilibrium potential as a reference point. The reaction occurring at the hydrogen electrode ( $\text{Pt(s)} \mid \text{H}_2(\text{g}) \mid \text{H}^+(\text{aq})$ ) is the redox reaction of hydrogen gas with dissolved hydronium ions. Several types of hydrogen electrodes can be distinguished. The potential of the standard hydrogen electrode (SHE) is defined at a hydrogen gas pressure of 0.1 MPa (1 bar) and at a pH of 0, where the activity of the hydrogen ions is 1. The absolute potential of the SHE at 25 °C is calculated to be  $4.44 \pm 0.02 \text{ V}$ .<sup>[189]</sup> However, as a basis for comparison, the potential of the SHE is defined to be 0 independent of temperature. The outdated normal hydrogen electrode (NHE) uses a solution of 1 N acid and hydrogen gas at ca. 1 atm pressure,<sup>[190]</sup> compared to the theoretically ideal conditions of an SHE.<sup>[50]</sup>

To measure the relative potential of the working electrode under practical laboratory conditions, a reference electrode with a stable, known potential is employed as reference electrodes. Reference electrodes of the first and second kind are differentiated.

Reference electrodes of the first kind consist of a metal in an aqueous electrolyte containing the metal's cations which are in equilibrium with the metal. Consequently, the electrode potential is dependent on the properties of the electrolyte. An example that is included in this category is the reversible hydrogen electrode (RHE). Compared to the SHE, the RHE is not separated from the electrolyte by a salt bridge and therefore dependent on the activity of the hydrogen ions, and accordingly on the pH of the electrolyte solution. The potential of the RHE relative to the SHE can be calculated with equation 4.13.<sup>[50]</sup> Though hydrogen is a gas, it is in equilibrium with the hydrogen ions in its electrolyte, hence the principle of a reference electrode of the first kind is applicable. In literature, the potential is often given against the RHE instead of the SHE. The advantages of the RHE lies in its low level of impurities.<sup>[188,191]</sup>

$$E_{\text{RHE}} = 0 \text{ V} - 0.0592 \text{ V} \cdot \text{pH} (25 \text{ }^\circ\text{C}) \quad (4.13)$$

In the case of reference electrodes of the second kind, the potential-determining metal ions in solution are in equilibrium with a poorly soluble salt precipitate of the electrode metal. Therefore, the equilibrium potential of the electrode depends on the solubility product of the precipitate. The activity of the anions, contained in the solubility product, can be controlled by the addition of an easily soluble

salt such as KCl. Hence, the electrode potential is dependent on the concentration of the KCl solution with a decreasing potential as the concentration increases. Furthermore, the solubility is temperature sensitive, leading to a decreasing potential with increasing temperature. Reference electrodes of the second kind typically have the advantage of a quick and reproducible adjustment of its equilibrium potential. Commonly employed reference electrodes of the second kind comprise the saturated calomel electrode (SCE,  $(\text{Hg}(\text{l}) \mid \text{Hg}_2\text{Cl}_2(\text{s}) \mid \text{Cl}^-(\text{aq.}))$ ) and the Ag/AgCl electrode ( $\text{Ag}(\text{s}) \mid \text{AgCl}(\text{s}) \mid \text{Cl}^-(\text{aq.})$ ).<sup>[188]</sup> Table 4.2 lists the electrode reactions and potentials of the most commonly used reference electrodes.

**Tab. 4.2:** Electrode potentials of common reference electrodes relative to the standard hydrogen electrode (SHE) at 25 °C and a pH of 1. Potentials of SCE and Ag/AgCl are given for saturated solutions of KCl.

Reference Electrode	Electrode reaction <sup>[188]</sup>	Potential vs. SHE / V
Reversible hydrogen electrode (RHE)	$2 \text{H}^+ + 2 \text{e}^- \rightarrow \text{H}_2$	-0.0592 <sup>[191]</sup>
Saturated calomel electrode (SCE)	$\text{Hg}_2\text{Cl}_2 + 2 \text{e}^- \rightarrow 2 \text{Hg} + 2 \text{Cl}^-$	+0.244 <sup>[192]</sup>
Silver/silver chloride electrode (Ag/AgCl)	$\text{AgCl} + \text{e}^- \rightarrow \text{Ag} + \text{Cl}^-$	+0.197 <sup>[192]</sup>

The reference electrode may be used directly in the measurement half-cell, or it can be connected to it *via* an electrolyte bridge. To reduce the voltage-drop due to the electrolyte resistance, the distance between the reference and the working electrode has to be minimised. The distance may also be bridged using a Luggin capillary.<sup>[188]</sup>

Additionally, the electrochemical cell is usually equipped with a gas inlet to flush the electrolyte with nitrogen to remove solved oxygen, or with oxygen to measure the oxygen reduction reaction. Furthermore, the temperature of the electrolyte should be kept constant, as the temperature influences the reaction velocity, albeit leading to only small differences in the measurement results.<sup>[186]</sup>

Commonly employed electrolytes are 0.1 M HClO<sub>4</sub> and 0.5 M H<sub>2</sub>SO<sub>4</sub>. Traditionally, sulphuric acid was utilised, but HSO<sub>4</sub><sup>-</sup> and SO<sub>4</sub><sup>2-</sup> ions are highly susceptible to the adsorption to Pt surfaces, which lowers the measured catalytic activity. The perchlorate anion of HClO<sub>4</sub> is comparably stable. Therefore, the 0.1 HClO<sub>4</sub> electrolyte is regarded as standard electrolyte for half-cell measurements. Nevertheless, the perchlorate ion degrades over time producing Cl<sup>-</sup> ions which inhibit the ORR. Hence, the employed HClO<sub>4</sub> is required to be fresh and the HClO<sub>4</sub> concentration should not exceed 0.1 M as the Cl<sup>-</sup> impurities are elevated at greater concentrations. Furthermore, since higher temperatures facilitate the perchlorate ion decomposition, measurement temperatures should be maintained at 25-30 °C.<sup>[186]</sup>

As the presence of impurities may compromise the accuracy of the measurements, all employed chemicals need to adhere to chemical grades of high purity. Therefore, a thorough cleaning process is also required prior to the measurement to eliminate all organic and inorganic impurities. This cleaning process may involve soaking of the glass and *Teflon* equipment in concentrated acids, such as sulphuric acid or peroxomonosulphuric acid, followed by repeated rinsing with ultrapure water.<sup>[186]</sup>

### 4.3.1. Cyclic Voltammetry

Cyclic voltammetry (CV) serves as a valuable technique for investigating processes occurring on the surface of electrocatalysts. In this methodology, a triangular voltage profile (fig. 4.23) is applied to the working electrode in a cyclic manner, and the resulting current response is measured. Typically, the reversal potentials  $E_{\text{rev-low}}$  and  $E_{\text{rev-up}}$  are selected within the range for hydrogen ( $E_{\text{H}_2\uparrow}$ ) and oxygen ( $E_{\text{O}_2\uparrow}$ ) evolution. Common reversal potentials for a full surface layer diagram include 0 or 0.05 V vs. RHE as lower and 1.0 or 1.2 V as upper reversal potential. To minimise a deactivation of the electrode during experimentation, a scan rate of at least 0.1 to 0.3 V s<sup>-1</sup> should be employed.<sup>[188]</sup>

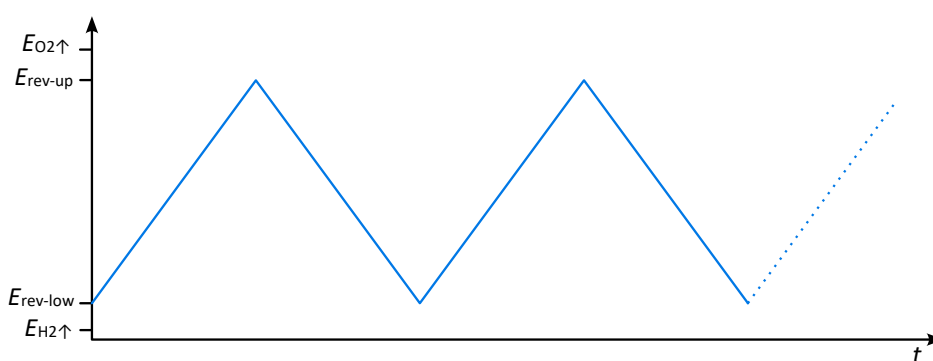


**Fig. 4.23:** Course of the applied potential of a CV measurement.

The measurement is conducted in a nitrogen-flushed electrolyte which contains no substances that can be electrochemically converted within the reverse potentials. Therefore, the resulting currents are solely based on the formation of surface chemisorption layers of hydrogen and oxygen. The current plotted against the respective potential of one cycle is called surface layer diagram. The layered structure diagrams are characteristic of each electrode in a specific electrolyte and can be used to compare the activities of different electrodes. A typical surface layer diagram of platinum in perchloric acid is shown in figure 4.24.<sup>[188]</sup>

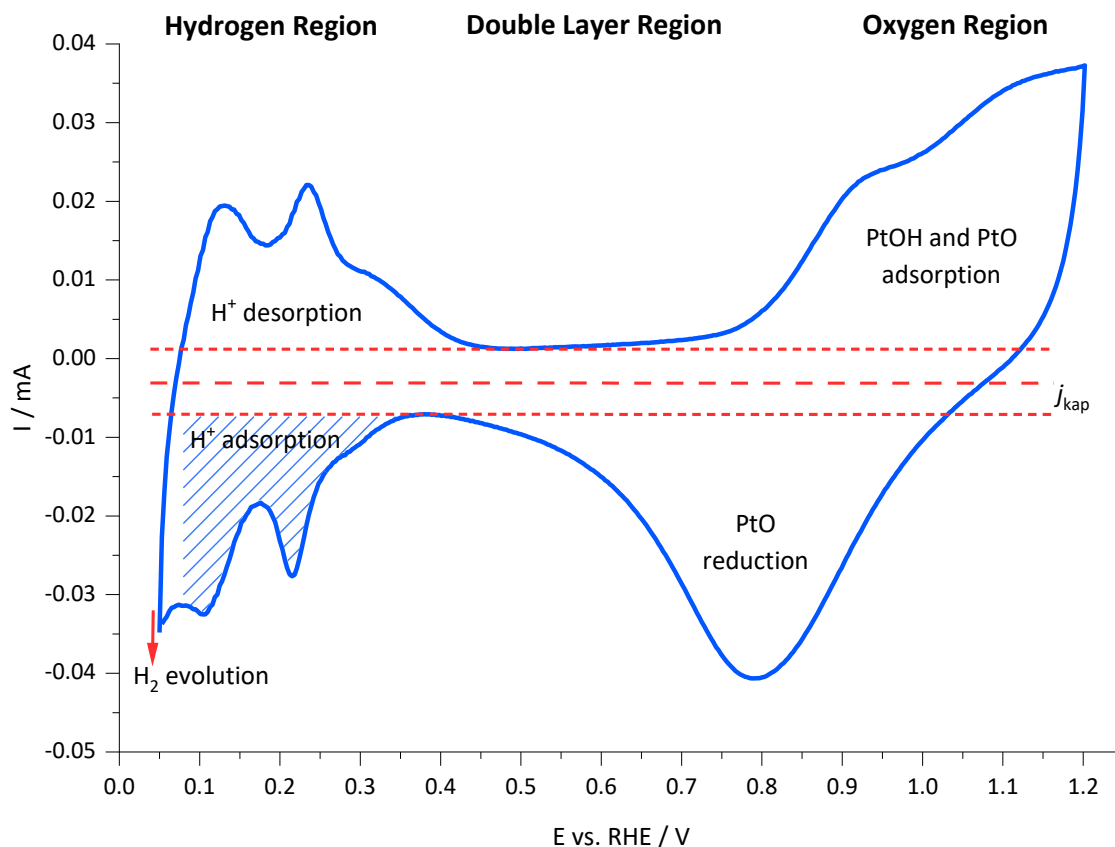


**Fig. 4.24:** Surface layer diagram of a polycrystalline Pt disc electrode in 0.1 HClO<sub>4</sub>, recorded with a scan rate of 0.1 V s<sup>-1</sup> from 0.05 to 1.2 V.

The surface layer diagram can be divided with increasing potentials into the hydrogen region, the double layer region and the oxygen region.

Upon application of a voltage, the electrolyte ions of the opposite charge adsorb to the electrode. Immediately adjacent to the electrode, counterions adsorb without a solvation shell, while at greater distances, a diffuse ion cloud is formed, encompassing a solvation shell. The concentration of this ion cloud diminishes with increasing distance from the electrode.<sup>[50]</sup> This ion layer is referred to as electric double layer. To overcome the electric double layer, the capacitive current  $j_{cap}$  is required, which is dependent on the double layer capacitance  $C_d$  and the scan rate as shown in equation 4.14. Therefore, at a constant scan rate, the double layer current remains constant across the entire potential range and adds to the currents originating from surface chemisorption. This can be seen in the centre of the surface layer diagram of platinum, where, despite the absence of chemisorption peaks, a current which can be attributed to the double layer current, is still recorded.<sup>[188]</sup>

$$j_{\text{cap}} = C_d \frac{dE}{dt} \quad (4.14)$$

Located on the right side of the surface layer diagram is the oxygen region. At potentials above approximately 0.8 V vs. RHE, an anodic peak occurs, originating from the chemical reactions outlined in equation 4.15 and 4.16. Upon reversal of the potential, the oxide layer is removed, giving rise to a cathodic peak in the range of approximately 1.0 to 0.4 V.<sup>[188]</sup> At potentials above ca. 1.5 V, the oxygen evolution reaction occurs, where molecular oxygen is formed.<sup>[193]</sup>



Below 0.4 V, a cathodic peak emerges which can be ascribed to the formation of a hydrogen adsorption layer according to equation 4.17. The reverse reaction occurs after reversal of the potential, resulting in an anodic peak. The different peaks within the hydrogen peak are attributable to different crystal facets of the platinum surface.<sup>[188]</sup>



The hydrogen adsorption peak transitions seamlessly into the hydrogen evolution peak at even lower potentials. The current originating from the hydrogen adsorption decreases gradually while the current originating from the hydrogen evolution increases gradually with decreasing potential. The cathodic minimum, which is visible in the surface layer diagram at ca. 0.075 V, can be attributed to the approximately equal rate for hydrogen adsorption and evolution.<sup>[194]</sup>

Since the hydrogen adsorption peak displays the current resulting from the formation of a monolayer of hydrogen, its area (shaded in figure 4.24) can be employed to calculate the electrochemical active surface area. The minimum, which signifies the transition to the hydrogen evolution reaction, should be designated as the lower x-limit of integration, while the capacitive double layer current should define the upper y-boundary for the integration. The integrated charge as a function of time yields the hydrogen adsorption charge  $Q_{\text{H,ad}}$ . It can be used to calculate the electrochemical active surface area (ECSA) according to equation 4.18. For this,  $Q_{\text{H,ad}}$  is divided by the theoretical charge of a full monolayer of H atoms on a clean polycrystalline Pt surface  $Q_{\text{H,theo}}$ , which amounts to  $210 \mu\text{C cm}^{-2}$ . Furthermore, the ECSA is given in relation to the mass of platinum  $m_{\text{Pt}}$  employed on the working electrode.<sup>[186,194]</sup>

$$\text{ECSA} = \frac{Q_{\text{H,ad}}}{m_{\text{Pt}} \cdot Q_{\text{H,theo}}} \quad (4.18)$$

### 4.3.2. Oxygen Reduction Reaction

The oxygen reduction reaction (ORR) that is occurring at the cathode of most fuel cells can be investigated as a half-cell reaction in a laboratory scale. Since the ORR has slower kinetics compared to the hydrogen oxidation reaction (HOR), researchers typically concentrate on improving fuel cell catalysts in regard to this reaction. In literature on novel fuel cell catalysts, the ORR activity is the most widely stated value for comparison of the catalytic activity.

The ORR is conducted using the standard three-electrode half-cell set-up described in section 4.3. Typically, prior to the actual measurement, a preliminary electrochemical cleaning step of the working electrode is conducted in the nitrogen-flushed electrolyte *via* potential cycling, for example between 0-1.2 V vs. RHE. The precise reversal potentials, number of cycles, and scan rate has to be individually adjusted to the specific catalyst. Subsequently, the ECSA is determined as described in section 4.3.1.<sup>[186]</sup>

Thereafter, the electrolyte is flushed with oxygen and the ORR polarisation curve is measured at 1600 rpm in a linear sweep, typically following the order 1.03 V → 0.05 V → 1.03 V. The measurement is conducted with a sweep rate of 5-20 mV s<sup>-1</sup> since the measurement is influenced to a larger extent by impurities at lower sweep rates and the capacitive effects are larger at higher sweep rates. To account for capacitive currents, a background sweep using the same measurement protocol in nitrogen-purged electrolyte is subtracted from the ORR polarisation curve.<sup>[186]</sup>

A typical ORR polarisation curve is displayed in figure 4.25. At high potentials, the ORR rate is kinetically controlled. The reaction proceeds slowly, resulting in very low increases of the current density as the potential decreases. In the potential region between 0.75 and 1.00 V, the reaction is mixed kinetic-diffusion-controlled. The reaction rate increases quickly, resulting in a steep drop of the current density. At ca. 0.7 V, the current density reaches a plateau, where it is limited by the diffusion rate of the reactants dependent on the rotation speed.<sup>[186,195]</sup>

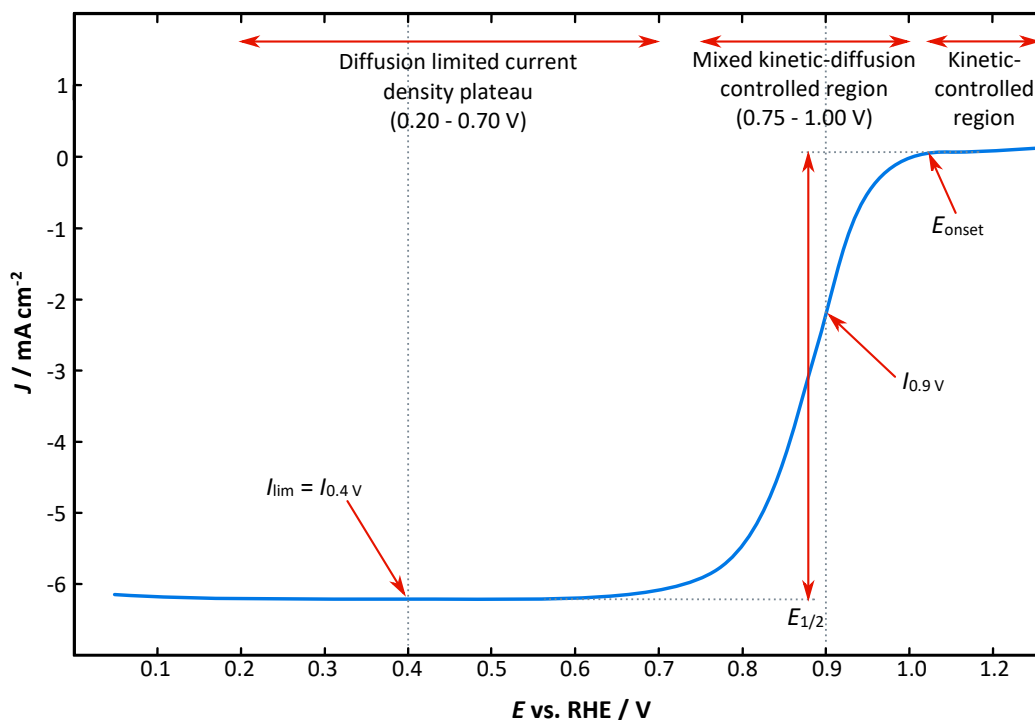


Fig. 4.25: Typical ORR polarisation curve.

From the polarisation curve, the onset-potential  $E_{\text{onset}}$  and the half-wave potential  $E_{1/2}$  can be obtained as visual benchmark values with good catalysts displaying higher potentials. Since  $E_{\text{onset}}$  is defined differently in literature,  $E_{1/2}$  is a more solid value for comparison.<sup>[186,195]</sup> For the calculation of the ORR activity, the back-ground-corrected currents at 0.4 V and at 0.9 V are employed to calculate the mass-transport corrected kinetic current  $I_k$ , according to equation 4.19. The current at 0.4 V gives the diffusion-limited current  $I_{\text{lim}}$ . The current at 0.9 V is used to quantify the electrocatalytic activity towards the ORR as interferences from mass-transport losses might have an influence at currents above 0.9 V.<sup>[186]</sup>

$$I_k = \frac{I_{0.4\text{V}} \cdot I_{0.9\text{V}}}{I_{0.4\text{V}} - I_{0.9\text{V}}} \quad (4.19)$$

The ORR activity of a catalyst is usually given in relation to the employed platinum on the working electrode as the mass-specific ORR activity  $I_m$  (eq. 4.20), or the surface area-specific ORR activity  $I_s$  (eq. 4.21).<sup>[186]</sup>

$$I_s = \frac{I_k \cdot Q_{\text{H,theo}}}{Q_{\text{H,ad}}} \quad (4.20)$$

$$I_m = \frac{I_k}{m_{\text{Pt}}} \quad (4.21)$$

### 4.3.3. Accelerated Stress Test

The gradual degradation of a fuel cell catalyst during operation leads to a decline of the cell voltage. Consequently, a significant amount of research focusses on the reduction of the degradation rate. Different types of degradation processes are discussed in section 4.2.5. The novel catalysts which are developed in a laboratory scale are examined in half-cell measurements with regard to their electrochemical stability. In this context, accelerated stress tests (AST) are employed to simulate fuel cell operations in a short time-frame. The aqueous acidic electrolyte is used to mimic the Nafion membrane. Through a combination of AST with imaging techniques, underlying degradation mechanisms can be investigated.<sup>[68,176]</sup>

During AST measurements, a specific sequence of potentials is applied to the working electrode for an extended duration. As different potential windows result in different types of degradation, a multitude of potential windows in the range of 0 to 1.5 V vs. RHE is employed. Furthermore, fluctuating potentials accelerate the catalyst degradation process compared to static potentials. Fluctuating potentials can be simulated as cyclic triangular-wave or square-wave potentials. To assess the degradation rate, the catalytic activity is measured as ORR or ECSA before, after, and after in-between cycles. Depending on the type of fuel cell operation to be simulated, varying AST protocols are employed. Typically, fuel cell load cycles or start-stop-conditions (fig. 4.26) are investigated as proposed by the Fuel Cell Commercialization Conference of Japan (FCCJ).<sup>[6,176]</sup>

The AST load cycle simulates the conditions during a normal fuel cell operation, where typically potentials between 0.6 and 1.0 V vs. RHE arise. 0.6 V corresponds to the maximum load and 1.0 V arise during idle stop operation. During AST, the potential is usually cycled between the two potentials in a square-wave potential.<sup>[196]</sup>

The dominantly detrimental effect on the catalyst degradation are the conditions during the start-up and shut-down of a fuel cell. Here, the gas purging is insufficient, resulting in cathode potentials locally rising up to 1.5 V.<sup>[6,68]</sup> AST protocols investigating the degradation during start-stop conditions typically apply a triangular-wave potential between 1.0 and 1.5 V<sup>[6]</sup> or a constant potential at 1.5 V<sup>[176]</sup>.

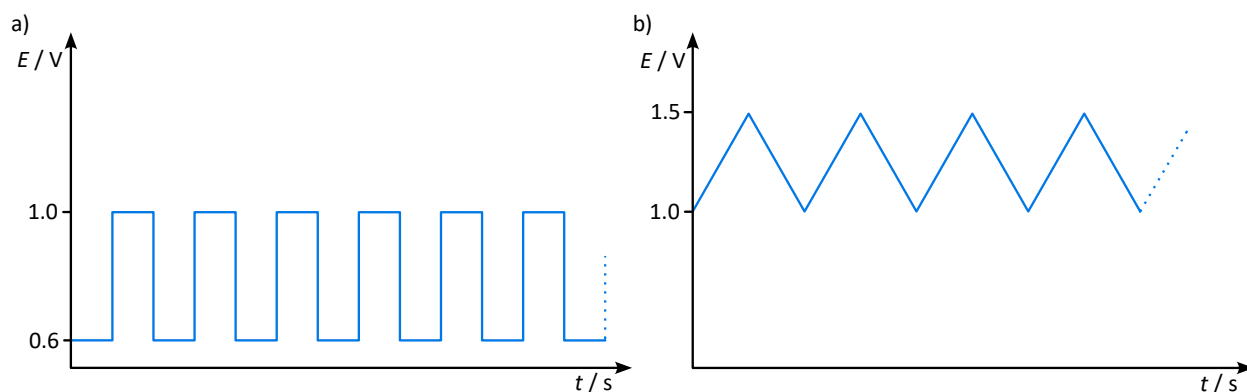


**Fig. 4.26:** Schematic representation of the course of the applied potential (vs. RHE) during AST as recommended by the FCCJ. **a)** Load cycles. **b)** Start-stop cycles.

#### 4.3.4. Catalyst Thin-Films

The disc-electrode half-cell measurements used to assess the catalytic activity of a novel catalyst on a laboratory scale is accompanied with the challenging production of suitable thin-films coated on the glassy carbon disc electrode. The thickness of the thin-film should not exceed  $0.2\ \mu\text{m}$  as thicker layer may increase the mass-transport resistance leading to lower measured activities. Consequently, inhomogeneously distributed thin-films, exhibiting varying morphologies across different measurements, reduce the reliability of the measurement.<sup>[186]</sup>

The effect of the film quality on the ECSA and ORR was illustratively presented by GARSANY *et al.*, depicted in figure 4.27. The detrimental effect of a non-uniform film is clearly visible as a lower hydrogen adsorption peak in the surface layer diagram (fig. 4.27a) and as a lower diffusion-limited and mixed kinetic-diffusion controlled current in the ORR polarisation curve (fig. 4.27b). The detrimental effect is more pronounced for the ORR compared to the ECSA, as the intermediate and good film show barely any difference in the hydrogen adsorption peak, while a clear difference is visible in the polarisation curves.<sup>[186]</sup>

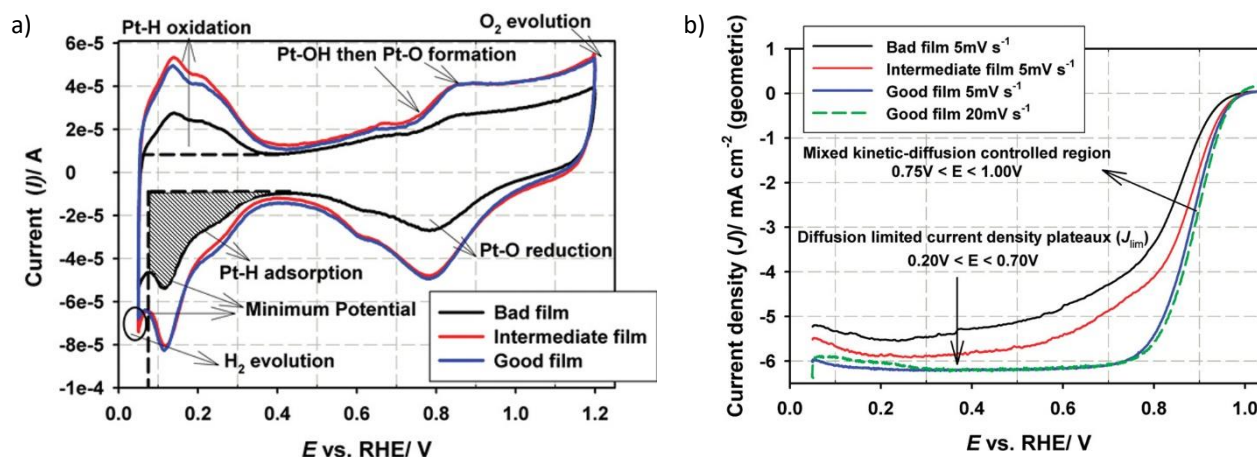


**Fig. 4.27:** Influence of the thin-film quality on the a) electrochemical active surface area (ECSA) and oxygen reduction reaction (ORR). Reprinted with permission from [186]. Copyright 2010 American Chemical Society.

For the preparation of the catalyst thin-film, the supported nanoparticle catalyst is suspended to form a so-called catalyst-ink. A drop of the ink is subsequently applied to a freshly-polished and cleaned glassy-carbon electrode and allowed to dry. This preparation procedure entails a problem, which is inherent to the drying of a drop of suspension: The suspended particles experience an outward-flow during drying, resulting in their precipitation in the form of a ring. This phenomenon is known as the coffee-ring effect which is described in detail in the next section.

To counter the coffee-ring effect, GARSANY *et al.*<sup>[197]</sup> introduced the rotational drying method. Here, the working electrode is placed upwards on a rotor and the drop of ink is applied. During drying, the electrode is rotated around its longitudinal axis with an optimal speed of 700 rpm. The group could achieve an improvement of the film-uniformity and ECSA and ORR reproducibility with this method. KE *et al.*<sup>[198]</sup> was able to produce homogenous thin-films by using an ‘intermittently microcontact-coating fine-droplets’ method. In this method, a multitude of 3 nL-sized catalyst drops was applied in an intermittent pattern with a micro-distance contact between the drops and the surface. The tiny drops containing a highly-volatile liquid evaporated in less than a second, leaving the catalyst particles anchored to the surface. The obtained evenly-distributed films resulted in higher ORR values, while negligible effects were observed towards ECSA.

An important factor towards the film quality is the stability of the catalyst ink. To produce a uniform film, the ink should be homogeneously suspended and stable, as aggregates increase the mass transport resistance. Usual ink suspending agents, employed for metal nanoparticles on carbon supports, consist of a mixture of water with different alcohols in varying ratios. The exact ink recipe depends on the exact catalyst and has to be optimised accordingly. For this, the concentration and the

pH of the ink formulation has to be taken into account as well. For the formation of the well suspended ink, an ultrasonic bath is often employed for mixing.<sup>[186,199,200]</sup>

In addition, *Nafion* is often added to the ink formulation, or coated directly onto the dried thin-film to improve the adhesion of the catalyst film to the glassy carbon electrode. Small *Nafion* additions to the ink formulation have been found to improve the stability of the suspension due to the repulsive energy of the negatively charged  $\text{SO}_2^-$  side chains. However, the presence of *Nafion* has an inhibiting effect on the ORR activity (with a minimal impact on ECSA). This inhibiting effect has been attributed to blockage of Pt surface sites due to the adsorption of the sulfonate anion to the Pt surface.<sup>[186,199,201,202]</sup>

#### 4.3.4.1. Coffee-ring effect and Marangoni effect

When a drop containing uniformly dispersed particles dries, the particles get deposited in form of a ring at the edge of the drop. The effect is often observed in daily life: When for example a drop of coffee, or tea is spilled and left to dry, the resulting residue forms a ring, hence the name of the phenomenon: coffee-ring effect.<sup>[203]</sup> The same effect also plays a great role in research and industrial applications such as printing<sup>[204]</sup>, coating<sup>[205]</sup>, and biology<sup>[206]</sup>.

The mechanism behind the phenomenon was extensively investigated by DEEGAN *et al.*<sup>[203,207,208]</sup> They pinpointed the reason for the ring-shaped deposition in the pinning of the drop's contact line and the higher evaporation rate at the contact line in comparison to the drop's centre.

Normally, a uniform evaporation would result in a receding contact line with constant contact angle, as shown in figure 4.28a. On the other hand, when the contact line is pinned, and the dispersant evaporates at the edge of the drop, more dispersant needs to be added from the centre to remain the drop's equilibrium height profile that is dictated by surface tension. This radial outward flow carries the dispersed particles with it and leads to a ring-shaped deposition at the drop's edge. Consequently, the contact angle will have to decrease during the drying process with the pinned contact line as seen in figure 4.28b.<sup>[203]</sup>

DEEGAN *et al.* describe the process of the pinned-contact line's origin as a self-pinning: It is suspected that initially, the first particles adsorb on the substrate's surface with a slight surface roughness or impurities acting as a foothold. From here, the process is self-reinforcing with the first adsorbates acting as the foothold for the next. Eventually, the adsorbates at the drop's edge will keep the contact line much longer fixed than just through the substrate.<sup>[208]</sup> In accordance, smooth *Teflon* shows no pinned contact line and thus no coffee-ring whereas rough *Teflon* does.<sup>[207]</sup>

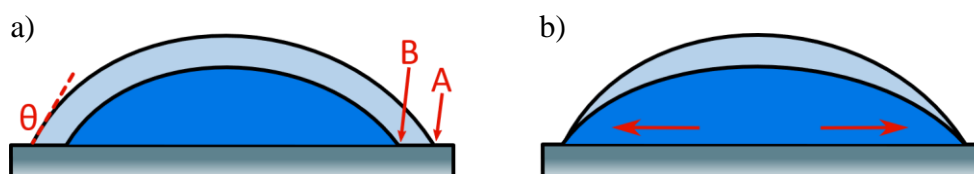


**Fig. 4.28:** Schematic illustration of the drying process **a)** without fixed contact line and **b)** with fixed contact line. The pale blue profile shows the drop before drying and the deep blue profile during the drying process. The points A and B indicate the motion of the contact line. The arrows indicate the radial outward flow that is responsible for the ring-shaped deposition.

The conditions under which the coffee-ring forms is the subject of research by many groups. DEEGAN *et al.*<sup>[203,207]</sup> showed in their experiments, that the coffee-ring formation is insensitive to a wide range of experimental conditions such as temperatures, humidity, and pressure. The effect occurs within a wide range of solute concentrations, solute sizes and drop sizes with a minimal kinetic drop-size limit of ca. 1<sup>[209]</sup> to 10<sup>[210]</sup>  $\mu\text{m}$ . Below this diameter, the fluid evaporates faster than the movement of the particles and no coffee-ring is formed.

DEEGAN *et al.*<sup>[207]</sup> observed the coffee-ring effect with various dispersants such as water, acetone, methanol, toluene, and ethanol. However, HU *et al.*<sup>[211]</sup> showed that when using octane as dispersant, no coffee-ring is formed, and the dispersed particles instead precipitate preferably at the drop's centre. In case of octane or other alkanes another effect plays a predominant role: the Marangoni effect.

The Marangoni effect derives from a surface tension gradient induced flow from low to high surface tension. Originally<sup>[212]</sup> described for a liquid-liquid interface, it can also derive from thermal differences. In a drying drop, the only heat source is the substrate, where the drop is drying on. Hence, the drop is the coldest on its tip where it is the furthest away from the substrate, even though this is the place with the least evaporative cold. Since the surface tension is inverse proportional to the temperature, the temperature gradient also leads to a surface tension gradient with the highest surface tension at the drop's tip. This induces a radial inwards flow – the Marangoni effect.<sup>[207]</sup>

This Marangoni inward flow counteracts the outward flow that is responsible for the coffee-ring effect. If the Marangoni effect, which is dependent upon the type of fluid,<sup>[211]</sup> is stronger than the coffee ring effect, it can reverse the deposition pattern.<sup>[207]</sup> However, surface contaminants with a concentration as little as 300 molecules  $\mu\text{m}^{-2}$ <sup>[213]</sup> can inhibit the Marangoni flux.<sup>[214]</sup>

Another way to control the flows arising during drying is by manipulating the evaporation rate. DEEGAN *et al.* linked the coffee-ring effect to the relation of the evaporation profile to the height profile of a drop. The evaporation profile describes the rate of evaporation relative to the radial distance from the drop's centre. This relationship was further investigated by DEEGAN *et al.* by

observing the drying process of three identical drops under different drying conditions. Figure 4.29 compares the evaporation profiles with the height profile of the drop.<sup>[207]</sup>

The first drop was allowed to dry normally. Here, the rate of evaporation is the highest at the drop's edge and decreases towards the centre. The drop formed a coffee-ring after drying. The second drop was mounted on a pedestal surrounded by a water bath which water level coincided with the base of the drop. This leads to an approximately spatially uniform evaporation rate. After drying, this drop also developed a coffee-ring, but with a broader ring. The third drop was placed in a chamber with a small hole above the drop's centre. In this case, the evaporation occurred primarily at the drop's centre with a decreasing evaporation rate towards the edge, so that the evaporation profile matched the drop's height profile. In this case, the solute dried in the form of a uniform deposit. Therefore, it can be concluded that a coffee-ring will be formed whenever the evaporation profile mismatches the height profile of the drop.<sup>[207]</sup>

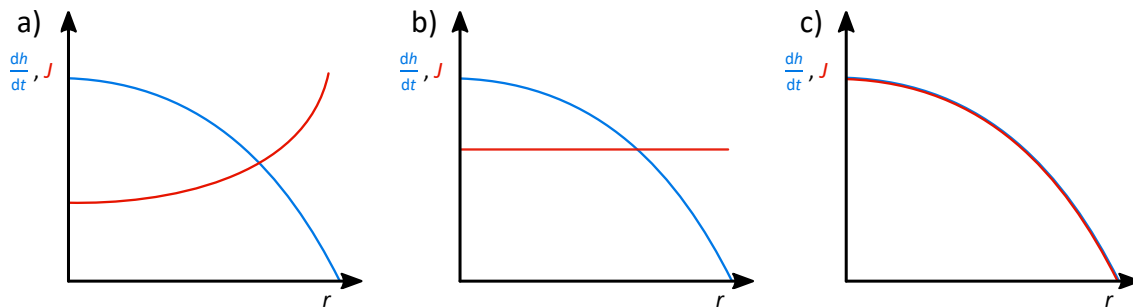


**Fig. 4.29:** Change in the interface height (blue) of the drop and evaporation profiles (red) of three different drying conditions: **a)** Allowed to dry normally. **b)** Mounted on a pedestal surrounded by water bath with a water level coinciding with the base of the drop. **c)** Surrounded by a chamber with a small hole above the centre of the drop.

Further research conducted on this subject identified further influences on the coffee-ring formation such as interparticle interaction,<sup>[215–217]</sup> additives,<sup>[217–219]</sup> drying orientation<sup>[220]</sup> or application of AC Voltage.<sup>[221]</sup> In many cases, the formation of a coffee-ring could be suppressed, yet every approach only applied to very specific conditions, wherefore the drying conditions have to be adjusted depending on the specific situation.

## 5. Objective

Fuel cells employ electrocatalysts to reduce the activation energies of the fuel oxidation and oxygen reduction reaction occurring at the anode and cathode, respectively.<sup>[7]</sup> Most catalysts are based on a heterogenic platinum or platinum-alloy catalyst. To increase the utilisation of the nanoparticle surfaces, the nanoparticles are supported on a high-surface, conducting substrate to form a nanoparticle-support-composite catalyst.<sup>[8,9]</sup> Hence, the interaction between the nanoparticles and their substrate is paramount for the catalyst's catalytic activity and their stability. The electrochemical degradation of the catalyst, which contributes to the fuel cell's eventual end-of-life, can be partially attributed to particle agglomeration and detachment. Accordingly, an improved binding strength of the particles to the substrate may lead to lower degradation rates and thus longer life-times.

The aim of this work was to introduce functional groups to the surface of the carbon-based support materials, which could serve as anchor groups with a stronger, more localised interaction with the catalytic nanoparticles. As a base material for functionalisation, the carbon black *Vulcan XC72R* was chosen, as it is one of the most widely employed support materials in fuel cell catalysts.<sup>[8,123]</sup> The functional groups introduced to the carbon black comprised of various oxide groups, amine groups and thiol groups.

Subsequently, the composite catalysts were to be synthesised by depositing colloidal platinum or platinum-alloy nanoparticles onto the functionalised support materials. The employed precipitation method for the particle deposition was to be customised to the functionalised carbons and the catalytic particles with the objective to achieve catalysts with homogeneously distributed catalytic nanoparticles.

For the quantification of the catalytic activity, thin-film disc-electrode half-cell measurements were employed as they offer a high screening throughput and require only minimal quantities of the test substance.<sup>[186]</sup> The measurement procedure and preparation were to be adjusted to increase the reproducibility and a test protocol with the goal to quantify the electrochemical degradation was to be established. Finally, the adjusted electrochemical measurement procedure was to be employed to evaluate the influence of the introduced functional groups in regard to electrocatalytic activity and stability.

## 6. Results and discussion

The catalyst in fuel cells commonly consists of a nanoparticle-support composite material, where the metal nanoparticles act as the catalytically active component that is distributed on a high surface, conductive substrate.<sup>[8,9]</sup> An improved interaction between catalytic nanoparticles and support material can improve the catalytic activity and stability. One approach to improve the particle-support interaction is the introduction of functional groups to the surface of the support material.<sup>[34–39]</sup> The first part of this work focusses on the surface modification and characterisation of carbon support materials. To form the catalyst, catalytic nanoparticles are deposited onto the surface of the support material. The second part of this work focusses on the catalyst synthesis and their electrochemical characterisation. The results are based on the practical work, conducted at the University of Hamburg between 2019 and 2024.

### 6.1. Functionalisation of Carbon Black

The most widely used support material for catalysts in fuel cells is carbon black<sup>[9,118]</sup> which has a similar chemical structure as graphite, but in an amorphous modification.<sup>[91]</sup> The metal nanoparticles are held onto the carbon black support *via* interaction with the carbon's  $\pi$ -system.<sup>[136,137]</sup> On the other hand, functional groups can bind through their electron lone pairs to the metal nanoparticles.<sup>[39]</sup> Thus, the introduction of functional groups to the support material's surface can lead to a stronger, more localised interaction of the nanoparticles with their support. A simple method for the introduction of functional groups is the chemical oxidation discussed in section 6.1.1. The incorporation of amine and thiol functionalisations can be achieved through a condensation reaction of a diamine or dithiol with the carboxylic acid groups previously introduced through oxidation, which is explored in section 6.1.2.

### 6.1.1. Oxidised Carbon Blacks

The carbon black *Vulcan XC72R* from *Cabot*, that is used in this work as a starting material, was oxidised in a first step following a modified synthesis method based on the work of EGUZABAL *et al.*<sup>[39]</sup> To achieve this, the carbon was stirred in a mixture of three parts concentrated sulphuric acid and one part concentrated nitric acid at room temperature for varying durations. Reference experiments utilising only nitric acid were additionally carried out. According to literature, the functional groups formed during this synthesis include a variety of oxide groups such as carboxylic acid, hydroxyl or lactone groups resulting from the unspecific oxidation reaction<sup>[92]</sup>, as described in detail in chapter 4.2.2.2.

Following the oxidation, the elemental composition was determined through organic elemental analysis. Figure 6.1 displays the elemental composition for *Vulcan XC72R* with oxidation times ranging from half an hour to two weeks using a 3:1 mixture of sulphuric acid and nitric acid.

The elemental composition of the unfunctionalised *Vulcan XC72R*, primarily composed of carbon, also contained around 3 a% of hydrogen. The graphene layers of carbon blacks are often saturated with hydrogen, which can be explained due to the manufacturing process using hydrocarbons as source material.<sup>[92]</sup> Furthermore, the sample contains traces of oxygen and sulphur, which can be attributed as remnants of the manufacturing process as well.<sup>[9,92]</sup>

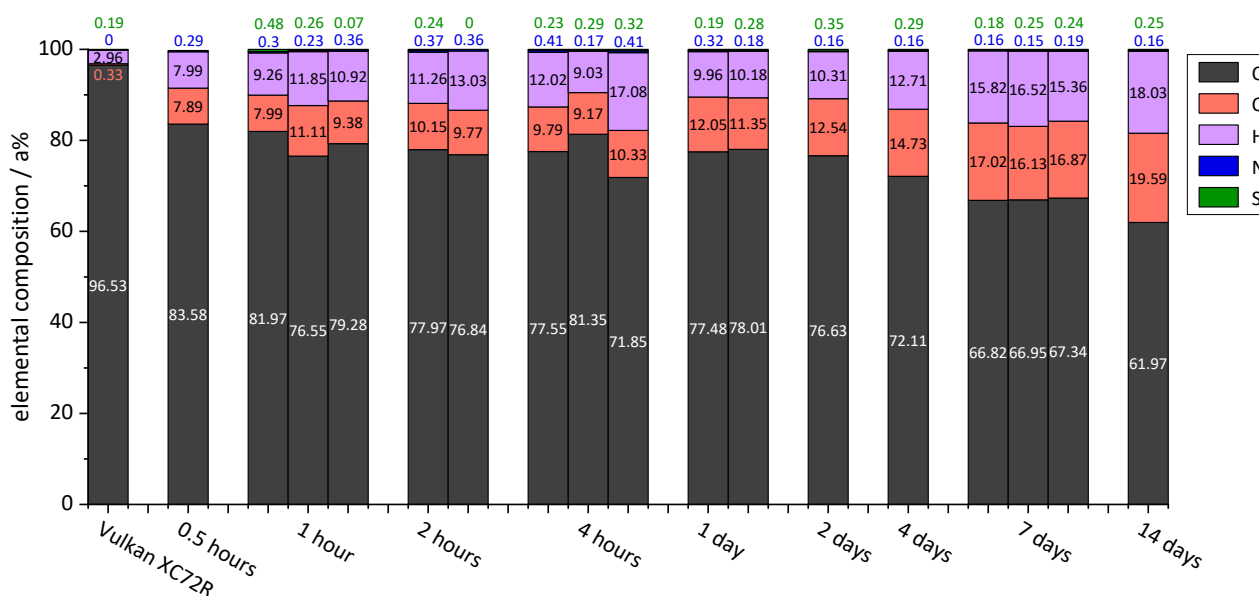


**Fig. 6.1:** Elemental composition of *Vulcan XC72R*, oxidised with a mixture of three parts concentrated sulphuric acid and one part concentrated nitric acid at room temperature for varying durations.

Even after short oxidation times, the atomic fraction of oxygen and hydrogen increases, which indicates the successful introduction of oxide groups. The oxygen and hydrogen contents progressively increase with oxidation time due to the ongoing oxidation process with a declining reaction rate as the reaction time proceeds, which aligns with the observations of VOET *et al.*<sup>[222]</sup> After half an hour of oxidation time, the sample contains around 8 a% oxygen and hydrogen and the content increases to ca. 20 a% oxygen and ca. 18 a% hydrogen after two weeks of oxidation. The traces of sulphur and nitrogen after oxidation can be attributed to the use of sulphuric acid and nitric acid, as well as remnant from the starting material in the case of sulphur.

Several oxidation experiments were repeated to assess their reproducibility. Deviations in elemental composition around 1-3 a% were observed in each instance, with the most significant deviation noted in the four-hour oxidation experiments, where, one sample contained ca. 9 % hydrogen, while the other contained around 17 % hydrogen. This variability can be attributed to the inhomogeneous nature of the amorphous carbon material. Nevertheless, the general trend of increased oxygen and hydrogen fractions with increased oxidation times is still notable.

A reference experiment was conducted using only concentrated nitric acid at room temperature as oxidant for varying oxidation times. The elemental composition of the oxidised carbons is displayed in figure 6.2. In contrast to the oxidation process using a mixture of nitric acid and sulphuric acid, the oxygen content of the oxidised carbon black only increased slightly to 2-3 a% and remained consistent throughout the two-week oxidation period, suggesting a less efficient oxidation process as also observed by CALVILLO *et al.*<sup>[223]</sup> The hydrogen content on the other hand increased up to around 9 a% after one day of oxidative treatment before continuously decreasing to ca. 4 a% after two weeks. While the oxidative treatment with a mixture of sulphuric acid and nitric acid resulted in roughly equal contents of hydrogen and oxygen, treatment with nitric acid alone led to a higher hydrogen-oxygen-ratio with a maximum of 4.3:1 after one day of oxidation. This suggest that a different kind of oxidant results in the formation of different oxygen groups. Likewise, TORRES *et al.*<sup>[26]</sup> observed that the utilisation of HNO<sub>3</sub> as oxidant resulted in the formation of both strong and mild oxide groups while H<sub>2</sub>O<sub>2</sub> or O<sub>3</sub> treatment produced predominantly mild oxide groups, as inferred from TPD experiments.

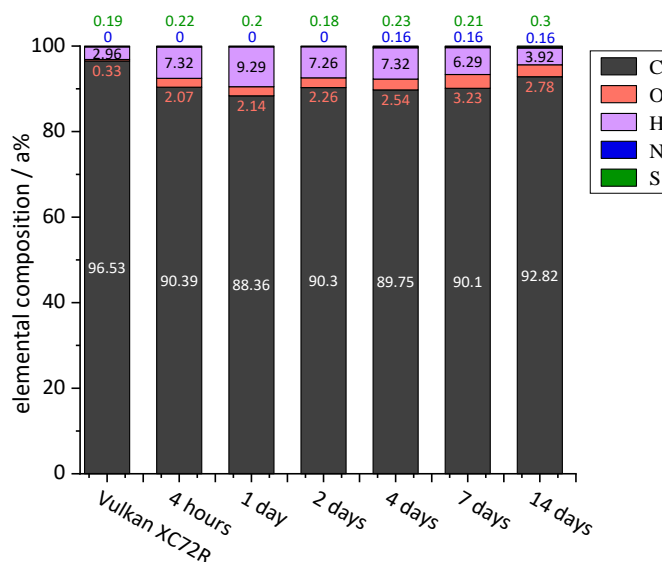


**Fig. 6.2:** Elemental composition of *Vulcan XC72R*, oxidised with concentrated nitric acid at room temperature for varying durations.

To further investigate the functional groups formed during oxidation, FT-IR spectra were recorded. Figure 6.3 shows exemplary spectra of *Vulcan XC72R* in its unfunctionalised form and oxidised with nitric acid or with a mixture of sulphuric acid nitric acid, respectively. Additional spectra of the other oxidised samples are available in the appendix.

It is generally noticeable that the intensity of the IR signals is relatively low, which can be explained by the strong IR absorption of carbon.<sup>[92]</sup> This may also contribute to the general slope observed in the IR spectra with decreasing intensity at higher wavenumbers, which is also found in IR spectra of carbon blacks in literature.<sup>[39,128]</sup> Moreover, mostly broad bands are observed, possibly arising from an overlap of bands at similar wavelengths. It is expected that a variety of oxide groups is formed during the oxidation process,<sup>[92]</sup> and the individual groups will experience a wide range of electronic environments stemming from the amorphous nature of the carbon black.<sup>[128,142]</sup> Therefore, the assignment of bands to functional groups is complex and not unambiguous.

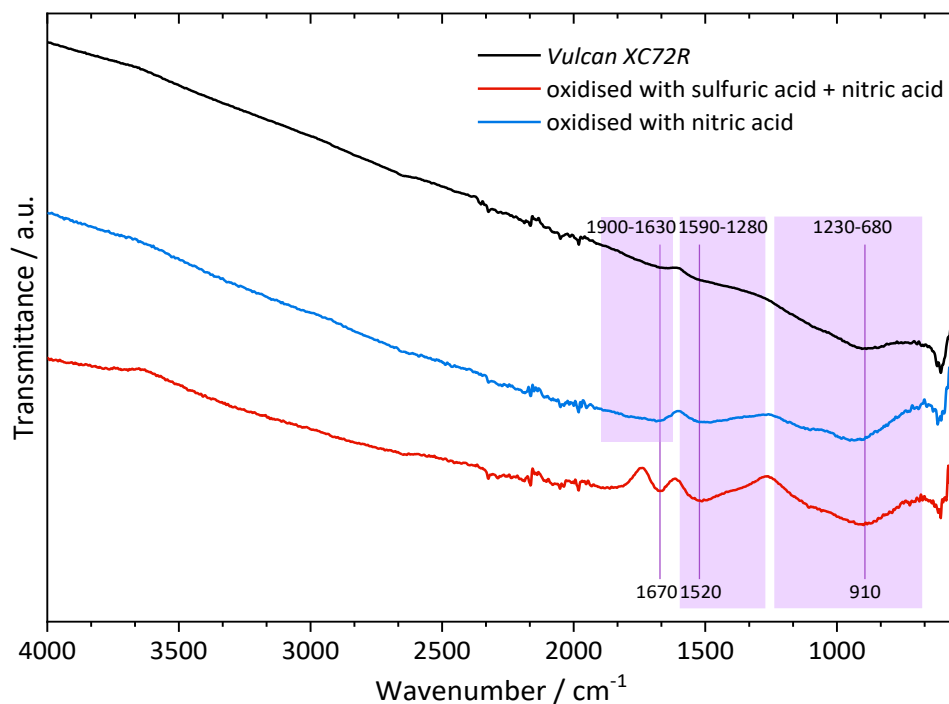


**Fig. 6.3:** FT-IR spectra of *Vulcan XC72R*, *Vulcan XC72R* oxidised for four hours at room temperature using a mixture of three parts concentrated sulphuric acid and one part concentrated nitric acid, and *Vulcan XC72R* oxidised for four hours at room temperature using concentrated nitric acid.

The unfunctionalized *Vulcan XC72R* exhibits one broad signal between 680 and 1230  $\text{cm}^{-1}$  with a minimum at 910  $\text{cm}^{-1}$ . Two more broad signals between 1280-1590  $\text{cm}^{-1}$  with a minimum at 1520  $\text{cm}^{-1}$  and between 1630-1900  $\text{cm}^{-1}$  are weakly discernible. The carbon sample oxidised with only nitric acid shows the same IR signals with slightly higher intensity. Even higher intensities of the two bands between 680 and 1230  $\text{cm}^{-1}$  and between 1280 and 1590  $\text{cm}^{-1}$  can be detected from the sample oxidised with the acid mixture. And additionally, the latter sample displays a narrow signal at 1670  $\text{cm}^{-1}$  that is missing in the other spectra. All samples using the same oxidation method, regardless of the oxidation time, exhibit the same signals.

In the specified regions, numerous functional groups display signals. Since the elemental composition of *Vulcan XC72R* exhibited only trace amounts of oxygen, the IR signals likely originate from vibrations of the aromatic system, or by surface hydrogen. However, it cannot be discounted that trace oxygen surface groups are accountable for some signals in the IR spectrum of *Vulcan XC72R*.

The first band between 680 and 1230  $\text{cm}^{-1}$  can be explained by aromatic C-H deformation vibration both in-plane and out-of-plane.<sup>[224]</sup> In the second region, extending from 1280 to 1590  $\text{cm}^{-1}$ , C=C aromatic stretching<sup>[142,224]</sup> may occur, while aromatic combination frequencies<sup>[224]</sup> could be attributed to the signals between 1630 and 1900  $\text{cm}^{-1}$ . It is plausible that these signals, deriving from carbon framework, can also be observed in oxidised carbon blacks.

Furthermore, the increase in intensity after oxidation may stem from the introduction of oxide groups that generate signals in these regions which mix with the underlying IR signals. The signals between 680 and 1230  $\text{cm}^{-1}$  may originate from phenolic C-OH stretching.<sup>[142,224]</sup> Also, carboxylic anhydrides, ethers, alcohols and carboxylic acids exhibit signals in that region.<sup>[142,224]</sup> In the region extending from 1280 to 1590  $\text{cm}^{-1}$ , O-H deformation vibrations<sup>[128,224]</sup> can occur. The narrow signal at 1670  $\text{cm}^{-1}$  can be attributed to some form of C=O stretching vibration originating from carboxylic acids, quinones, lactones or aldehydes.<sup>[128,142,224]</sup> Another interpretation for the signals displayed by the carbon oxidised with the acid mixture, are vibrations stemming from the carboxylate ion. The asymmetric and symmetric stretching vibrations display two signals between 1610-1550 and 1450-1400  $\text{cm}^{-1}$ , respectively, and deformation vibrations around 700  $\text{cm}^{-1}$ .<sup>[224]</sup> This could explain the occurrence of the two signals, while the third signal is contributing to the broad band between 680 and 1230  $\text{cm}^{-1}$ .

Interestingly, in no spectrum, signals above 2000  $\text{cm}^{-1}$  were recorded even though aromatic C-H, phenolic O-H, and COO-H stretching vibrations are expected to be present in the region between 2500 and 3500  $\text{cm}^{-1}$ .<sup>[142,224]</sup>

The lower intensity displayed by the carbon oxidised with only nitric acid and its spectrum missing the signal at 1670  $\text{cm}^{-1}$  leads to the conclusion that the oxidation process is less successful compared to using a mixture of sulphuric and nitric acid. This observation aligns with the findings from organic elemental analysis, which revealed a smaller increase in oxygen content after the oxidation with only nitric acid. Moreover, the absence of the signal at 1670  $\text{cm}^{-1}$  suggests that different oxide groups are formed with each oxidising agent. This assumption is supported by the differing ratios of oxygen and hydrogen content revealed by organic elemental analysis.

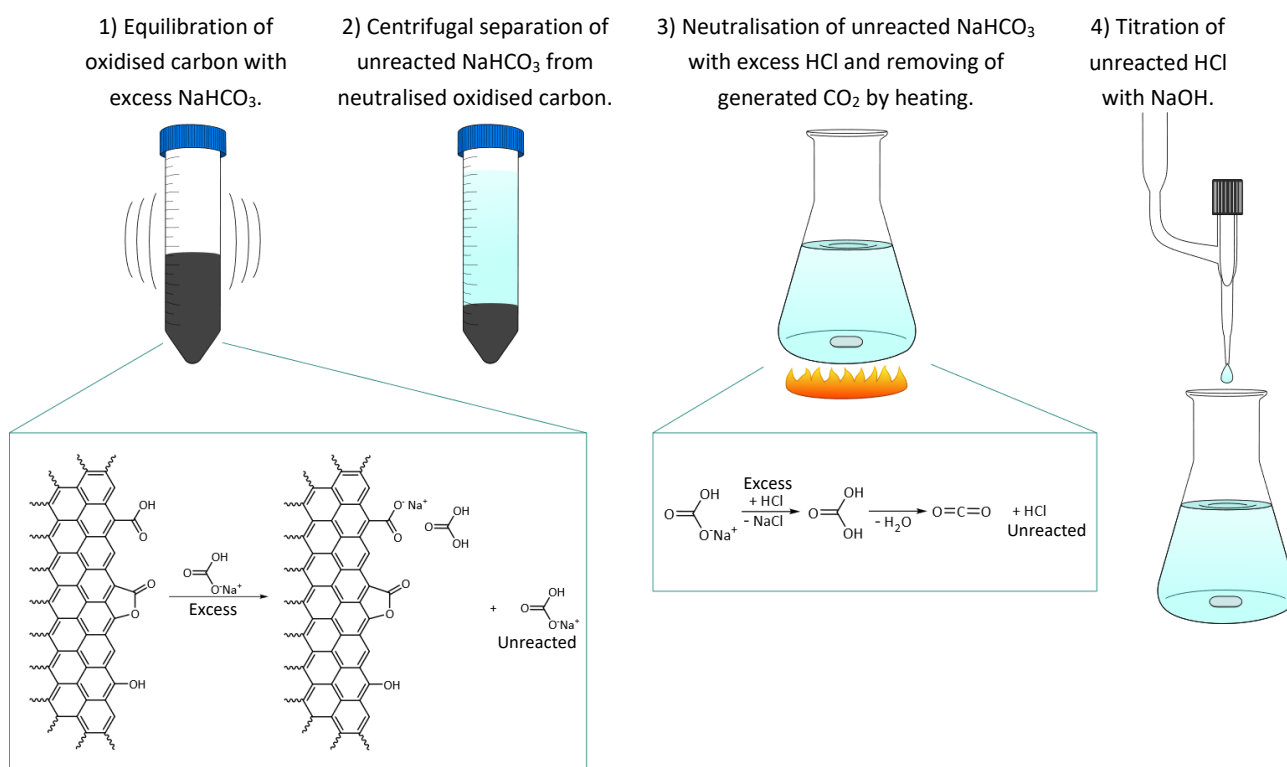


**Fig. 6.4:** Schematic illustration of the utilized titration procedure.

The surface oxygen groups were further examined with emphasis on carboxylic acid groups. For this the neutralisation adsorption titration experiment established by BOEHM *et al.*<sup>[92]</sup> was employed as illustrated in figure 6.4. Briefly, the oxidised carbon black sample to be investigated was equilibrated with a surplus of an aqueous sodium hydrogen carbonate solution which, due to its low basicity ( $pK_a = 6.35$ <sup>[225]</sup>), only neutralised the comparably strong acidic ( $pK_a \sim 3.5-4.2$ <sup>[226]</sup>) carboxylic acid group. Subsequently, the unreacted  $\text{NaHCO}_3$  solution was separated from the oxidised carbon by centrifugation before adding a surplus amount of an aqueous  $\text{HCl}$  solution. Since the added  $\text{HCl}$  reacted with the unreacted  $\text{NaHCO}_3$  to form  $\text{NaCl}$  and  $\text{H}_2\text{CO}_3$ , the solution was heated to boiling to remove the carbonic acid in the form of carbon dioxide. Finally, the excess  $\text{HCl}$  was titrated with  $\text{NaOH}$  to determine the amount of carboxylic acid groups on the oxidised carbon black sample.

Figure 6.5 shows the amount of detected carboxylic acid groups per sample weight. No  $\text{COOH}$  groups were detected on the unfunctionalised base material, which corresponds well with the results of the organic elemental analysis, where only trace amounts of oxygen were detected. After a short oxidation period with a mixture of sulphuric acid and nitric acid of only 30 minutes, the number of  $\text{COOH}$  groups increased to  $0.94 \pm 0.06 \text{ mmol g}^{-1}$ . With increasing oxidation time, the number of carboxylic acid groups increased at a declining rate as the oxidation time proceeds, reaching  $3.1 \pm 0.2 \text{ mmol g}^{-1}$  after seven days.

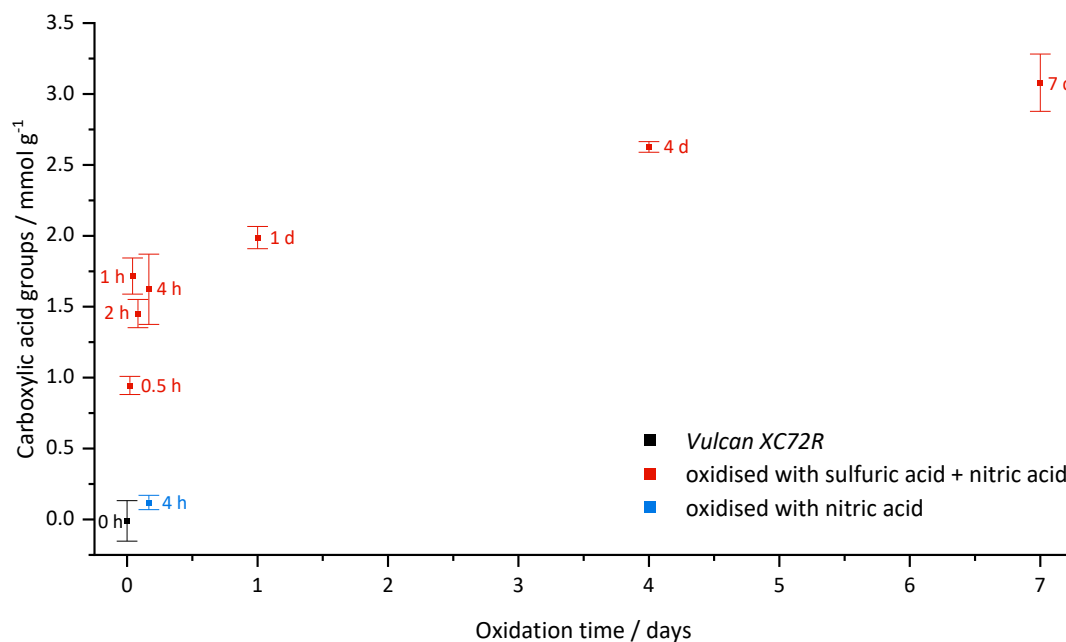


**Fig. 6.5:** Amount of carboxylic acid groups per weight detected by titration with sodium hydrogen carbonate. The samples include *Vulcan XC2R* prior to oxidation and after oxidation with a 3:1 mixture of concentrated sulphuric acid and nitric acid or with only concentrated nitric acid at room temperature for varying oxidation times.

In contrast, on the sample oxidised with only nitric acid, only  $0.12 \pm 0.05$  mmol g<sup>-1</sup> COOH groups were detected after four hours oxidation time, which is significantly less than the  $1.6 \pm 0.3$  mmol g<sup>-1</sup> detected after four hours of oxidation with the acid mixture. These results align well with the differences detected in the organic elemental analysis and the IR spectra. The lower oxygen content (2.1 % vs. 9.8 %), the higher hydrogen to oxygen ratio (3.5 vs. 1.2) and the missing IR band at  $1670$  cm<sup>-1</sup>, attributed to C=O stretching, indicate a less efficient oxidation and a difference in the type of oxide groups formed after oxidation with only nitric acid.

Upon comparison of the oxygen content detected by organic elemental analysis with the amount of COOH groups per sample weight detected by titration, it is apparent that the entirety of the oxygen cannot be attributed to COOH groups. This aligns with literature,<sup>[92]</sup> where the formation of a variety of oxygen groups are to be expected.

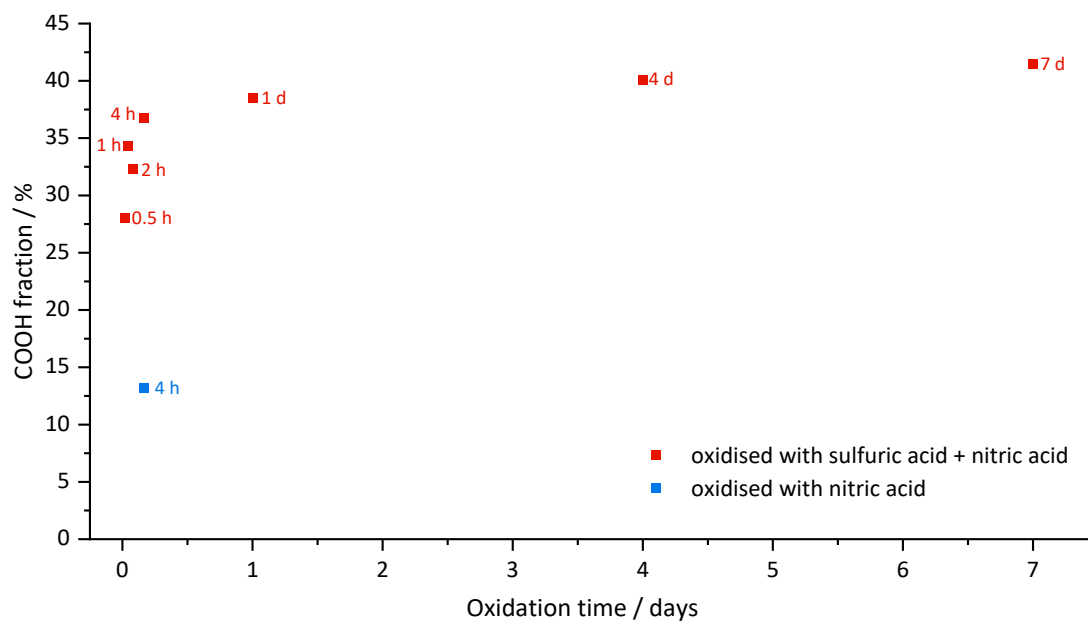


**Fig. 6.6:** Fraction of oxygen content measured by organic elemental analysis that can be attributed to carboxylic acid groups detected by titration with sodium hydrogen carbonate. The samples comprise of *Vulcan XC2R* after oxidation at room temperature with a 3:1 mixture of concentrated sulphuric and nitric acid, or only nitric acid, for varying oxidation times.

The fraction of oxygen content arising from carboxylic acid groups was calculated and is presented in figure 6.6. In agreement with the results presented before, after oxidation with sulphuric and nitric acid, the most significant increase is noticeable at the onset with a declining rate as the oxidation time proceeds. Starting with 28 % after 30 minutes of oxidation, the COOH fraction rises quickly to 38 % after 24 hours, before remaining relatively stable and only increasing by 3 % in the next 6 days of oxidation time. This suggests that the oxidation with sulphuric and nitric acid proceeds in multiple steps, where other initially formed oxide groups are transformed into carboxylic acid groups, before stagnating at a constant value. For example, primary alcohols can be oxidised to aldehydes, which can be further oxidised to carboxylic acid.<sup>[227,228]</sup>

With the sole use of nitric acid as oxidant a COOH fraction of only 13 % was obtained. This confirms the assumption that other oxide groups prevail over carboxylic acid groups with this oxidation method.

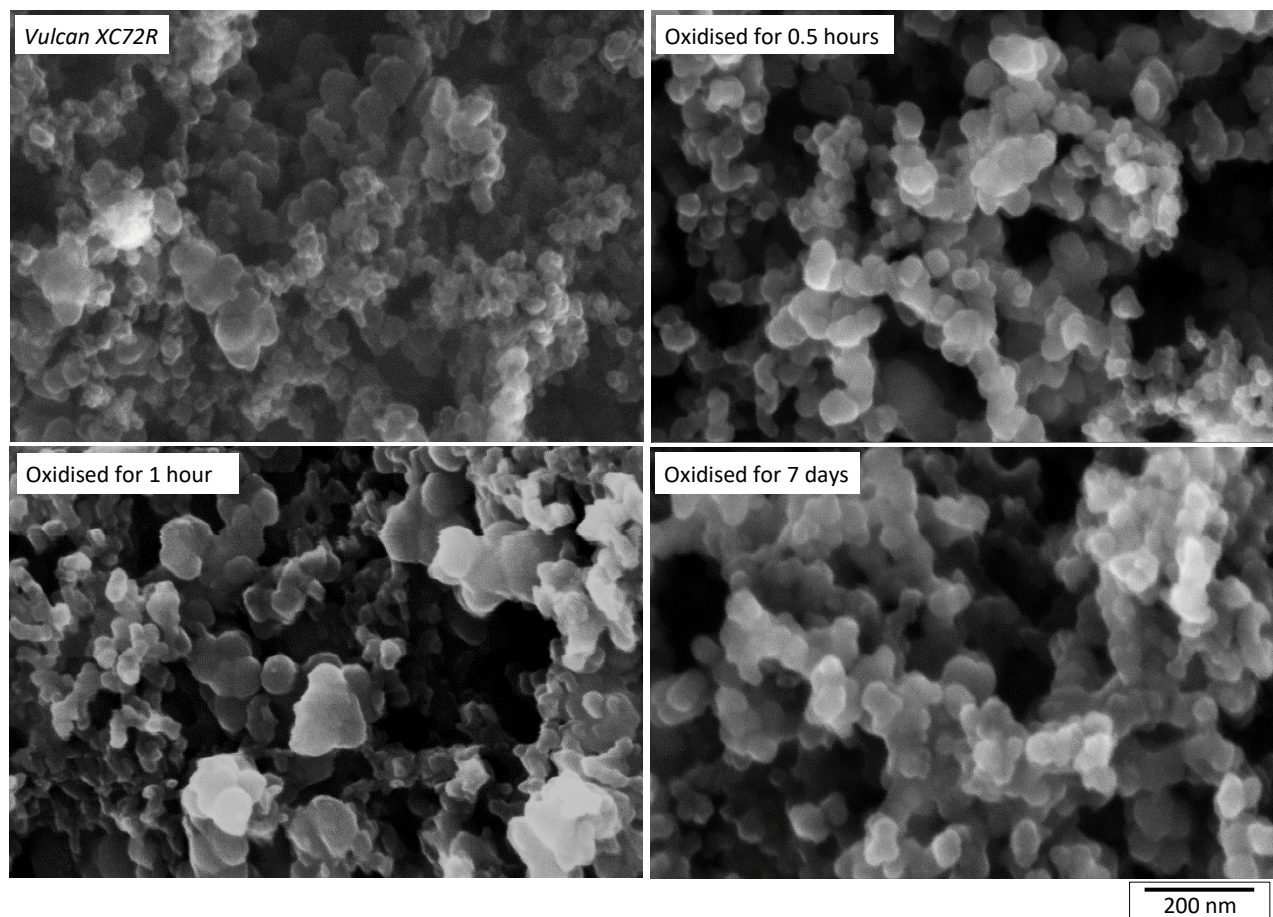


**Fig. 6.7:** SEM images of *Vulcan XC2R* prior to oxidation and after oxidation with a 3:1 mixture of concentrated sulphuric acid and nitric acid at room temperature for varying oxidation times.

The influence of the oxidation process on the morphology was investigated using scanning electron microscopy as depicted in figure 6.7. It is clearly observable that the fine structures, visible on the unfunctionalised *Vulcan XC72R*, are reduced after oxidation. The morphology appears to be coarser with increased oxidation time. Thus, it can be assumed that the oxidation process leads to some form of carbon corrosion.

Since a coarser structure indicates a loss in specific surface area, nitrogen physical adsorption measurements were undertaken. Exemplary isotherms are shown in figure 6.8. They show the typical course of the classical type II isotherms of macro porous or non-porous substances as classified by IUPAC.<sup>[229]</sup> By comparison of the isotherms after different states of oxidation, it is noticeable that the volume of adsorbed gas decreased with increasing oxidation time indicating a loss in specific surface area.

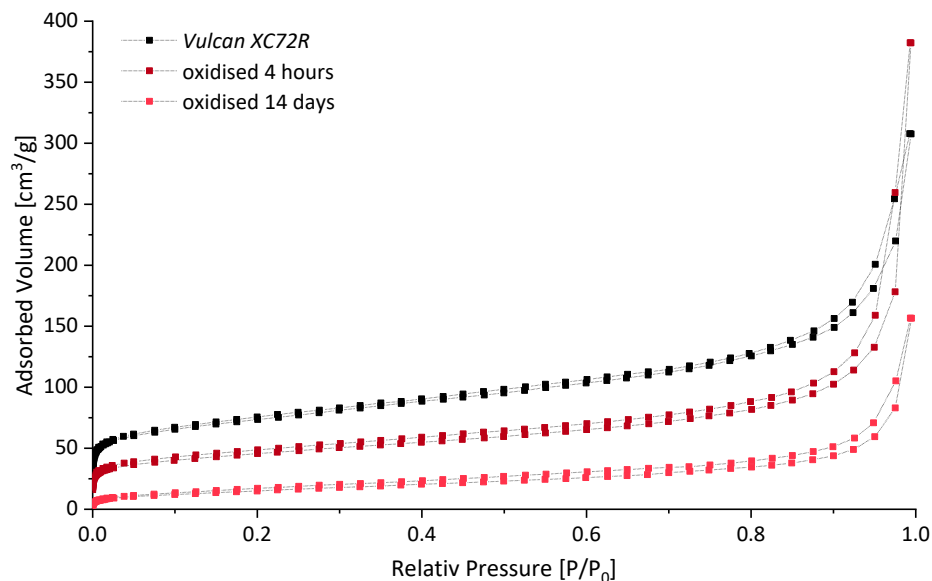


**Fig. 6.8:** Isotherms of *Vulcan XC2R* prior to oxidation and after oxidation with a 3:1 mixture of concentrated sulphuric acid and nitric acid at room temperature for varying oxidation times.

The calculated BET surface area is plotted against the oxidation time in figure 6.9. Similar to the increase of oxygen content determined by organic elemental analysis shown in figure 6.1, the most significant decrease in surface area occurs at the onset of the oxidation process with a declining rate as the oxidation time proceeds. The unfunctionalised *Vulcan XC2R* exhibits a BET surface area of  $265 \pm 2 \text{ m}^2 \text{ g}^{-1}$ . After only 0.5 hours of oxidation time, the BET surface area decreased by 30 % to  $186 \pm 2 \text{ m}^2 \text{ g}^{-1}$  and after two weeks of oxidation, only 20 % of the initial BET surface area ( $54 \pm 4 \text{ m}^2 \text{ g}^{-1}$ ) remained. The decrease in specific surface area due to oxidative acid treatment is well known in literature.<sup>[100,128,129,132,181,223]</sup> It can be explained by a decarboxylation process, where the oxidant further oxidises the surface oxide groups until carboxylic acid is oxidised to carbon dioxide and the carbon is gasified.<sup>[230,231]</sup>

In contrast, the oxidation method using only nitric acid results first in a decrease of BET surface area by 22 % after four hours of oxidation before increasing again unsteadily. After 14 days of oxidation, the BET surface area was even slightly higher ( $269 \pm 5 \text{ m}^2 \text{ g}^{-1}$ ) than the initial one. The smaller reduction of the surface area using nitric acid as oxidant, compared to using the acid mixture, confirms the assumption that this oxidant is less potent. The later increase in surface area throughout the course of oxidation may be attributed to the clearing of pore blockage.<sup>[232]</sup>

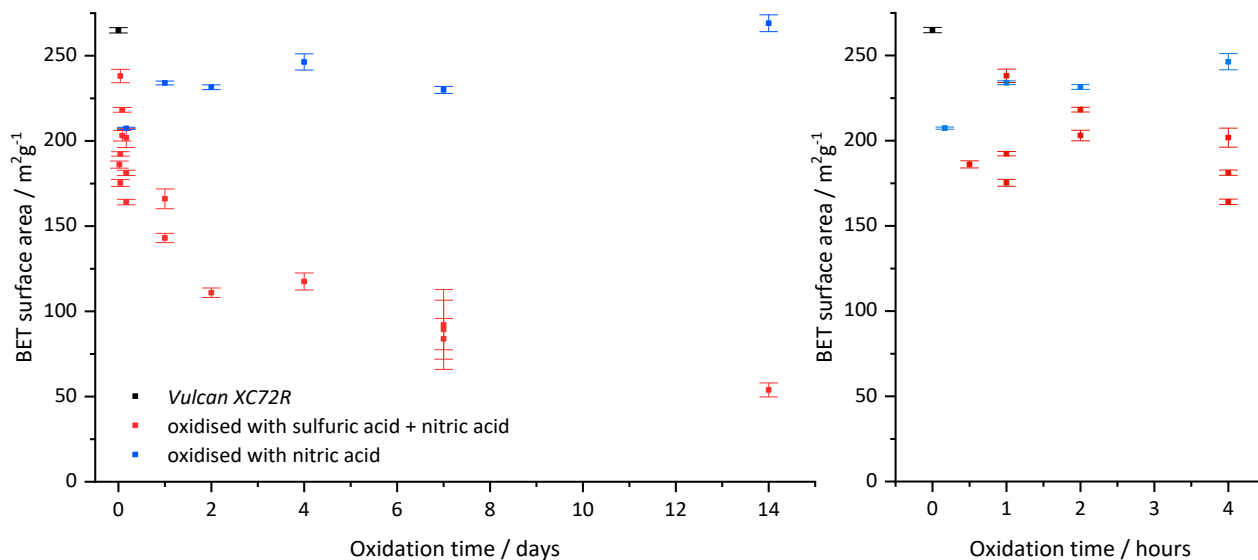


**Fig. 6.9:** BET surface area of *Vulcan XC72R* prior to oxidation and after oxidation with a 3:1 mixture of concentrated sulphuric acid and nitric acid or with only concentrated nitric acid at room temperature for varying oxidation times.

The amount of surface COOH groups per area can be calculated using the respective results from the nitrogen physical adsorption and the titration experiments. In figure 6.10, the number of groups per square nanometre is depicted for the carbon blacks with varying oxidation times. The graph reveals that the density of the surface COOH groups increases with oxidation time using sulphuric and nitric acid as oxidant. After 30 minutes, the surface featured  $3.1 \text{ groups} \cdot \text{nm}^{-2}$  and after 7 days,  $20.8 \text{ groups} \cdot \text{nm}^{-2}$  were present. For comparison, carbon black features around 38 carbon atoms per square nanometre on its top-side (graphene layer) and 20-28 carbon atoms on its side if distortions due to amorphousness are disregarded.\* Here as well, the rate appears to be faster at the onset of the oxidation, before increasing with a constant rate after four hours of ca.  $2.2 \text{ groups} \cdot \text{nm}^{-2}$  per day.

\*Calculated from a bond length of  $0.14215 \text{ nm}^{[107]}$  and a bond angle of  $120^\circ$  in the graphite layers and an inter-layer distance of  $0.344\text{-}0.395 \text{ nm}^{[91]}$

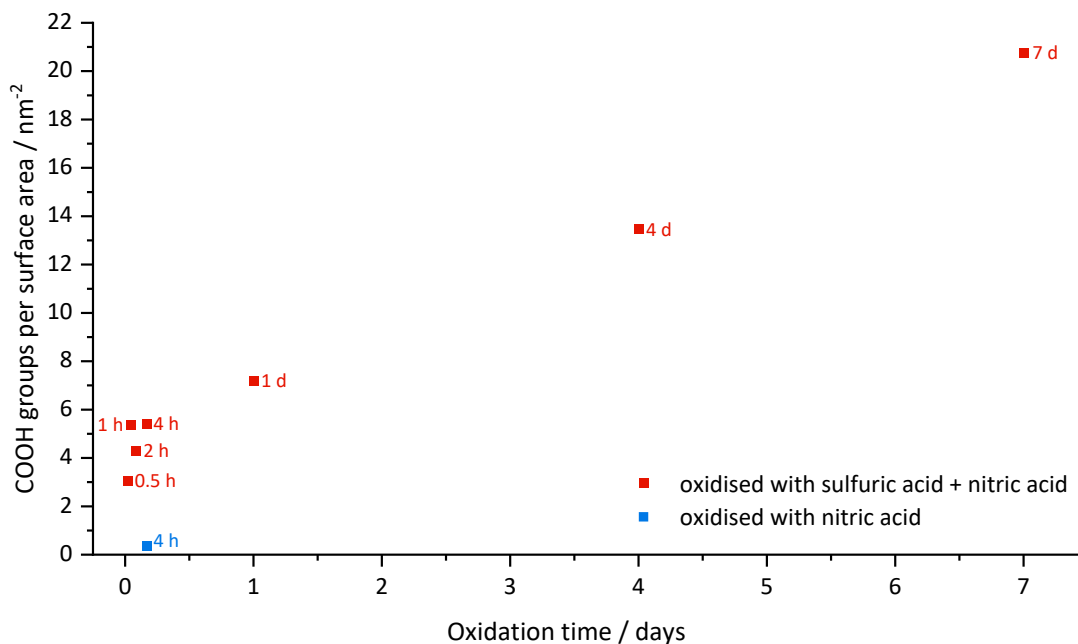


**Fig. 6.10:** COOH groups per surface area of *Vulcan XC2R* after oxidation with a 3:1 mixture of concentrated sulphuric acid and nitric acid or with only concentrated nitric acid at room temperature for varying oxidation times, calculated from titration experiments with sodium hydrogen carbonate and the respective BET surface areas.

In conclusion, various surface oxide groups could be successfully introduced by oxidation of *Vulcan XC72R* with concentrated acids. The utilisation of a mixture of 3:1 sulphuric acid and nitric acid was markedly more efficient than nitric acid alone, as evidenced by the oxygen content detected by organic elemental analysis. Furthermore, the type of functional groups appears to differ with each oxidation method, as indicated by the different O/H-ratios detected by organic elemental analysis. Particularly, the amount of COOH groups is significantly higher after oxidation with the acid mixture. This was demonstrated through titration and is implied by the distinct IR-peak at  $1670\text{ cm}^{-1}$ , attributed to C=O stretching vibrations, which only appears after oxidation with the acid mixture.

As a side effect, the oxidative treatment with sulphuric and nitric acid led to a decrease in BET surface area attributed to carbon gasification, which increased in severity as the oxidation time proceeded. The rate of oxidation and surface degradation was faster at shorter oxidation durations, slowing down as the oxidation time advanced. Furthermore, the data derived from titration suggests that initially other surface oxide groups are formed, which are subsequently converted into COOH groups, as indicated by the increase of the fraction of oxide groups that are carboxylic acid groups at short oxidation times below four hours. However, the density of COOH groups per carbon surface continued to increase even after prolonged oxidation periods of one week. Therefore, the optimal oxidation time must be found by compromising between the high specific surface area necessary for

the deposition of catalytic nanoparticles on the surface and the number of carboxylic acid groups that serve as an anchor for said particles or as starting point for a further functionalisation with amines, as described in the next section. Hence, this work focusses on oxidation times ranging from one to four hours as the BET surface area was still adequately high ( $164\text{-}238\text{ m}^2\text{ g}^{-1}$ ) while a sufficient amount of carboxylic acid groups ( $1.5\text{-}1.7\text{ mmol g}^{-1}$  and  $4.3\text{-}5.4\text{ nm}^{-2}$ ) was formed.

### 6.1.2. Amine and Thiol Functionalisation

As described in the previous chapter, the oxidation of the carbon black *Vulcan XC72R* from *Cabot* with a mixture of sulphuric and nitric acid led to the introduction of various oxide groups on the carbon surface. Amongst other, COOH groups were formed, as detected by titration. For the introduction of amine groups to the carbon surface, diamines were employed to form amide bonds with the COOH groups, leaving one free amine group to interact with the catalytic metal nanoparticles.

The synthesis were conducted using either a modified direct synthesis method according to EGUIZABAL *et al.*<sup>[39]</sup>, or a modified two-step synthesis method according to KUO *et. al.*<sup>[37]</sup>. Both reaction routes are displayed schematically in figure 6.11. During the direct amine functionalisation, the oxidised carbon black was dispersed in the liquid diamine and heated to  $100\text{ }^\circ\text{C}$  for two days. During the two-step synthesis, the oxidised carbon was first treated with thionyl chloride for one day at  $65\text{ }^\circ\text{C}$  before the excess thionyl chloride was removed by distillation. Subsequently, the diamine was added, and the mixture was heated to  $100\text{ }^\circ\text{C}$  for two days as well. Both reaction ways led to the formation of an amide linkage.

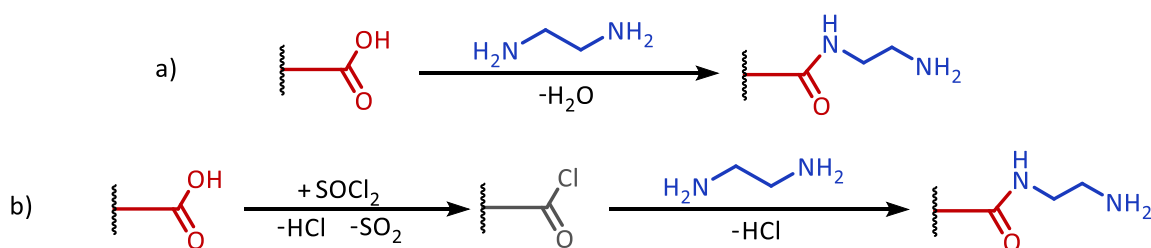


**Fig. 6.11:** Schematic representation of the employed synthesis routes for the amine functionalisation. **a)** Direct synthesis route. **b)** Two-step synthesis route with acyl chloride intermediate.

Figure 6.12 shows the elemental composition of three different oxidised carbon blacks after the direct amine functionalisation with ethylenediamine or triethylenetetramine. The data shows that the nitrogen contents increased to ca. 3 a% after the amine treatment, suggesting the successful introduction of amine groups. Furthermore, the amine functionalisation leads to a decreased oxygen

content, which can be explained by the oxygen-containing leaving group. The increase of hydrogen content after the amine functionalisation can be attributed to the hydrogen atoms present in the diamine molecule.

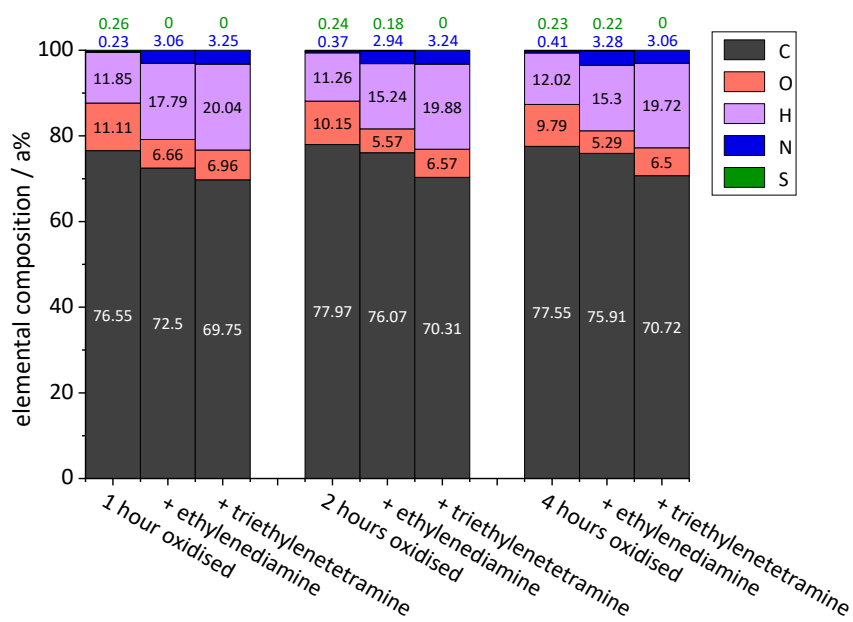


**Fig. 6.12:** Elemental composition of *Vulcan XC72R*, oxidised for 1, 2 or 4 hours and the same materials after a direct amine functionalisation with either ethylenediamine or triethylenetetramine.

The number of diamine molecules that were introduced to the carbon surface can be calculated from the elemental composition. In figure 6.13, this number is compared to the amount of COOH group, detected by titration, from the respective oxidised carbon starting material. The comparison shows that the direct functionalisation with ethylenediamine proceeded with a very high conversion rate of ca. 84 to 95 %. On the other hand, the functionalisation with triethylenetetramine was much less successful with approximately only half the number of functional groups introduced. This leads to the hypothesis that the longer triethylenetetramine molecule was bound to the COOH groups through both terminal primary amine groups, resulting in a bridged functionalisation. In this case, mainly secondary amine groups would be available as anchor groups for catalytic nanoparticles.

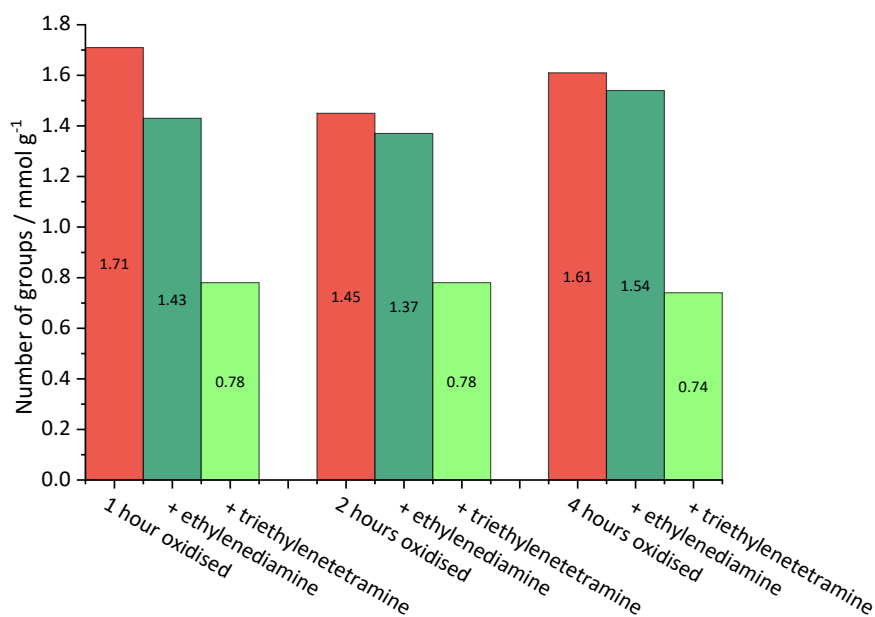


**Fig. 6.13:** Number of COOH groups detected by titration of *Vulcan XC72R*, oxidised for 1, 2 or 4 hours. Compared to the number of ethylenediamine or triethylenetetramine groups, detected by elemental analysis, introduced to the respective oxidised carbons.

Although the amine content detected by organic elemental analysis clearly suggests a successful amide linkage, the efficacy of the direct amide linkage route remains a subject of contention in the literature.<sup>[38,166–168]</sup> Alternatively to the amide linkage, an ammonium carboxylate zwitterion may be formed, which would also account for the increase in nitrogen content. To further investigate whether the amide or the zwitterion was formed, reference experiments were conducted using an ethylenediamine-functionalised carbon sample.

Since it is presumed that treatment with HCl would lead to the cleavage of the ammonium carboxylate ions, in one experiment, the ethylenediamine-functionalised carbon was treated with 1 M HCl at room temperature for four hours. For the hydrolysis of amides, it is necessary to boil the amide for several hours in concentrated aqueous acids or bases, with bases typically exhibiting greater efficacy.<sup>[227,230]</sup> Therefore, the ethylenediamine-functionalised carbon was also refluxed in 2 M KOH for four hours. Additionally, one experiment was carried out in water at 100 °C for four hours. All treated samples were subsequently washed vigorously with four centrifugation steps and the nitrogen content was determined using organic elemental analysis as displayed in figure 6.14.

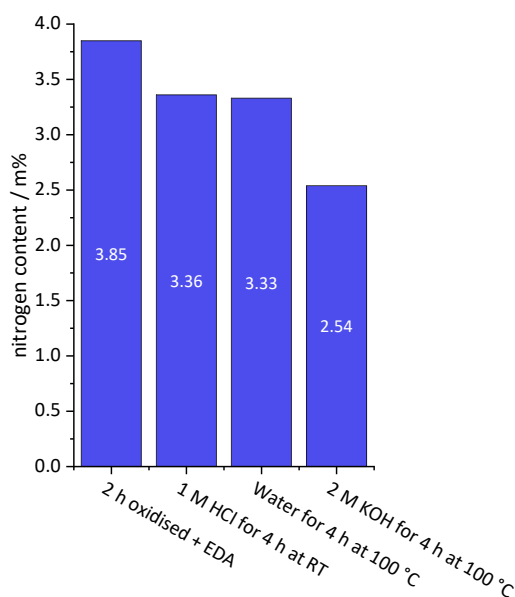


**Fig. 6.14:** Nitrogen content of *Vulcan XC72R*, oxidised for two hours and functionalised with ethylenediamine. Before and after amide hydrolysis experiments using 1 M HCl at room temperature, 2 M KOH at 100 °C or water at 100 °C.

Figure 6.14 shows a modest decrease of 13 % in nitrogen content following treatment with 1 M HCl at room temperature or with water at 100 °C. In contrast, the reduction in nitrogen content is significantly greater with 34 %, after treatment with 2 M KOH at 100 °C.

The observation that a slight reduction in nitrogen content occurred under mild treatment conditions suggests that a small amount of diamine may indeed be bound ionically. However, it appears that the majority of diamine is bound more strongly, implying an amide bond. Although the harsh treatment with KOH could hydrolyse a fraction of the amide linkages, the duration of refluxing for four hours in 2 M KOH seems insufficient to reach a full hydrolysis. Consequently, it may be concluded that a strong amide bond was successfully formed which is also expected to remain stable under fuel cell conditions.

One explanation for the successful formation of the amide bond could be the employment of a significant excess of diamine by using the diamine as solvent. The amide linkage was carried out for two days at 100 °C. It is believed that the elevated temperature facilitates the amide bond formation as well. For comparison, experiments were also conducted at room temperature over a duration of seven days. The elemental composition of samples subjected to different temperatures is depicted in figure 6.15.

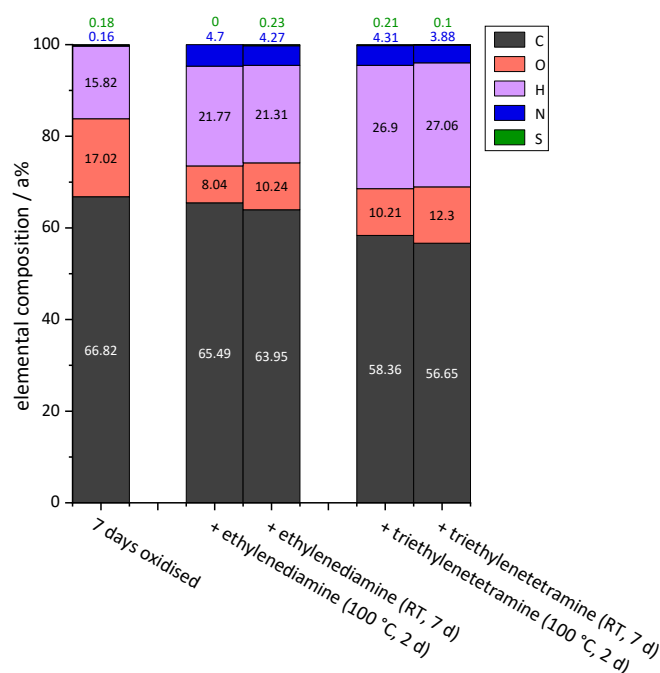


**Fig. 6.15:** Elemental composition of *Vulcan XC72R*, oxidised for 7 days and treated directly with ethylenediamine or triethylenetetramine for either 2 days at 100 °C or 7 days at room temperature.

The elemental composition in figure 6.15 reveals that the lower reaction temperature results in a slightly lower nitrogen content compared to the reaction at 100 °C. The longer reaction time, on the other hand appears to facilitate a sufficiently high amine conversion.

The usual synthesis route for the formation of an amide bond includes an intermediate step involving the conversion of the carboxylic acid group to the acyl chloride or the methyl ester.<sup>[227,230,233]</sup> For comparison, additional experiments employing the acyl chloride intermediate step were carried out. In figure 6.16, the elemental compositions of these samples are compared to samples using the direct synthesis route. It can be inferred from the graph that the two-step synthesis route led to a 30 % higher nitrogen content for ethylenediamine and a 17 % higher nitrogen content for triethylenetetramine, suggesting a more successful amine conversion. The lower increase of nitrogen for triethylenetetramine, compared to ethylenediamine can be explained by the binding of both terminal amine groups.

On the other hand, the amine functionalisation with thionyl chloride also entails an increase in sulphur content from 0-0.25 % to 0.49-0.59 % which can be attributed to residual thionyl chloride. Minor as it is this sulphur content increase could yet lead to a decrease in catalytic performance. Electrochemical tests were conducted and are discussed in chapter 6.2.3.

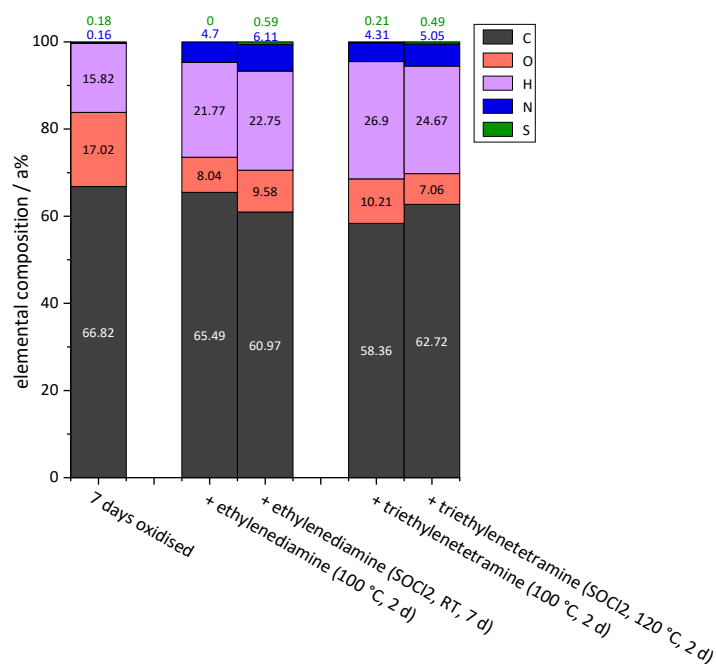


**Fig. 6.16:** Elemental composition of *Vulcan XC72R*, oxidised for 7 days and treated with ethylenediamine or triethylenetetramine either directly for 2 days at 100 °C or using the two-step method with acyl chloride intermediate step.

In addition to ethylenediamine and triethylenetetramine, functionalisations with phenylenediamine and butanedithiol were carried out. Figure 6.17 shows the elemental composition of phenylenediamine-functionalised carbon black of three different synthesis routes and the elemental composition of butanedithiol-functionalised carbon black using the two-step synthesis route.

Given that phenylenediamine is solid at 120 °C, the synthesis was conducted either in toluene as solvent or by heating the phenylenediamine to 170 °C and employing it in its molten form. Both approaches were tested using acyl chloride as intermediate step and the synthesis in toluene was conducted using the direct synthesis route as well. Both approaches presented distinct challenges. While the molten state was hard to maintain for two days using standard equipment, *p*-phenylenediamine oxidised immediately in most solvents, indicated by the occurrence of a deep red colour. Toluene did not facilitate the oxidation of *p*-phenylenediamine. However, the solubility of *p*-phenylenediamine in toluene was notably low, and toluene's relatively low boiling point was suboptimal for this synthesis. As discernible in figure 6.17, the approach using toluene as solvent led to lower nitrogen contents of around 2.5 a%, while the synthesis in molten phenylenediamine reached a nitrogen content comparable to those obtained with ethylenediamine or triethylenetetramine with 4.5 a%. This indicates that the approach using molten phenylenediamine was the most successful, whereas the synthesis in toluene only led to a low conversion rate.

In addition to diamines, one test was conducted using the dithiol butanedithiol. The synthesis was conducted using the two-step method analogous to the diamine-functionalisation. Additionally, a catalytic amount of pyridine was added as it is believed to increase the conversion rate.<sup>[234]</sup> Figure 6.17 reveals an increase in sulphur content of ca. 1.5 a%, which is very low compared to all functionalisations using diamines. It can be concluded that the formation of the thioester was successful, albeit with a low conversion yield.

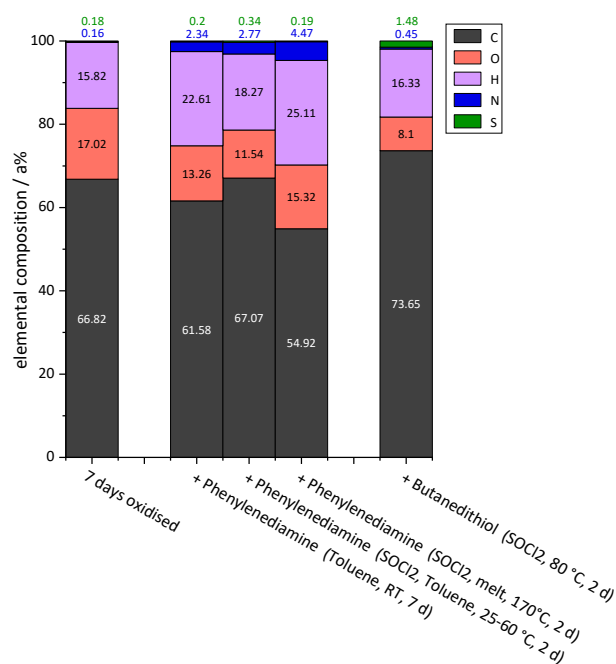


**Fig. 6.17:** Elemental composition of *Vulcan XC72R*, oxidised for 7 days and treated with phenylenediamine or butanedithiol using different synthesis conditions.

The functionalised carbon blacks were further investigated in respect to their functional group using infrared spectroscopy. Figure 6.18 displays the FT-IR spectra of *Vulcan XC72R* after oxidation and after functionalisation with ethylenediamine, triethylenetetramine, *p*-phenylenediamine, or butanedithiol.

As already described in section 6.1.1, the IR spectra display signals with relative low intensity, explained by the strong IR absorption of carbon,<sup>[92]</sup> and a general slope with decreasing intensity at higher wavenumbers also found in literature.<sup>[39,128]</sup> Furthermore, due to the complexity of the amorphous carbon carrying various functional groups on its surface, mostly broad bands are displayed, possibly when signals of functional groups that experience a wide range of electronic environments overlap.<sup>[128,142]</sup>

After the oxidation using a mixture of nitric acid and sulphuric acid, two distinct peaks at 1670 and between 1280-1590  $\text{cm}^{-1}$  appeared. The signal at 1670  $\text{cm}^{-1}$  likely stems from some form of C=O

stretching vibration originating from carboxylic acids, quinones, lactones or aldehydes<sup>[128,142,224]</sup> or from asymmetric carboxylate ion stretching vibrations.<sup>[224]</sup> The signal at 1280-1590 cm<sup>-1</sup> can be allocated to O-H deformation vibrations,<sup>[128,224]</sup> or symmetric carboxylate ion stretching vibrations.<sup>[224]</sup> The IR spectrum of the oxidised carbon furthermore displays a broad band between 680 and 1230 cm<sup>-1</sup> which is also present in the unfunctionalised carbon and can mostly be attributed to aromatic C-H deformation vibrations.<sup>[224]</sup>

After the amine or thiol functionalisations, the broad band at 680 and 1230 cm<sup>-1</sup> is still present in all samples. Furthermore, all samples exhibit signals between 1280-1590 cm<sup>-1</sup>, but with slightly different minima.

The sample functionalised with ethylenediamine displays only one signal with its minimum around 1510 cm<sup>-1</sup>, which can be allocated to N-H deformation vibrations of the amide bond or the primary amine group.<sup>[224]</sup> The disappearance of the signal at 1670 cm<sup>-1</sup> suggests that the amide linkage interferes the stretching vibrations of the carboxylic acid group.

After the functionalisation with triethylenetetramine, the N-H deformation signal at 1500 cm<sup>-1</sup> occurs, as well as a weaker signal at 1640 cm<sup>-1</sup>. Since triethylenetetramine contains also secondary amine groups, the latter signal may be allocated to their deformation vibrations.<sup>[224]</sup>

The phenylenediamine-functionalised carbon black shows a higher number of distinct IR signals at 1590, 1510, 1427, 1234, 879 and 821 cm<sup>-1</sup>. The signal at 1510 cm<sup>-1</sup> can again be interpreted as N-H deformation vibrations of the amide bond or the primary amine group.<sup>[224]</sup> The other signals may be explained by vibrations of the aromatic ring of phenylenediamine. Aromatic rings display skeletal vibrations around 1450-1525 and 1575-1625 cm<sup>-1</sup>,<sup>[224]</sup> combination frequencies at 1650-2000 cm<sup>-1</sup>,<sup>[224]</sup> and in-plane C-H deformation vibrations at 950-1250 cm<sup>-1</sup>.<sup>[224]</sup>

In the IR spectrum of the carbon functionalised with butanedithiol, the two bands of the oxidised carbon black at 1670 and 1280-1590 cm<sup>-1</sup> (minimum at 1555 cm<sup>-1</sup>) are still present. Given the low conversion rate of the thioester formation detected by elemental analysis, it can be concluded that these signals originate from the unreacted carboxylic acid groups. Two weakly distinctive signals at 1097 and 1220 cm<sup>-1</sup> can be attributed to CH<sub>2</sub> deformation vibrations of butanedithiol while the C-S stretching vibrations that are expected between 800 and 915 cm<sup>-1</sup> likely contribute to the broad IR band between 680 and 1230 cm<sup>-1</sup>.

Reference spectra<sup>[235]</sup> of the pure diamines and butanedithiol can be found in the appendix. Contrary to expectations, the strong IR absorption bands of the reference spectra do not correspond to the signals detected from the functionalised carbons. This can be explained with the different chemical

environments of the functionalisations attached to the amorphous, oxidised carbon compared to the pure substances. Nevertheless, the differences in the IR spectra of the differently functionalised samples can be taken as an indication for the successful introduction of functional groups to the carbon surface. Furthermore, all samples functionalised in a similar manner display similar IR signals as well, as can be seen in the IR spectra of all amine-functionalised samples in the appendix. One exception are the three samples functionalised with phenylenediamine. Here, the two samples functionalised using toluene as solvent display an additional peak around  $1700\text{ cm}^{-1}$  that can be interpreted as the C=O stretching vibrations stemming from unreacted carboxylic acid groups. This aligns well with the observations from the IR spectrum of butanedithiol-functionalised carbon, which, similar to the carbon functionalised with phenylenediamine in toluene, suffered from a low conversion rate according to elemental analysis.

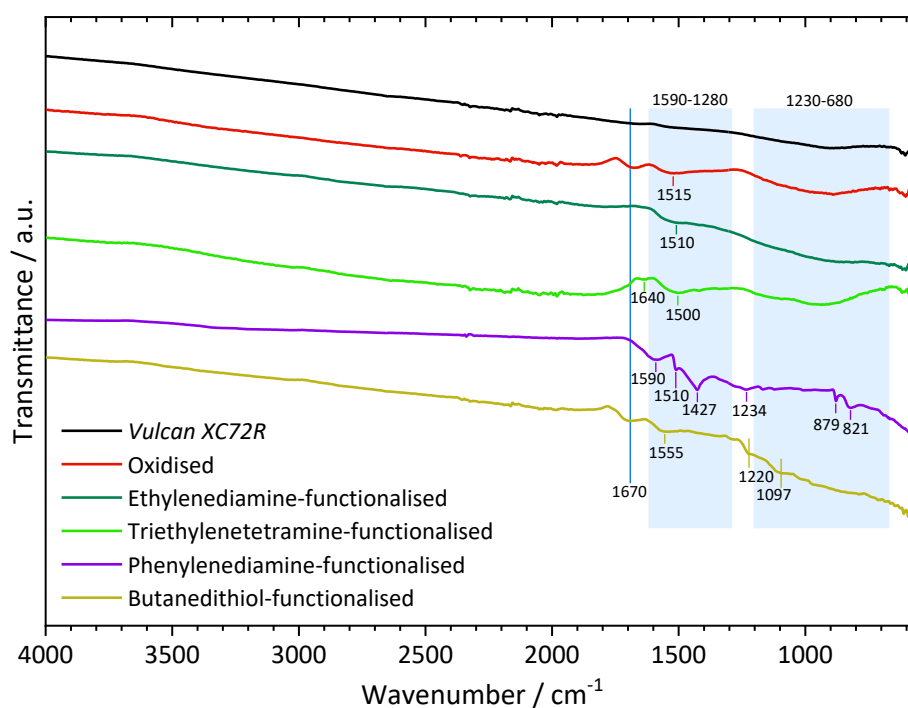


**Fig. 6.18:** FT-IR spectra of *Vulcan XC72R*, *Vulcan XC72R* oxidised for four hours and *Vulcan XC72R* treated with a diamine or dithiol after oxidation.

To investigate whether the carbon surface is altered due to the amine-functionalisation, the BET surface areas of ethylenediamine and triethylenetetramine-functionalised carbons were measured. As revealed in figure 6.19, the functionalisation led to a significant decrease of the BET surface area in most cases. The decrease was more severe after treatment with triethylenetetramine (36-40 %) compared to ethylenediamine (3-29 %).

The decrease of the surface area following the oxidation in the first reaction step was attributed to the oxidative gasification<sup>[230,231]</sup> of the carbon substrate. The decrease of the surface area after the diamine treatment is unlikely due to the same reason. Another explanation for a decrease of surface area is the blockage of micropores,<sup>[131–133]</sup> which could be applicable in this context with the larger triethylenetetramine molecule being accountable for a more severe decrease.

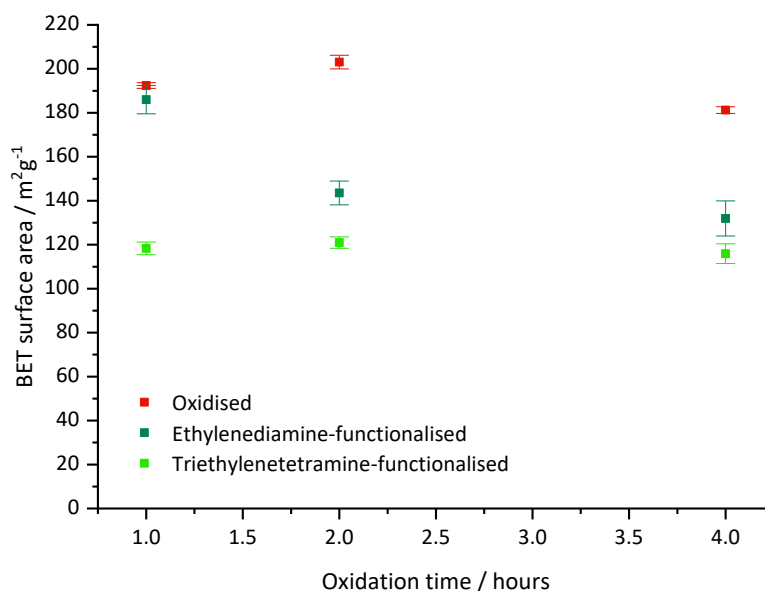


**Fig. 6.19:** BET surface area of *Vulcan XC72R*, oxidised for 1, 2 or 4 hours and the same materials after a direct amine functionalisation with either ethylenediamine or triethylenetetramine.

Overall, all approaches were successful in introducing amines as functional groups as revealed by the increase in nitrogen content according to organic elemental analysis and the differences in the IR spectra of differently functionalised carbons. It was shown that some functionalisation approaches were more successful than others. Generally, two reaction approaches of either a direct synthesis route or the two-step route with an acyl chloride intermediate step, were utilised.

In regard to the functionalisation with ethylenediamine or triethylenetetramine, the two-step route led to a higher increase in nitrogen content, but also to a slight increase in sulphur content, attributed to residual thionyl chloride. When employing the direct functionalisation route, it was demonstrated that an increase in reaction temperature was slightly more favourable than a long reaction time. Given that the number of triethylenetetramine molecules that were introduced to the surface was roughly half the amount of ethylenediamine molecules, it is plausible that the triethylenetetramine formed an amide linkage with both terminal amine groups, whereas the ethylenediamine only formed one amide linkage. Furthermore, an amide cleavage test revealed that predominantly amide bonds were formed in contrast to a low amount of ionic bonds.

For the functionalisation with phenylenediamine, the synthesis was more successful when conducted in a phenylenediamine melt rather than using toluene as the solvent.

One synthesis was conducted using butanedithiol for the formation of a thioester. However, the elemental composition indicated that it was considerably less successful than the amine functionalisations.

Finally, nitrogen physical adsorption experiments revealed a decrease of the BET surface area after direct functionalisations with ethylenediamine and triethylenetetramine, which may be due to pore blocking.

Altogether, it was possible to successfully introduce amines as functional groups to the carbon black surface. However, the most significant aspect is their impact on electrocatalytic activity and electrochemical long-term stability. Therefore, the following chapters focus on the deposition of catalytic nanoparticles onto the functionalised surfaces and their subsequent electrochemical characterisation.

## 6.2. Synthesis and Investigation of Nanoparticle-Support Catalysts

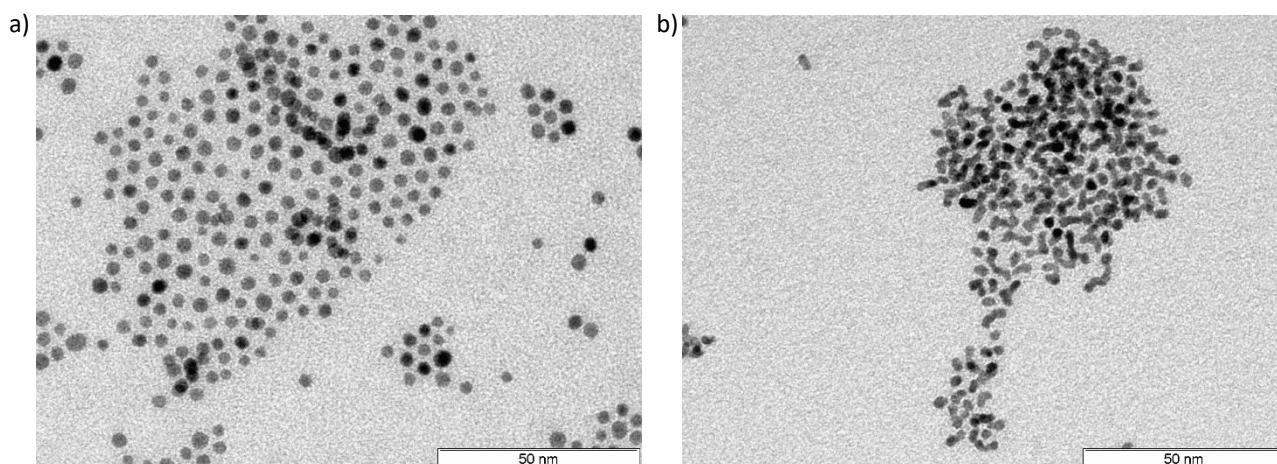
The surface-modified carbon blacks described in section 6.1 were employed as support materials for catalytic platinum and platinum-nickel alloy nanoparticles to form nanoparticle-support composite catalysts. The nanoparticles were deposited onto the differently functionalised support materials using a precipitative approach, as elaborated in section 6.2.1. The catalytic activity of the synthesised catalysts was assessed employing catalyst thin-films on a glassy carbon working electrode in electrochemical half-cell measurements. Due to the considerable impact of the thin-film quality on the measured catalytic activity, the fabrication of the catalyst ink dispersion and its coating on the working electrode was investigated in section 6.2.2. In section 6.2.3, the influence of the functionalisation on the catalyst's electrochemical activity and stability was evaluated using cyclic voltammetric measurement results.

### 6.2.1. Catalyst Synthesis

The objective of the support material is to optimise the catalytic performance by increasing the available catalytic active surface area of the heterogenic catalyst. This can be achieved through an effective distribution of the catalytic nanoparticles on the support material.

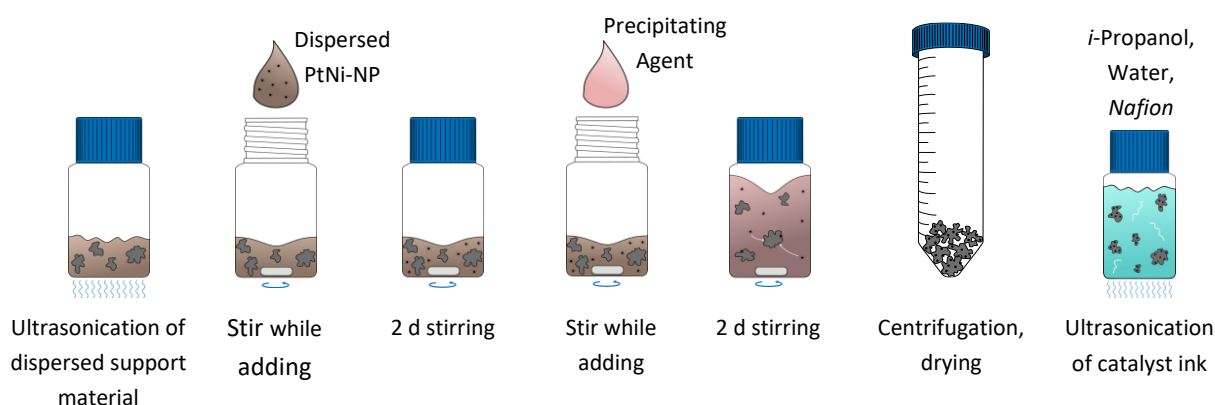
In this work, catalytic nanoparticles and functionalised support materials were synthesised separately, followed by the deposition of the nanoparticles onto the surface of the support material. The employed nanoparticles comprised mainly of platinum-nickel alloy nanoparticles and reference experiments were conducted using platinum nanoparticles. Both nanoparticle types were synthesised using a colloidal approach established by K. AHRENSTORF<sup>[236]</sup> using a ligand mixture of oleylamine and oleic acid. The synthesis of the platinum-nickel nanoparticles was conducted in a continuous flow reactor by S. WODERICH<sup>[237]</sup> while the platinum nanoparticles were synthesised using a batch approach.

Figure 6.20 shows TEM images of both particle types employed in this study. The platinum-nickel nanoparticles consisted of spherical nanoparticles with a diameter of  $3.4 \pm 0.5$  nm. The ratio of Pt to Ni was determined by elemental analysis to be 84 m% Pt and 16 m% Ni. The diameter of the pure platinum nanoparticles was somewhat smaller with  $2.9 \pm 0.7$  nm. Compared to the PtNi nanoparticles, their size distribution was also broader, and their shape was slightly irregular.



**Fig. 6.20:** TEM images of **a)**  $3.4 \pm 0.5$  nm PtNi nanoparticles and **b)**  $2.9 \pm 0.7$  nm Pt nanoparticles employed in this study.

The particles were deposited onto the support material following a precipitative approach which is schematically shown in figure 6.21. Briefly, the support material and the nanoparticles were dispersed and mixed well in a suitable dispersing agent using ultrasonication and stirring. Subsequently, a suitable precipitating agent was added slowly while continuously stirring which was continued for two days. Due to the continuous stirring, the unstable nanoparticles are believed unable to precipitate to the bottom of the container and deposited onto the surface of the support material forming the nanoparticle-support-composition catalyst. The catalyst was separated from the dispersing and precipitating agents by centrifugation. After drying, the catalyst was dispersed in a mixture of isopropanol, water and *Nafion* to form the catalyst ink.



**Fig. 6.21:** Schematic overview over the catalyst synthesis process including the deposition of catalytic nanoparticles onto the support material.

The key aspect for following the precipitation method for catalyst synthesis is an appropriate choice of both dispersing agent and precipitating agent. This becomes apparent when examining the TEM images of catalysts with different support materials shown in figure 6.22. In TEM image a and b,

toluene was utilised as dispersing agent and ethanol as precipitating agent. While this approach leads to well dispersed particles for the unfunctionalised *Vulcan XC72R* support material shown in TEM image a, nanoparticle clusters form when employing the same method for oxidised carbon black as support material as seen in TEM image b. TEM Image c shows a catalyst with oxidised carbon black as support material, synthesised with acetone as precipitating agent instead of ethanol. Here, the distribution of the particles improved compared to TEM image b.

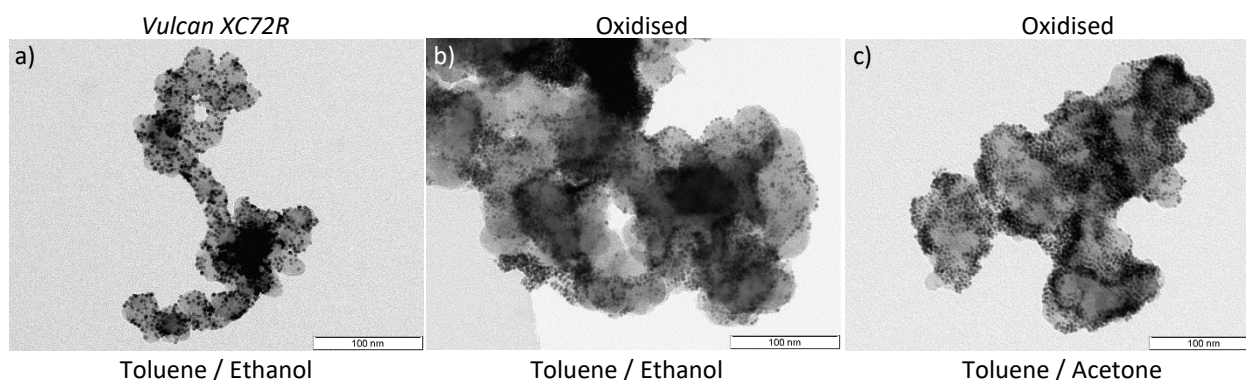


**Fig. 6.22:** TEM images of PtNi-nanoparticle-support-composition catalysts synthesised using the precipitation method with toluene as dispersing agent and ethanol (a, b), or acetone (c) as precipitating agents. The support materials employed were *Vulcan XC72R* (a) or oxidised *Vulcan XC72R* (b, c).

One important factor to consider in regard of dispersion and precipitation is polarity. *Vulcan XC72R* is hydrophobic<sup>[98]</sup> while its oxidation greatly enhances its hydrophilicity.<sup>[92,98]</sup> Accordingly, it was observed that *Vulcan XC72R* could be easily dispersed in the nonpolar toluene, whereas the oxidised carbon black did not disperse as effectively. Therefore, the dispersant was changed to THF, as it is more polar than toluene<sup>[238]</sup> while still being nonpolar enough to disperse the hydrophobic PtNi-nanoparticles well. The catalyst synthesis using THF as dispersing agent was investigated using methanol, ethanol and isopropanol as precipitating agent, as illustrated in figure 6.23. The TEM images clearly illustrate the trend that particle distribution improves with a decreasing polarity of the precipitating agent. The effect is especially pronounced on the oxidised carbon substrate compared to the unfunctionalised one. This indicates that a slower precipitation process is essential for achieving a uniform particle distribution. It also emphasises the importance of a slow addition of the precipitating agent to the dispersed nanoparticle-support mixture, as a rapid addition would lead to a sudden increase of the precipitating agent's concentration at the surface of the mixture.

Consequently, it was found that the best combination for both oxidised and unoxidized carbon supports is THF as dispersing agent and isopropanol as precipitating agent since it leads to a good nanoparticle distribution. However, it should be noted that the inhomogeneous character of the support material and a potentially inhomogeneous surface functionalisation may lead to deviations

from the optimal particle distribution. Furthermore, the two-dimensional display of the three-dimensional catalyst in TEM images may create the impression of a closer proximity of the nanoparticles on the side of a carbon flake compared to the top side.

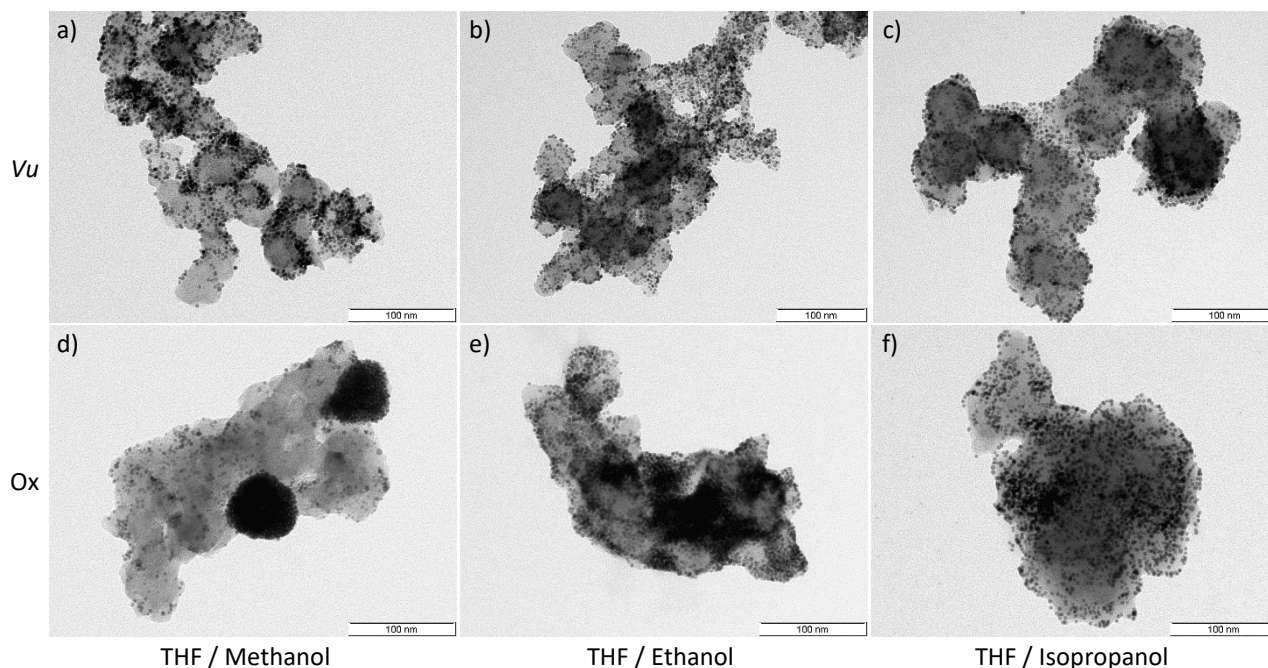


**Fig. 6.23:** TEM images of PtNi-nanoparticle-support-composition catalysts synthesised using the precipitation method with THF as dispersing agent and methanol (a, d), ethanol (b, e), or isopropanol (c, f) as precipitating agents. The support materials employed were *Vulcan XC72R* (a-c) or 7 d oxidised *Vulcan XC72R* (d-f).

In summary, the catalyst synthesis utilising the precipitation method was tailored to cater to polar substrates, as well as nonpolar ones. It was found, that THF as dispersing agent and isopropanol as precipitating agent led to a good particle distribution for oleylamine/oleic acid-stabilised PtNi nanoparticles on all tested substrates. It is hypothesised that the two primary factors contributing to the formation of nanoparticle clusters on the support material are inadequate dispersion of the nanoparticles and support material, as well as a too fast precipitation.

### 6.2.2. Investigation of Catalyst Thin-Films on Working Electrodes

A suitable method to determine the electrocatalytic activity of novel fuel cell catalysts is the employment of electrochemical half-cell measurements. Nanoparticle-support-composition materials can be conveniently screened using smooth disc electrodes in a three-electrode set-up. To achieve this, a thin layer of catalyst ink is applied to the disc electrode tip to serve as the working electrode.

This method offers the advantage of short screening times and only small amounts of catalyst are required.<sup>[186]</sup>

The method of thin-film disc electrode half-cell measurements is highly sensitive, particularly as only small quantities of the catalyst are employed. A critical factor influencing the measured activity is the morphology of the catalyst thin-film on the disc electrode. Thicker catalyst films can increase mass-transport resistance, which may lower the potentially measurable catalytic activity, with CV measurements generally being less influenceable by bad films than ORR measurements.<sup>[186]</sup> Naturally, unevenly distributed catalyst films are also prone to decrease the reproducibility of the measurements.<sup>[197]</sup>

The first step to achieve a thin, homogeneous catalyst layer involves the homogeneous dispersion of the catalyst in a suitable suspension agent to form the catalyst ink. Alcohol-water mixtures are typically employed, whereby the mixture has to be tailored to suit the respective type of catalyst.<sup>[186]</sup> Small additions of *Nafion* to the mixture can help to improve the homogeneity of the catalyst ink,<sup>[239]</sup> and can also be helpful for the catalyst's adhesion to the working electrode and film quality on the working electrode, while on the other hand impeding electrochemical activity.<sup>[201]</sup> The suspending agents used in this work consisted of 0-20 w% isopropanol, 0-0.1 w% *Nafion* and ultrapure water.

During the dispersion, it is essential to break apart the flakes that agglomerated during centrifugation to ensure an optimal performance in the half-cell electrochemical measurements. For the measurements, a small amount of the catalyst ink is applied to a glassy carbon working electrode and dried. The presence of large agglomerates is presumed to lower the specific catalytic activity since enclosed particles may not contribute to the catalytic reaction, and the diffusion path to reach those particles is longer. Therefore, the catalyst morphology was investigated using SEM images, as shown in figure 6.24, to study the effect of a prolonged ultrasonic treatment.

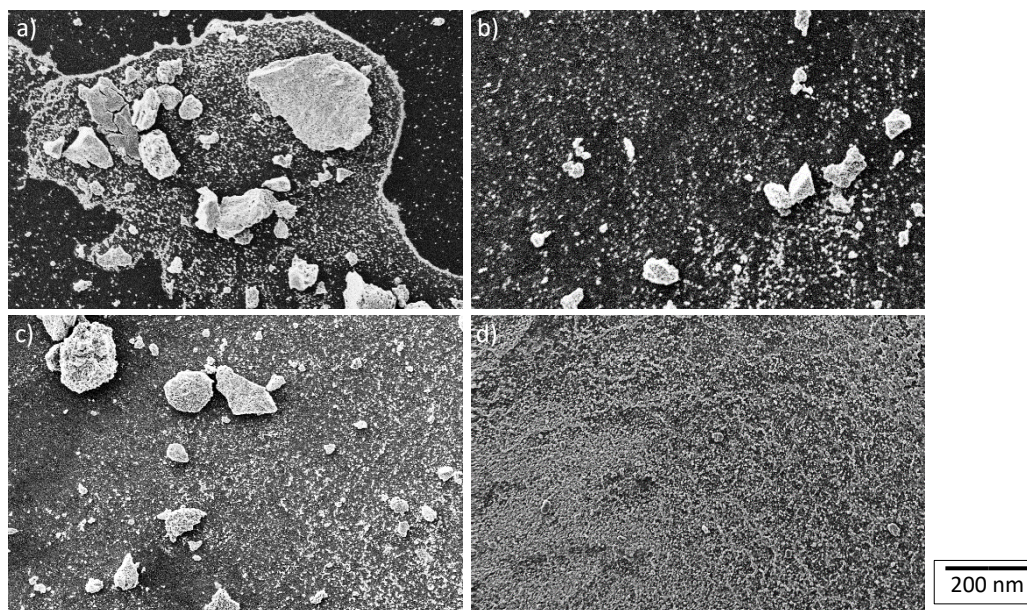


**Fig. 6.24:** SEM images of catalyst ink (PtNi on 2 d oxidised carbon black, dispersed in 10 v% isopropanol, 0.02 v% *Nafion* and ultrapure water) ultrasonicated for **a)** 0 hours, **b)** 1 hour, **c)** 6 hours, **d)** 12 hours.

The SEM images in figure 6.24 reveal that prior to ultrasonication, large aggregates are present. With prolonged ultrasonication duration, the aggregates were still present, albeit with smaller diameter and number. Only after 12 hours of ultrasonication, a homogeneous ink was obtained with only smaller aggregates visible.

This emphasises the importance of a thorough mixing of the catalyst ink through ultrasonication. Empirical findings further demonstrate that regular agitation of the catalyst ink amid ultrasonication facilitates a homogeneous suspension. As a rule of thumb, a catalyst ink was deemed ready for application on the working electrode, when no precipitate was visible upon inversion of the catalyst ink sample flask. The catalyst preparation included at least ten hours of ultrasonication prior to the first application to the working electrode, with an additional ultrasonication period of at least 30 minutes conducted before subsequent applications following storage. Since a prolonged use of an ultrasonic bath can entail elevated temperatures up to 65 °C, a cooled ultrasonic bath was employed at 15 °C to avoid catalyst degradation.

Subsequently, the standard procedure to obtain a catalyst thin-film on the disc electrode is to apply a drop of the catalyst ink onto the electrode and allow it to dry. The attainment of uniform thin-films using this method is not trivial and entails a number of challenges. Firstly, a homogeneous catalyst ink suspension with a sufficiently low concentration is essential to achieve a uniform thin-film. Another challenge arises with the drying of the catalyst ink drop. As described in detail in section 4.3.4.1, a ring-shaped deposition (coffee-ring) is formed in most cases after drying a drop of a

suspension on a surface. This phenomenon is also frequently observable during the drying process of a catalyst ink on a disc electrode.

Therefore, extensive studies have been conducted regarding the manufacturing of catalyst thin-films.<sup>[197]</sup> Figure 6.25 illustrates three different drying approaches that were employed in this work.

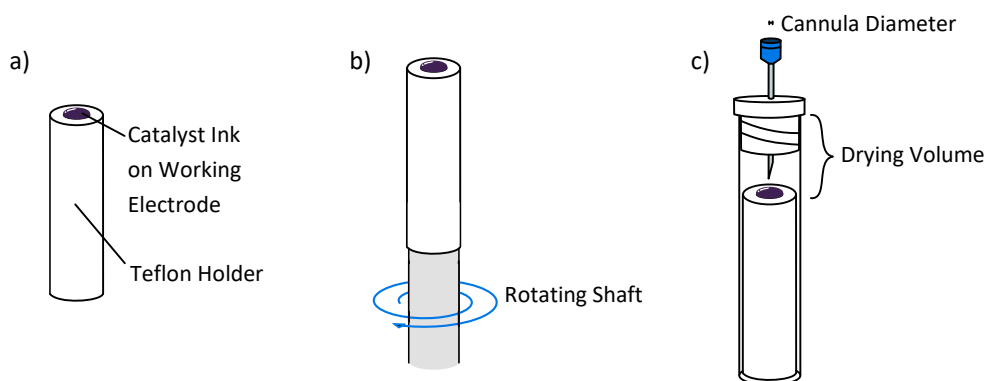


**Fig. 6.25:** Schematic overview over different drying techniques for catalyst thin films on the working electrode. **a)** Stationary drying technique. **b)** Rotating drying technique. **c)** Flow-restricted drying technique.

The first approach is a simple stationary drying technique without use of any special measures. As demonstrated in the SEM images in figure 6.26, this method usually leads to the formation of coffee-rings. According to DEEGAN *et al.*<sup>[203,207,208]</sup>, this phenomenon occurs when the drop's contact line is pinned. Hence, to retain the drop's equilibrium shape that is dictated by surface tension, the evaporation rate is increased at the edge which results in an outward flow that carries the suspended particles to the edge.

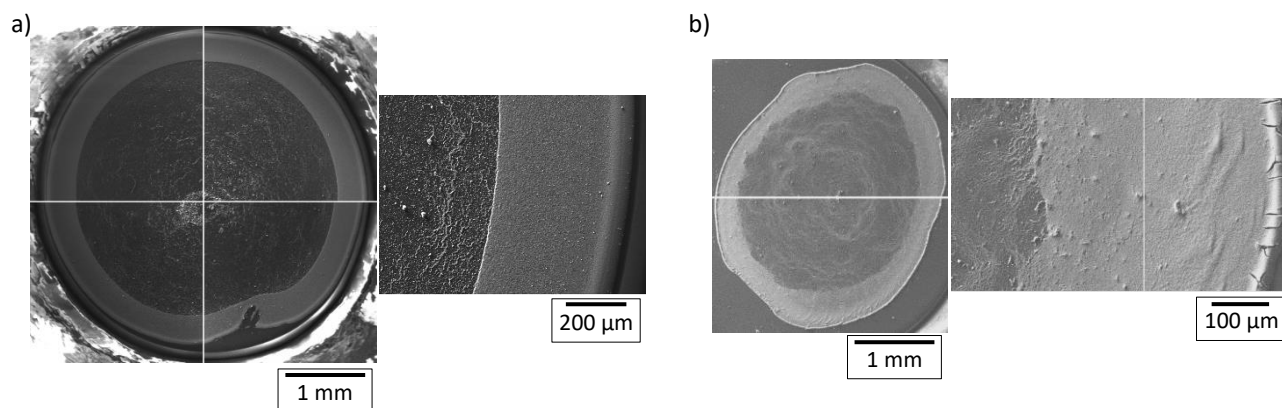


**Fig. 6.26:** SEM images of catalyst ink (PtNi on 4h oxidised carbon black) dried on a glassy carbon electrode using the stationary drying technique. **a)** Dried at room temperature. (40 v% isopropanol, 0.05 v% Nafion, and ultrapure water). **b)** Dried at 40 °C. (0.05 v% Nafion in ultrapure water).

The second, rotating drying technique was developed by GARSANY *et al.*<sup>[197]</sup>, where the disc electrode encased in a *Teflon* holder is rotated during the drying of the catalyst drop. The group

observed the formation of more uniform thin-films resulting in better electrochemical performances using this method with their catalyst inks.

Figure 6.27 displays SEM images of glassy carbon electrodes coated with a catalyst ink employing the rotary drying technique at two different rotation speeds. Despite the positive results obtained by GARSANY *et al.*, the application of these findings to the catalyst inks employed in this work, resulted in the formation of coffee-rings of variable severity. Furthermore, a low reproducibility concerning the film quality when employing this drying technique, was observed.

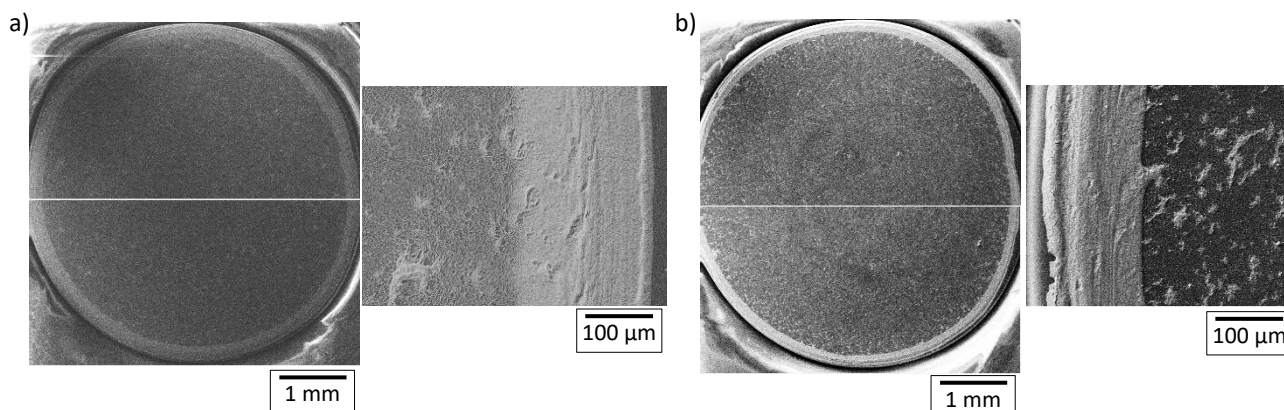


**Fig. 6.27:** SEM images of catalyst ink (PtNi on 4 h oxidised carbon black, dispersed in 10 v% isopropanol, 0.05 v% *Nafion* and ultrapure water) dried on a glassy carbon electrode using the rotating drying technique at room temperature. Dried at a) 700 rpm. b) 950 rpm.

The third approach utilises a restriction in airflow during drying, inspired by experiments conducted by DEEGAN *et al.*<sup>[207]</sup> Here, an aliquot of the catalyst ink was positioned on the glassy carbon electrode, encased in a *Teflon* holder and the electrode holder was placed in a container that was closed, save for a cannula that was placed over the drop's tip. In principle, the evaporation rate at the drop's tip is increased due to the hole over the drop's tip counterbalancing the radial outward flow induced by the increased evaporation at the drop's edge.

In order to find the optimal conditions while employing this drying technique for the synthesised inks, systematic experiments were conducted using design of experiment (DoE). The investigated parameters and ranges were deemed as relevant according to preliminary tests. The composition of the ink was varied with fractions of isopropanol ranging from 0 to 40 v% and with *Nafion* fractions of 0-0.1 v%. Furthermore, in the drying setup, depicted in figure 6.25c, the inner diameter of the cannula was varied between 0.4 and 0.8 mm and the size of the container was varied resulting in air volumes over the drying drop varying from 0.64 to 7.41 mL. The combinations of parameter values were predetermined by the DoE software *Cornerstone* using a D-optimal design as listed in table 8.2

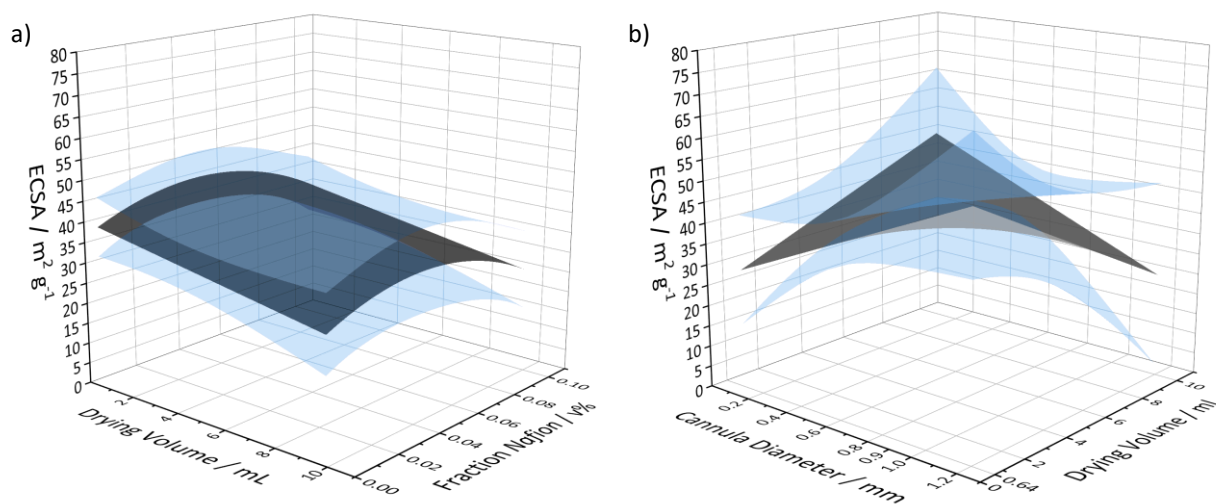
and the maximal ECSA value of each measurement was employed as the response for the evaluation by the DoE software. A residual probability plot was employed to obtain a linear regression model. For this, an untransformed fitting function was selected and parameters with a significance over 0.1 were considered not relevant and removed from the model. The calculated regression coefficients are listed in table 6.1 with the statistical metrics of each parameter.

**Tab. 6.1:** Regression coefficients of the linear regression model with statistical metrics calculated by the *Cornerstone* DoE software.

Parameter	Coefficient	Standard Error	T-Value	Significance	Variance Inflation Factor
Constant	18.9	8.02	2.36	0.0335	0
Cannula Diameter / mm	28.2	12.5	2.256	0.0403	1.72
Drying Volume / mL	2.77	1.48	1.86	0.0817	3.44
Fraction Nafion / v%	265	110	2.40	0.0308	3.26
(Fraction Nafion) <sup>2</sup> / (v%) <sup>2</sup>	-3020	1090	-2.78	0.0148	3.26
Cannula Diameter · Drying Volume / mm · mL	-5.08	2.40	-2.11	0.0530	3.64
R <sup>2</sup>	Adjusted R <sup>2</sup>	Root Mean Square Error	Pure Error	Residual Degrees of Freedom	
0.511	0.337	5.814	6.377	14	

According to the linear regression model, the ink's isopropanol content was regarded as insignificant in relation to ECSA values. Therefore, it was not considered in this model. Since the surface tension of inks with lower alcohol contents led to drop diameters (10 µL) lower than the glassy carbon electrode diameter, leading to an incomplete electrode coverage, a 40 % isopropanol fraction was adopted as standard.

When plotting the model's predicted ECSA values against the *Nafion* content and the drying volume at a constant cannula diameter or against the *Nafion* content and the cannula diameter at constant a drying volume, it can be observed that the predicted ECSA has a parabolic shape depending on the *Nafion* content. As seen in figure 6.28a and in the appendix in figures 10.9 and 10.10, the parabola has its maximum between 0.04 and 0.05 v% within the investigated range. On this basis, a *Nafion* content of 0.05 v% was used in further investigations.



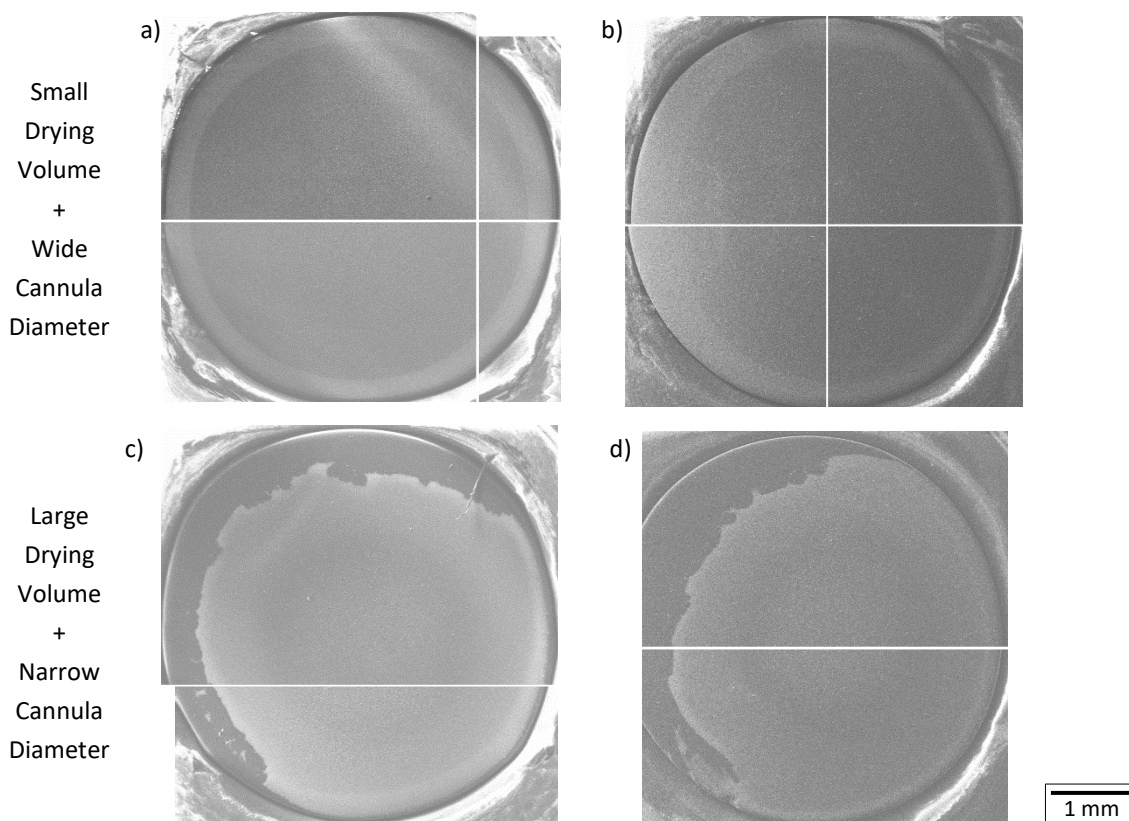
**Fig. 6.28:** Predicted ECSA (black) and upper and lower confidence intervals with 95 % significance (blue) of the linear regression model calculated by the *Cornerstone DoE* software. **a)** Constant cannula diameter of 0.76 %. **b)** Constant *Nafion* fraction of 0.05 v%.

Figure 6.28b shows the predicted ECSA as a function of cannula diameter and drying volume at a constant *Nafion* content of 0.05 v%. It can be inferred from the graph that both the combinations of a small drying volume with a wide cannula diameter and a large drying volume with a narrow cannula diameter are the most beneficial for high ECSA values.

However, the plot shows no local maximum, so it is not discernible to which extent the parameters can be changed in the directions of the global maxima to still exert a beneficial effect. It is anticipated that physical limitations of the cannula diameter and drying volume will impose restrictions at a certain point. For example, drying volumes below ca. 0.64 mL have been found to be practically unfeasible.

Furthermore, the regression model demonstrates only a moderate reliability as seen in moderate values of the statistical metrics listed in table 6.1. One factor contributing to this lies in the high sensitivity of the electroanalytical approach using half-cell measurements on disc electrodes. Only low sample quantities in the microgram range are utilized, which renders this method sensitive to slight variabilities. Consequently, a higher number of repeated experiments are necessary to obtain a more robust model. Another contributing factor is the variance in film morphology observed under identical drying conditions. This phenomenon was particularly probable when the ink composition contained amounts of isopropanol lower than 40 v%. Here, it was frequently observed that the edge of the catalyst film was irregular and often frayed, as demonstrated in figure 6.29c and d for a catalyst ink containing 20 v% isopropanol. Nevertheless, this model still provides some valuable insight regarding the general trends of drying conditions.

Figure 6.29 shows SEM images of glassy carbon electrodes coated with catalyst inks after employing the flow-restricted drying technique with the more beneficial parameters according to the linear regression model. SEM images a and b depict catalyst films dried in a small drying volume using a wide cannula diameter. SEM images c and d represent a large drying volume and a narrow cannula diameter. The ink formulation of both presented inks contained the optimal *Nafion* content of 0.05 v% and either (a, b) 40 v% or (c, d) 20 v% isopropanol.



**Fig. 6.29:** SEM images of catalyst ink (PtNi on 4 h oxidised carbon black) dried on a glassy carbon electrode using the flow-restricted drying technique at room temperature. **a and b)** Ink containing 40 v% isopropanol, 0.05 v% *Nafion* and ultrapure water, dried in a 0.64 mL drying volume with a 0.8 mm cannula. **c and d)** Ink containing 20 v% isopropanol, 0.05 v% *Nafion*, and ultrapure water, dried in a 7.41 mL drying volume with a 0.4 mm cannula.

Both parameter combinations lead to coffee-rings that are discernible in the SEM images. Yet the coffee-rings appear to be less pronounced compared to the ones when employing the stationary or rotating drying techniques shown in figures 6.26 and 6.27. Since it is challenging to evaluate the catalyst ink film's thickness based on SEM images alone, selected samples were further investigated using AFM. Figure 6.30 gives an overview over the thicknesses at different positions of the film. A more detailed representation is depicted in section 10.5 in the appendix.

It can be inferred from figure 6.30 a and b that the manifestation of the coffee-ring is indeed less pronounced when employing the flow-restricted drying technique. Here, the thickness of the edge amounted to an average of ca. 1000 to 1500 nm compared to ca. 500 to 600 in the centre. On the other hand, the stationary drying technique in figure 6.30c reveals an edge thickness of ca. 5500 nm and a thickness of ca. 130 nm in the centre.

Interestingly in image a, the film thickness first decreases towards the edge before rising to form the coffee-ring. A possible explanation for this formation of a cap in the centre could be the thermal Marangoni effect. The Marangoni effect describes a flow from lower to higher surface tensions. The surface tension is inverse proportional to the temperature, and a drying drop only has the substrate it is drying on as heat source. Therefore, the tip of the drying drop is the coldest, has the highest surface tension, and a radial inward flow is introduced.<sup>[207,211]</sup>

The limitations for the investigations *via* AFM lie in the small measuring range (here: max. 100·100  $\mu\text{m}$ ) and long measuring durations for each measurement. Therefore, it is only possible to present small sections of the catalyst films. The catalyst films exhibit a significant roughness as can be inferred from the high standard deviations and can be seen in the appendix. Additionally, the catalyst films feature randomly distributed, sporadic larger aggregates that may be included in the measured section by chance. This may significantly affect the average height. Consequently, the AFM images do not provide a complete representation of the height distribution, but merely offer an impression of the thickness at different positions. In comparison to the observations made in the SEM images, the AFM images confirm the general trend.

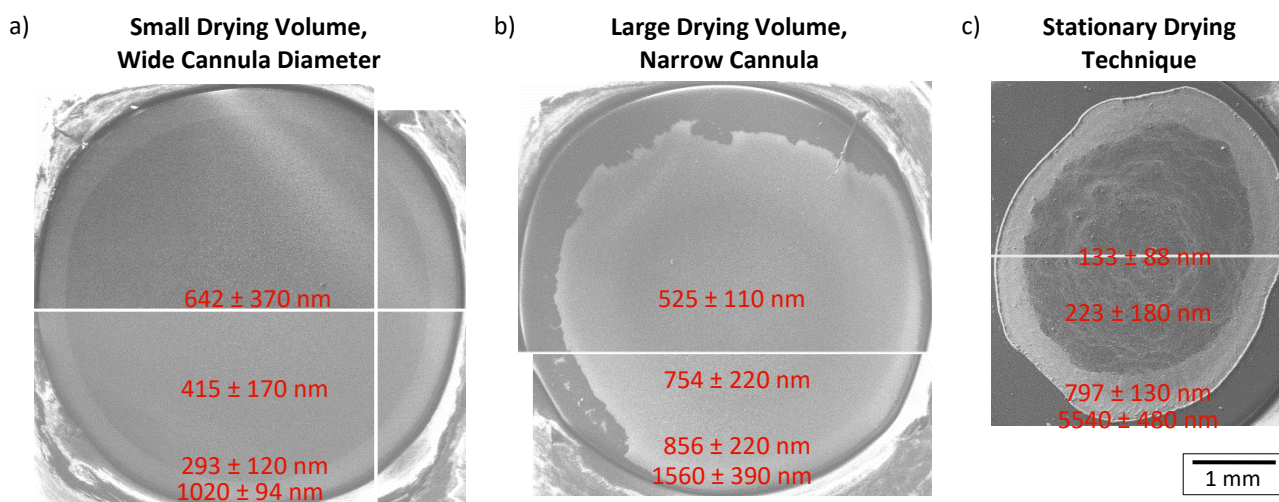


**Fig. 6.30:** Overview of catalyst ink (PtNi on 4 h oxidised carbon black) film thicknesses at different positions of the film according to AFM measurements. **a)** Dried using the flow-restricted drying technique at room temperature in a 0.64 mL drying volume with a 0.8 mm cannula. (40 v% isopropanol, 0.05 v% *Nafion*, and ultrapure water) **b)** Dried using the flow-restricted drying technique at room temperature in a 7.41 mL drying volume with a 0.4 mm cannula. (20 v% isopropanol, 0.05 v% *Nafion*, and ultrapure water) **c)** Dried using the stationary drying technique at 40 °C. (0.05 v% *Nafion* in ultrapure water).

To further evaluate the influence of the catalyst film's morphology on the performance in electrochemical measurements, cyclic voltammetric measurements were performed comparing the flow-restricted and the stationary drying techniques. For the flow-restricted approach, a small drying volume and a wide cannula diameter was chosen, as it resulted in the most uniform catalyst films attainable according to SEM images. The stationary drying technique on the other hand, consistently resulted in the formation of a coffee-ring. Figure 6.31 shows the maximal ECSA values of both drying techniques for four different samples and the respective catalyst film morphologies.

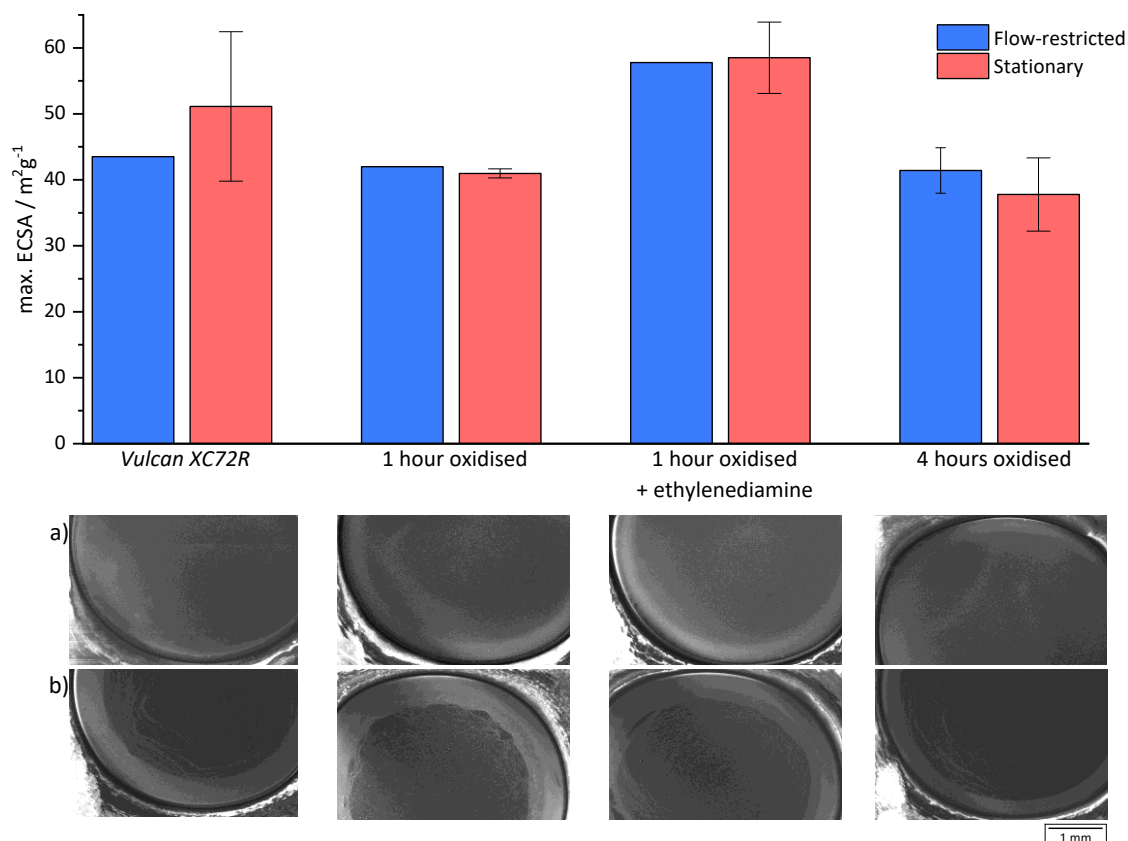


**Fig. 6.31:** Maximal ECSA values of catalyst inks (PtNi on different substrates) dried using the flow-restricted drying technique (0.64 mL drying volume; 0.8-0.9 mm cannula diameter) compared to the stationary drying technique at room temperature. For comparison, a representative SEM image of one coated electrode using each drying technique (**a:** flow-restricted, **b:** stationary) per sample is presented. (Ink formulation: 40 v% isopropanol, 0.05 v% Nafion, and ultrapure water)

The data presented in figure 6.31 shows that both drying techniques lead to similar ECSA values, inferring a limited dependency on the film morphology. Similar results were obtained in literature, where the catalyst film's morphology<sup>[197,198]</sup>, the catalyst ink's *Nafion* content<sup>[201]</sup> and the catalyst ink's pH value<sup>[200]</sup> was observed to have a low impact on ECSA values, while significantly influencing ORR specific activities. Therefore, ORR measurements were conducted comparing catalyst films obtained through both drying techniques, as presented in figure 6.32.

While no significant differences of the measured currents could be detected in the kinetic-controlled region above 1.0 V vs. RHE, the curves split at 0.8 V in the mixed kinetic-diffusion controlled region with the more uniform catalyst film exhibiting higher cathodic currents that persist at a higher level within the diffusion-limited region below 0.7 V. This is consistent with the observations made by GARSANY *et al.*<sup>[186]</sup> where films with lower uniformity exhibited lower cathodic currents. The  $E_{1/2}$  benchmark is 0.82 V for both films. This is the same value achieved by GARSANY *et al.* for a low-

quality film, while the group measured 0.85-0.89 V for a uniform catalyst film. The lower cathodic currents in the diffusion-controlled region can be attributed to the catalyst film's thickness, which varies in non-uniform films with the thicker parts being less permeable for the reactants by diffusion. A similar detrimental effect on the diffusion-controlled and mixed-controlled regions in the ORR polarisation curves could be observed by KOCHA *et al.*<sup>[201]</sup> after adding *Nafion* to the catalyst ink. In this work, 0.05 v% *Nafion* was employed in the catalyst inks as it was observed to be the optimal amount for high ECSA values.

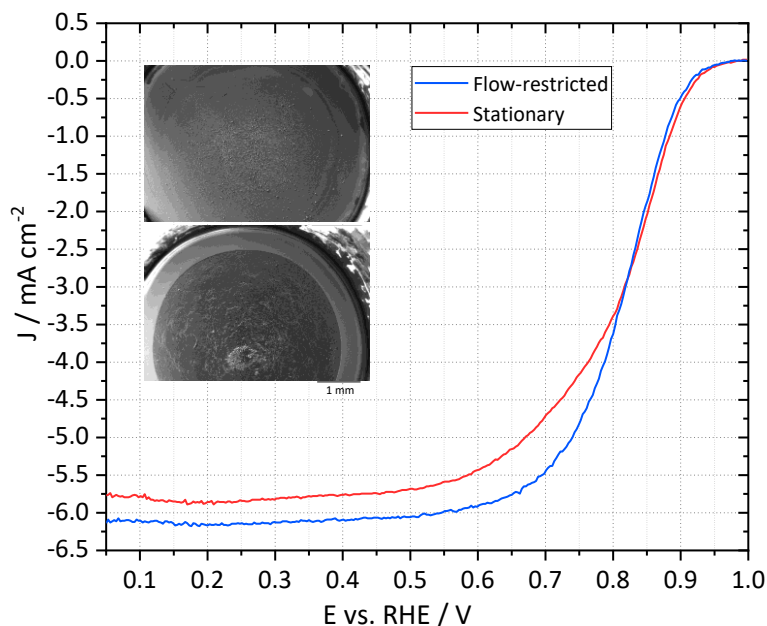


**Fig. 6.32:** ORR polarisation curves (anodic sweeps prior to background current subtraction) and SEM images of catalyst inks (PtNi on *Vulcan XC72R*) dried using the flow-restricted drying technique (0.64 mL drying volume; 0.9 mm cannula diameter) compared to the stationary drying technique at room temperature. Ink formulation: 40 v% isopropanol, 0.05 v% *Nafion*, and ultrapure water. Recorded in  $O_2$ -saturated 0.1 M  $HClO_4$  at 25 °C at 20  $mV s^{-1}$  and 1600 rpm with a Pt loading of 8.1  $\mu g_{Pt} cm^{-2}$ .

Both films show a very low  $E_{onset}$  resulting in very small currents at 0.9 V, consequently leading to very low specific activities presented in table 6.2. According to the mass-specific activity  $I_m$ , which is calculated after subtracting the background current recorded in  $N_2$ -saturated electrolyte, the less uniform catalyst film using the stationary drying technique is slightly more active than the more uniform film. Nevertheless, both mass-specific activities are lower than values measured for commercial Pt/C catalysts and even several orders of magnitudes lower than the values measured for octahedral  $Pt_3Ni/C$  of comparable sizes as listed in table 6.2. Furthermore, ORR polarisation curves were recorded using a polycrystalline platinum disc after thorough cleaning of all glassware with peroxymonosulphuric acid. Its area-specific activity  $I_s$  was determined to be 47.0  $\mu A cm^{-2}$  at 0.9 V

while GARSANY *et al.*<sup>[186]</sup> declared 1500-3000  $\mu\text{A cm}^2$  as a benchmark for a successfully cleaned polycrystalline platinum disc. This suggests the presence of impurities during the measurement with one possible source being the ligands (oleic acid and oleylamine) bound to the catalytic nanoparticle's surface, which detach from the surface during electrochemical cycling. Before each ORR measurement, a rigorous cleaning procedure of the glassware, which involved an overnight soak in peroxymonosulphuric acid, was conducted. Additionally, prior to each measurement, electrochemical cleaning cycles were performed in a separate measurement cell. Nevertheless, residues cannot be excluded. Especially during measurements of catalyst ink films, remaining ligands may continue to detach. Another possible explanation may stem from undiscovered issues with the set-up or the measurement apparatus.

**Tab. 6.2:** Characteristic currents and mass-specific activities  $I_m$  obtained from ORR polarisation curves (figure 6.32) after background current subtraction ( $\text{N}_2$ -saturated 0.1 M  $\text{HClO}_4$  at 0 rpm) and literature values for mass-specific activities.

Film drying technique	$I$ at 0.9 V vs. RHE / mA	$I_{lim}$ at 0.4 V vs. RHE / mA	$I_m / \text{A mgPt}^{-1}$
Flow-restricted	-0.0971	-1.17	0.0666
Stationary	-0.128	-1.11	0.0913
Oct. $\text{Pt}_3\text{Ni}/\text{C}$ ( $4.2 \pm 0.2$ nm) <sup>[14]</sup>			1.80
Oct. $\text{Pt}_3\text{Ni}/\text{C}$ (4.5 nm) <sup>[240]</sup>			1.08
<i>HiSPEC 13100</i> Pt/C <sup>[241]</sup>			0.19
<i>TKK 60%</i> Pt/C <sup>[241]</sup>			0.28

In conclusion, an SEM study revealed the importance of a sufficiently long ultrasonic treatment for the attainment of a homogeneous catalyst ink, which is necessary to achieve homogeneous catalyst thin-films. It was observed that a cooled ultrasonication of at least ten hours prior to electrochemical measurements is necessary to avoid catalyst agglomerates.

Furthermore, it was possible to increase the catalyst film quality using a flow-restricted drying approach using a small drying volume and a wide cannula diameter. After drying, a coffee-ring was still observable, but according to AFM measurements, the height difference was a lot less severe compared to a stationary drying technique. CV investigations revealed a limited influence of the catalyst film uniformity on the ECSA value. On the other hand, deviations in the ORR polarisation curves indicate improved diffusion properties of the more uniform thin film. Unfortunately, all ORR measurements showed very low catalytic activities suggesting an underlying problem with the oleic acid/oleylamine ligands, the cleaning process, or the measurement set-up. Since the origin of the

decrease in catalytic activity remains unclear, further electrochemical investigations focussed on CV measurements. On account of the low impact of the catalyst film morphology on ECSA values and the disadvantage of prolonged drying times of 6-7 days using the flow-restricted drying compared to <1 day using the stationary drying technique, the latter was mainly employed in the electrochemical measurements described in the following chapter.

### 6.2.3. Catalyst Characterisation

Nanoparticle-support composite catalysts were synthesised consisting of platinum or platinum-nickel alloy nanoparticles and surface-modified support materials. The introduction of functional groups to the support's surface can lead to an improved particle-support interaction, which may also have a beneficial influence on the catalytic performance, especially a reduced rate in degradation.<sup>[34]</sup> Hence, the influence of the support functionalisation on the electrochemical activity and stability was investigated employing cyclic voltammetry.

Prior to the particle deposition, the base substrate *Vulcan XC72R* and one oxidised *Vulcan XC72R* sample were electrochemically investigated using cyclic voltammetry. The surface layer diagrams of both samples were compared in regard to their electrochemical behaviour and stability. As shown in figure 6.33, 3000 full CV cycles were recorded for each substrate.

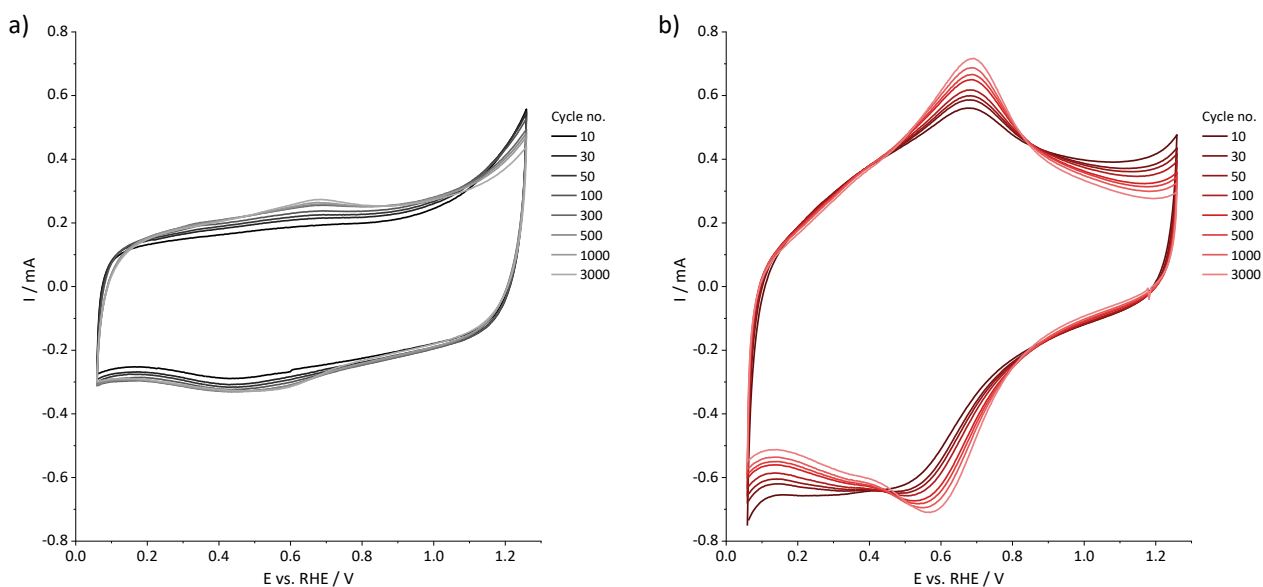


**Fig. 6.33:** Surface layer diagrams of **a)** *Vulcan XC72R* and **b)** *Vulcan XC72R* oxidised for 43 hours with 3:1 sulphuric acid and nitric acid, at increasing numbers of full 0.06-1.2 V, 0.1 V s<sup>-1</sup> cycles, measured in 0.1 perchloric acid.

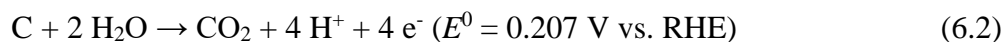
The surface layer diagrams reveal an increased capacitive current after the oxidation, which can be explained by the increased hydrophilicity due to the introduction of functional groups.<sup>[100,242]</sup> The

middle region, between 0.4 and 0.8 V vs. RHE, exhibits a faradaic charge couple that can be attributed to the quinone/hydroquinone redox couple<sup>[243]</sup> described by equation 6.1.<sup>[244]</sup>



This redox couple is associated with surface oxides. The oxidised carbon exhibits a greater number of surface groups, resulting in a surface layer diagram that displays more pronounced peaks compared to the unfunctionalised *Vulcan XC72R*. Furthermore, in both voltammograms, the intensity of the peaks increases with the number of cycles, which suggests an increased degree of oxidation. While the first cycle of *Vulcan XC72R* displays no anodic peak and only a minor cathodic peak in that region, the peak couple becomes apparent with an increasing number of cycles. Thus, it can be concluded, that the unfunctionalised carbon also undergoes an electrochemical oxidation process during potential cycling between 0.06 and 1.2 V vs. RHE, which was previously observed by AVASARALA *et al.*<sup>[182]</sup> as well.

At the peak potential of 1.2 V vs. RHE, a second anodic current is observed. As demonstrated by the investigations conducted by AVASARALA *et al.*<sup>[182]</sup> and PÉREZ-RODRÍGUEZ *et al.*<sup>[100]</sup>, this peak is likely attributable to the irreversible carbon gasification to CO<sub>2</sub> according to equation 6.2.<sup>[185]</sup>



The gasification leads to carbon corrosion which is one type of catalyst degradation. As it reduces the surface area for the catalytic particles, a carbon corrosion entails the detachment or agglomeration of the catalytic nanoparticles.

Though PÉREZ-RODRÍGUEZ *et al.* observed an increased gasification current with increased degree of oxidation due to the surface oxide groups facilitating the CO<sub>2</sub> formation, the same observation could not be made in this work. Here, the absolute current at 1.2 V of the initial cycles is similar, albeit slightly higher for the unfunctionalised *Vulcan XC72R* with 0.56 mA, compared to 0.48 mA for the oxidised carbon. One possible explanation for this discrepancy may be a different composition of the various surface oxide groups. PÉREZ-RODRÍGUEZ *et al.* used a 1:1 mixture of nitric and sulphuric acid or only nitric acid in their oxidation process resulting in a significantly lower amount of carboxylic acid groups (ca. 0.2-0.5 mmol g<sup>-1</sup>) detected by temperature programmed desorption (TPD) compared to carboxylic acid groups detected by titration (ca. 1-3 mmol g<sup>-1</sup>) in this work.

With increasing number of cycles, the anodic gasification peak decreases, as also observed by AVASARALA *et al.* This may arise from easily oxidisable defects or surface impurities that are more

prevalent in the initial material and are gradually removed as the oxidation process progresses with an increasing number of cycles.<sup>[182]</sup>

In essence, two oxidation processes of oxidised and unoxidised *Vulcan XC72R* can be distinguished. At lower potentials around 0.7 V vs. RHE, surface oxidation processes occur with increasing severity at increasing number of cycles. Simultaneously, oxidation to CO<sub>2</sub> occurs at potentials above 1 V vs. RHE, which decreases in severity with increasing number of potential cycles. A third type of oxidation, the oxidation of water to oxygen, namely the oxygen evolution reaction (OER) may theoretically also occur at potentials above 1 V vs. RHE, but PÉREZ-RODRÍGUEZ *et al.*<sup>[100]</sup> found no evidence of a notable OER rate of carbon or oxidised carbon in the absence of metal nanoparticles.

The surface layer diagrams of unfunctionalised and functionalised *Vulcan XC72R*, after deposition of PtNi or Pt nanoparticles can be seen in figure 6.34. The surface layer diagrams consist of a superposition of the currents originating from the respective support material and catalytic nanoparticles.

The impact of the support material is well visible in the middle region of the diagrams from ca. 0.3 to 0.6 V vs. RHE, which is also known as the ‘double layer region’. In parallel with the surface layer diagrams without particles in figure 6.33, the functionalised carbons display a higher capacitive current due to the increased hydrophilicity,<sup>[100]</sup> which can be attributed to an increased counter ion adsorption with increasing hydrophilicity, beneficial for charging and discharging efficiencies.<sup>[245]</sup> Here as well, the quinone/hydroquinone charge couple is visible between 0.4 and 0.8 V when using the oxidised carbon as support material. Interestingly, after further functionalisation of the oxidised carbon with ethylenediamine (EDA) or triethylenetetramine (TETA), the quinone/hydroquinone peaks are missing in the surface layer diagrams, yet an elevated double layer current can still be detected.

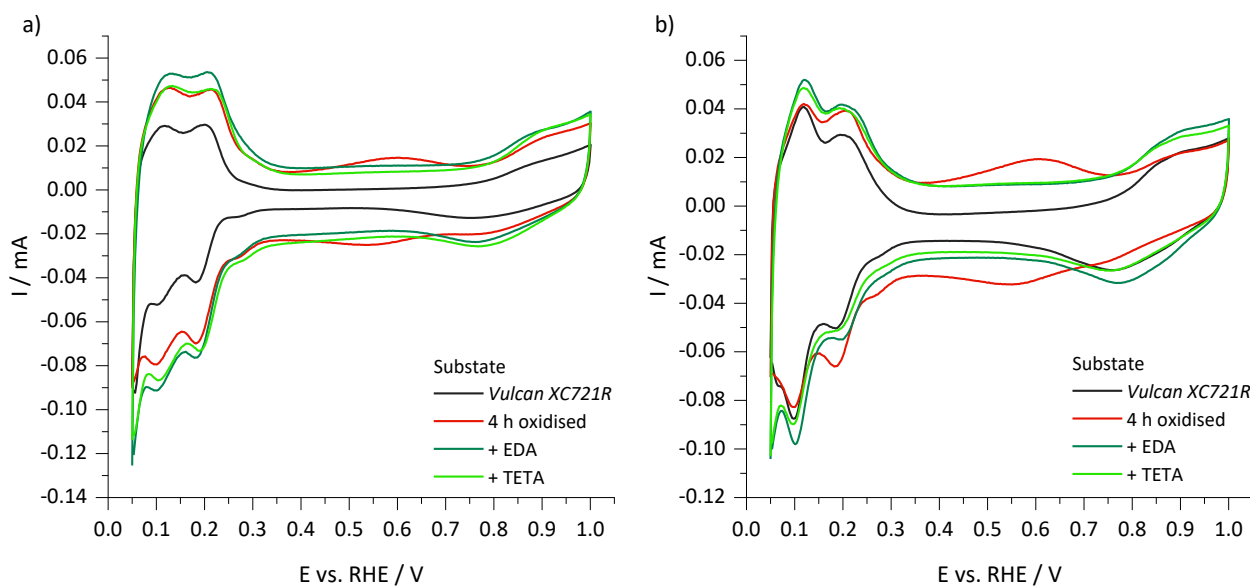


**Fig. 6.34:** Surface layer diagrams (AST cycle no. 4000) of **a)** PtNi nanoparticles and **b)** Pt nanoparticles on different substrates (*Vulcan XC72R*, *Vulcan XC72R* oxidised for four hours with 3:1 sulphuric acid and nitric acid and further functionalised with ethylenediamine (EDA) or triethylenetetramine (TETA). Recorded in 0.1 M perchloric acid at  $50 \text{ mV s}^{-1}$ .

The PtNi and Pt nanoparticles both display cathodic hydrogen adsorption and anodic hydrogen desorption peaks in the range of ca. 0.08 to 0.35 V vs. RHE. Within the hydrogen adsorption/desorption region, two anodic peaks at ca. 0.12-0.13 and 0.20-0.21 V and two cathodic peaks at slightly lower potentials of ca. 0.10 and 0.18-0.19 V are detected. Notably, in the case of pure Pt particles, the first peaks (lower potential) are more pronounced than the second peaks, whereas this is not the case with PtNi. According to CV curves of Pt and Pt<sub>3</sub>Ni displaying single crystal facets recorded by STAMENKOVIC *et al.*,<sup>[24]</sup> both peaks can likely be attributed to the (110) facet. Other facets may contribute to the hydrogen adsorption/desorption region as well, especially since the (111) facet displays only a weak current without any pronounced peaks compared to other facets. This points at a cubic, cuboctahedral, or truncated octahedral geometry of the catalytic particles, as these geometries display (110), and in the latter two cases also (111) facets.<sup>[81]</sup>

Figure 6.35 displays CV curves of PtNi or Pt nanoparticles on *Vulcan XC72R* after varying numbers of accelerated stress test (AST) cycles illustrating the influence of proceeding electrochemical stress on the catalysts. The area of the respective hydrogen adsorption region is utilised as a measure of the catalytic activity as ECSA according to equation 4.18. It is recommended<sup>[186]</sup> to use the hydrogen evolution onset as the minimum potential for integration, which can be identified as a cathodic current minimum around 0.08 V vs. RHE.<sup>[194]</sup> Since not all CV cycles display the hydrogen evolution

minimum, in this work a minimum potential of 0.05 V was chosen for integration of the hydrogen adsorption peak.

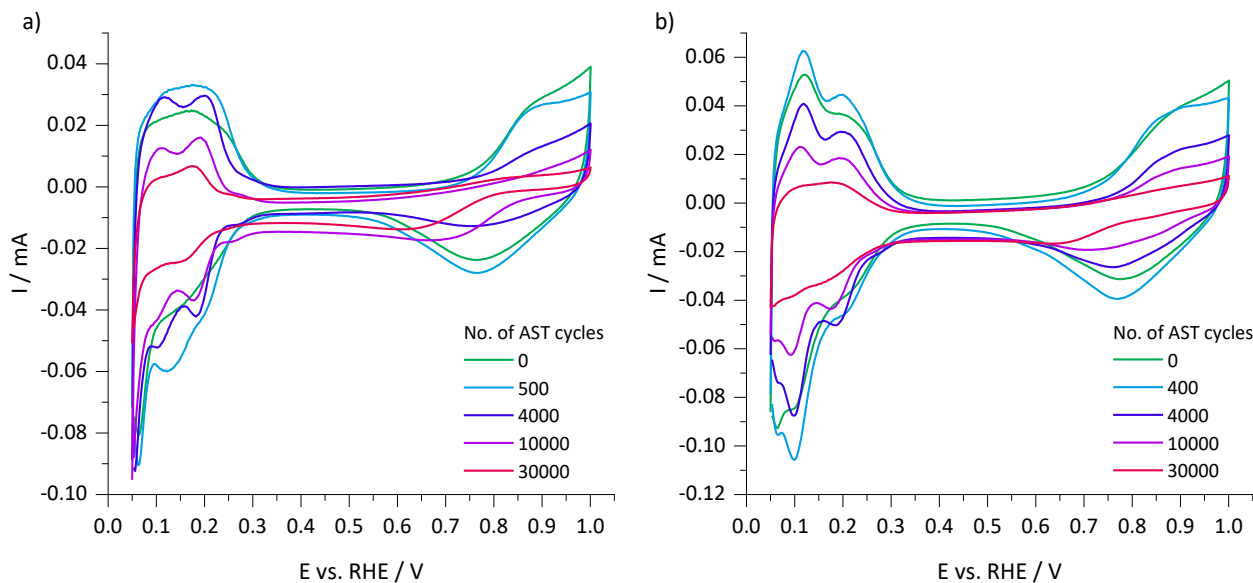


**Fig. 6.35:** Surface layer diagrams of **a)** PtNi nanoparticles and **b)** Pt nanoparticles on *Vulcan XC72R* after increasing numbers of AST cycles. Recorded in 0.1 M perchloric acid at  $50 \text{ mV s}^{-1}$ .

It is apparent that the hydrogen adsorption area decreases with increasing number of AST cycles. This is also illustrated in figure 6.36 which displays a typical course of the ECSA plotted against the number of AST cycles. Figure 6.36 shows an increase in catalytic activity in the first few hundred cycles, which may be attributed to electrochemical cleaning of the particles. After traversing the maximum ECSA, due to electrochemical degradation, the catalytic activity decreased with decreasing rate.<sup>[10]</sup>

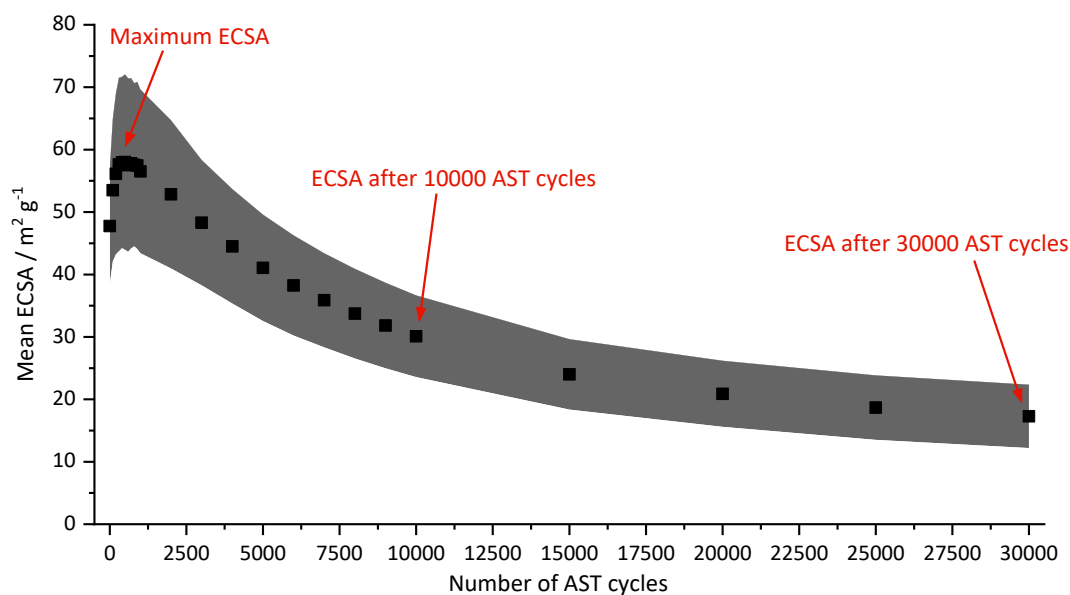


**Fig. 6.36:** Average ECSA with standard deviation of PtNi nanoparticles on *Vulcan XC72R* plotted against the number of AST cycles.

When comparing the intensities of the two (110) peaks of the pure platinum catalyst, the first peak remains more pronounced than the second peak during the first 20000 cycles, albeit with decreasing ratio as the measurement proceeds. After 30000 cycles, the hydrogen region displays no distinct peaks suggesting a loss of particle geometry due to electrochemical degradation and a superposition of currents resulting from a variety of facets. The TEM images in figure 6.37d reveal an increase in particle size with irregular shapes, which supports this assumption. The degradation of the catalytic particles can be explained by electrochemical *Ostwald* ripening, or agglomeration as described in detail in section 4.2.5.

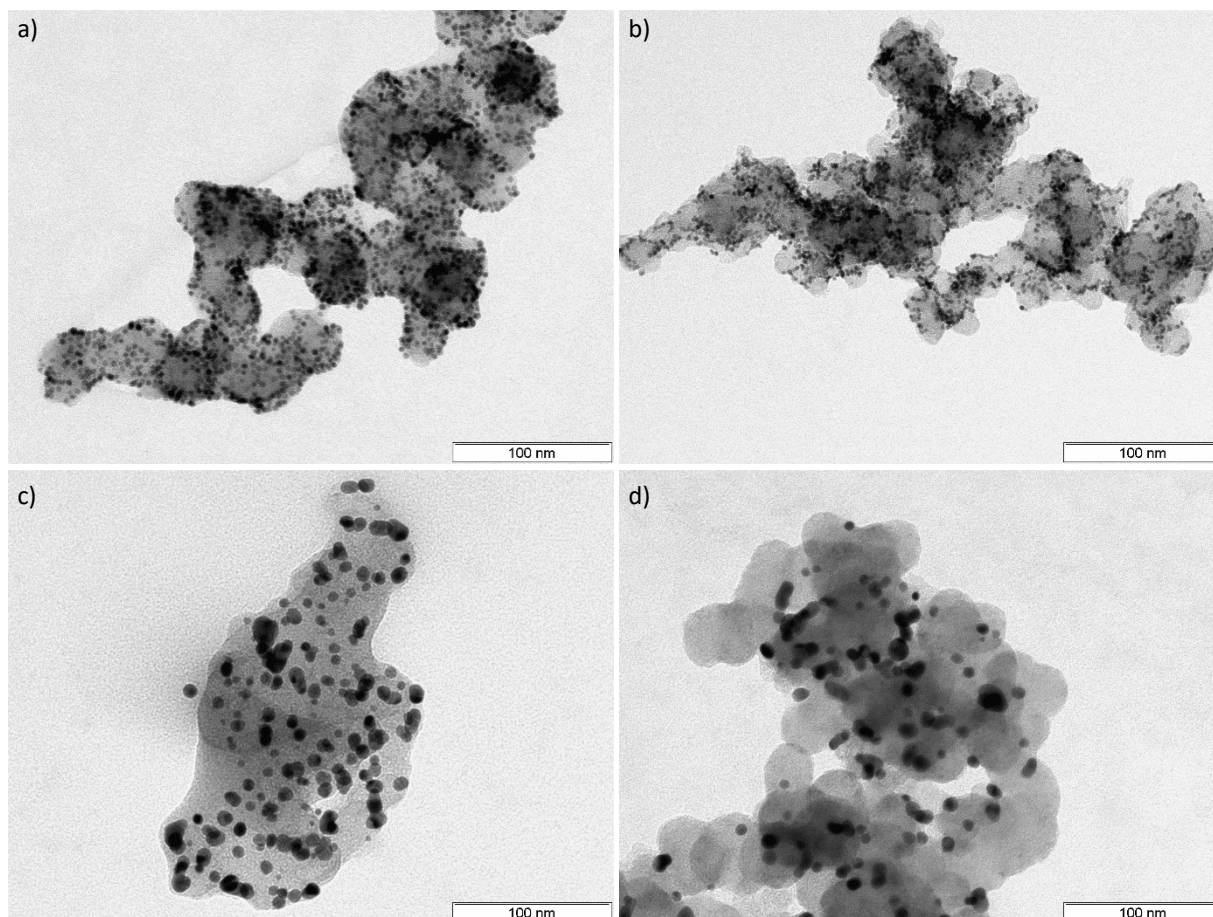


**Fig. 6.37:** TEM images of catalysts before and after 30000 AST cycles. **a)** PtNi on *Vulcan XC72R* before AST and **c)** after AST. **b)** Pt on *Vulcan XC72R* before AST and **d)** after AST.

In the case of the PtNi nanoparticles, the early cycles display no pronounced peaks within the hydrogen region before gradually developing the (110) peaks during cycles 500-2000 with similar intensities. From the 6000th cycle onwards, the second peak gradually increases in intensity relative to the first peak and after 25000 cycles, only the second peak remains visible in the hydrogen region. The progress of the peak development can be explained by Ni leaching out of the nanoparticles during potential cycling.<sup>[178,246,247]</sup> At the onset of the measurement, the intact platinum-nickel alloy may display a variety of crystal facets due to its bimetallic nature. In the process of potential cycling, the nickel continues to be removed from the particles while developing distinct (110) peaks. The predomination of the second peak during the advanced cycling may be explained by a porous platinum-rich structure of the particles. The TEM images in figure 6.37c show an increase in particle size and irregular shaped particles similar to the pure platinum particles.

For the comparison of the catalytic activity of different catalysts employing the ECSA, three key points were considered, as illustrated in figure 6.36. The maximum ECSA was chosen as reference value to minimise the impeding influences of ligands on the particle surface. The respective maximum

values are compared to the ECSAs after the 10000th (and 30000th) cycle to demonstrate the severity of the electrochemical degradation due to potential cycling. Each catalyst ink was applied to the working electrode multiple times and the respected CV curves were recorded, to form the average value with standard deviation.

As elucidated in section 6.2.2, the thin-film disc electrode half-cell measurement method is fairly challenging, resulting in large variances of the maximal ECSAs of the same sample prepared in an identical fashion. To illustrate the repercussions of the disc electrode measurements, one catalyst ink sample was measured for 23 times and the respective maximal ECSAs are plotted in figure 6.38.

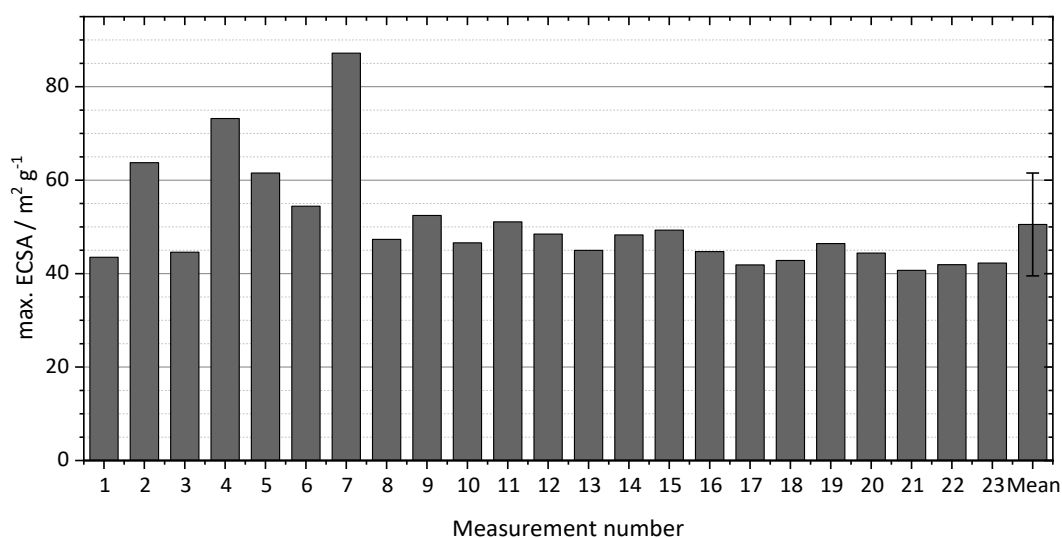


**Fig. 6.38:** Respective maximum ECSAs of the same PtNi / *Vulcan XC72R* ink of 23 individual CV measurements in order of recording and their mean value with standard deviation. The catalyst ink thin films were prepared using the stationary drying technique except for no. 1 (0.64 mL drying volume, 0.9 mm cannula) and no. 3 (7.41 mL drying volume, 0.4 mm cannula), dried with the flow-restricted approach.

In figure 6.38, most measurement attempts exhibited a similar maximal ECSA of  $46 \pm 4 \text{ m}^2 \text{ g}^{-1}$ . Exceptions include measurements no. 2, 4, 5 and 7 with 33 to 89 % higher ECSAs, which are responsible for an elevated standard deviation. A potential cause may be an inhomogeneous dispersion of the catalyst ink, where the extracted aliquot inadvertently contained a higher concentration of the catalyst. The platinum content of catalyst ink concentration was determined by atomic absorption spectroscopy after acid digestion of 300  $\mu\text{L}$  catalyst ink dispersion and the utilised platinum content on the working electrode was calculated using the aliquot volume of 10  $\mu\text{L}$ . Due to the very small sample sizes, it was not possible to determine the quantity of sample that actually adhered to the electrode, leaving room for errors.

In order to prevent an inhomogeneous ink dispersion, thorough ultrasonic treatment was conducted as described in section 6.2.2 before the first CV measurement (10+ hours) and to a lesser extent before each thin-film preparation (15-60 minutes). However, it cannot be ruled out that the ultrasonic treatment was not sufficiently long in each individual case. It is noteworthy that most deviating ECSAs occur in the beginning of the measurement series, which supports this thesis since the ultrasonic treatment was continued before each thin-film preparation. Due to the densely black colour of the catalyst ink, a visual examination of the extracted aliquot was proven to be challenging, and only very low concentrations could be distinguished.

Interestingly, the drying method of the catalyst thin-film appears to exert no significant impact on the maximal ECSA, as measurement number one and three do not significantly deviate from the majority of the measurements. This corroborates the findings from section 6.2.2.

The maximal ECSA and the ECSA after potential cycling was utilised to compare the influence of the functionalisation of the support material on the catalytic activity. As described in chapter 6.1, the *Vulcan XC72R* support material was first oxidised using a mixture of sulphuric and nitric acid for varying times. The respective oxidised carbon supports were further functionalised using ethylenediamine (EDA), triethylenetetramine (TETA), phenylenediamine (PDA) or butanedithiol (BDT) using either a direct functionalisation route, or a two-step synthesis involving an  $\text{SOCl}_2$  intermediate step. The catalytic nanoparticles were deposited on the respective support material to form the catalyst according to section 6.2.1.

In a first step, preliminary studies were conducted using a seven days oxidised carbon, which was functionalised using a variety of approaches and loaded with PtNi. Figure 6.39 compares the maximal ECSA of each catalyst with the remaining ECSA after 10000 full CV cycles.

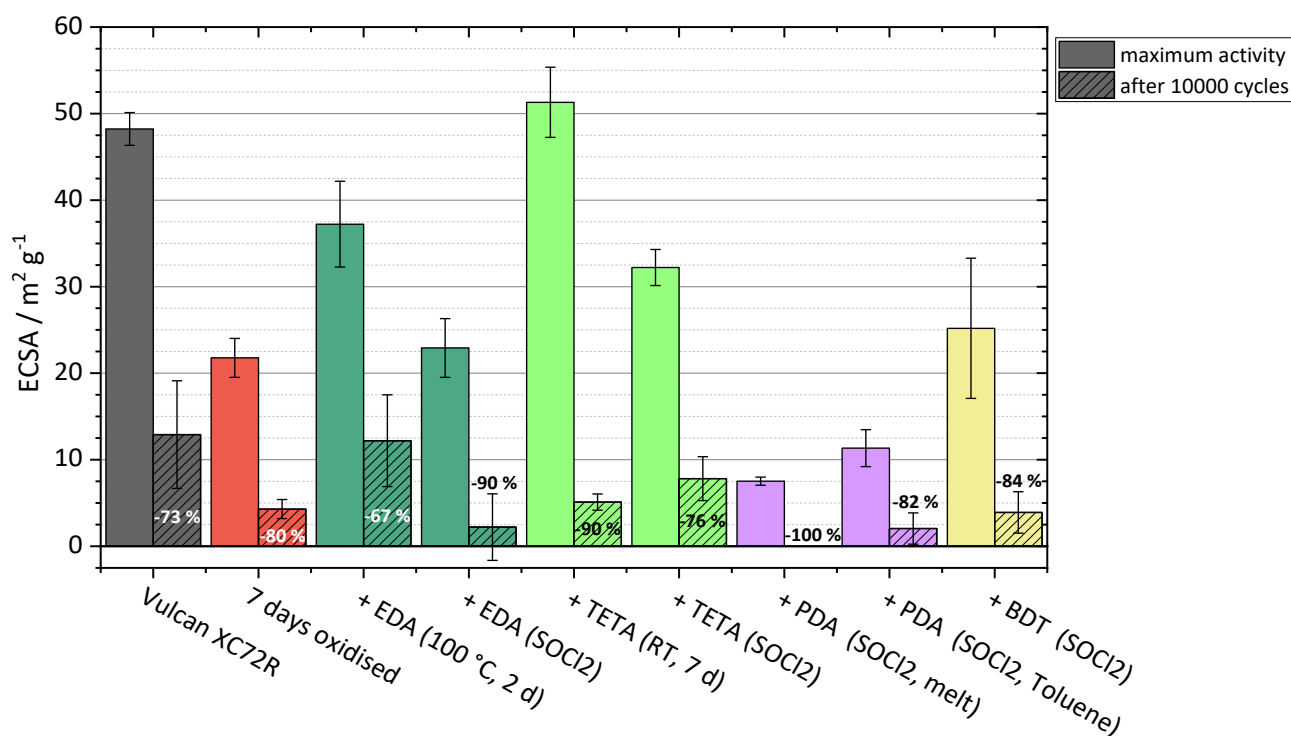


**Fig. 6.39:** Average maximum ECSA and ECSA after 10000 full CV cycles (-0.059-1.259 V vs. RHE) of PtNi nanoparticles on *Vulcan XC72R*, *Vulcan XC72R* oxidised for 7 days (sulphuric and nitric acid), and further functionalised with various diamines or butanedithiol.

When comparing the maximal ECSA of the catalysts with the unfunctionalised *Vulcan XC72R* support material against the catalyst featuring the seven days oxidised support, it is apparent that the catalytic activity was significantly reduced after oxidation. One reason may be a decrease in conductivity of the oxidised support due to the introduction of surface oxide groups possibly disrupting the amorphous carbon's  $\pi$ -system. Furthermore, the BET surface area of the support was significantly reduced after oxidation for seven days from  $265 \pm 12 \text{ m}^2 \text{ g}^{-1}$  to  $92 \pm 15 \text{ m}^2 \text{ g}^{-1}$  which can lead to a decreased spatial distribution and thus decreased accessibility of the catalytic particles for the reactants.

The direct functionalisation of the oxidised carbon support with ethylenediamine led to an improved maximal catalytic activity compared to the oxidised carbon support. Since the specific surface area generally decreases by ca. 30 % due to functionalisation with a diamine (figure 6.19) compared to its oxidised carbon, and the  $\pi$ -system disrupting oxide groups are still present on the surface, an improved catalytic performance due to an increased particle-support or ionomer-support interaction is likely. Similar results were observed after functionalisation with triethylenetetramine. Here, the maximal ECSA after the direct functionalisation even surpassed the unfunctionalised *Vulcan XC72R*.

Both for EDA and TETA, it was observed that the two-step synthesis route employing thionyl chloride led to reduced catalytic activities. These results are unexpected since the two-step synthesis led to elevated nitrogen content of the functionalised supports by 17-30 % (figure 6.16) indicating a higher degree of functionalisation. On the other hand, also elevated amounts of sulphur impurities were detected for the two-step synthesis compared to the direct functionalisation. This suggests an inhibiting influence of the sulphur impurities counteracting against the enhancing influence of the amine surface functionalisation.

The functionalisation with phenylenediamine was examined since its aromatic structure implied an elevated conductivity of the functional group. According to the elemental composition (figure 6.17), PDA was successfully introduced to the support's surface, especially the synthesis conducted in the PDA melt. However, the catalysts featuring the PDA-functionalised support displayed very low catalytic performances as shown in figure 6.39.

Lastly, the catalytic activity of PtNi on butanedithiol-functionalised carbon was investigated. Here, regardless of the comparably low functionalisation grade determined in the elemental composition (figure 6.17), an increase in maximal catalytic activity compared to the oxidised support was detected. This indicated for a beneficial influence of the thiol functionalisation.

The decrease of the catalytic activity after 10000 cycles serves as an indicator for the severity of the catalyst's electrochemical degradation. The catalyst featuring unfunctionalised *Vulcan XC72R* displayed an ECSA loss of -73 % after 10000 cycles. Most of the tested support materials led to a similar or more severe decrease up to 100 % in catalytic activity. Solely the catalyst featuring the support that was EDA-functionalised using the direct route displayed a lower degree of degradation of -67 % leading with  $12.2 \pm 5.3 \text{ m}^2 \text{ g}^{-1}$  to roughly the same remaining ECSA after 10000 cycles as the unfunctionalised *Vulcan XC72R* exhibiting  $12.9 \pm 6.2 \text{ m}^2 \text{ g}^{-1}$ . This suggests a stabilising effect of the ethylenediamine group regarding catalyst degradation.

Overall, during the preliminary studies, it was found that the direct EDA- and TETA-functionalisation displayed the most promising characteristics. While the TETA-functionalised catalyst displayed the overall highest catalytic activity, the EDA-functionalised catalyst exhibited the lowest degree of electrochemical degradation. Therefore, further investigations were conducted using these two types of functionalisations. Since the preliminary studies were conducted based on the seven days oxidised *Vulcan XC72R* with a significantly lower BET surface area, which may impede the catalytic performance, further investigations focussed on oxidised carbons with shorter oxidation times since these substrates featured significantly higher BET surface areas (figure 6.9, 6.19). Figure

6.40 compares the catalytic activity of PtNi on *Vulcan XC72R*, which was oxidised for 1, 2, and 4 hours and the respective further functionalisations with EDA and TETA. The electrochemical degradation was investigated using accelerated stress tests (AST), which comprised of three-second potential steps at 0.6 and 1.0 V vs. RHE for 10000 cycles.

As a general trend, it is observable that the oxidised support led to a decrease of the maximal catalytic activity by 30 % (with the exception of the two hours oxidised support). After the EDA-functionalisation, the maximal activity increased again to slightly lower than *Vulcan XC72R*. In contrast to the preliminary test, the TETA-functionalisation showed no beneficial influence compared to the oxidised supports. In section 6.1.2, it was hypothesised that the majority of TETA-molecules were bound to the oxidised carbon's carboxylic acid groups *via* both primary amine groups, featuring a bridged functionalisation while the shorter EDA-molecules mainly exhibited monofunctional amines. This implies that the catalytic nanoparticles would interact with the primary  $\text{NH}_2$ -groups in the case of the EDA-functionalisation and with secondary NH-groups in the case of the TETA-functionalisation. The electrochemical results imply that the former interaction exhibits a higher strength than the latter, as well as compared to the interaction with the oxide groups.

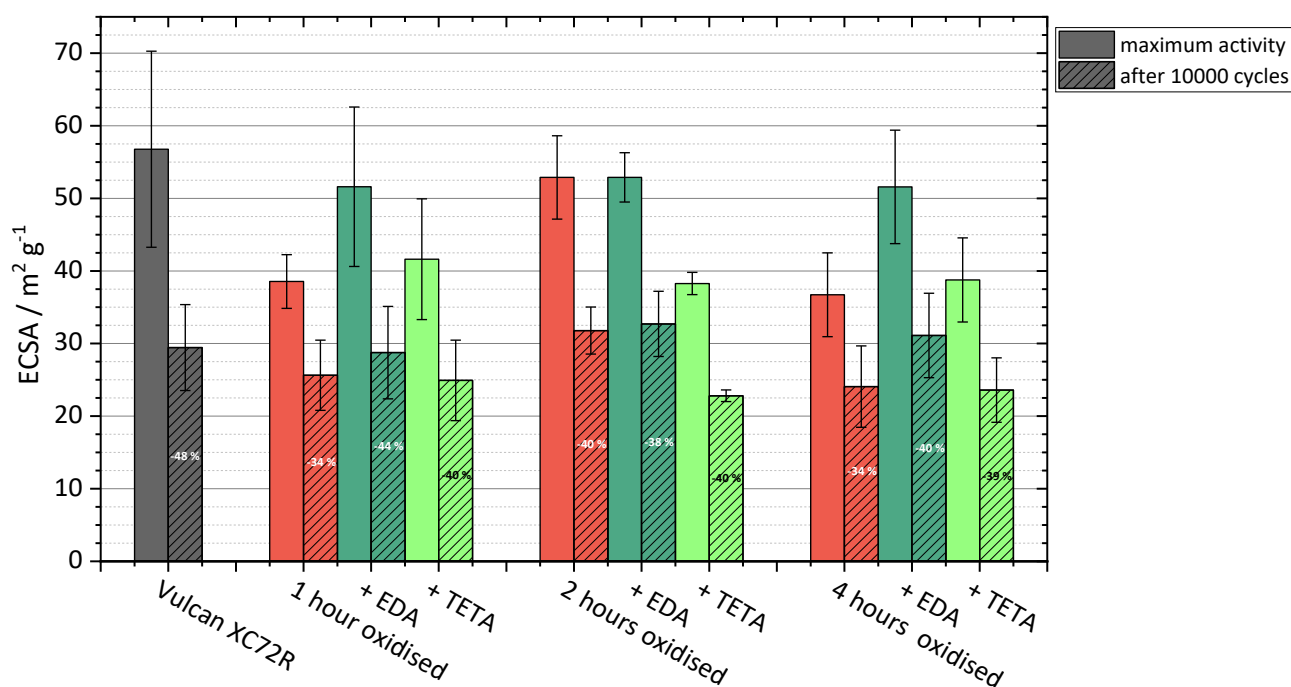


**Fig. 6.40:** Average maximum ECSA and ECSA after 10000 AST cycles (0.3-0.6 V vs. RHE) of PtNi nanoparticles on *Vulcan XC72R*, *Vulcan XC72R* oxidised for varying times (sulphuric and nitric acid), and further functionalised with ethylenediamine (EDA) or triethylenetetramine (TETA).

In regard of the electrochemical degradation, all functionalised substrates in figure 6.40 feature a less severe percentual decrease in catalytic activity compared to *Vulcan XC72R*. Even the absolute ECSA values after 10000 AST cycles of the PtNi nanoparticles on two EDA-functionalised substrates exceed those of *Vulcan XC72R*-supported PtNi. This clearly demonstrates the beneficial effect of the EDA-functionalisation of the catalyst support in regard of electrochemical stability. To further investigate the long-term stability of the catalysts featuring different functionalisations, a more detailed study of the four-hour oxidised carbon support with EDA- or TETA-functionalisation comprising of 30000 AST cycles was undertaken as illustrated in figure 6.41. The support materials were loaded with either PtNi or Pt nanoparticles to examine the functional group's interaction with the different metal surfaces. Furthermore, the catalytic activities were compared to the commercial catalyst *HiSPEC 3000*, prepared in the same fashion.

In figure 6.41, the PtNi catalysts show the same trends as in the previous graph with the unfunctionalised and EDA-functionalised catalysts exhibiting the highest maximal ECSAs while the oxidised and TETA-functionalised catalysts display a decrease of the maximal ECSAs by ca. 30 %. In terms of degradation, as in figure 6.40, the support functionalisations led to a lower relative electrochemical degradation compared to *Vulcan XC72R* after AST 10000 cycles. The difference is even more pronounced after 30000 cycles, where the functionalised substrates led to decrease in ECSA of only 54-57 % compared to *Vulcan XC72R* with a 70 % decrease. The particles supported on the EDA-functionalised carbon displayed the highest absolute remaining ECSA after 30000 cycles while the otherwise functionalised support materials showed remaining ECSA-values similar to *Vulcan XC72R*. Compared to figure 6.40, the results deviate slightly, since only measurements with 30000 AST cycles were evaluated.

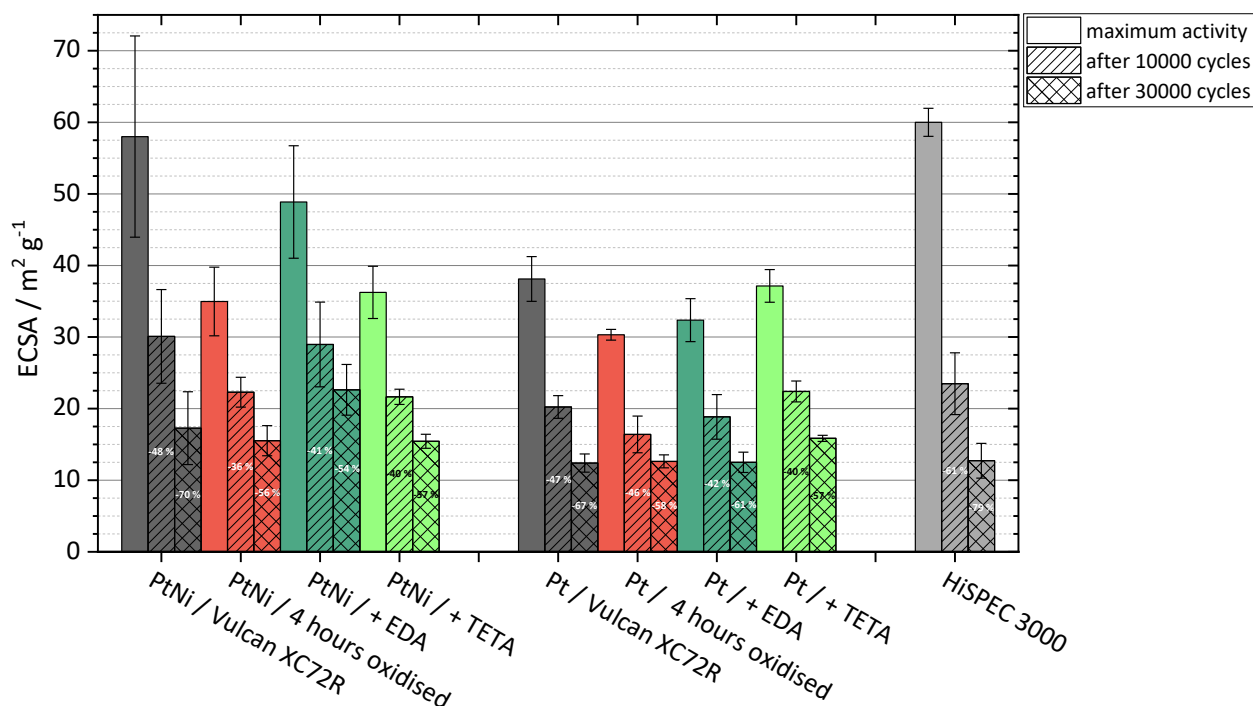


**Fig. 6.41:** Average maximum ECSA and ECSA after 10000 and 30000 AST cycles (0.3-0.6 V vs. RHE) of PtNi and Pt nanoparticles on *Vulcan XC72R*, *Vulcan XC72R* oxidised for four hours (sulphuric and nitric acid), and further functionalised with ethylenediamine (EDA) or triethylenetetramine (TETA). Compared to the commercial catalyst *HiSPEC 3000* (Alfa Aesar).

The Pt catalysts generally exhibit lower catalytic activities than the PtNi catalysts, which is in agreement with NAGAI *et al.*<sup>[179]</sup> who investigated the catalytic activity of PtNi-alloys in relation to Pt:Ni ratio. The average sizes of both particle types are similar as shown in figure 6.41, albeit slightly smaller for the Pt nanoparticles. Since smaller nanoparticles display a higher surface to volume ratio leading to a higher catalytic surface area per mass and thus ECSA,<sup>[248]</sup> the lower ECSA values cannot be contributed to the particle sizes.

In contrast to the PtNi catalysts, the TETA-functionalisation exhibited the most beneficial characteristics for the Pt catalysts, with only a slightly lower maximal catalytic activity than the *Vulcan XC72R*-supported Pt catalyst and the highest remaining ECSA after 30000 AST cycles of all synthesised Pt catalysts. The oxidised and EDA-functionalised supports both show maximal ECSAs reduced by 15-20 % and a similar remaining ECSA-value after 30000 cycles compared to Pt on *Vulcan XC72R*.

A potential explanation for the beneficial influences of the EDA-functionalisation for the PtNi catalysts, and the TETA-functionalisation for the Pt catalysts is the improved stabilisation of the catalytic nanoparticles through electrostatic interactions<sup>[37,39]</sup> with the support's NH<sub>2</sub> or NH groups,

respectively. The increased particle-support interaction may inhibit particle detachment and particle movement across the support's surface leading to a lower degree of degradation. Moreover, the increased particle-support interaction may facilitate an improved particle dispersion during the particle deposition, rendering the particle surfaces more accessible for reactants, which leads to higher maximal ECSAs. However, this could not be confirmed upon visual inspection of TEM images (appendix section 8.8), where the support's functionalisation generally led to a less uniform distribution of the particles. It has been found that carboxylic acids are stronger ligands than amines for PtNi particles while amines are stronger ligands than carboxylic acids for Pt particles.<sup>[249]</sup> Therefore, a stronger stabilising effect for the PtNi particles was expected for the oxidised support material compared to the EDA-functionalised support. However, in this work, the primary amine group exhibited the most advantageous characteristics for PtNi particles. In case of the pure Pt particles, an elevated stabilisation effect of the primary EDA-functionalised support compared to the oxidised support was expected, which showed only minimal differences. Here, the secondary amine groups displayed the most advantageous effect on the stability of the Pt nanoparticles.

In addition to the increased particle-support interaction, it was shown<sup>[40,250]</sup> that the introduction of N-groups also entails an increased interaction of the support with the  $\text{SO}^{3-}$  side-chains of the *Nafion* ionomer. This results in a more homogeneous distribution of the ionomer, which can lead to a reduced oxygen transport resistance and thus increased catalytic activity.

Another possible contributing factor to the elevated stability may be the loss of the carbon support's fine structure due to the initial oxidative treatment. The BET results in figure 6.9 and the SEM images in figure 6.7 in section 6.1.1 clearly demonstrate a reduction of the porous carbon's fine structures after oxidation times as short as 0.5 hours with declining rate throughout increasing oxidation times. Since the fine structures are easiest to oxidise using acid, leading to carbon gasification, it is reasonable to assume that this also applies for electrochemical carbon corrosion. Carbon gasification is an important form of catalyst degradation<sup>[68,182,183]</sup> as it leads to a loss of foothold for the surface bound catalytic particles and a reduced space on carbon surface. This results in the detachment of particles from the surface or the agglomeration of particles, both of which contribute to a decline in catalytic activity. Should the most pronounced phase of carbon degradation occur prior to the electrochemical measurement, the relative degradation compared to the measured maximal ECSA is expected to be reduced, as observed in the electrochemical experiments.

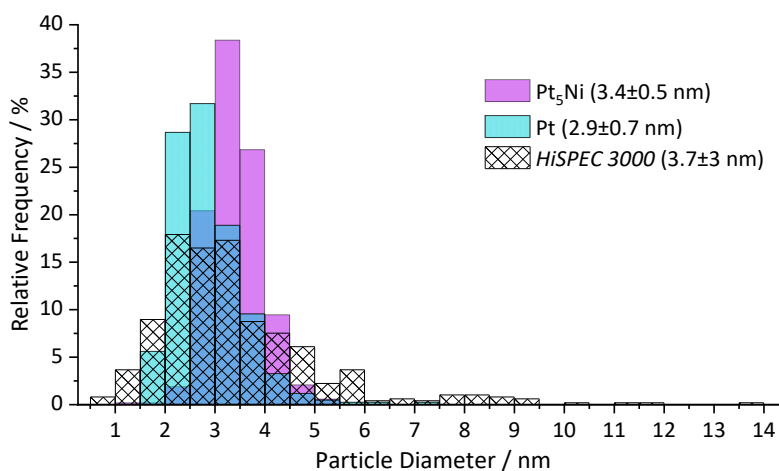
The catalytic activity and stability of the synthesised PtNi and Pt catalyst were compared to the commercial Pt catalyst *HiSPEC 3000*, which displayed the overall highest maximal ECSA of all investigated catalysts. Since the average particle diameter of the commercial catalyst was slightly

higher compared to the synthesised catalysts and no alloy material was involved, the beneficial properties of smaller particle sizes and co-metal can be ruled out as contributing factors. One potential cause for the lower catalytic activity of the synthesised catalysts involves the inhibiting effect of the ligands on the nanoparticle surface. The oleic acid and oleylamine ligands which are necessary for the colloidal nanoparticle synthesis may block the catalytic active surface for potential reactants to a certain degree. Though electrochemical cleaning was conducted, it is unclear to which extent the surfaces were cleared. Figure 6.36 shows clearly that the electrochemical cleaning process is still ongoing during the AST measurements. Furthermore, during electrochemical cleaning, the electrochemical degradation process may have been initiated already before reaching a clean surface, which could lead to lower recorded maximal ECSAs. Lastly, the removed ligands may persist in the measurement cell to a certain degree in form of impurities that interfere with the measurement.

An additional factor that is possibly influencing the ECSA is the amount of particle loading per surface area as higher particle loadings may lead to aggregates. The commercial catalyst exhibited a Pt loading of 20 % according to the manufacturer. The synthesised catalysts were fabricated with the objective of achieving a 33% Pt loading, but due to the small sample sizes of few milligrams, the direct verification of the Pt loading was not possible. Instead, the Pt content was determined after dispersing the catalyst to form the catalyst ink, from which the Pt loading can be indirectly inferred. However, this process is also prone to error since it involves the weighing of single-digit milligram quantities (two significant digits) which might lead to variations in catalyst concentration. Hence, the considerable degree of variance, ranging from 0.16 to 0.34 mg mL<sup>-1</sup> of the platinum concentration, as inferred from table 10.3 in the appendix, is not surprising. The average platinum concentration of the synthesised catalysts of 0.27±0.05 mg mL<sup>-1</sup> is considerably higher than the platinum concentration of the commercial catalyst displaying 0.17 mg mL<sup>-1</sup>. Additionally, the platinum concentration does not entail the nickel content in the PtNi catalysts, which would account for a 20 % increase in total particle loading. Thus, a lower platinum loading may indeed be a contributing factor in the higher ECSA value of the commercial catalyst.

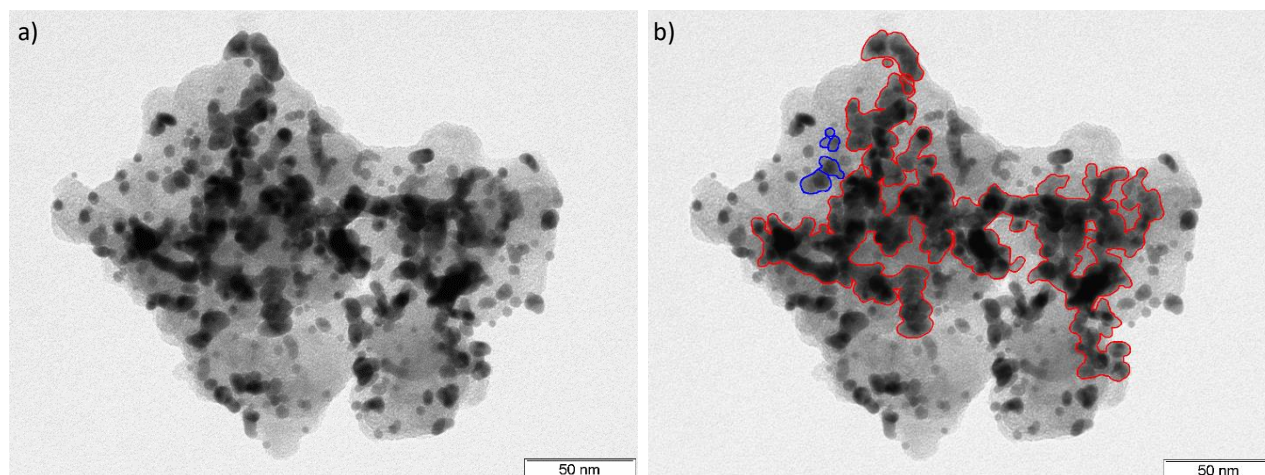
A suspected variance in particle loading may also play a role when comparing the synthesised catalysts among themselves. However, it is unclear to which extent the variances result from variations in platinum loading or catalyst concentration and a visual examination of the TEM images (appendix section 10.6) did not appear to correspond with the platinum content values. On the contrary, the PtNi/*Vulcan XC72R* catalyst with an especially low platinum concentration exhibited a comparably high particle loading according to TEM.

In contrast to the highest catalytic activity, the commercial catalyst also displayed the highest degree of degradation of all investigated catalysts with a remaining ECSA after 30000 cycles that is lower compared to all PtNi catalysts. The high degradation rate may be related to the very broad size distribution, visualised in figure 6.42, which renders the particles more prone to electrochemical degradation.<sup>[68]</sup>



**Fig. 6.42:** Particle Size distribution obtained from TEM images of the catalytic nanoparticles investigated using electrochemistry.

The stabilising effect of the introduced functional groups in regard to electrochemical degradation was further investigated by evaluating TEM images of the EDA-functionalised *Vulcan XC72R*-supported PtNi catalyst and the unfunctionalised *Vulcan XC72R*-supported PtNi catalyst after electrochemical degradation. The EDA-functionalised catalyst displayed improved stability compared to the unfunctionalised catalyst with an average degradation rate of only -54 % compared to -70 %, respectively. Since the ECSA is closely related to the particle surface, one hypothesis revolves around the EDA-functionalisation inhibiting particle agglomeration and growth to an increased degree. To confirm this theory, the particle areas of both catalysts were determined after 30000 AST cycles from TEM images. The area was chosen as dimension for comparison since the particles often displayed irregular shapes as exemplified in figure 6.43. Further TEM images of catalysts after AST can be found in the appendix. Figure 6.44 compares the areas of the evaluated particles before and after 30000 AST cycles.



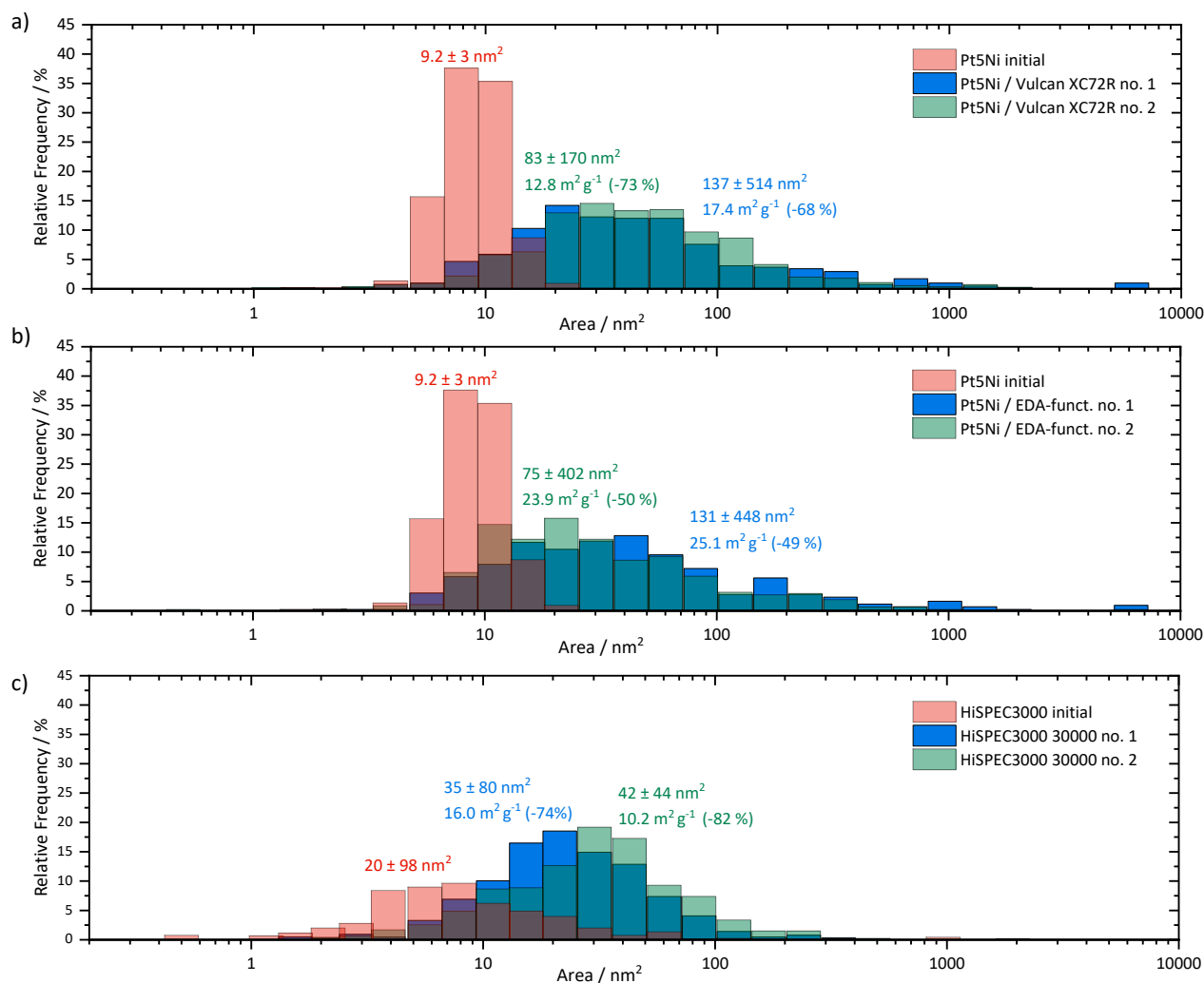
**Fig. 6.43:** TEM image of PtNi nanoparticles on ethylenediamine-functionalised *Vulcan XC72R*, after 30000 AST cycles with exemplary particle outlines used during evaluation in **b**).

Figure 6.44 clearly demonstrates an increase in particle size after 30000 AST cycles compared to the initial catalysts. However, when comparing the EDA-functionalised catalyst to the unfunctionalised catalysts after 30000 cycles, hardly any difference in particle area size is detectable even though the EDA-functionalised catalyst displays a significantly higher remaining ECSA. The degradation of the synthesised particles was also compared to the commercial catalyst, which exhibited even lower average particle areas after 30000 cycles despite displaying the lowest remaining ECSA. One discernible conclusion is that the cause of the reduced ECSA is attributable to factors other than particle growth.

However, the evaluation of particle sizes using TEM images is of limited reliability. To begin with, TEM images are taken from very small sample sizes which do not necessarily represent the bulk sample. And the great variety in carbon and particles makes it particularly challenging to obtain a representable evaluation. In addition, the evaluation of three-dimensional particles using two-dimensional images is inherently difficult, especially for irregularly shaped particles (red outline figure 6.43). For example, two close-together lying individual particles may appear as one in the 2D perspective (blue outline figure 6.43) or the particle size may be underestimated due to the perspective. Moreover, the varying thicknesses of the carbon support and the particles occasionally lead to a low particle/carbon contrast, making it difficult to discern the particle outlines.

Bearing the difficulties arising from the evaluation in mind, the key aspect for the ECSA is the specific surface area of the 3D particle for which the 2D particle area only offers a limited quantification. On the other hand, the evaluated TEM images give no measure for the Pt and Ni atoms that were removed from the catalyst after dissolving.

Hence, the cause for the decreased particle degradation after EDA-functionalisation may be a reduced rate of Pt and Ni dissolution, or the formation of large, high-surface particles as represented in figure 6.43.



**Fig. 6.44:** Particle areas of catalysts before and after 30000 AST cycles (from two individual AST measurements) as obtained from TEM images. The histogram bars are labelled with the average particle area with standard deviation. The histogram bars after 30000 AST cycles are also labelled with the maximal ECSA of the particular sample and the percentile ECSA reduction after 30000 AST cycles. **a)** PtNi nanoparticles on *Vulcan XC72R*. **b)** PtNi nanoparticles on ethylenediamine-functionalised *Vulcan XC72R*. **c)** *HiSPEC 3000 (Alfa Aesar)*.

In summary, the functionalised support materials displayed an increased capacitive current due to their increased hydrophilicity compared to unfunctionalised *Vulcan XC72R*. During potential cycling, the support materials underwent two types of oxidation processes. For one, a reversible quinone/hydroquinone redox-reaction occurred between 0.4 and 0.8 V vs. RHE with increasing severity during the ongoing potential cycling. Secondly, at potentials above 1 V vs. RHE, the irreversible carbon gasification to CO<sub>2</sub>, an indication of carbon corrosion, emerged with decreasing

severity as the cycling proceeded. Compared to *Vulcan XC72*, the oxidised *Vulcan XC72* displayed a more pronounced quinone/hydroquinone redox-reaction while the gasification peak was more prevalent for *Vulcan XC72*.

After deposition of PtNi and Pt nanoparticles onto the differently functionalised substrates, the catalysts displayed hydrogen adsorption and desorption currents in the range of ca. 0.08 to 0.35 V vs. RHE. During the ongoing potential cycling, the hydrogen adsorption/desorption peaks first increased due to electrochemical cleaning and subsequently decreased due to electrochemical degradation. Two distinct peaks within the hydrogen region can be attributed to prevalent (110) facets.

The electrochemical accelerated stress tests revealed a beneficial influence of the EDA-functionalisation on the catalytic properties of PtNi catalysts while the TETA-functionalisation was more beneficial for Pt catalysts. Both combinations displayed similar maximal ECSA values as the respective *Vulcan XC72*-supported catalyst while maintaining a lower degree of degradation. This leads to the conclusion that the primary amine group of ethylenediamine exhibits the strongest or most favourable interaction with the PtNi surface while this is the case for the secondary amine groups of triethylenetetramine towards pure Pt surfaces. All synthesised catalysts displayed lower maximal ECSAs compared to the commercial Pt catalyst. However, the commercial catalyst also displayed the highest degree of electrochemical degradation. In conclusion, the functionalisation of the support materials could successfully increase the electrochemical stability of the nanoparticle-support-composite catalysts.

## 7. Outlook

For a future application of the amine-functionalised carbon support materials in commercial fuel cells, a more (cost) efficient synthesis method for the functionalised support has to be established. The precipitation approach gives the option to easily exchange the type of colloidal nanoparticle which is deposited on the surface. However, the addition of colloidal nanoparticles entails the issue of nanoparticle ligands impeding the catalytic activity. Therefore, further research has to be conducted to attach ligand-free catalytic nanoparticles.

Due to the lasting issue of carbon corrosion inherent to carbon support materials,<sup>[9]</sup> further investigations should concentrate on inorganic supporting materials. Despite showing good electric conductivity and increased electrochemical stability, most inorganic materials still suffer from low specific surface areas necessary for well dispersed catalytic particles.<sup>[116]</sup> The beneficial characteristics of the amine-functionalisation may be transferred *via* surface modification to a novel, inorganic support material.

Further interesting approaches forego the use of a support material altogether, for instance by employing aerogels<sup>[251]</sup> or unsupported nanowires<sup>[252]</sup>. The opposing approach involves omitting any form of catalytic metal, utilising solely a doped carbon surface material as the catalyst.<sup>[253]</sup>

## 8. Experimental part

### 8.1. Chemicals

The following chemicals were used in this work with producer and if applicable purity grade as stated. The chemicals were used as acquired without further purification, if not otherwise stated. The safety information of the can be found in the appendix.<sup>[254–264]</sup>

Acetone (*VWR Chemicals*); buffer solutions (pH 4.01, 7.01, 10.01; *Hanna instruments*); 1,4-butanedithiol (*Apollo Scientific*); diphenyl ether (99 %; *Reagent Plus*; *Sigma Aldrich*); 1,2-dichlorobenzene (98 % min; HPLC grade; *Alfa Aesar*); ethanol (absolute; *VWR Chemicals*); ethylenediamine ( $\geq 99.5$  %; *p.a.*; *Sigma Aldrich*); 1,2-hexadecanediol ( $> 98.0$  %; *TCI*); *HiSPEC*<sup>®</sup> 3000 (Platinum, nominally 20% on carbon black; *Alfa Aesar*; Lot: 61601012); hydrochloric acid (30 %; *Suprapur*; *Supelco*, *Merck*); hydrochloric acid (37 %; *Emsure*; *Supelco*, *Merck*); hydrogen peroxide (30 %; *Supelco*; *Merck*); methanol (99.5 %; *Grüssing*); *Nafion-117*-Solution (~5 % in a mixture of low molecular weight aliphatic alcohols and water; *Sigma Aldrich*; Lot: BCCB5065); nitric acid (65 %; pure; *Roth*); nitric acid (65 %; *Suprapur*; *Supelco*, *Merck*); nitrogen (in-house line); nitrogen (liquid; *Linde*); oleic acid (90 %; Technical grade; *Sigma Aldrich*); oleylamine ( $> 98$  %; *Sigma Aldrich*); oxalic acid dihydrate (99 %; pure; *Grüssing*); oxygen (99.995 vol %; 4.5; *Westfalen*); perchloric acid (65-71 %; *Normatom*; *VWR Chemicals*; Lot: 2119121, 2121110); perchloric acid (70 %; *Ultrex II*; J.T. Baker; Batch: 2221070); *p*-phenylenediamine (for synthesis; *Sigma Aldrich*); platinum acetylacetonate (98 %; abcr); potassium hydroxide (for analysis; *Emsure*; *Supelco*, *Merck*); 2-propanol (*VWR Chemicals*); 2-propanol (*Uvasol*; *Merck*); pyridine (*Sigma Aldrich*); sodium hydrogen carbonate (for analysis; *Emsure*; *Supelco*, *Merck*); sodium hydroxide (99 %; pure; *Grüssing*); sulphuric acid (95-97 %; *p.a.*; *Chemsolute*); sulphuric acid (96 %; *Supelco*; *Merck*); tetrahydrofuran (Stabilised with 0.025-0.04 BHT; *VWR Chemicals*); thionyl chloride (99.7 %; *Acros Organics*); toluene ( $\geq 99.8$  %; *Fischer Chemical*); triethylenetetramine (mixture of isomers; *Sigma Aldrich*); *Vulcan XC72R* (*Cabot*; Lot: 4425035); water (ultrapure grade; 18.2 M $\Omega$ cm; filtered with *Purelab flex* model PF2XXXXM1 from *Elga LabWater*).

## 8.2. Synthesis

### 8.2.1. Oxidation of Carbon Black

*Vulcan XC72R* was oxidised using a modified synthesis method based on the work of EGUZABAL *et al.*<sup>[39]</sup>

For the standard procedure, 1.00 g of *Vulcan XC 72R* (Cabot; Lot: 4425035) was suspended in 60 mL 95-97 % sulphuric acid (*Chemolute*) for 30 minutes using an ultrasonic bath. 20 mL 65 % nitric acid (*Roth*) were added, and the mixture was stirred at room temperature for varying times (0.5 hours to 14 days).

The mixture was then poured into 300 mL of ice water (ultrapure grade) and centrifuged at 15000g and 15 °C for 20 minutes. The precipitate was resuspended in water and centrifuged again. This cleaning step was repeated with increasing centrifugation velocity up to 20000g until the oxidised carbon did not precipitate anymore. Then, the suspension was transferred to a dialysis tube (MWCO = 3.5 kD; *Spectrum; Spectra/Por 3*) and dialysed in 4.5 L ultrapure water while changing the water daily until the conductivity of the water remained at 1.2  $\mu\text{S}/\text{cm}$ . At last, the purified oxidised carbon black was freeze-dried using liquid nitrogen at 0.18 mbar.

Reference experiments employing only nitric acid as oxidant were conducted analogously.

### 8.2.2. Direct Functionalisation with Diamines

A direct amine functionalisation of the oxidised carbon blacks with diamines was performed using an adapted synthesis method originally proposed by EGUZABAL *et al.*<sup>[39]</sup> The diamines used in this synthesis route were ethylenediamine (EDA;  $\geq 99.5\%$ ; *Sigma Aldrich*), triethylenetetramine (TETA; mixture of isomers; *Sigma Aldrich*) and *p*-phenylenediamine (PDA; *Sigma Aldrich*). The ethylenediamine was stored over a molecular sieve under nitrogen and the triethylenetetramine and the phenylenediamine were stored in the glovebox. The chemicals were used without further purification.

In a typical experiment, 100 mg oxidised carbon were mixed with an excess amount of amine (15 to 30 mL) and stirred under nitrogen as inert gas for 48 hours at 100 °C. 50 mL of acetone was added, and the mixture was centrifuged for 20 minutes at 10000g and 15 °C. The precipitate was suspended in 10 mL ultrapure water and 35 mL acetone was added. This centrifugation procedure was repeated

until the supernatant's pH stayed neutral and was then repeated for one last time. The precipitate was again suspended in ultrapure water and freeze-dried using liquid nitrogen at 0.18 mbar.

Additional experiments were carried out comprising diamine treatment for seven days at room temperature. Here, 100 mg oxidised carbon were mixed with 65 mL amine or 50 mL of 11.3 mM *p*-phenylenediamine in toluene. The purification was conducted in the same manner.

For the investigation of the successful amide linkage through the direct synthesis route, amide cleavage reference experiments were conducted. 4-6 mg of a sample of *Vulcan XC72R*, oxidised for 2 hours, and functionalised with ethylenediamine was stirred under nitrogen as inert gas for four hours in a) 22.5 mL 2 M KOH at 100 °C b) 25 mL ultrapure water at 100 °C and c) 25 mL 1 M HCl at room temperature. Subsequently, 50 mL of isopropanol were added to the mixtures, and they were centrifuged for 30 Minutes at 20000g and 15 °C. The precipitate was washed three more times by suspension in 10 mL ultrapure water and addition of 30 mL isopropanol before centrifugation. After the centrifugation steps, the supernatant displayed a neutral pH value. Finally, the precipitate was suspended in 5 mL ultrapure water and freeze-dried using liquid nitrogen at 1.4 mbar.

### 8.2.3. Functionalisation with Acyl Chloride Intermediate

An alternative synthesis route for the further functionalisation of oxidised carbon blacks utilising an acyl chloride intermediate step was employed. The modified synthesis procedure was based on the work of KUO *et al.*<sup>[37]</sup> and carried out by T.-Y. YU in the context of her bachelor's thesis<sup>[265]</sup>. The chemicals used in this approach were (EDA; ≥99.5 %; *Sigma Aldrich*), triethylenetetramine (TETA; mixture of isomers; *Sigma Aldrich*), *p*-phenylenediamine (PDA; *Sigma Aldrich*) and 1,4-butanedithiol (*Apollo Scientific*). Ethylenediamine was stored over a molecular sieve under nitrogen. Triethylenetetramine and phenylenediamine were stored in the glovebox. All chemicals were used without further purification.

The typical experiment started by mixing 80 mg oxidised carbon black with 40 mL thionyl chloride (99.7 %; *Acros Organics*) and stirring the mixture at 65 °C under nitrogen as inert gas for 24 hours. The unreacted thionyl chloride was distilled first at 120 °C under atmospheric pressure, followed by a distillation at 60 °C and 1 mbar.

Subsequently, an excess of diamine or dithiol was added, and the mixture was stirred under nitrogen as inert gas, as specified in table 8.1. Since *p*-phenylenediamine is solid at room temperature, the synthesis was either conducted in a *p*-phenylenediamine melt, or as solution in toluene. For the

functionalisation with 1,4-butanedithiol, 500  $\mu\text{L}$  of pyridine (*Sigma Aldrich*) was added to act as catalyst.

Afterwards, the mixture was purified by centrifugation at 20000g and 10 °C for 10-50 minutes after adding three times the amount of acetone as precipitant. The precipitate was resuspended in ultrapure water and the centrifugation step was repeated thrice after addition of acetone as precipitant. Following this, the precipitant, suspended in ultrapure water, was freeze-dried using liquid nitrogen at 0.18 mbar.

**Tab. 8.1:** Amount of added diamine or dithiol for the further functionalisation of oxidised carbon blacks the respective reaction conditions.

Added Diamine/Dithiol	Reaction Conditions
30 mL Ethylenediamine ( $\geq 99.5\%$ ; <i>Sigma Aldrich</i> )	Room temperature, 7 days
30 mL Triethylenetetramine (mixture of isomers; <i>Sigma Aldrich</i> )	120 °C, 2 days
1.1 g <i>p</i> -Phenylenediamine ( <i>Sigma Aldrich</i> ) in 40 mL toluene	25-60 °C, 2 days
25 g <i>p</i> -Phenylenediamine ( <i>Sigma Aldrich</i> )	170 °C, 2 days
15 mL 1,4-Butanedithiol ( <i>Apollo Scientific</i> )	80 °C, 2 days

#### 8.2.4. Synthesis of platinum-nickel alloy nanoparticles (PtNi-NP)

The nickel-platinum alloy nanoparticles used in this work were prepared by S. WODERICH<sup>[237]</sup> using a continuous flow reactor equipped with two *BlueShadow 40 P* pumps (*Knauer*).

Briefly, 4.916 g (12.5 mmol) platinum acetylacetonate and 12.34 mL (37.5 mmol) oleylamine were dissolved in 59.4 mL 1,2-dichlorobenzene and 178 mL diphenyl ether. Additionally, 3.211 g (12.5 mmol) nickel acetylacetonate, and 3.231 g (12.5 mmol) 1,2-hexadecanediol, 11.8 mL (37.5 mmol) oleic acid and 4.11 mL (12.5 mmol) oleylamine were dissolved in 234 mL diphenyl ether at 60 °C in an ultrasonic bath.

In the continuous flow reactor, both solutions were mixed using a laminar interdigital mixer (*Micro4Industries*) at 200 °C with a ratio of 1:1 and reacted at 240 °C at 5 bar over a growth length of 27 mL with a pump rate of 1.93 mL/min. The first and the last 5 mL of the reacted mixture were discarded, respectively.

Threefold the volume of ethanol was added to the particle suspension as precipitant, and the mixture was stored in a refrigerator overnight. Subsequently, the mixture was cleaned using three centrifugation steps at 10000 rcf and 10 °C for 10 minutes. In between, the precipitate was

redispersed in toluene and triple the volume ethanol was added before the next centrifugation step. Finally, the precipitate was dispersed in 20 mL toluene 100  $\mu$ L oleylamine was added.

### 8.2.5. Synthesis of platinum nanoparticles (Pt-NP)

The platinum nanoparticles were prepared according to an adapted synthesis developed by K. AHRENSTORF *et al.*<sup>[236]</sup>

170 mg 1,2-hexadecanediol (>98.0 %; *TCI*) were dissolved in 40 mL diphenyl ether (99 %; *Reagent Plus; Sigma Aldrich*) and 0.8 mL oleic acid (90 %; Technical grade; *Sigma Aldrich*) and 0.8 mL oleylamine (>98 %; *Sigma Aldrich*) were added. The mixture was heated under nitrogen as inert gas to 60 °C and subsequently under vacuum ( $\sim 4.5 \cdot 10^{-2}$  mbar) to 80 °C. The mixture was kept under vacuum for 60 minutes at 80 °C while flushing the apparatus several times with nitrogen and heating with a heat gun.

Thereafter, the mixture was heated under nitrogen to 200 °C and 291 mg (0.739 mmol) platinum acetylacetonate (98 %; abcr), dissolved in 2.4 mL 1,2-dichlorobenzene (98 % min; HPLC grade; *Alfa Aesar*), were rapidly injected using a syringe while rapidly stirring at 1000 rpm. The mixture darkened and turned black 1.5 minutes after the injection. Subsequently, the mixture was stirred at 200 °C and 1000 rpm for 25 minutes before cooling to room temperature.

Triple the volume of ethanol was added and the mixture was kept at 6 °C overnight before cleaning through multiple centrifugation steps at 20000g at 10 °C for 30 to 90 minutes. Each time, the precipitate was redispersed in toluene and threefold the volume of ethanol was used as precipitant. Finally, the precipitate was dispersed in toluene ( $\geq 99.8$  %; *Fischer Chemical*).

### 8.2.6. Nanoparticle deposition on a carbon substrate

The catalysts were prepared by depositing PtNi or Pt nanoparticles on the functionalised carbon blacks or *Vulcan XC72R* as reference.

In a standard nanoparticle deposition process, 12 mg support material and 4 mL of tetrahydrofuran (THF; Stabilised with BHT; *VWR Chemicals*) were mixed in a cooled ultrasonic bath at 15 °C until a homogeneous suspension was achieved (after two to four hours). While stirring at 1000 rpm, a nanoparticle dispersion containing 6 mg of platinum (PtNi-NP: 2 mL with 3 mg/L in toluene and THF; Pt-NP 1.28 mL with 4.7 mg/L in toluene) was slowly added to the suspension. The mixture was stirred at room temperature for one day. Then, 10 mL isopropanol were slowly added while stirring

continuously. After stirring at room temperature for at least one day, 4 mL isopropanol (*Uvasol*; *Merck*) were added while stirring and the mixture was stirred for at least another day.

The mixture was centrifuged at 20000g at 10-15 °C for 20 minutes. The intensity of the brown supernatant was an indication for the amount of non-deposited nanoparticles with a clear supernatant indicating the complete deposition. The precipitate was suspended in 5 mL ultrapure water and centrifuged again. Thereafter, the precipitate was dried at ambient air and room temperature.

The deposition process was systematically studied by varying the dispersing agent among THF (THF; Stabilised with BHT; *VWR Chemicals*) and toluene ( $\geq 99.8\%$ ; *Fischer Chemical*) and the precipitating agent was varied among acetone (*VWR Chemicals*), ethanol (absolute; *VWR Chemicals*), methanol (99.5 %; *Grüssing*) and isopropanol (*Uvasol*; *Merck*).

## 8.3. Characterisation

### 8.3.1. Elemental Analysis

The contents of platinum and nickel in the nanoparticle dispersions and in the catalyst ink suspensions were determined using atomic absorption spectroscopy (AAS). The measurements were conducted by the Central Element Analytics Service (NURAY EROGLU) in the Chemistry Department of the University of Hamburg.

The *AAnalyst 600* graphite furnace atomic absorption spectrometer from *Perkin Elmer* was used for the determination of the platinum content and the nickel content was determined using *Solaar S Series* flame atomic absorption spectrometer from *Thermo*.

Prior to the measurements, 50-300  $\mu\text{L}$  of a sample was pipetted into a 10 mL Teflon (or polypropylene) digestion vessel using a mechanical pipette (*Eppendorf Research*) and the suspension agent was left to dry completely. To the dry residue, 333  $\mu\text{L}$  65 % nitric acid (*Suprapur; Supelco Merck*) and 999  $\mu\text{L}$  30 % hydrochloric acid (*Suprapur; Supelco Merck*) were subsequently added. The digestion vessel was closed, placed into an autoclave (*DAB-2; Berghof*), and heated in a heating block (*DAH-406; Berghof*) to 80 °C for 36 hours. Alternatively, the polypropylene digestion vessel was placed in an oven at 80 °C for 36 hours. Afterwards, the sample was diluted with 18.67  $\mu\text{L}$  ultrapure water. Each sample was prepared at least three times, and the mean value was used.

### 8.3.2. Organic Elemental Analysis

The elemental composition of the functionalised and unfunctionalised carbon blacks was investigated using organic elemental analysis. The measurements were carried out by the Central Element Analytics Service in the Chemistry Department (BIRGIT ALPERS) of the University of Hamburg. The *Unicube (Elementar)* and *EA3000 (EuroVektor)* organic elemental analysers were utilised for the determination of carbon, hydrogen, nitrogen and sulphur. For the determination of oxygen, the oxygen analyser *Oxycube (Elementar)* was used.

### 8.3.3. Titration

The oxidised carbon blacks were analysed for surface carboxylic acid content using the titration method established by BOEHM *et al.*<sup>[92]</sup>

The titration was performed using a 50 mL burette (*Brand*;  $\pm 0.05$  mL; AS 20 °C; Ex + 30 s; Iso 385) and a 100 mL Erlenmeyer flask. During the titration, the analyte solution was stirred at 250 rpm and the pH value was determined with a pH meter (*Si-Analytix*; *Lab 875*; equipped with the pH electrodes *Blue Line 14* or *24*).

The analytes were weighed using a semi-microbalance scale (*ABT 100-5M*; *Kern*). The weight was determined by subtracting half of the empty scale weight from the measured weight, and the scale was zeroed before each measurement. Each measurement involved weighing the empty weighing dish first, followed by weighing the weighing dish containing the sample three times, respectively, and subtracting the mean values.

Prior to the titration of the carbon blacks, standard solutions of HCl and NaOH were prepared and their titres was determined. The 0.01 M HCl standard solution was prepared by diluting 1.057 mL 30 % HCl (30 %; *Suprapur*; *Supelco*, *Merck*) to 1 L with ultrapure water. The titre was determined by titration of ca. 15 mg NaHCO<sub>3</sub> (for analysis; *Emsure*; *Merck*). For the calculation of the equivalence point, equation 8.1<sup>[50]</sup> was employed, where  $C_{\text{eq.p.}}$  is the analyte concentration at the equivalence point. For  $pK_{\text{analyte}}$ , the second acid dissociation constant of NaHCO<sub>3</sub> (6.35<sup>[225]</sup>) was used. For the preparation of the 0.01 M NaOH standard solution, 752.8 mg NaOH (99 %; pure; *Grüssing*) was dissolved in 18.82 mL ultrapure water and 10 mL of that solution was diluted to 1 L using ultrapure water. The determination of the titre was conducted by titration of ca. 10 mg of oxalic acid dihydrate (99 %; pure; *Grüssing*). The pH value of the equivalence point was calculated using equation 8.1. For  $pK_{\text{analyte}}$ , the second base dissociation constant of oxalic acid (9.72<sup>[225]</sup>) was employed.

$$pH_{\text{eq.p.}} = \frac{pK_{\text{analyte}} - \log(C_{\text{eq.p.}})}{2} \quad (8.1)$$

For the titration of the oxidised carbons, ca. 25 mg oxidised carbon was weighed, followed by addition of ca. 15 mg NaHCO<sub>3</sub>, using the semi-microbalance scale as described. 10 mL ultrapure water was added, and the mixture was equilibrated for at least one day while shaking at room temperature. 30 mL isopropanol was added before centrifuging at 20000g and 15 °C for 20 minutes. The supernatant was transferred and the centrifugation step was repeated to ensure the complete separation from the precipitate. Following the second centrifugation step, the supernatant was transferred to an Erlenmeyer flask and ca. 30 mL of a 0.01 M HCl standard solution was added. The volume of the added HCl standard solution was determined using its weight and the density of water at the respective temperature. Subsequently, the mixture was boiled to eliminate the dissolved CO<sub>2</sub>.

The titration was carried out against the 0.01 M NaOH standard solution, and the equivalence point was assumed to be at pH 7. The amount of substance of surface carboxylic acid groups per mass oxidised carbon  $C_{\text{COOH}}$  was calculated according to equation 8.2, where  $n_{\text{NaHCO}_3}$  and  $n_{\text{HCl}}$  are the amount of substance added to the oxidised carbon black, respectively, and  $n_{\text{NaOH-tit}}$  is the amount of substance titrated until the equivalence point.

$$C_{\text{COOH}} = \frac{n_{\text{NaHCO}_3} - n_{\text{HCl}} + n_{\text{NaOH-tit}}}{m_{\text{oCB}}} \quad (8.2)$$

In equation 8.2, the amount of titrated NaOH at the equivalence point is equal to the amount of HCl in the solution that did not react with the amount of NaHCO<sub>3</sub> present in the supernatant after centrifugation. The amount of NaHCO<sub>3</sub> in the supernatant after centrifugation is the surplus amount that did not react with the carboxylic acid groups on the oxidised carbon's surface. Therefore, as shown in equation 8.3 to 8.6, the amount of carboxylic acid groups on the oxidised carbon's surface is equivalent to the amount of added NaHCO<sub>3</sub> minus the amount of added HCl plus the amount of titrated NaOH.

$$n_{\text{COOH}} = n_{\text{NaHCO}_3} - n_{\text{NaHCO}_3\text{-unreacted}} \quad (8.3)$$

$$n_{\text{COOH}} = n_{\text{NaHCO}_3} - (n_{\text{HCl}} - n_{\text{HCl-unreacted}}) \quad (8.4)$$

$$n_{\text{COOH}} = n_{\text{NaHCO}_3} - (n_{\text{HCl}} - n_{\text{NaOH-tit}}) \quad (8.5)$$

$$n_{\text{COOH}} = n_{\text{NaHCO}_3} - n_{\text{HCl}} + n_{\text{NaOH-tit}} \quad (8.6)$$

#### 8.3.4. Infrared spectroscopy (IR)

For the investigation of functional groups, Attenuated Total Reflection Fourier-Transform Infrared Spectroscopy (ATR FT-IR) was utilised. The measurements were undertaken using the *Invenio R* spectrometer from *Bruker*. The spectrometer was equipped with a *Golden Gate* ATR System from *Specac*. The samples were directly applied to the ATR diamond without further preparations. The device was operated and the data was analysed with the *OPUS* (v. 8.1) software from *Bruker*. Each measurement consisted of 128 scans with a resolution of 4 cm<sup>-1</sup>.

#### 8.3.5. Nitrogen physical adsorption

The BET surface area of the functionalised and unfunctionalised carbon blacks was determined using nitrogen physical adsorption at 77.35 K. For the measurement, the *Autosorb iQ* from gas sorption

analyser *Quantachrome* (*Anton Paar*) was employed. The apparatus was operated and the data analysis was performed using the *ASiQwin* software (version 3.01) from *Quantachrome*. The nitrogen measurement gas was sourced from the in-house line and was purified using a click on oxygen trap (*SGT-CO1002-B2*; *SGT*).

Prior to the measurement, 100-500 mg sample were filled into the measurement cell (9 mm without rod and the sample was degassed in vacuum at 60 °C for 1080 minutes. The measurement was conducted in liquid nitrogen and helium was used to determine the void volume. For each sample, one complete isotherm was recorded comprising of 67 adsorption points and 47 desorption points over a relative pressure range of 0.0001 to 0.995  $p/p_0$ . Additionally, 2-5 measurements were conducted with only 39 adsorption points with a relative pressure range of 0.0001-0.3  $p/p_0$ . The Micropore BET Assistant was used to determine the relative pressure range which was used to calculate the BET surface area.

### 8.3.6. Atomic Force Microscopy (AFM)

Atomic force microscopy was employed to investigate the thickness of the catalyst ink layer deposited on the glassy carbon electrode. The measurements were conducted by J. RÜBBÜLT in the context of her bachelor's thesis<sup>[266]</sup> using the *Nanowizard III* atomic force microscope from *JPK*, equipped with an *ACTA-50* cantilever from *AppNano* featuring a silicon tip. The measurement was controlled with the software NanoWizard Control Software (v. 5). For the measurements, the intermittent mode was used with a target amplitude of 2.4 and a setpoint of 1.3 to 1.5 V.

The measurements were conducted directly on the glassy carbon electrode, which was encased in the Teflon holder used for electrochemical measurements. The samples were prepared by introducing a thin scratch across the middle of the catalyst layer, thereby exposing the glassy carbon electrode. The image was captured with a scan range of 5 x 50  $\mu\text{m}$  with a measurement velocity of 8  $\mu\text{m/s}$ . The scans were conducted with the longer dimension of the scan window perpendicular to the scratch with approximately 5 x 10  $\mu\text{m}$  of the scan area covering the bare glassy carbon electrode as baseline. Measurements were undertaken at varied locations on the electrode, typically including the centre, the edge, and at least one intermediate point. At each designated location, a set of two and five scans was performed. The measurement data was processed using the software *Gwydion* (v. 2.20 and 2.63). Each scan was baseline corrected using the scan's bare electrode segment as baseline. The average film thickness with standard deviation of each measurement was calculated according to equation 8.7 and 8.8 using the height  $x_i$  of each measurement point and its frequency  $y_i$ .

$$\bar{x} = \frac{\sum_{i=1}^n x_i \cdot y_i}{\sum_{i=1}^n y_i} \quad (8.7)$$

$$\sigma = \sqrt{\frac{\sum_{i=1}^n (\bar{x} - x_i) \cdot y_i}{\sum_{i=1}^n y_i}} \quad (8.8)$$

### 8.3.7. Transmission Electron Microscopy (TEM)

The transmission electron microscopic measurements were conducted by the Service Centre for Electron Microscopy within the Department of Chemistry of the University of Hamburg (STEFAN WERNER). The utilised instrument was a JEOL JEM 1011 operated at an acceleration voltage of 100 kV and equipped with a LaB<sub>6</sub> cathode and an SIS CCD camera system with a resolution of 1376x1032 pixels.

The samples were prepared for the measurement by applying 10 µL of a diluted suspension of the sample in a water-isopropanol mixture onto a carbon-coated copper grid (400 mesh, *Plano*). Fifteen seconds after deposition, the excess fluid was removed using a filter paper.

The analysis of the TEM images was undertaken using the software *Image J* (v. 1.53e).

### 8.3.8. Scanning Electron Microscopy (SEM)

The SEM images were captured using the *Evo MA 10* scanning electron microscope from *Zeiss*, equipped with a thermal LaB<sub>6</sub> emitter. The SEM images were taken with the software *SmartSEM* (v. 05.04.05.00) from *Zeiss*.

Additionally, SEM measurements were conducted by the Service Centre for Electron Microscopy within the Department of Chemistry of the University of Hamburg (ROBERT SCHÖN). Herein, the *LEO Gemini 1550* scanning electron microscope from *Zeiss*, equipped with a field emission gun and an *Everhart-Thornley* detector was utilised.

To study the morphology of the functionalised carbon blacks and catalyst inks *via* SEM, the powder was applied to a conductive adhesive sticker (*plano*), or the powder was dispersed and dried on a silicon wafer. Samples prepared for transmission electron microscopy on a TEM grid could also be used for scanning electron microscopic images.

For the investigation of the catalyst ink layer deposited on the glassy carbon electrode, the Teflon holder encasing the glassy carbon electrode was installed into an aluminium holder to ensure the discharge of electrons directed at the sample, as depicted in figure 8.1. The measurements were conducted with an acceleration voltage of 10.00 kV and a working distance of 4.0 to 5.0 mm.

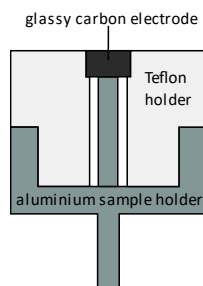


**Fig. 8.1:** Cross-section of the sample holder used for the scanning electron microscopic images of catalyst ink layer deposits on a glassy carbon electrode.

### 8.3.9. Electrochemical Measurements

The synthesised catalysts were investigated electrochemically using half-cell measurements. The measurement set-up, procedure and preparation is described in the following chapters.

#### 8.3.9.1. Glassy-Electrode Polishing

The glassy carbon electrodes were polished and cleaned prior to the application of the sample. For the removal of the old sample, the electrodes were ultrasonicated first in a (1:1) mixture of ultrapure water and isopropanol for ca. 5 minutes, followed by ultrasonication in ultrapure water for the same time.

The electrodes were polished using a polishing cloth (*Buehler; MicroCloth*) and 0.3 and 0.05  $\mu\text{m}$  Alumina polishing agents (*Buehler; MicroPolish*). Each polishing step was carried out in a figure-eight motion for five minutes to ensure uniformity. The typical polishing procedure involved a 0.3  $\mu\text{m}$  polishing step once a month or when the last polishing was more than two weeks ago, followed by a 0.5  $\mu\text{m}$  polishing step. Otherwise, only the 0.05  $\mu\text{m}$  polishing step was performed.

After polishing, the electrodes were cleaned by four consecutive 5-minute ultrasonication steps in ultrapure water, isopropanol and twice in ultrapure water. The cleaned electrodes were installed in the Teflon holder, rinsed with ultrapure water, and dried using nitrogen from the pressure line.

### 8.3.9.2. Catalyst Ink Preparation

The dried inks were mixed with the appropriate amount of a *Nafion*-isopropanol-water (*Nafion*-117-Solution; *Sigma Aldrich*; Lot: BCCB5065; isopropanol *Uvasol*; *Merck*; Lot: I0980793844; Ultrapure water) mixtures to obtain a catalyst ink with concentration of 1 mg dried ink per millilitre. The amount of *Nafion* in the stock solution varied from 0 to 0.1 % and the amount of isopropanol varied from 0 to 40 % with standard concentrations of 0.05 % *Nafion* and 40 % isopropanol.

The homogenisation of the catalyst ink was achieved through ultrasonication in a cooled ultrasonic bath (*Sonocool*; *Bandelin*) at 15 °C for a minimum of 10 hours. The process was accelerated by shaking the container at regular intervals. To assess the homogenization level, the container bottom was inspected for precipitate, which would indicate an incomplete homogenisation, thereby necessitating prolonged (1-10 hours) ultrasonication.

### 8.3.9.3. Sample deposition on working electrode

Prior to each application the catalyst inks were thoroughly mixed by ultrasonication (*Sonocool*; *Bandelin*) at 15 °C for at least one hour. Precipitate on the container's bottom would indicate an incomplete homogenisation, requiring an extension of the ultrasonication period for 15 to 60 minutes.

10 µL of the catalyst inks were deposited on a freshly polished and cleaned glassy carbon electrode encased in a Teflon electrode holder using a mechanical pipette (*Eppendorf Research*). Three different kinds of drying methods were employed:

A) Standard drying method: The electrode holders were covered with a 20 mL glass vial and dried at ambient atmospheric conditions (14-54 % relative humidity) at room temperature (21-24 °C).

B) Rotating drying method: The electrode holders were connected to the rotator used for electrochemical measurements with the electrode facing upwards. The catalyst ink was applied while rotating at 700 rpm and dried at the same speed while covered with a glass vial.

C) Slowed drying method: The electrode holders were placed in a container that is sealed, except for a cannula inserted through the centre of the lid, as depicted in figure 8.2. The drying volume (container volume minus the volume of electrode holder) equals 0.64 mL, and the cannula had an inner diameter of 0.9 mm and a length of 2.5 mm (*Sterican*; *Braun*).

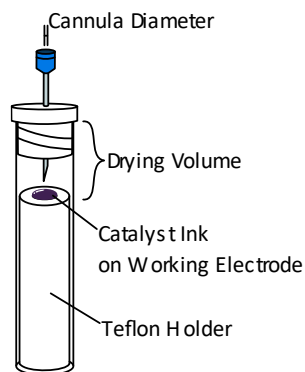


**Fig. 8.2:** Set-up of the slowed drying method for the catalyst ink on the glassy carbon working electrode.

#### 8.3.9.4. Optimisation of catalyst ink film drying

For the improvement of the catalyst ink layer distribution on the glassy carbon electrode, optimisation experiments using the slowed drying method, were performed by JOHANNA RÜBBÜLT in the context of her bachelor's thesis. The optimisation was conducted according to the principle of design of experiment (DOE).

The catalyst inks were prepared using *Nafion*-isopropanol-mixtures as dispersant with varying *Nafion* and isopropanol fractions as listed in table 8.2. 10  $\mu\text{L}$  of the catalyst ink suspension was applied to a glassy carbon working electrode encased in a Teflon holder. As depicted in figure 8.2, the holder was located in a container that was, with exception of a cannula inserted through the lid, otherwise sealed. The cannula, enabling gas exchange, was placed in the centre over the drying catalyst ink droplet. The volume of the container was varied according to table 8.2 with the drying volume defined as the volume of the container minus the volume of the electrode holder. Furthermore, the inner diameter of the inserted cannula (*Sterican; Braun*) was varied according to table 8.2 while maintaining a length of 25 mm. To establish an external relative humidity of 0 %, the container was placed in a nitrogen-flushed chamber. The drying proceeded at room temperature (21-24 °C).

The selection of experiments combining the varied parameters was carried out by the software *Cornerstone* (v. 8.0; *camLine*) and is listed in table 8.2. Data analysis was also performed using the same software.

Two reference experiments were carried out employing different drying methods. First, a stationary drying method at 40 °C was employed using a suspension agent containing 0 % isopropanol and 0.05 % *Nafion*. Second, the rotating drying method at 700 rpm was utilised with a suspension agent containing 20 % isopropanol and 0.05 % *Nafion*.

**Tab. 8.2:** Experiments conducted for the optimisation of catalyst ink film drying employing the slowed drying method. The fractions of isopropanol and *Nafion* refer to the ink suspending agent, while the drying volume and the cannula diameter relate to the drying set-up.

Fraction Isopropanol / %	Fraction <i>Nafion</i> / %	Drying Volume / mL	Inner Cannula Diameter / mm
0	0	0.64	0.6
0	0	7.41	0.4
0	0.05	0.64	0.4
0	0.05	0.64	0.4
0	0.05	7.41	0.8
0	0.1	0.64	0.8
0	0.1	4.03	0.4
0	0.1	7.41	0.6
20	0	4.03	0.8
20	0	4.03	0.8
20	0.05	7.41	0.4
20	0.05	7.41	0.4
20	0.1	0.64	0.6
40	0	0.64	0.4
40	0	7.41	0.4
40	0	7.41	0.8
40	0.05	0.64	0.8
40	0.05	0.64	0.8
40	0.05	4.03	0.6
40	0.1	0.64	0.8
40	0.1	4.03	0.4
40	0.1	7.41	0.8

### 8.3.9.5. Measurement Set-Up

The electrochemical set-up is depicted in figure 8.3. The measurements were conducted in an electrochemical half-cell filled with 0.1 M perchloric acid and equipped with a water jacket connected to a thermostat to keep a constant measurement temperature of 25 °C. A three-electrode set-up was used, and the measurement cell was equipped with a two-way gas inlet, enabling the flushing of gas through the electrolyte or the atmosphere above the electrolyte. The working electrode containing the sample consisted of a 5 mm glassy carbon disc (*Pine Research*) encased in a Teflon holder (*Pine Research*). It was connected *via* a shaft to a rotator (*Princeton Applied Research; 616A*) allowing for

measurement during rotation. A 0.1 mm diameter platinum wire in a frit a was used as counter electrode. As reference electrode either a standard calomel electrode (*Amel; 303/SCG/12*) or a reversible hydrogen electrode (*Gaskatel; Mini-HydroFlex*) were employed. The electrodes were connected through a potentiostat (*Ivium Technologies; IviumStat*) with a computer controlling the measurement via the software *IviumSoft* (*Ivium Technologies; v. 4.935*).

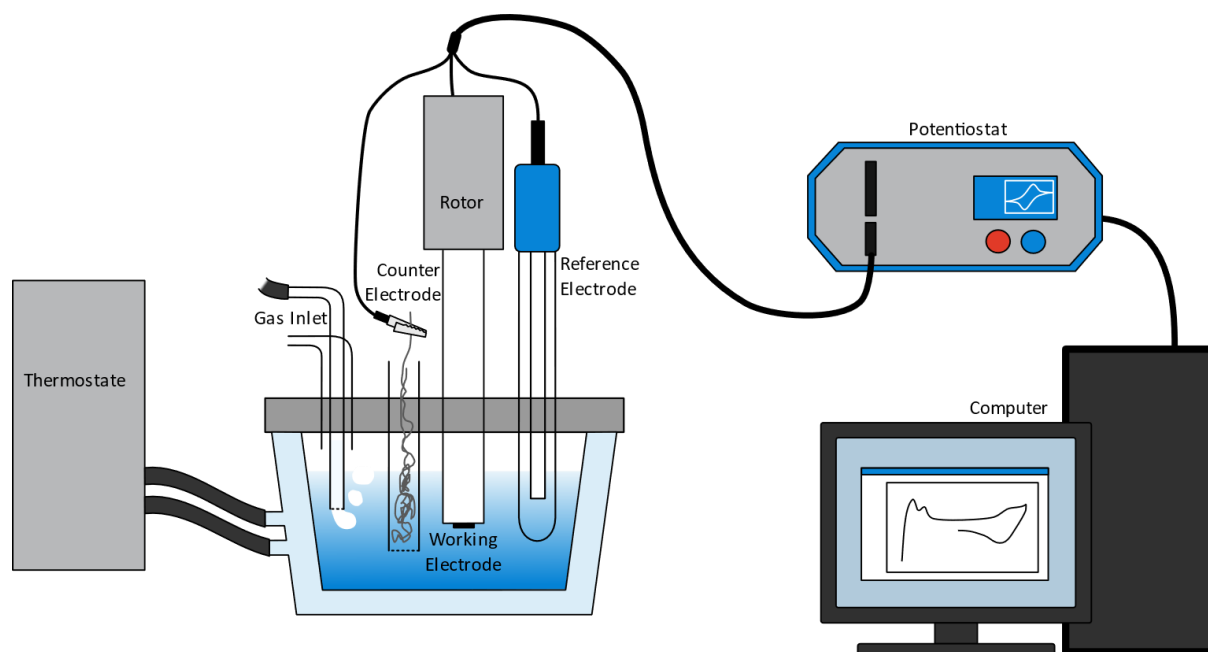


**Fig. 8.3:** Schematic Illustration of the set-up used for electrochemical measurements.

### 8.3.9.6. Accelerated Stress Tests (AST)

The catalytical activity and stability of the catalysts was examined using an adapted accelerated stress test protocol proposed by the Fuel Cell Commercialization Conference of Japan (FCCJ)<sup>[196]</sup>. The protocol consisted of a sequence of different electrochemical measurements conducted in nitrogen-purged 0.1 M perchloric acid (65-71%; *Normatom; VWR Chemicals; Lot: 2119121, 2121110*; diluted with ultrapure water) at 25 °C, using a standard calomel electrode (SCE) as reference electrode. Prior to each measurement, the sample that was applied on the working electrode is wetted with ultrapure water for five minutes.

Cyclovoltammetry (CV) was used for the determination of the electrochemical active surface area (ECSA). The measurements were carried out between -0.253 and 0.697 V vs. SCE with a scan rate of 50 mV/s and a voltage step size of 3 mV. The same method was used for electrochemical cleaning with a scan rate of 500 mV/s.

To simulate catalyst degradation during the operational load cycle of a fuel cell, chronoamperometric measurements were conducted, where one cycle comprised two consecutive voltage steps at 0.297 V and 0.697 V, each maintained for a duration of three seconds.

The electrolyte resistance was monitored using electrochemical impedance spectroscopy (EIS) at -0.253 V vs. SCE over a frequency range of 1000000 to 1000 Hz with an amplitude of 0.01 V with typical electrolyte resistance values ranging from 20 to 30  $\Omega$ . Prior to each measurement sequence, baseline measurements including one EIS scan and three CV scans were conducted. This was followed by 500 cyclovoltammetric cleaning cycles after which the measurement cell was exchanged with a new one, containing fresh, nitrogen-purged electrolyte.

The measurement sequence was started with one EIS scan, followed by three CV scans, designated as number zero. Subsequent to this, chronoamperometric load cycles were performed, interspersed with three CV scans, which were labelled according to the number of preceding load cycles. The measurement sequence concluded with one final EIS scan.

The measured data were processed using the software *Origin (OriginLab; v. 2019 to 2023b)*. From each sequence of three CV cycles, the third scan was employed for the calculation of the ECSA. The current was plotted as a function of time and the area of the hydrogen adsorption peak was integrated (grey area in figure 8.4) to acquire the charge  $Q_H$ . For the integration, the  $x$ -axis boundaries were usually set at around 31 s and 37.98 s and the lowest negative current within the boundaries (usually at 31 s) was chosen as  $y$ -axis boundary to exclude the influence of capacitive currents.

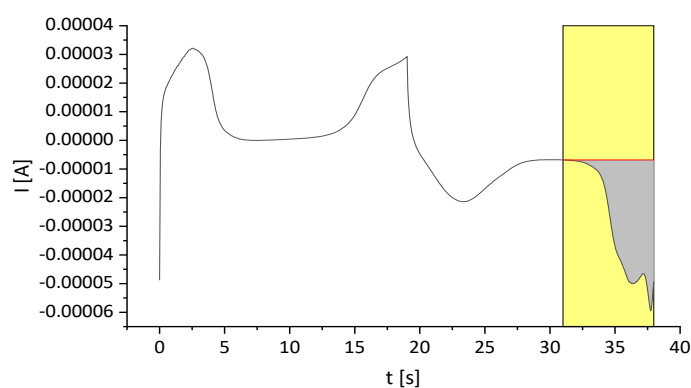


**Fig. 8.4:** Current plotted as a function of time of a cyclic voltammetry surface layer diagram. The grey area was integrated to obtain the charge  $Q_H$  of the hydrogen adsorption peak.

The preliminary studies (figure 6.40) were conducted using a similar approach; however, surface layer diagrams were recorded from -0.244 to 0.956 V vs. SCE at 100 mV/s. In this case, the AST cycles between ECSA cycles comprised of complete CV cycles from -0.244 to 0.956 V vs. SCE at

250 mV/s. The determination of the charge  $Q_H$  was conducted using ca. 31 s and the hydrogen minimum potential, which varied between each measurement, as the  $x$ -axis boundaries for the integration.

The surface layer diagrams involving only the support material without catalytic nanoparticles were recorded from -0.244 to 0.956 V vs. SCE at 100 mV/s and all AST cycles were carried out in the same manner from -0.244 to 0.956 V vs. SCE at 100 mV/s.

### 8.3.9.7. Oxygen reduction reaction (ORR)

The measurement protocol followed an adapted procedure described by GARSANY *et al.*<sup>[186]</sup>

Prior to the ORR measurements, the measurement equipment was thoroughly cleaned using peroxomonosulphuric acid. To achieve this, the measurement cell was equipped with the frits and glass stoppers employed in the following ORR measurement, filled with peroxomonosulphuric acid, and allowed to soak overnight. The equipment was rinsed with boiling ultrapure water thrice and seven times with room-temperature ultrapure water.

The ORR measurements were conducted in ultrapure 0.1 M perchloric acid (70 %; *Ultrex*; *JT Baker*, Batch: 2221070, diluted with ultrapure water) at 25 °C using a reversible hydrogen electrode (RHE) as reference electrode.

In preparation for the ORR measurement, an electrochemical cleaning step was carried out in a measurement cell containing nitrogen-purged 0.1 M perchloric acid. First, the working electrode containing the catalyst sample was wetted with ultrapure water for five minutes. Then, 1000 cyclovoltammetric cycles between 0.05 and 1.00 V vs. RHE at 500 mV/s and a voltage step size of 3 mV were carried out.

The measurement cell was swapped with another one containing fresh, nitrogen-purged 0.1 M perchloric acid. Electrochemical impedance spectroscopy (EIS) was employed to monitor the electrolyte resistance at 0.05 V vs. RHE over a frequency range of 1000000 to 1000 Hz with an amplitude of 0.01 V. Typical electrolyte resistance values ranged from 20 to 30  $\Omega$ . To obtain the electrochemical active surface area (ECSA), three cyclovoltammetric cycles were measured between 0.05 and 1.00 V vs. RHE at 50 mV/s and a voltage step size of 3 mV of which the third cycle was used for the calculation of the ECSA. The background current was determined through a linear sweep from 0.05 to 1.03 V vs. RHE at 20 mV/s at 0 rpm with a voltage step size of 3 mV.

Subsequently, the electrolyte was purged with oxygen (4.5) for 30 minutes and the ORR polarisation curves were obtained by conducting a linear sweep from 0.05 to 1.03 V vs. RHE at 20 mV/s at 1600 rpm.

The measured data was analysed using the software *Origin (OriginLab; v. 2019 to 2023b)*. The real impedance ( $Z_1$ ) at 1000 Hz was defined as the electrolyte resistance  $R_E$ . To correct the potential in regard of the solution resistance, the electrolyte resistance was multiplied by the current at the respective potential and subtracted from the potential as shown in equation 8.9.

$$E_{\text{corr}} = E - I \cdot R_E \quad (8.9)$$

The mass-specific activities  $I_m$ , was calculated from the background-corrected polarisation curves according to equation 4.19 and 4.21.

## 9. Literature

- [1] "A hydrogen strategy for a climate-neutral Europe", can be found under <https://eur-lex.europa.eu>, **2020**. (Access Date 04.10.2024).
- [2] "Energiewende", can be found under <https://www.bmbf.de>. (Access Date 04.10.2024).
- [3] K. Jiao, J. Xuan, Q. Du, Z. Bao, B. Xie, B. Wang, Y. Zhao, L. Fan, H. Wang, Z. Hou et al., *Nature* **2021**, 595, 361.
- [4] I. Staffell, D. Scamman, A. Velazquez Abad, P. Balcombe, P. E. Dodds, P. Ekins, N. Shah, K. R. Ward, *Energy Environ. Sci.* **2019**, 12, 463.
- [5] "Fuel Cell Technical Team Roadmap", can be found under <https://energy.gov>, **2013**. (Access Date 04.10.2024).
- [6] A. Ohma, T. Mashio, K. Sato, H. Iden, Y. Ono, K. Sakai, K. Akizuki, S. Takaichi, K. Shinohara, *Electrochimica Acta* **2011**, 56, 10832.
- [7] A. Dicks, D. A. J. Rand, *Fuel cell systems explained*, Wiley, Hoboken NJ USA, **2018**.
- [8] E. Antolini, *Applied Catalysis B: Environmental* **2009**, 88, 1.
- [9] S. Sharma, B. G. Pollet, *Journal of Power Sources* **2012**, 208, 96.
- [10] M. Wilson, F. Garzon, K. Sickafus, S. Gottesfeld, *J. Electrochem. Soc.* **1993**, 140, 2872.
- [11] T. Toda, H. Igarashi, H. Uchida, M. Watanabe, *J. Electrochem. Soc.* **1999**, 146, 3750.
- [12] U. A. Paulus, A. Wokaun, G. G. Scherer, T. J. Schmidt, V. R. Stamenkovic, V. Radmilovic, N. M. Markovic, P. N. Ross, *J. Phys. Chem. B* **2002**, 106, 4181.
- [13] K.-W. Park, J.-H. Choi, B.-K. Kwon, S.-A. Lee, Y.-E. Sung, H.-Y. Ha, S.-A. Hong, H. Kim, A. Wieckowski, *J. Phys. Chem. B* **2002**, 106, 1869.
- [14] X. Huang, Z. Zhao, L. Cao, Y. Chen, E. Zhu, Z. Lin, M. Li, A. Yan, A. Zettl, Y. M. Wang et al., *Science (New York, N.Y.)* **2015**, 348, 1230.
- [15] Y. Kang, J. Snyder, M. Chi, D. Li, K. L. More, N. M. Markovic, V. R. Stamenkovic, *Nano Lett.* **2014**, 14, 6361.
- [16] C. Wang, D. van der Vliet, K. L. More, N. J. Zaluzec, S. Peng, S. Sun, H. Daimon, G. Wang, J. Greeley, J. Pearson et al., *Nano letters* **2011**, 11, 919.
- [17] L. Chong, J. Wen, J. Kubal, F. G. Sen, J. Zou, J. Greeley, M. Chan, H. Barkholtz, W. Ding, D.-J. Liu, *Science* **2018**, 362, 1276.
- [18] V. R. Stamenkovic, B. S. Mun, K. J. J. Mayrhofer, P. N. Ross, N. M. Markovic, J. Rossmeisl, J. Greeley, J. K. Nørskov, *Angew Chem Int Ed* **2006**, 45, 2897.
- [19] C. Gyan-Barimah, J. S. P. Mantha, H.-Y. Lee, Y. Wei, C.-H. Shin, M. I. Maulana, J. Kim, G. Henkelman, J.-S. Yu, *Nature communications* **2024**, 15, 7034.
- [20] M. Li, Z. Zhao, T. Cheng, A. Fortunelli, C.-Y. Chen, M. Li, A. Fortunelli, C.-Y. Chen, R. Yu, Q. Zhang et al., *Science (New York, N.Y.)* **2016**, 354, 1414-1419.
- [21] X. Tian, X. Zhao, Y.-Q. Su, L. Wang, H. Wang, D. Dang, B. Chi, H. Liu, E. J. Hensen, X. W. Lou et al., *Science* **2019**, 366, 850.
- [22] C. Chen, Y. Kang, Z. Huo, Z. Zhu, W. Huang, H. L. Xin, J. D. Snyder, D. Li, J. A. Herron, M. Mavrikakis et al., *Science (New York, N.Y.)* **2014**, 343, 1339.
- [23] R. Jamil, M. Sohail, N. Baig, M. S. Ansari, R. Ahmed, *Scientific reports* **2019**, 9, 15273.
- [24] V. R. Stamenkovic, B. Fowler, B. S. Mun, G. Wang, P. N. Ross, C. A. Lucas, N. M. Marković, *Science (New York, N.Y.)* **2007**, 315, 493.
- [25] P. Ehrburger, O. P. Mahajan, P. L. Walker, *Journal of Catalysis* **1976**, 43, 61.

- [26] G. C. Torres, E. L. Jablonski, G. T. Baronetti, A. A. Castro, S. R. de Miguel, O. A. Scelza, M. D. Blanco, M. A. Peña Jiménez, J. L. G. Fierro, *Applied Catalysis A: General* **1997**, *161*, 213.
- [27] C. Prado-Burguete, A. Linares-Solano, F. Rodriguez-Reinoso, C. Salinas-Martinez de Lecea, *Journal of Catalysis* **1989**, *115*, 98.
- [28] D. J. Suh, T.-J. Park, *Carbon* **1993**, *31*, 427.
- [29] S. R. de Miguel, O. A. Scelza, M. C. Román-Martínez, C. Salinas-Martinez de Lecea, D. Cazorla-Amorós, A. Linares-Solano, *Applied Catalysis A: General* **1998**, *170*, 93.
- [30] A. Guerrero-Ruiz, P. Badenes, I. Rodríguez-Ramos, *Applied Catalysis A: General* **1998**, *173*, 313.
- [31] F. Coloma, A. Sepulveda-Escribano, J. L. G. Fierro, F. Rodriguez-Reinoso, *Langmuir* **1994**, *10*, 750.
- [32] M. C. Román-Martínez, D. Cazorla-Amorós, A. Linares-Solano, C. Salinas-Martinez de Lecea, H. Yamashita, M. Anpo, *Carbon* **1995**, *33*, 3.
- [33] H. Shioyama, K. Honjo, M. Kiuchi, Y. Yamada, A. Ueda, N. Kuriyama, T. Kobayashi, *Journal of Power Sources* **2006**, *161*, 836.
- [34] P. Urchaga, M. Weissmann, S. Baranton, T. Girardeau, C. Coutanceau, *Langmuir* **2009**, *25*, 6543.
- [35] F. Xu, M. Wang, L. Sun, Q. Liu, H. Sun, E. A. Stach, J. Xie, *Electrochimica Acta* **2013**, *94*, 172.
- [36] N. Rubio, T. Suter, Z. Rana, A. J. Clancy, S. Masuda, H. Au, G. Coulter, P. Sirisinudomkit, P. F. McMillan, C. A. Howard et al., *Journal of materials chemistry. A* **2022**, *10*, 20121.
- [37] P.-L. Kuo, W.-F. Chen, C.-Y. Lin, *Journal of Power Sources* **2009**, *194*, 234.
- [38] S. Murugesan, K. Myers, V. Subramanian, *Applied Catalysis B: Environmental* **2011**, *103*, 266.
- [39] A. Eguizabal, L. Uson, V. Sebastian, J. L. Hueso, M. P. Pina, *RSC Adv.* **2015**, *5*, 90691.
- [40] S. Ott, A. Orfanidi, H. Schmies, B. Anke, H. N. Nong, J. Hübner, U. Gernert, M. Gliech, M. Lerch, P. Strasser, *Nature materials* **2020**, *19*, 77.
- [41] S. Zhang, S. Chen, *Journal of Power Sources* **2013**, *240*, 60.
- [42] H. Schmies, E. Hornberger, B. Anke, T. Jurzinsky, H. N. Nong, F. Dionigi, S. Kühl, J. Drnec, M. Lerch, C. Cremers et al., *Chem. Mater.* **2018**, *30*, 7287.
- [43] Z. Yang, Y. Shi, X. Wang, G. Zhang, P. Cui, *Journal of Power Sources* **2019**, *431*, 125.
- [44] A. Kozhushner, O. Lori, D. A. Cullen, H. C. Honig, Y. Persky, L. Peles-Strahl, Q. Li, L. Elbaz, *Carbon* **2024**, *227*, 119290.
- [45] F. Ostwald, *Zeitschrift für Elektrotechnik und Elektrochemie* **1894**, *4*, 122.
- [46] C. F. Schœnbein, *The London, Edinburgh, and Dublin Philosophical Magazine and Journal of Science* **1839**, *14*, 43.
- [47] W. R. Grove, *The London, Edinburgh, and Dublin Philosophical Magazine and Journal of Science* **1839**, *14*, 127.
- [48] F. T. Bacon, *Electrochimica Acta* **1969**, *14*, 569.
- [49] M. Klell, H. Eichseder, A. Trattner, *Wasserstoff in der Fahrzeugtechnik*, Springer Fachmedien Wiesbaden, Wiesbaden, **2018**.
- [50] P. W. Atkins, *Physikalische Chemie*, VCH, Weinheim, **1996**.
- [51] M. Winter, R. J. Brodd, *Chemical reviews* **2004**, *104*, 4245.
- [52] V. M. Schmidt, *Elektrochemische Verfahrenstechnik. Grundlagen, Reaktionstechnik, Prozeßoptimierung*, Wiley-VCH, Weinheim, **2003**.

- [53] S. Tsushima, K. Teranishi, S. Hirai, *ECS Trans.* **2006**, 3, 91.
- [54] P. Kurzweil, *Brennstoffzellentechnik*, Springer Fachmedien Wiesbaden, Wiesbaden, **2016**.
- [55] "The Fuel Cell Industry Review 2022", can be found under [www.erm.com](http://www.erm.com), **2022**. (Access Date 22.10.24).
- [56] E. Riedel, C. Janiak, *Anorganische Chemie*, De Gruyter, Berlin, **2011**.
- [57] O. T. Holton, J. W. Stevenson, *Platinum Metals Review* **2013**, 57, 259.
- [58] P. K. Shen, *Electrochemical Oxygen Reduction*, Springer Singapore, Singapore, **2021**.
- [59] D. Banham, S. Ye, *ACS Energy Lett.* **2017**, 2, 629.
- [60] J. M. Thomas, E. L. Evans, M. Barber, P. Swift, *Trans. Faraday Soc.* **1971**, 67, 1875.
- [61] J. K. Nørskov, J. Rossmeisl, A. Logadottir, L. Lindqvist, J. R. Kitchin, T. Bligaard, H. Jónsson, *J. Phys. Chem. B* **2004**, 108, 17886.
- [62] J. M. Jaksic, N. M. Ristic, N. V. Krstajic, M. M. Jaksic, *Int. J. Hydrogen Energy* **1998**, 23, 1121.
- [63] P. Strasser, S. Koh, T. Anniyev, J. Greeley, K. More, C. Yu, Z. Liu, S. Kaya, D. Nordlund, H. Ogasawara et al., *Nature chemistry* **2010**, 2, 454.
- [64] K. H. Kangasniemi, D. A. Condit, T. D. Jarvi, *J. Electrochem. Soc.* **2004**, 151, E125-E132.
- [65] H. Igarashi, T. Fujino, Y. Zhu, H. Uchida, M. Watanabe, *Phys. Chem. Chem. Phys.* **2001**, 3, 306.
- [66] C. M. Sánchez-Sánchez, A. J. Bard, *Analytical chemistry* **2009**, 81, 8094.
- [67] P. S. Ruvinskiy, A. Bonnefont, C. Pham-Huu, E. R. Savinova, *Langmuir : the ACS journal of surfaces and colloids* **2011**, 27, 9018.
- [68] J. C. Meier, C. Galeano, I. Katsounaros, A. A. Topalov, A. Kostka, F. Schüth, K. J. J. Mayrhofer, *ACS Catal.* **2012**, 2, 832.
- [69] M. Pourbaix, *Lectures on Electrochemical Corrosion*, Springer Plenum Press, New York, **1973**.
- [70] M. Lefèvre, E. Proietti, F. Jaouen, J.-P. Dodelet, *Science (New York, N.Y.)* **2009**, 324, 71.
- [71] K. Gong, F. Du, Z. Xia, M. Durstock, L. Dai, *Science (New York, N.Y.)* **2009**, 323, 760.
- [72] Y. Qiu, Le Xin, F. Jia, J. Xie, W. Li, *Langmuir : the ACS journal of surfaces and colloids* **2016**, 32, 12569.
- [73] M. Shao, A. Peles, K. Shoemaker, *Nano letters* **2011**, 11, 3714.
- [74] G. A. Tritsarlis, J. Greeley, J. Rossmeisl, J. K. Nørskov, *Catal Lett* **2011**, 141, 909.
- [75] F. J. Perez-Alonso, D. N. McCarthy, A. Nierhoff, P. Hernandez-Fernandez, C. Strebler, I. E. L. Stephens, J. H. Nielsen, I. Chorkendorff, *Angewandte Chemie (International ed. in English)* **2012**, 51, 4641.
- [76] M. Peuckert, T. Yoneda, R. A. Dalla Betta, M. Boudart, *J. Electrochem. Soc.* **1986**, 133, 944.
- [77] K. Kinoshita, *J. Electrochem. Soc.* **1990**, 137, 845.
- [78] K. Shinozaki, Y. Morimoto, B. S. Pivovar, S. S. Kocha, *Electrochimica Acta* **2016**, 213, 783.
- [79] T. Yoshida, K. Kojima, *Interface magazine* **2015**, 24, 45.
- [80] *Advances in Science and Technology*, Trans Tech Publications LtdSwitzerland, **2014**.
- [81] Y.-J. Wang, W. Long, L. Wang, R. Yuan, A. Ignaszak, B. Fang, D. P. Wilkinson, *Energy Environ. Sci.* **2018**, 11, 258.
- [82] D. V. Talapin, A. L. Rogach, M. Haase, H. Weller, *J. Phys. Chem. B* **2001**, 105, 12278.
- [83] J. Park, J. Joo, S. G. Kwon, Y. Jang, T. Hyeon, *Angewandte Chemie (International ed. in English)* **2007**, 46, 4630.

- [84] N. T. K. Thanh, N. Maclean, S. Mahiddine, *Chemical reviews* **2014**, *114*, 7610.
- [85] V. K. LaMer, R. H. Dinegar, *Journal of the American Chemical Society* **1950**, *72*, 4847.
- [86] C. B. Murray, D. J. Norris, M. G. Bawendi, *J. Am. Chem. Soc.* **1993**, *115*, 8706.
- [87] J. R. Shimpf, D. S. Sidhaye, B. L. V. Prasad, *Langmuir : the ACS journal of surfaces and colloids* **2017**, *33*, 9491.
- [88] Y. Yin, P. Alivisatos, *Nature* **2005**, *437*, 664.
- [89] N. Tian, Z.-Y. Zhou, S.-G. Sun, Y. Ding, Z. L. Wang, *Science* **2007**, *316*, 732-735.
- [90] S. P. McDarby, C. J. Wang, M. E. King, M. L. Personick, *Journal of the American Chemical Society* **2020**, *142*, 21322.
- [91] H. P. Boehm, E. Diehl, W. Heck, R. Sappok, *Angew. Chem. Int. Ed.* **1964**, *3*, 669.
- [92] H.-P. Boehm, *Carbon* **1994**, *32*, 759.
- [93] D. Pantea, H. Darmstadt, S. Kaliaguine, L. Sümchen, C. Roy, *Carbon* **2001**, *39*, 1147.
- [94] G. Álvarez, F. Alcaide, O. Miguel, P. L. Cabot, M. V. Martínez-Huerta, J. L. G. Fierro, *Electrochimica Acta* **2011**, *56*, 9370.
- [95] J. Wang, G. Yin, Y. Shao, S. Zhang, Z. Wang, Y. Gao, *Journal of Power Sources* **2007**, *171*, 331.
- [96] S. Pérez-Rodríguez, D. Sebastián, M. J. Lázaro, E. Pastor, *Journal of Catalysis* **2017**, *355*, 156.
- [97] E. A. Aksoylu, M. Madalena, A. Freitas, M. F. R. Pereira, J. L. Figueiredo, *Carbon* **2001**, *39*, 175.
- [98] A. S. Arico, V. Antonucci, M. Minutoli, N. Giordano, *Carbon* **1989**, *27*, 337.
- [99] J. L. La Gómez de Fuente, M. V. Martínez-Huerta, S. Rojas, P. Terreros, J. L. G. Fierro, M. A. Peña, *Carbon* **2005**, *43*, 3002.
- [100] S. Pérez-Rodríguez, E. Pastor, M. J. Lázaro, *International Journal of Hydrogen Energy* **2018**, *43*, 7911.
- [101] J. C. Calderón, M. J. Nieto-Monge, S. Pérez-Rodríguez, J. I. Pardo, R. Moliner, M. J. Lázaro, *International Journal of Hydrogen Energy* **2016**, *41*, 19556.
- [102] M. J. Lázaro, C. Alegre, M. J. Nieto-Monge, D. Sebastián, M. E. Gálvez, E. Pastor, R. Moliner in *Advances in Science and Technology*, Trans Tech Publications LtdSwitzerland, **2014**, pp. 41–49.
- [103] D. A. Stevens, M. T. Hicks, G. M. Haugen, J. R. Dahn, *Journal of The Electrochemical Society* **2005**, *152*, A2309-A2315.
- [104] M. Liu, R. Zhang, W. Chen, *Chem. Rev.* **2014**, *114*, 5117.
- [105] S. H. Hur, J.-N. Park, *Asia-Pacific J Chem Eng* **2013**, *8*, 218.
- [106] S. Kang, H. Kim, Y.-H. Chung, *Nano Convergence* **2018**, *5*.
- [107] E. Wiberg, N. Wiberg, A. F. Holleman, *Anorganische Chemie*, De Gruyter, Berlin, Boston, **2017**.
- [108] S. Stankovich, D. A. Dikin, G. H. B. Dommett, K. M. Kohlhaas, E. J. Zimney, E. A. Stach, R. D. Piner, S. T. Nguyen, R. S. Ruoff, *Nature* **2006**, *442*, 282.
- [109] L. Rizzi, A. Zienert, J. Schuster, M. Köhne, S. E. Schulz, *ACS applied materials & interfaces* **2018**, *10*, 43088.
- [110] P. Serp, *Applied Catalysis A: General* **2003**, *253*, 337.
- [111] A. Y. Kasumov, H. Bouchiat, B. Reulet, O. Stephan, I. I. Khodos, Y. B. Gorbatov, Colliex C., *Europhys. Lett.* **1998**, *43*, 89.
- [112] P.-C. Ma, N. A. Siddiqui, G. Marom, J.-K. Kim, *Composites Part A: Applied Science and Manufacturing* **2010**, *41*, 1345.

- [113] X. Wang, W. Li, Z. Chen, M. Waje, Y. Yan, *Journal of Power Sources* **2006**, *158*, 154.
- [114] E. Bekyarova, M. E. Itkis, N. Cabrera, B. Zhao, A. Yu, J. Gao, R. C. Haddon, *Journal of the American Chemical Society* **2005**, *127*, 5990.
- [115] C. A. Bessel, K. Laubernds, N. M. Rodriguez, R. T. K. Baker, *J. Phys. Chem. B* **2001**, *105*, 1115.
- [116] E. Antolini, E. R. Gonzalez, *Solid State Ionics* **2009**, *180*, 746.
- [117] S.-Y. Huang, P. Ganesan, B. N. Popov, *Applied Catalysis B: Environmental* **2011**, *102*, 71.
- [118] A. L. Dicks, *Journal of Power Sources* **2006**, *156*, 128.
- [119] K. Biastoch, U. Hofmann, *Angewandte Chemie* **1940**, *53*, 327.
- [120] H.-P. Boehm, *Zeitschrift anorg allge chemie* **1958**, *297*, 315.
- [121] P. A. Marsh, A. Voet, T. J. Mullens, L. D. Price, *Rubber Chemistry and Technology* **1970**, *43*, 470.
- [122] T. Soboleva, X. Zhao, K. Malek, Z. Xie, T. Navessin, S. Holdcroft, *ACS applied materials & interfaces* **2010**, *2*, 375.
- [123] S. Tang, G. Sun, J. QI, S. Sun, J. Guo, Q. XIN, G. M. Haarberg, *Chinese Journal of Catalysis* **2010**, *31*, 12.
- [124] M. Uchida, Y. Aoyama, M. Tanabe, N. Yanagihara, N. Eda, A. Ohta, *J. Electrochem. Soc.* **1995**, *142*, 2572.
- [125] Z.-B. Wang, G.-P. Yin, P.-F. Shi, *Carbon* **2006**, *44*, 133.
- [126] N. Rajalakshmi, H. Ryu, M. Shaijumon, S. Ramaprabhu, *Journal of Power Sources* **2005**, *140*, 250.
- [127] M. Monthieux, Smith, B.W., B. Burtiaux, A. Claye, Fischer, J.E., Luzzi, D.E., *Carbon* **2001**, *39*, 1251.
- [128] B. K. Pradhan, N. K. Sandle, *Carbon* **1999**, *37*, 1323.
- [129] J. G. de La Fuente, S. Rojas, M. V. Martínez-Huerta, P. Terreros, M. A. Peña, J. L. G. Fierro, *Carbon* **2006**, *44*, 1919.
- [130] J. G. de La Fuente, M. V. Martínez-Huerta, S. Rojas, P. Terreros, J. L. G. Fierro, M. A. Peña, *Catalysis Today* **2006**, *116*, 422.
- [131] M. Carmo, M. Linardi, J. G. Rocha Poco, *International Journal of Hydrogen Energy* **2008**, *33*, 6289.
- [132] H. Tamon, M. Okazaki, *Carbon* **1996**, *34*, 741.
- [133] V. Gómez-Serrano, M. Acedo-Ramos, A. J. López-Peinado, C. Valenzuela-Calahorro, *Thermochimica Acta* **1997**, *291*, 109.
- [134] E. Papirer, E. Guyon, *Carbon* **1978**, *16*, 127.
- [135] D. S. Cameron, S. J. Cooper, I. L. Dodgson, B. Harrison, J. W. Jenkins, *Catalysis Today* **1990**, *7*, 113.
- [136] F. Rodriguez-Reinoso, *Carbon* **1998**, *36*, 159.
- [137] P. L. Antonucci, V. Alderucci, N. Giordano, D. L. Cocke, H. Kim, *Journal of Applied Electrochemistry* **1994**, *24*, 58.
- [138] S. Neffe, *Carbon* **1987**, *25*, 441.
- [139] Y. Matsumura, S. Hagiwara, H. Takahashi, *Carbon* **1976**, *14*, 163.
- [140] J. L. Figueiredo, M. F. R. Pereira, M. M. A. Freitas, J. J. M. Órfao, *Carbon* **1999**, *37*, 1379.
- [141] E. Papirer, E. Guyon, N. Perol, *Carbon* **1978**, *16*, 133.
- [142] P. E. Fanning, M. A. Vannice, *Carbon* **1993**, *31*, 721.
- [143] C. Kozłowski, P. M. A. Sherwood, *J. Chem. Soc., Faraday Trans. 1* **1985**, *81*, 2745.
- [144] S. R. Kelemen, K. D. Rose, P. J. Kwiatek, *Applied Surface Science* **1993**, *64*, 167.

- [145] H. P. Boehm in *Advances in Catalysis* (Ed.: W. G. Frankenberg), Elsevier, **1966**, pp. 179–274.
- [146] N. Tsubokawa, K. Kobayashi, Y. Sone, *Polymer Bulletin* **1985**, *13*, 215.
- [147] M. Toupin, D. Bélanger, *J. Phys. Chem. C* **2007**, *111*, 5394.
- [148] S. Ravindran, S. Chaudhary, B. Colburn, M. Ozkan, C. S. Ozkan, *Nano Lett.* **2003**, *3*, 447.
- [149] J. Chen, M. A. Hamon, H. Hu, Y. Chen, A. M. Rao, P. C. Eklund, R. C. Haddon, *Science* **1998**, *282*, 95.
- [150] E. T. Mickelson, I. W. Chiang, J. L. Zimmerman, P. J. Boul, J. Lozano, J. Liu, R. E. Smalley, R. H. Hauge, J. L. Margrave, *J. Phys. Chem. B* **1999**, *103*, 4318.
- [151] W. E. Ford, A. Jung, A. Hirsch, R. Graupner, F. Scholz, A. Yasuda, J. M. Wessels, *Advanced Materials* **2006**, *18*, 1193.
- [152] M. Prato, M. Maggini, *Accounts of Chemical Research* **1998**, *31*, 519.
- [153] J. Osterodt, F. Voegtle, *Chem. Commun.* **1996**, 547.
- [154] M. Tsuda, T. Ishida, T. Nogami, *Tetrahedron Letters* **1993**, *34*, 6911.
- [155] K. A. Worsley, P. Ramesh, S. K. Mandal, S. Niyogi, M. E. Itkis, R. C. Haddon, *Chemical Physics Letters* **2007**, *445*, 51.
- [156] P. Nednoor, N. Chopra, V. Gavalas, L. G. Bachas, B. J. Hinds, *Chem. Mater.* **2005**, *17*, 3595.
- [157] D. Pantarotto, C. D. Partidos, R. Graff, J. Hoebeke, J.-P. Briand, M. Prato, A. Bianco, *Journal of the American Chemical Society* **2003**, *125*, 6160.
- [158] S. S. Wong, E. Joselevich, A. T. Woolley, C. L. Cheung, C. M. Lieber, *Nature* **1998**, *394*, 52.
- [159] M. Holzinger, O. Vostrowsky, A. Hirsch, F. Hennrich, M. Kappes, R. Weiss, F. Jellen, *Angew. Chem. Int. Ed.* **2001**, *40*, 4002.
- [160] M. Maggini, G. Scorrano, M. Prato, *J. Am. Chem. Soc.* **1993**, *115*, 9798.
- [161] V. Georgakilas, K. Kordatos, M. Prato, D. M. Guldi, M. Holzinger, A. Hirsch, *Journal of the American Chemical Society* **2002**, *124*, 760.
- [162] J. L. Bahr, J. M. Tour, *Chem. Mater.* **2001**, *13*, 3823.
- [163] J. L. Bahr, J. Yang, D. V. Kosynkin, M. J. Bronikowski, R. E. Smalley, J. M. Tour, *Journal of the American Chemical Society* **2001**, *123*, 6536.
- [164] F. Liang, A. K. Sadana, A. Peera, J. Chattopadhyay, Z. Gu, R. H. Hauge, W. E. Billups, *Nano Lett.* **2004**, *4*, 1257.
- [165] E. T. Mickelson, C. B. Huffman, A. G. Rinzler, R. E. Smalley, R. H. Hauge, J. L. Margrave, *Chemical Physics Letters* **1998**, *296*, 188.
- [166] E. V. Basiuk, V. A. Basiuk, J.-G. Bañuelos, J.-M. Saniger-Blesa, V. A. Pokrovskiy, T. Y. Gromovoy, A. V. Mischanchuk, B. G. Mischanchuk, *J. Phys. Chem. B* **2002**, *106*, 1588.
- [167] J. Chen, A. M. Rao, S. Lyuksyutov, M. E. Itkis, M. A. Hamon, H. Hu, R. W. Cohn, P. C. Eklund, D. T. Colbert, R. E. Smalley et al., *J. Phys. Chem. B* **2001**, *105*, 2525.
- [168] F. Morales-Lara, M. Domingo-García, R. López-Garzón, M. Luz Godino-Salido, A. Peñas-Sanjuán, F. J. López-Garzón, M. Pérez-Mendoza, M. Melguizo, *Science and technology of advanced materials* **2016**, *17*, 541.
- [169] N. Tsubokawa, K. Kobayashi, Y. Sone, *Polymer Journal* **1987**, *19*, 1147.
- [170] A. Peñas-Sanjuán, R. López-Garzón, M. Domingo-García, F. J. López-Garzón, M. Melguizo, M. Pérez-Mendoza, *Carbon* **2012**, *50*, 3977.
- [171] L. Liu, D. Deng, Y. Xing, S. Li, B. Yuan, J. Chen, N. Xia, *Electrochimica Acta* **2013**, *89*, 616.

- [172] J. Quinson, S. Neumann, T. Wannmacher, L. Kacenauskaite, M. Inaba, J. Bucher, F. Bizzotto, S. B. Simonsen, L. Theil Kuhn, D. Bujak et al., *Angewandte Chemie (International ed. in English)* **2018**, *57*, 12338.
- [173] X. Yu, S. Ye, *Journal of Power Sources* **2007**, *172*, 133.
- [174] J. Speder, L. Altmann, M. Roefzaad, M. Bäumer, J. J. K. Kirkensgaard, K. Mortensen, M. Arenz, *Physical chemistry chemical physics : PCCP* **2013**, *15*, 3602.
- [175] A. A. Topalov, I. Katsounaros, M. Auinger, S. Cherevko, J. C. Meier, S. O. Klemm, K. J. J. Mayrhofer, *Angewandte Chemie (International ed. in English)* **2012**, *51*, 12613.
- [176] Y. Zhang, S. Chen, Y. Wang, W. Ding, R. Wu, L. Li, X. Qi, Z. Wei, *Journal of Power Sources* **2015**, *273*, 62.
- [177] K. Yu, D. J. Groom, X. Wang, Z. Yang, M. Gummalla, S. C. Ball, D. J. Myers, P. J. Ferreira, *Chem. Mater.* **2014**, *26*, 5540.
- [178] H. R. Colón-Mercado, B. N. Popov, *Journal of Power Sources* **2006**, *155*, 253.
- [179] T. Nagai, K. Kodama, *J. Electrochem. Soc.* **2021**, *168*, 24514.
- [180] Z. Gu, P. B. Balbuena, *The journal of physical chemistry. A* **2006**, *110*, 9783.
- [181] J. H. Kim, J. Y. Cheon, T. J. Shin, J. Y. Park, S. H. Joo, *Carbon* **2016**, *101*, 449.
- [182] B. Avasarala, R. Moore, P. Haldar, *Electrochimica Acta* **2010**, *55*, 4765.
- [183] H.-S. Oh, J.-H. Lee, H. Kim, *International Journal of Hydrogen Energy* **2012**, *37*, 10844.
- [184] J. Willsau, J. Heitbaum, *J. Electroanal. Chem.* **1984**, *161*, 93.
- [185] R. Borup, J. Meyers, B. Pivovar, Y. S. Kim, R. Mukundan, N. Garland, D. Myers, M. Wilson, F. Garzon, D. Wood et al., *Chem. Rev.* **2007**, *107*, 3904.
- [186] Y. Garsany, O. A. Baturina, K. E. Swider-Lyons, S. S. Kocha, *Anal. Chem.* **2010**, *82*, 6321.
- [187] A. Dekanski, J. Stevanovic, R. Stevanovic, B. Z. Nolic, V. M. Jovanovic, *Carbon* **2001**, *39*, 1195.
- [188] C. H. Haman, W. Vielstich, *Elektrochemie*, Wiley-VCH, Weinheim, **2005**.
- [189] S. Trasatti, *Pure and Applied Chemistry* **1986**, *58*, 955.
- [190] R. W. Ramette.
- [191] G. Jerkiewicz, *ACS Catal.* **2020**, *10*, 8409.
- [192] D. Harvey, "Instrumental Analysis", can be found under <https://chem.libretexts.org/>, **2024**. (Access Date 17.11.2024).
- [193] M. H. Miles, E. A. Klaus, B. P. Gunn, J. R. Locker, W. E. Serafin, S. Srinivasan, *Electrochimica Acta* **1978**, *23*, 521.
- [194] T. Biegler, D. A. J. Rand, R. Woods, *J. Electroanal. Chem.* **1971**, *29*, 269.
- [195] W. Xia, A. Mahmood, Z. Liang, R. Zou, S. Guo, *Angewandte Chemie (International ed. in English)* **2016**, *55*, 2650.
- [196] A. Ohma, K. Shinohara, A. Iiyama, T. Yoshida, A. Daimaru, *ECS Trans.* **2011**, *41*, 775.
- [197] Y. Garsany, I. L. Singer, K. E. Swider-Lyons, *Journal of Electroanalytical Chemistry* **2011**, *662*, 396.
- [198] K. Ke, K. Hiroshima, Y. Kamitaka, T. Hatanaka, Y. Morimoto, *Electrochimica Acta* **2012**, *72*, 120.
- [199] K. Shinozaki, J. W. Zack, S. Pylypenko, B. S. Pivovar, S. S. Kocha, *J. Electrochem. Soc.* **2015**, *162*, F1384-F1396.
- [200] M. Inaba, J. Quinson, M. Arenz, *Journal of Power Sources* **2017**, *353*, 19.
- [201] S. S. Kocha, J. W. Zack, S. M. Alia, K. C. Neyerlin, B. S. Pivovar, *ECS Trans.* **2013**, *50*, 1475.

- [202] S. Shukla, S. Bhattacharjee, A. Z. Weber, M. Secanell, *J. Electrochem. Soc.* **2017**, *164*, F600-F609.
- [203] R. D. Deegan, O. Bakajin, T. F. Dupont, G. Huber, S. R. Nagel, T. A. Witten, *Nature* **1997**, *389*, 827.
- [204] J. Park, J. Moon, *Langmuir : the ACS journal of surfaces and colloids* **2006**, *22*, 3506.
- [205] A. B. Bediwi, W. J. Kulnis, Y. Luo, D. Woodland, W. N. Unertl, *Mat. Res. Soc. Symp. Proc.* **1995**, *372*, 277.
- [206] V. Dugas, J. Broutin, E. Souteyrand, *Langmuir : the ACS journal of surfaces and colloids* **2005**, *21*, 9130.
- [207] R. D. Deegan, O. Bakajin, T. F. Dupont, G. Huber, S. R. Nagel, T. A. Witten, *Phys. Rev. E* **2000**, *62*, 756.
- [208] R. D. Deegan, *Phys. Rev. E* **1998**, *61*, 475.
- [209] N. M. Kovalchuk, A. Trybala, V. M. Starov, *Current Opinion in Colloid & Interface Science* **2014**, *19*, 336.
- [210] X. Shen, C.-M. Ho, T.-S. Wong, *J. Phys. Chem. B* **2010**, *114*, 5269.
- [211] H. Hu, R. G. Larson, *J. Phys. Chem. B* **2006**, *110*, 7090.
- [212] C. Marangoni, *Annalen der Physik* **1871**, *219*, 337.
- [213] H. Hu, R. G. Larson, *Langmuir : the ACS journal of surfaces and colloids* **2005**, *21*, 3972.
- [214] R. Savino, D. Paterna, N. Favaloro, *Journal of Thermophysics and Heat Transfer* **2002**, *16*, 562.
- [215] P. J. Yunker, T. Still, M. A. Lohr, A. G. Yodh, *Nature* **2011**, *476*, 308.
- [216] R. Bhardwaj, X. Fang, P. Somasundaran, D. Attinger, *Langmuir : the ACS journal of surfaces and colloids* **2010**, *26*, 7833.
- [217] M. Anyfantakis, Z. Geng, M. Morel, S. Rudiuk, D. Baigl, *Langmuir* **2015**, *31*, 4113.
- [218] L. Cui, J. Zhang, X. Zhang, L. Huang, Z. Wang, Y. Li, H. Gao, S. Zhu, T. Wang, B. Yang, *ACS applied materials & interfaces* **2012**, *4*, 2775.
- [219] T. Still, P. J. Yunker, A. G. Yodh, *Langmuir* **2012**, *28*, 4984.
- [220] I. Sandu, C. T. Fleaca, *Journal of Colloid and Interface Science* **2011**, *358*, 621.
- [221] H. B. Eral, D. M. Augustine, M. H. G. Duits, F. Mugele, *Soft Matter* **2011**, *7*, 4954.
- [222] A. Voet, J. B. Donnet, P. A. Marsh, J. Schultz, *Carbon* **1966**, *4*, 155.
- [223] L. Calvillo, M. J. Lázaro, I. Suelves, Y. Echegoyen, E. G. Bordejé, R. Moliner, *Journal of nanoscience and nanotechnology* **2009**, *9*, 4164.
- [224] E. Pretsch, P. Bühlmann, M. Badertscher, *Spektroskopische Daten zur Strukturaufklärung organischer Verbindungen*, Springer Berlin Heidelberg, Berlin, Heidelberg, **2010**.
- [225] G. Jander, K. F. Jahr, *Maßanalyse*, De Gruyter, Berlin, **2022**.
- [226] R. Williams, "pKa Values in Water Compilation", can be found under [organicchemistrydata.org](http://organicchemistrydata.org), **2022**. (Access Date 20.11.2024).
- [227] *Organikum. Organisch-chemisches Grundpraktikum*, Wiley-VCH, Weinheim, **2001**.
- [228] H. P. Latscha, U. Kazmaier, H. A. Klein, *Organische Chemie*, Springer Berlin Heidelberg, Berlin, Heidelberg, **2008**.
- [229] M. Thommes, K. Kaneko, A. V. Neimark, J. P. Olivier, F. Rodriguez-Reinoso, J. Rouquerol, K. S. Sing, *Pure and Applied Chemistry* **2015**, *87*, 1051.
- [230] J. Buddrus, B. Schmidt, *Grundlagen der organischen Chemie*, De Gruyter, Berlin, New York, **2011**.
- [231] N. Krishnankutty, M. A. Vannice, *Chem. Mater.* **1995**, *7*, 754.
- [232] J. Li, L. Ma, X. Li, C. Lu, H. Liu, *Ind. Eng. Chem. Res.* **2005**, *44*, 5478.

- [233] A. Hädener, H. Kaufmann, *Grundlagen der organischen Chemie*, Birkhäuser Verlag, Basel, Boston, Berlin, **2006**.
- [234] M. J. Janssen in *The chemistry of functional groups, Vol. 6,2* (Ed.: S. Patai), Interscience Publ, London, **1991**, pp. 705–764.
- [235] National Institute of Advanced Industrial Science and Technology, "IR reference spectra", can be found under <https://sdbs.db.aist.go.jp/>. (Access Date 06.08.2024).
- [236] K. Ahrenstorf, O. Albrecht, H. Heller, A. Kornowski, D. Görlitz, H. Weller, *Small (Weinheim an der Bergstrasse, Germany)* **2007**, *3*, 271.
- [237] S. Woderich, *Dissertation*, University of Hamburg, Hamburg, **2024**.
- [238] C. Reichardt, T. Welton, *Solvents and Solvent Effects in Organic Chemistry*, Wiley - VCH, Weinheim, **2011**.
- [239] I. Takahashi, S. S. Kocha, *Journal of Power Sources* **2010**, *195*, 6312.
- [240] C. Zhang, S. Y. Hwang, Z. Peng, *J. Mater. Chem. A* **2014**, *2*, 19778.
- [241] C. M. Pedersen, M. Escudero-Escribano, A. Velázquez-Palenzuela, L. H. Christensen, I. Chorkendorff, I. E. L. Stephens, *Electrochimica Acta* **2015**, *179*, 647.
- [242] L. Wei, G. Yushin, *Nano Energy* **2012**, *1*, 552.
- [243] K. Kinoshita, J. A. S. Bett, *Carbon* **1973**, *11*, 403.
- [244] M. R. Tarasevich, V. A. Bogdanovskaya, N. M. Zagudaeva, *J. Electroanal. Chem.* **1987**, *223*, 161.
- [245] C. Lian, X. Kong, H. Liu, J. Wu, *Journal of physics. Condensed matter : an Institute of Physics journal* **2016**, *28*, 464008.
- [246] L. Gan, M. Heggen, S. Rudi, P. Strasser, *Nano letters* **2012**, *12*, 5423.
- [247] L. Gan, M. Heggen, R. O'Malley, B. Theobald, P. Strasser, *Nano Lett.* **2013**, *13*, 1131.
- [248] J. Perez, V. A. Paganin, E. Antolini, *Journal of Electroanalytical Chemistry* **2011**, *654*, 108.
- [249] V. Gutknecht, J. Rüter, E. Felgenhauer, H. Heller, H. Weller, *Chem. Mater.* **2024**, *36*, 3628.
- [250] A. Orfanidi, P. Madkikar, H. A. El-Sayed, G. S. Harzer, T. Kratky, H. A. Gasteiger, *J. Electrochem. Soc.* **2017**, *164*, F418-F426.
- [251] S. Henning, L. Kühn, J. Herranz, J. Durst, T. Binninger, M. Nachtegaal, M. Werheid, W. Liu, M. Adam, S. Kaskel et al., *J. Electrochem. Soc.* **2016**, *163*, F998-F1003.
- [252] S. M. Alia, K. Jensen, C. Contreras, F. Garzon, B. Pivovar, Y. Yan, *ACS Catal.* **2013**, *3*, 358.
- [253] R. A. Sidik, A. B. Anderson, N. P. Subramanian, S. P. Kumaraguru, B. N. Popov, *The journal of physical chemistry. B* **2006**, *110*, 1787.
- [254] abcr, "Safety Data Sheet", can be found under <https://abcr.com/de>. (Access Date 05.10.24).
- [255] Apollo Scientific, "Safety Data Sheet", can be found under <https://store.apolloscientific.co.uk>. (Access Date 05.10.24).
- [256] Cabot, "Sicherheitsdatenblatt", can be found under <https://www.cabotcorp.com>). (Access Date 05.10.2024).
- [257] Grüssing, "Sicherheitsdatenblatt", can be found under <https://www.gruessing-shop.de>. (Access Date 05.10.2024).
- [258] Linde, "Safety Data Sheet", can be found under <https://produkte.linde-gas.at>. (Access Date 05.10.2024).
- [259] Merck, "Sicherheitsdatenblatt", can be found under <https://www.merckmillipore.com>. (Access Date 05.10.2024).

- [260] Sigma-Aldrich, "Safety Data Sheet", can be found under <https://www.sigmaaldrich.com>. (Access Date 05.10.24).
- [261] TCI Europe, "Safety Data Sheet", can be found under <https://www.tcichemicals.com>. (Access Date 05.10.2024).
- [262] Thermo Fisher Scientific, "Safety Data Sheet", can be found under <https://www.fishersci.co.uk>. (Access Date 05.10.24).
- [263] VWR BDH Chemicals, "Safety Data Sheet", can be found under <https://us.vwr.com>. (Access Date 05.10.2024).
- [264] Westfalen, "Safety Data Sheet", can be found under <https://www.westfalen.com/de/de>. (Access Date 05.10.24).
- [265] T.-Y. Yu, *Bachelor thesis*, University of Hamburg, Hamburg, **2022**.
- [266] J. S. Rüßbült, *Bachelor thesis*, University of Hamburg, Hamburg, **2024**.

## 10. Appendix

### 10.1. Safety

**Tab. 10.1:** GHS safety classification of employed chemicals according to the manufacturer's information. The GHS pictograms can be found in Figure 10.1.<sup>[254-264]</sup>

Chemical	GHS symbol	H Statements	P Statements
Acetone	02, 07	225, 319, 336	210, 243, 280, 304+340, 312, 403+235
1,4-Butanedithiol	07	335, 315, 319	271, 261, 280, 264, 305+351+338, 312, 337+313, 302+352, 304+340, 332+313, 362+364, 405, 403+233, 501
1,2-Dichlorobenzene	07, 09	315, 317, 319, 335, 410, 302+332	301+330+331, 312, 304+340, 302+352, 333+313, 337+313, 280, 332+313
Diphenyl ether	07, 09	319, 410	264, 273, 280, 305+351+338, 337+313, 391
Ethanol	02	225	210, 243, 280
Ethylenediamine	02, 05, 06, 08	226, 302+332, 311, 314, 317, 334, 412	210, 273, 280, 303+361+353, 304+340+310, 305+351+338
1,2-Hexadecanediol	-	-	-
HiSPEC® 3000: Platinum, nominally 20% on carbon black	02	228	210
Hydrochloric acid (37 %)	05, 07	290, 314, 335	234, 261, 271, 280
Hydrogen peroxide (30 %)	05	318, 412	280, 305+351+338
Methanol	02, 06, 08	225, 301+311+331, 370	210, 233, 241, 280, 301+310, 303+361+353, 304+340
Nafion-117-Solution	02, 05, 07	225, 318, 336	210, 233, 240, 241, 280, 305+351+338
Nitric acid (65 %)	03, 05, 06	272, 290, 314, 331	210, 220, 280, 303+361+353, 304+340+310, 305+351+338
Nitrogen (liquid)	04	281	282, 336+315, 403
Oleic acid	-	-	-
Oleylamine	05, 07, 08, 09	302, 304, 314, 335, 373, 410	273, 280, 301+330+331, 303+361+353, 304+340+310, 305+351+338
Oxalic acid dihydrate	05, 07	302+312, 318	280, 302+352, 305+351+338, 313

Chemical	GHS symbol	H Statements	P Statements
Oxygen (gas)	03, 04	270, 280	220, 244, 370+376, 403
Perchloric acid (65-71 %)	03, 05, 07, 08	271, 290, 302, 314, 373	210, 220, 280, 303+361+353, 304+340, 305+351+338, 308+310, 371+380+375
<i>p</i> -Phenylenediamine	06, 08, 09	301+311+331, 317, 319, 370, 410	273, 280, 301+310, 302+352+312, 304+340+311, 305+351+338
platinum acetylacetonate	07, 08	302+312+332, 315, 319, 361fd	280, 261, 304+340, 305+351+338, 302+352, 301+330
Potassium hydroxide	05, 07	290, 302, 314	234, 260, 280, 301+312, 303+361+353, 305+351+338
2-Propanol	02, 07	225, 319, 336	210, 280, 305+351+338
Pyridine	02, 07	225, 302+312+332, 315, 319	210, 280, 303+361+353, 304+340+312, 305+351+338
Sodium hydrogen carbonate	-	-	-
Sodium hydroxide	05	290, 314	260, 280, 301+330+331, 303+361+353, 304+340, 305+351+338, 310
Sulphuric acid (96 %)	05	290, 314	234, 280, 301+330+331, 303+361+353, 304+340+310, 305+351+338
Tetrahydrofuran	02, 07, 08	225, 302, 319, 335, 351	201, 202, 210, 233, 240, 241, 242, 243, 261, 264+302, 270, 271, 280
Thionyl chloride	05, 06	302, 314, 331, 335, 014, 029	280, 301+330+331, 303+361+353, 304+340, 305+351+338, 310
Toluene	02, 07, 08	225, 304, 315, 336, 361d, 373, 412	210, 280, 301+330+331, 303+361+353, 304+340, 310
Triethylenetetramine	05, 07	312, 314, 317, 412	261, 272, 273, 280, 303+361+353, 305+351+338
<i>Vulcan XC72R</i>	-	-	-

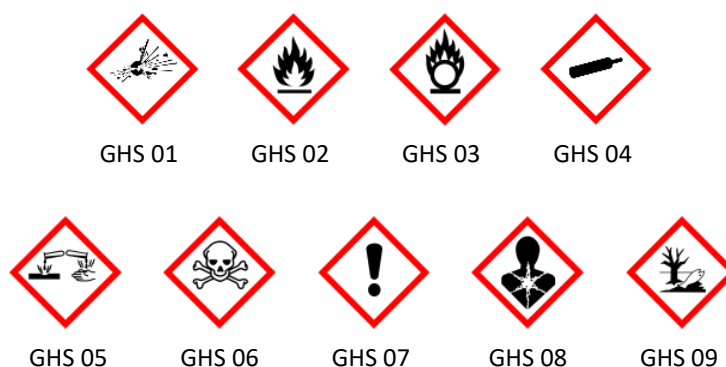


**Fig. 10.1:** GHS hazard pictograms 01-09.

## 10.2. IR spectra of functionalised carbons and reference spectra

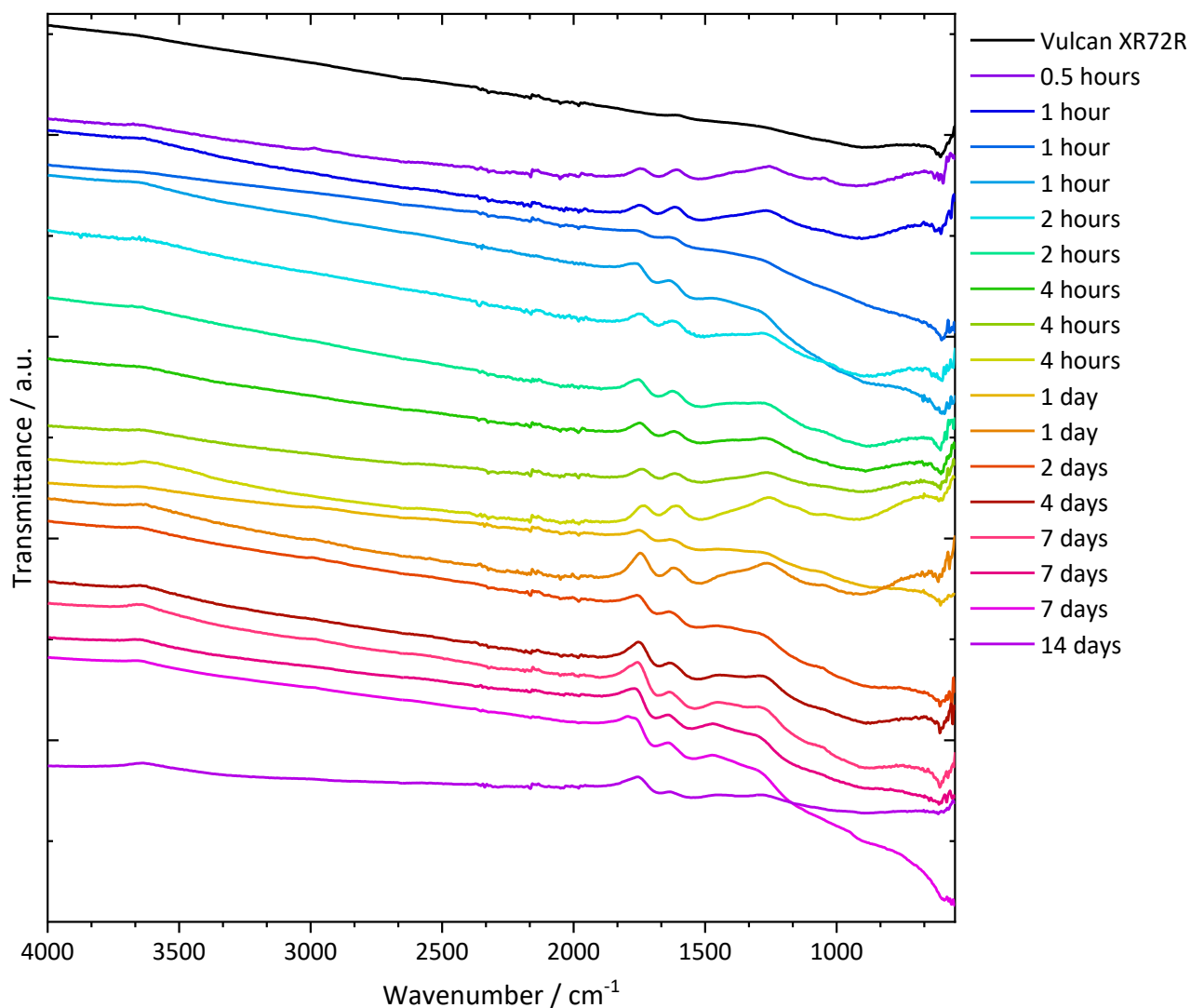


**Fig. 10.2:** FT-IR spectra of *Vulcan XC72R*, and *Vulcan XC72R* oxidised for varying durations at room temperature using a mixture of three parts concentrated sulphuric acid and one part concentrated nitric acid.

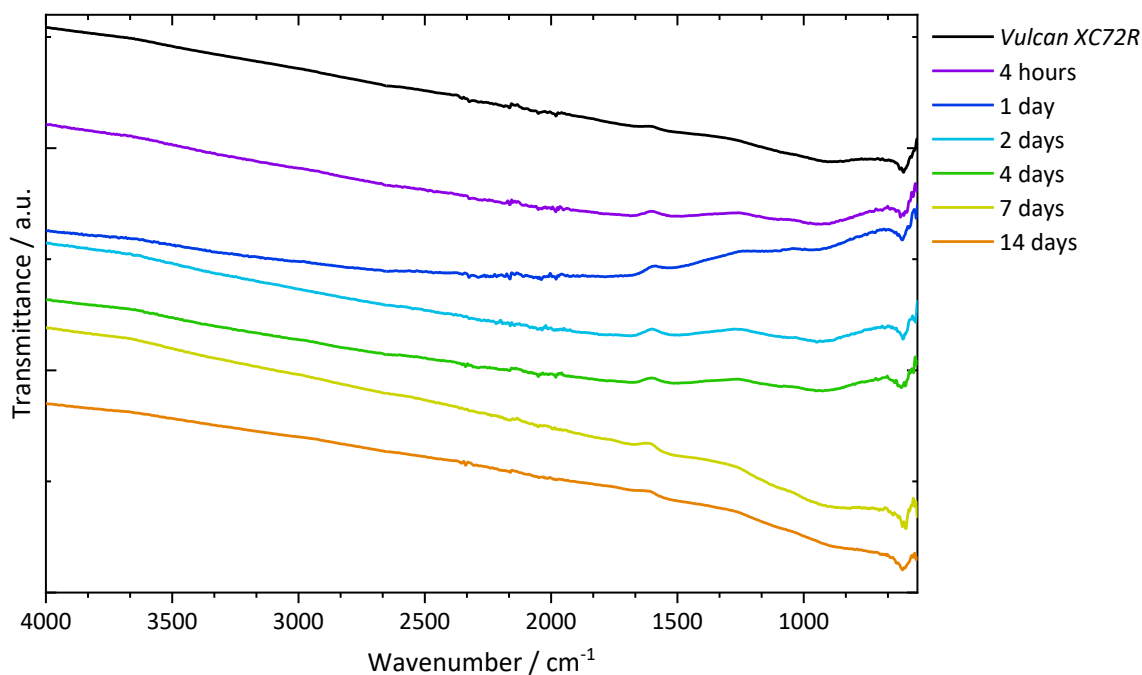


**Fig. 10.3:** FT-IR spectra of *Vulcan XC72R*, and *Vulcan XC72R* oxidised for varying durations at room temperature using concentrated nitric acid.

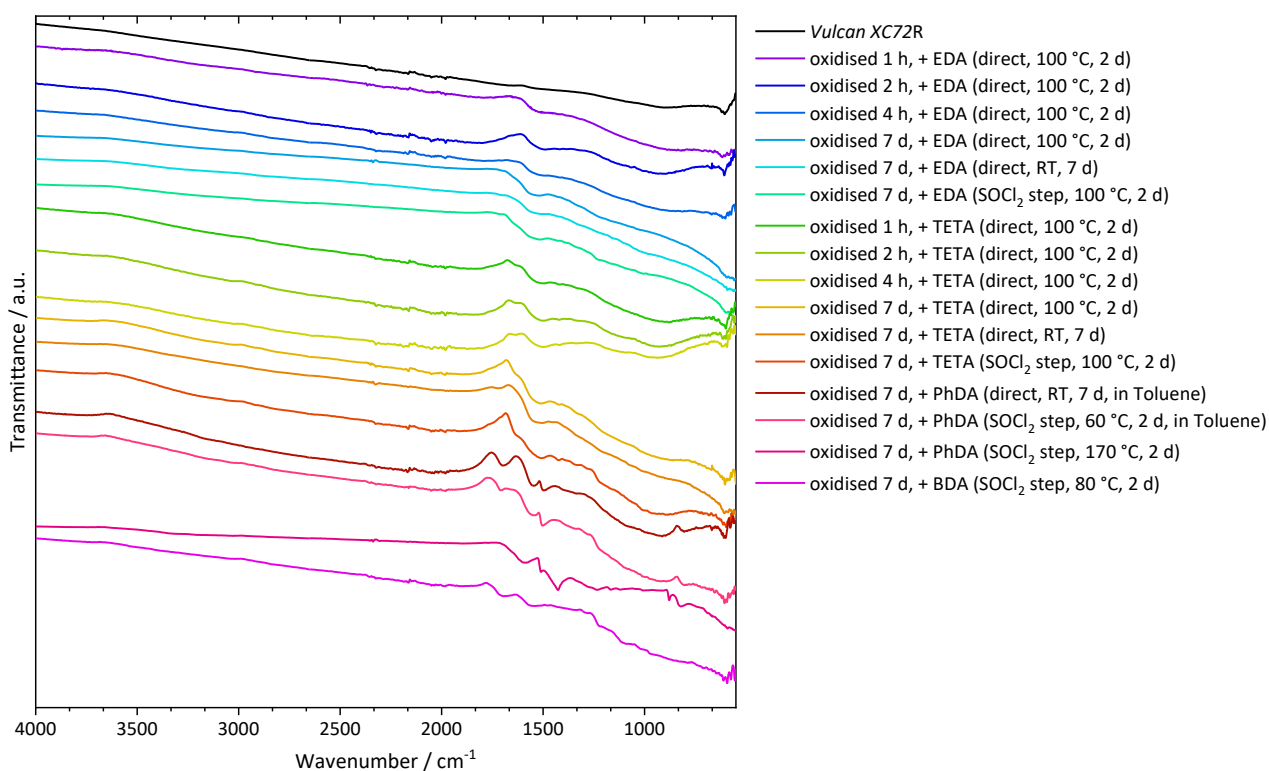


**Fig. 10.4:** FT-IR spectra of *Vulcan XC72R*, *Vulcan XC72R* oxidised for varying durations at room temperature using a mixture of three parts concentrated sulphuric acid and one part concentrated nitric acid, and oxidised *Vulcan XC72R* further functionalised with various diamines.

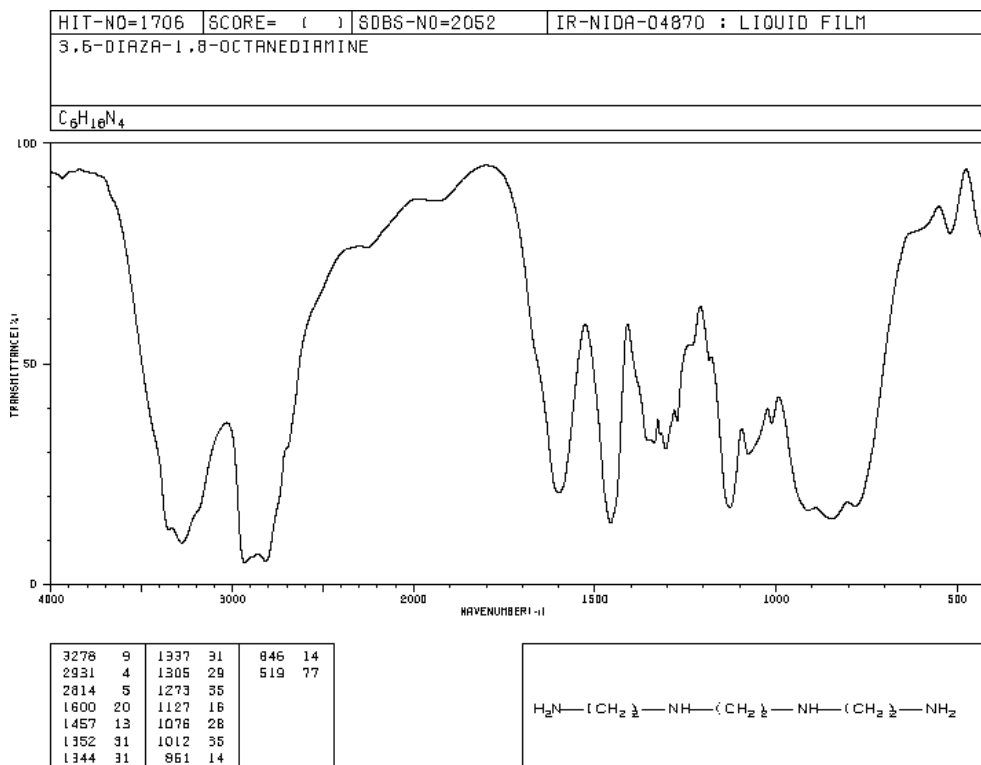


Fig. 10.5: IR reference spectrum of ethylenediamine.<sup>[235]</sup>

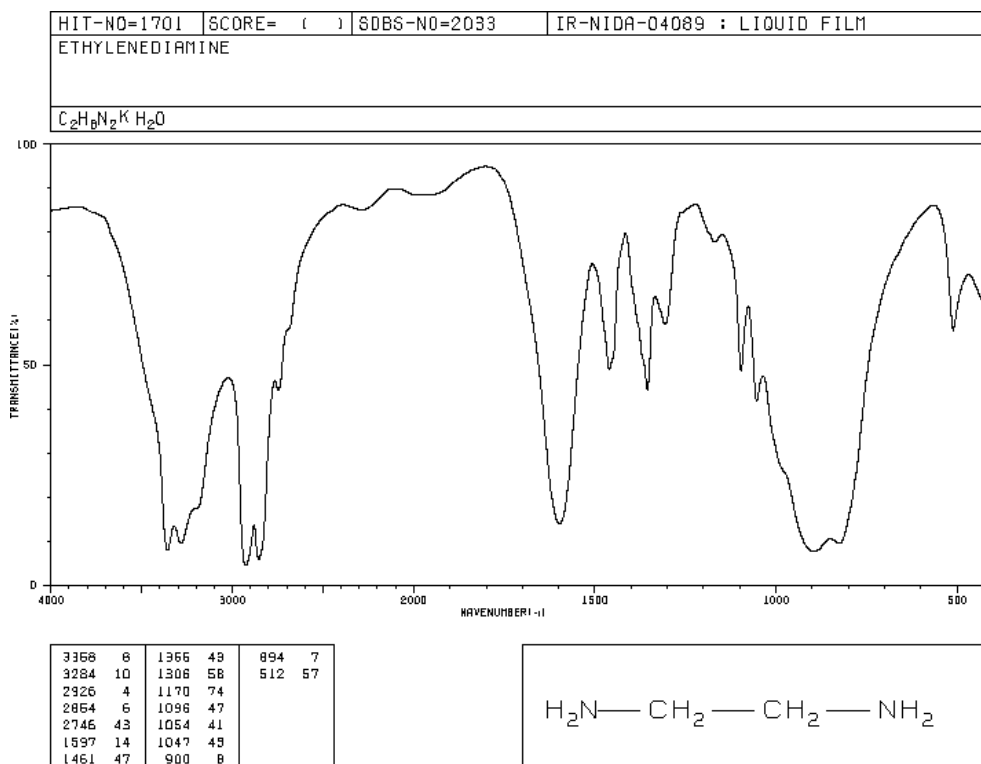
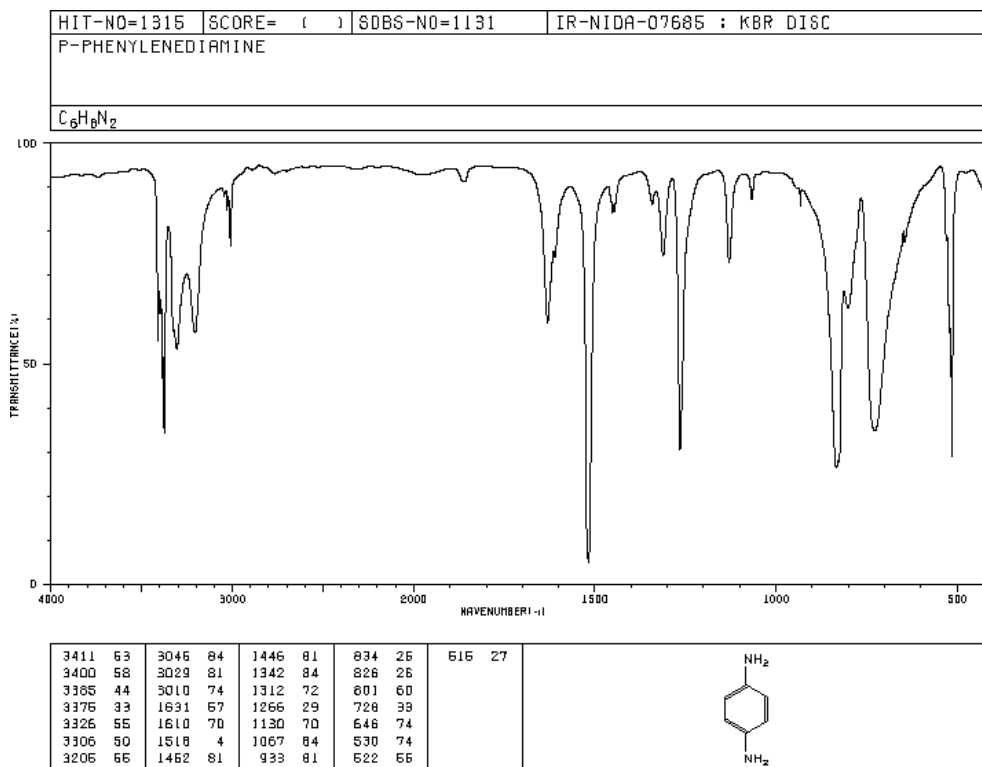
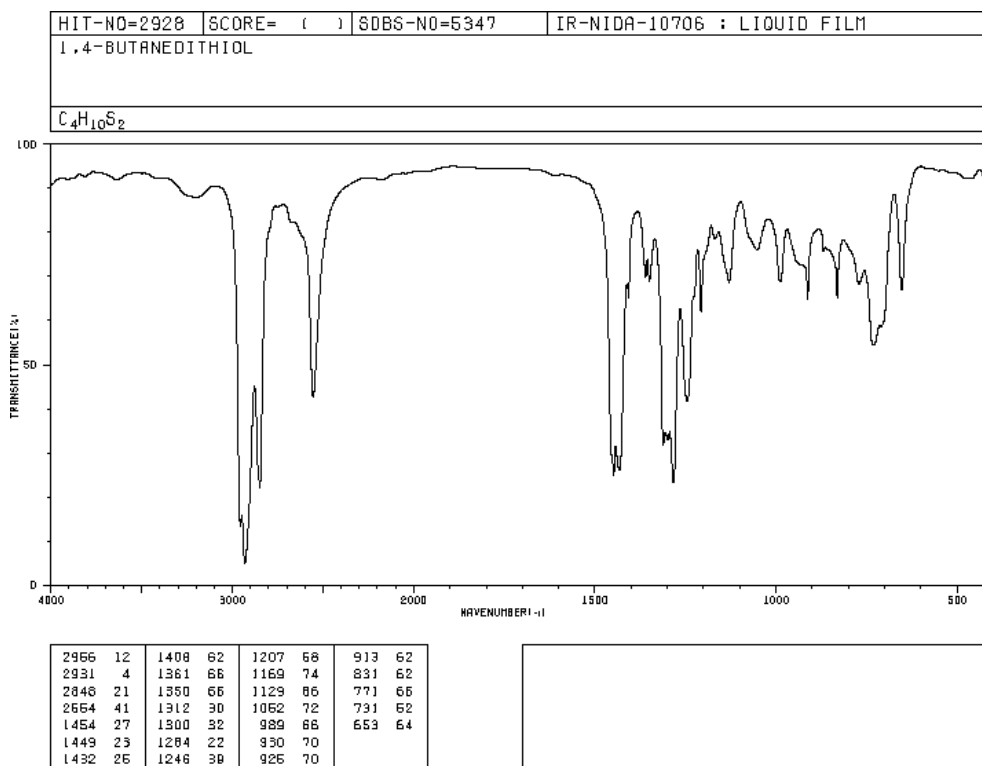


Fig. 10.6: IR reference spectrum of Triethylenetetramine.<sup>[235]</sup>



**Fig. 10.7:** IR reference spectrum of *p*-Phenylenediamine.<sup>[235]</sup>



**Fig. 10.8:** IR reference spectrum of 1,4-butanedithiol.<sup>[235]</sup>

### 10.3. Platinum contents of catalyst inks

**Tab. 10.2:** Platinum contents of catalyst inks used in preliminary measurements in figure 6.39, determined by elemental analysis (atomic absorption spectroscopy, average of 3-5 measurements).

Catalyst ink	Pt content / mg mL <sup>-1</sup>
Vulcan XC72R	0.291
7 days oxidised	0.195
7 days oxidised + ethylenediamine (100 °C, 2 d)	0.512
7 days oxidised + ethylenediamine (RT, 7 d)	0.244
7 days oxidised + ethylenediamine (SOCl <sub>2</sub> )	0.261
7 days oxidised + triethylenetetramine (RT, 7 d)	0.126
7 days oxidised + triethylenetetramine (SOCl <sub>2</sub> )	0.288
7 days oxidised + Phenylenediamine (SOCl <sub>2</sub> , melt)	0.243
7 days oxidised + Phenylenediamine (SOCl <sub>2</sub> , Toluene)	0.259
7 days oxidised + Butandithiol (SOCl <sub>2</sub> )	0.270

**Tab. 10.3:** Mean of platinum contents of catalyst inks used in AST measurements in figure 6.40 and 6.41, determined by three to five elemental analysis measurements (atomic absorption spectroscopy).

Catalyst ink	Pt content / mg mL <sup>-1</sup>	Standard deviation / %
PtNi / Vulcan XC72R	0.159	4.5
PtNi / 1 h oxidised	0.288	2.6
PtNi / 1 h oxidised + EDA	0.268	1.3
P <sub>5</sub> Ni / 1 h oxidised + TETA	0.290	3.9
PtNi / 2 h oxidised	0.225	2.7
PtNi / 2 h oxidised + EDA	0.228	9.1
PtNi / 2 h oxidised + TETA	0.341	0.24
PtNi / 4 h oxidised	0.301	2.3
PtNi / 4 h oxidised + EDA	0.226	2.3
PtNi / 4 h oxidised + TETA	0.327	1.4
Pt / Vulcan XC72R	0.299	2.6
Pt / 4 h oxidised	0.314	1.7
Pt / 4 h oxidised + EDA	0.295	3.5
Pt / 4 h oxidised + TETA	0.273	4.9
HiSPEC 3000	0.173	1.9

## 10.4. Predicted ECSAs depending on thin-film drying conditions

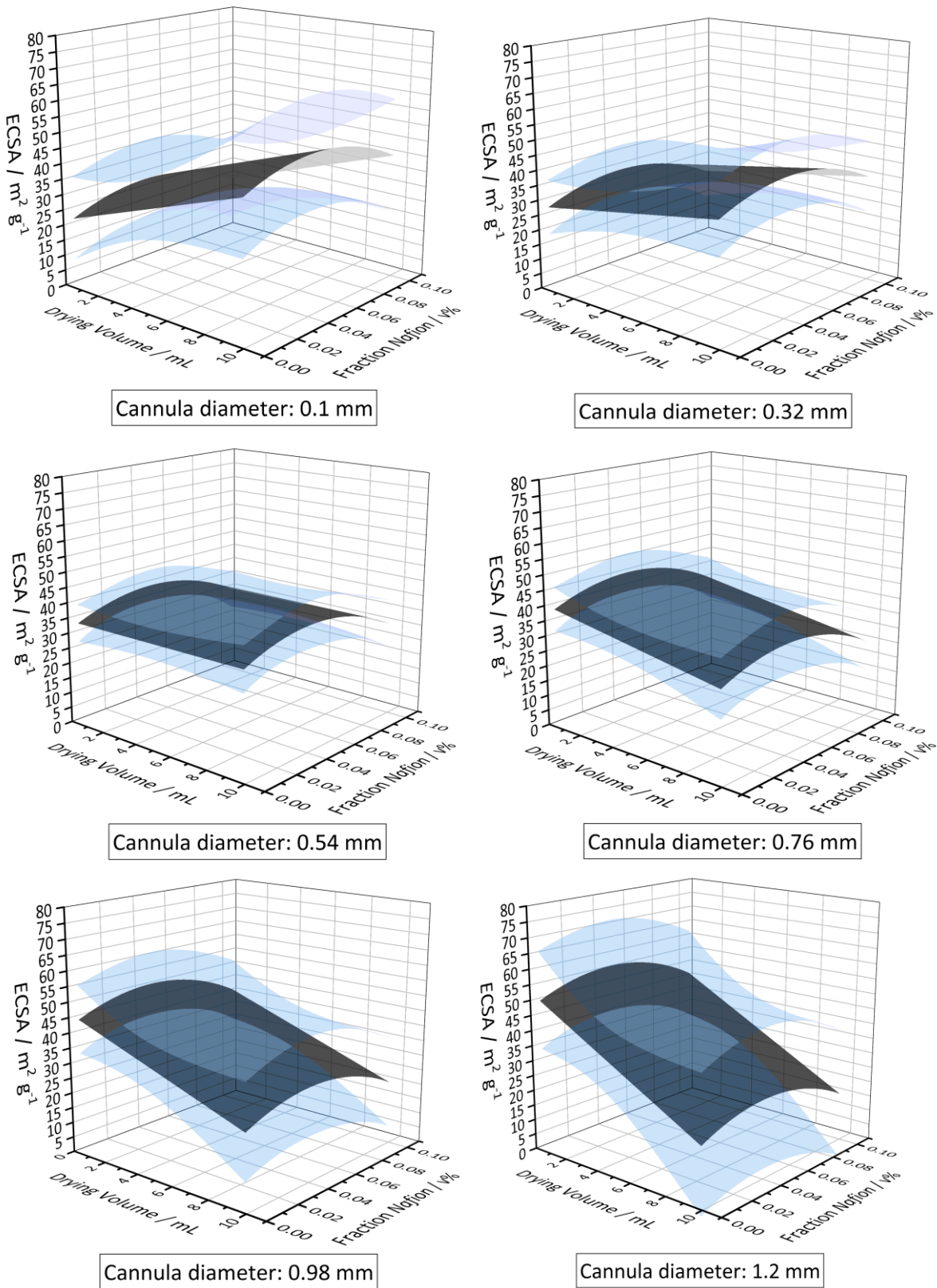


**Fig. 10.9:** Predicted ECSA (black) and upper and lower confidence intervals with 95 % significance (blue) of the linear regression model calculated by the *Cornerstone* DoE software with varying cannula diameters.

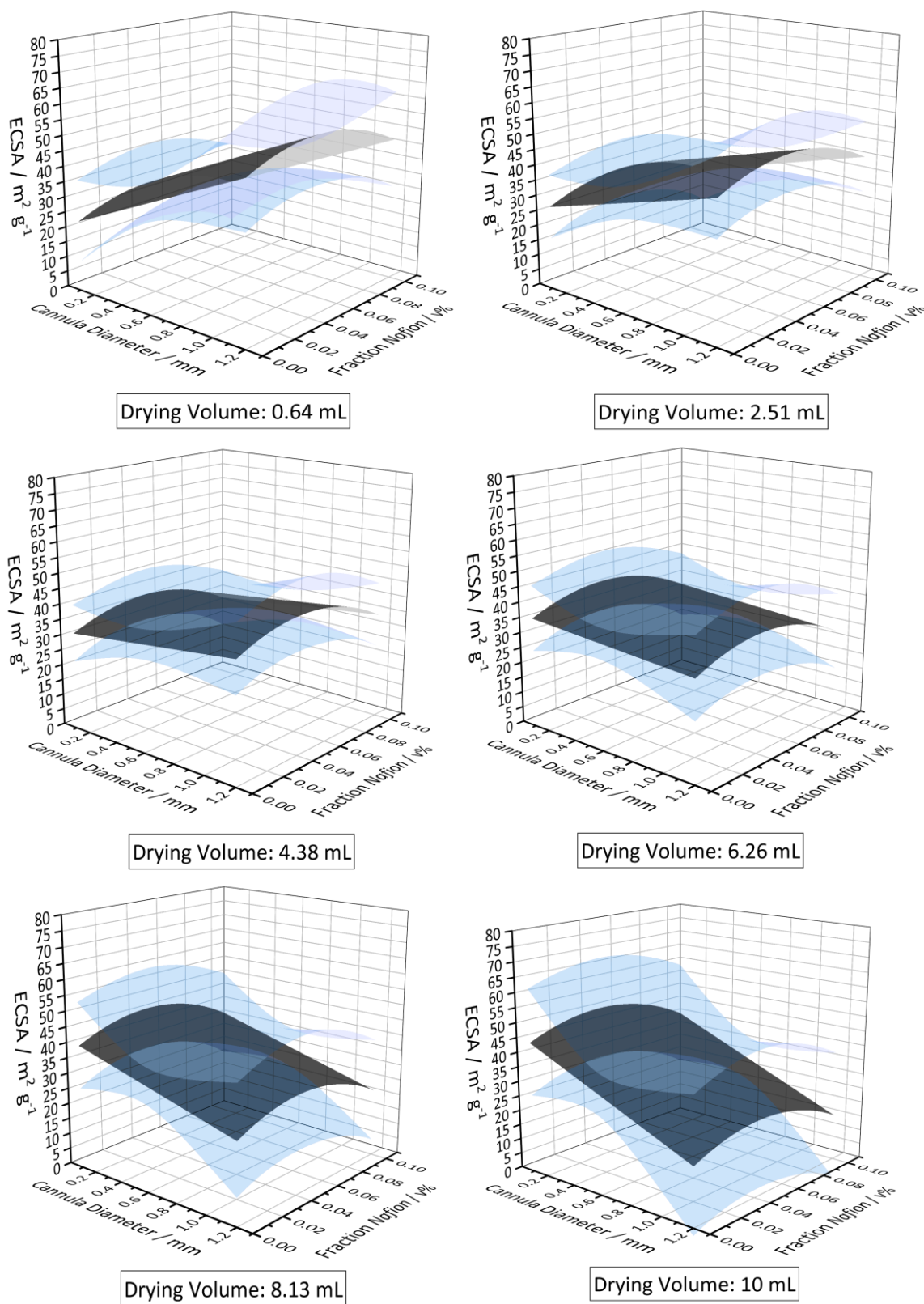


**Fig. 10.10:** Predicted ECSA (black) and upper and lower confidence intervals with 95 % significance (blue) of the linear regression model calculated by the *Cornerstone* DoE software with varying drying volumes.

## 10.5. AFM measurements of catalyst thin-films

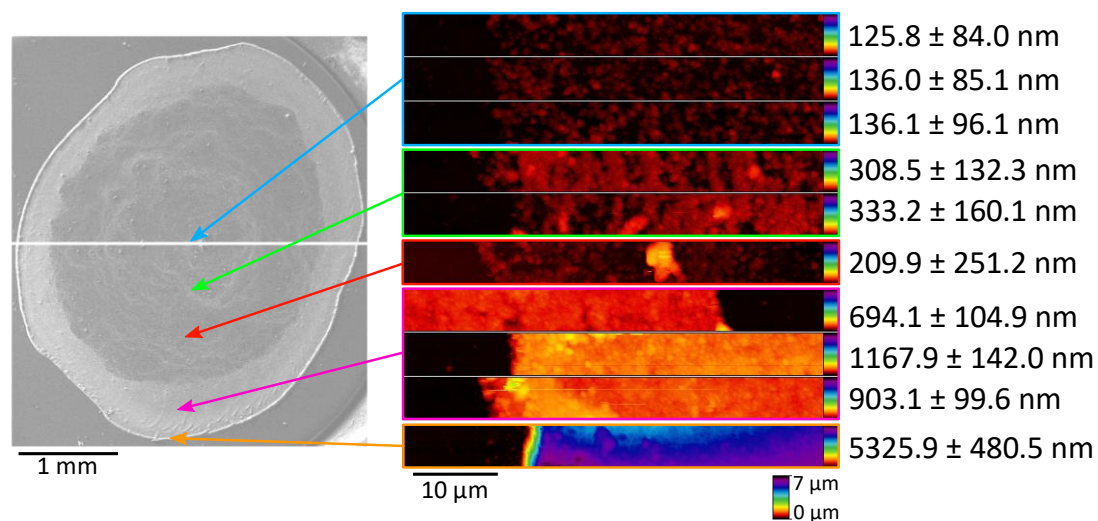


**Fig. 10.11:** SEM images and AFM height distributions of catalyst ink (PtNi on 4 h oxidised carbon black) film dried using the stationary drying technique at 40 °C. (0.05 v% Nafion, 99.95 v% ultrapure water).

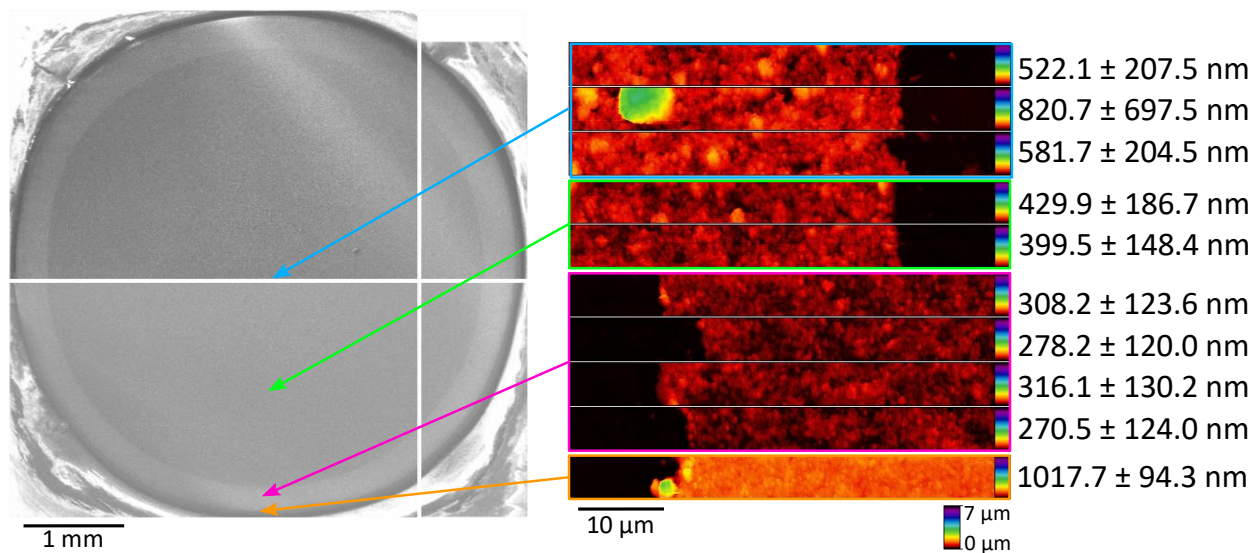


**Fig. 10.12:** SEM images and AFM height distributions of catalyst ink (PtNi on 4 h oxidised carbon black) film dried using the flow-restricted drying technique at room temperature in a 0.64 mL drying volume with a 0.8 mm cannula. (40 v% isopropanol, 0.05 v% Nafion, 59.95 v% ultrapure water).

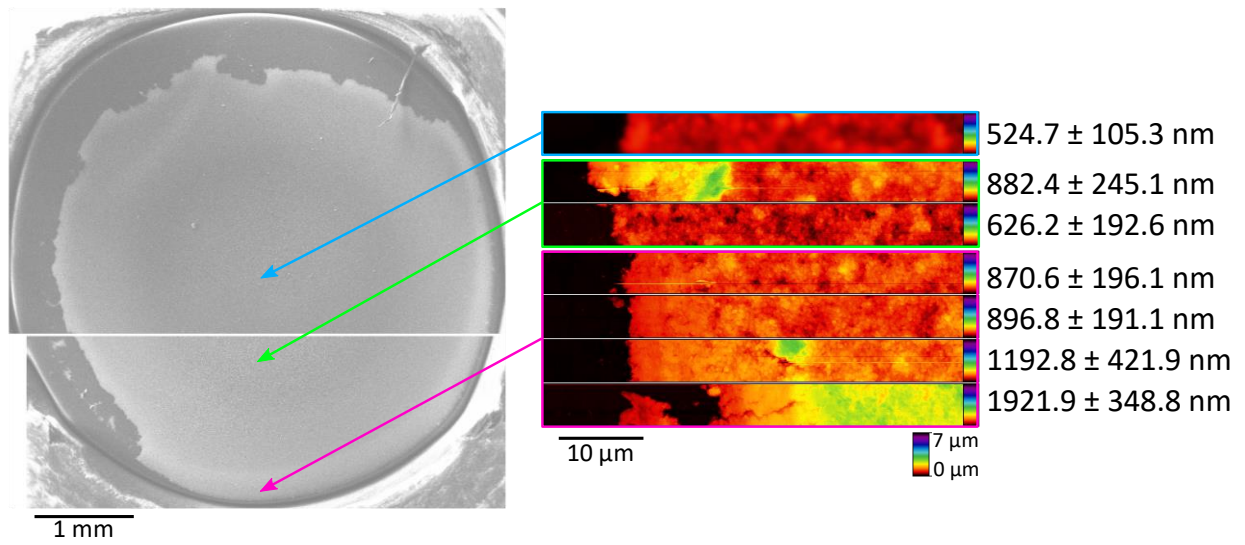


**Fig. 10.13:** SEM images and AFM height distributions of catalyst ink (PtNi on 4 h oxidised carbon black) film dried using the flow-restricted drying technique at room temperature in a 7.41 mL drying volume with a 0.4 mm cannula. (20 v% isopropanol, 0.05 v% Nafion, 79.95 v% ultrapure water)

## 10.6. TEM images of catalysts before and after AST cycling

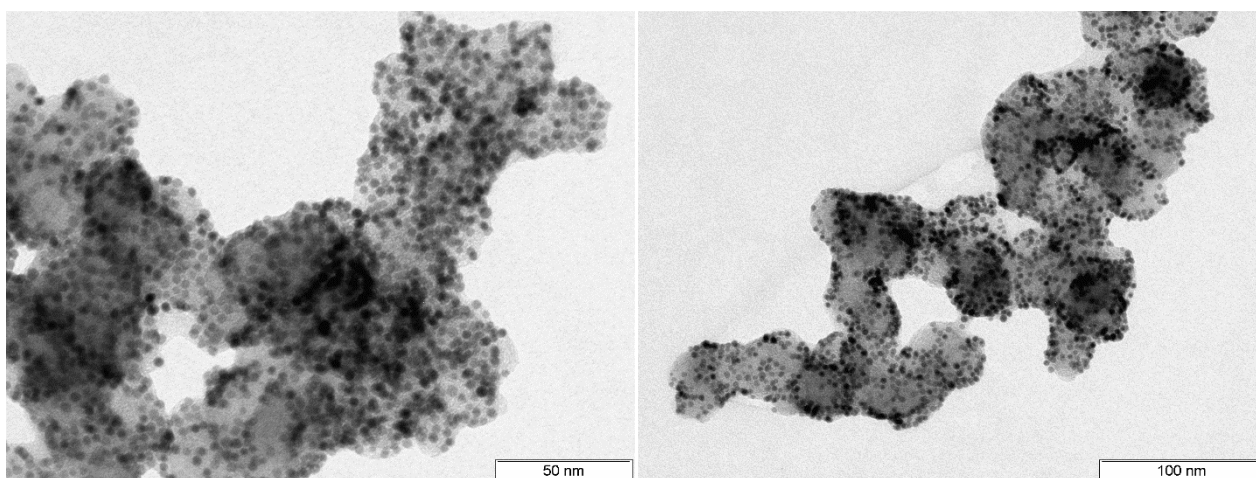


**Fig. 10.14:** TEM images of PtNi on *Vulcan XC72R*.

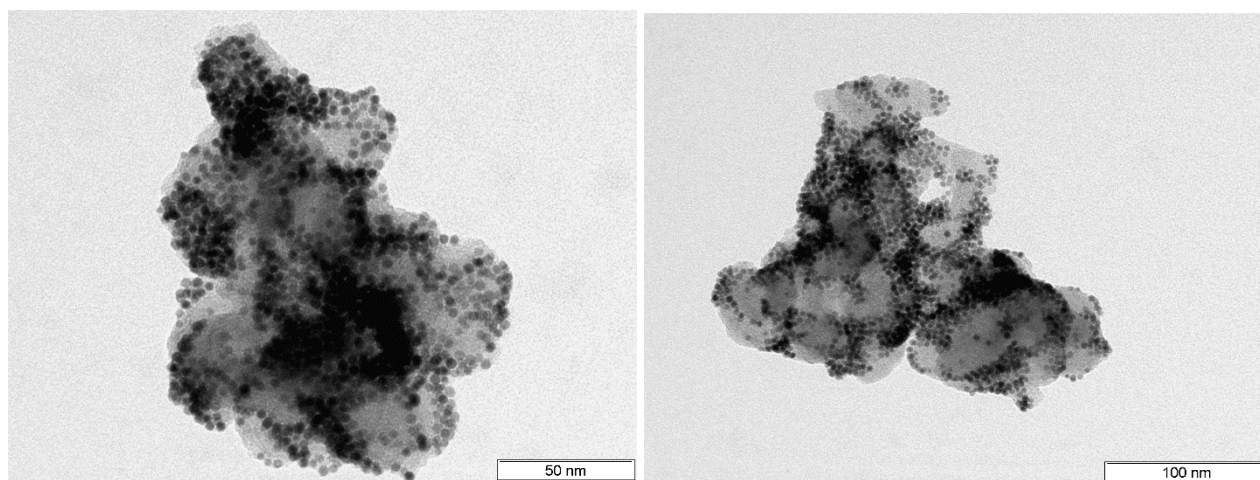


**Fig. 10.15:** TEM images of PtNi on *Vulcan XC72R*, oxidised for one hour.

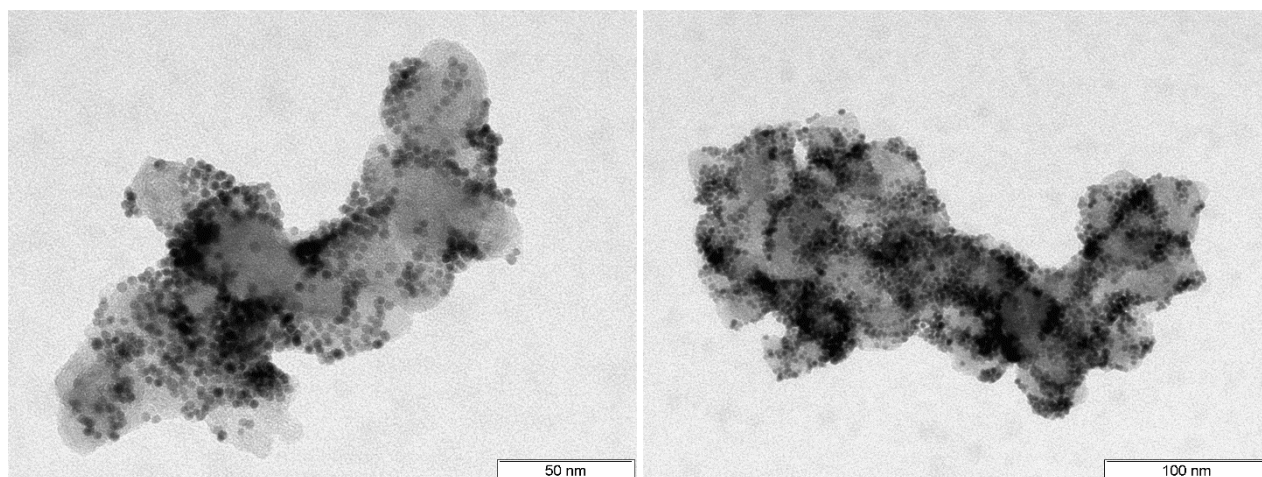


**Fig. 10.16:** TEM images of PtNi on *Vulcan XC72R*, oxidised for one hour and ethylenediamine-functionalised.

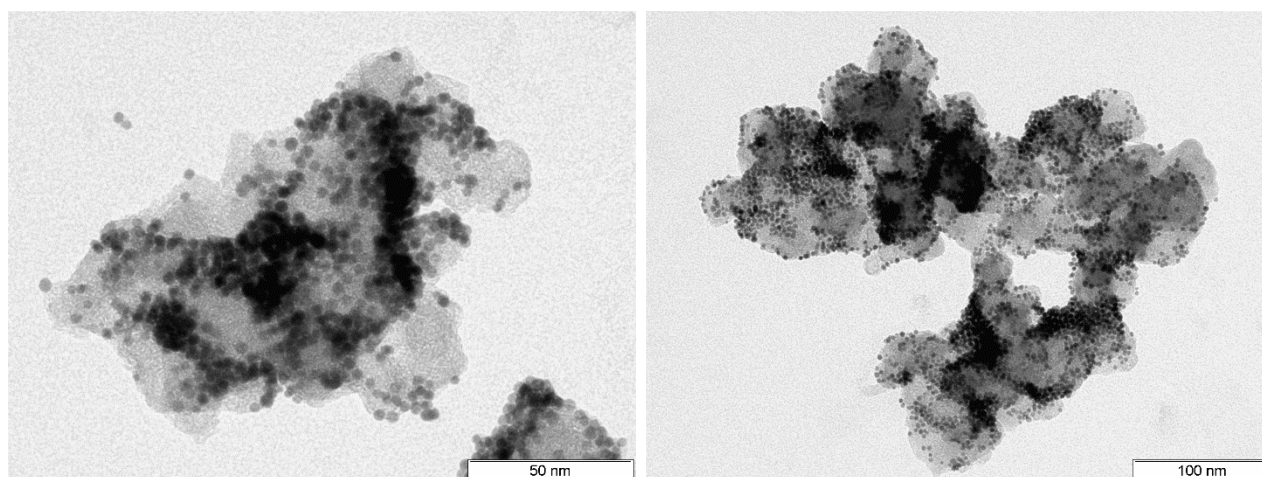


**Fig. 10.17:** TEM images of PtNi on *Vulcan XC72R*, oxidised for one hour and triethylenetetramine-functionalised.

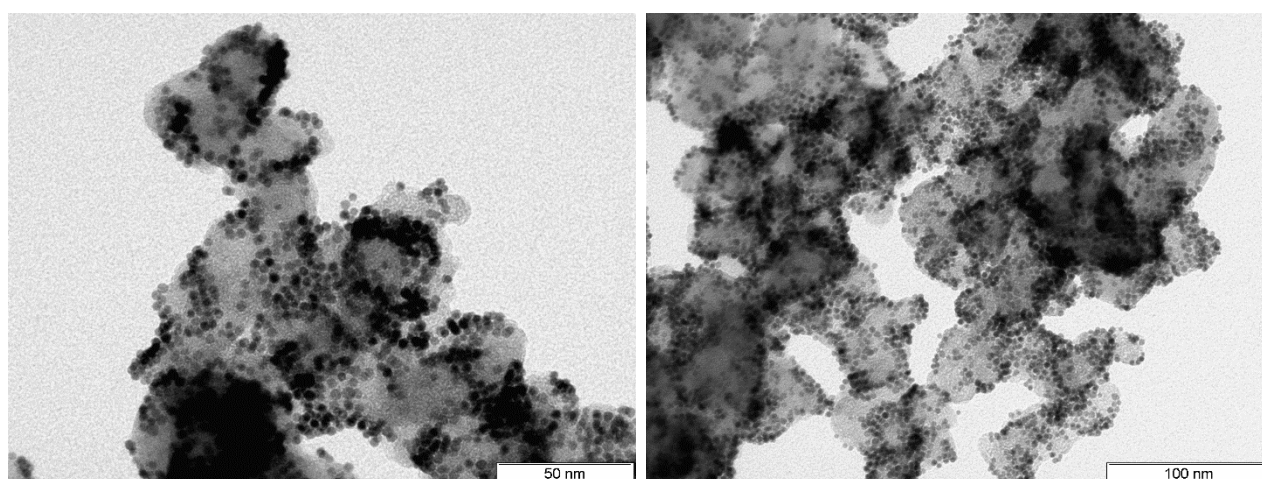


**Fig. 10.18:** TEM images of PtNi on *Vulcan XC72R*, oxidised for two hours.

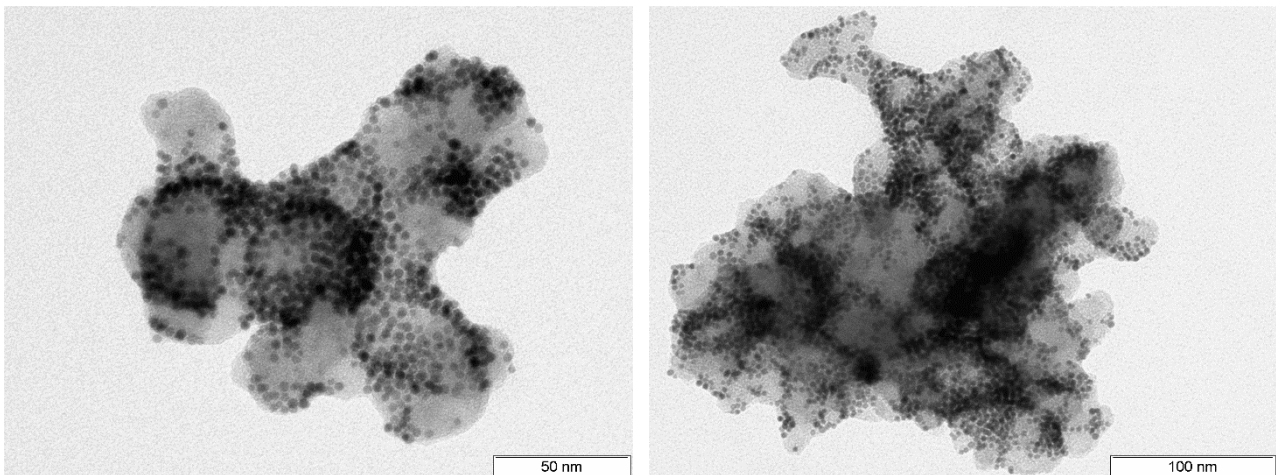


**Fig. 10.19:** TEM images of PtNi on *Vulcan XC72R*, oxidised for two hours and ethylenediamine-functionalised.

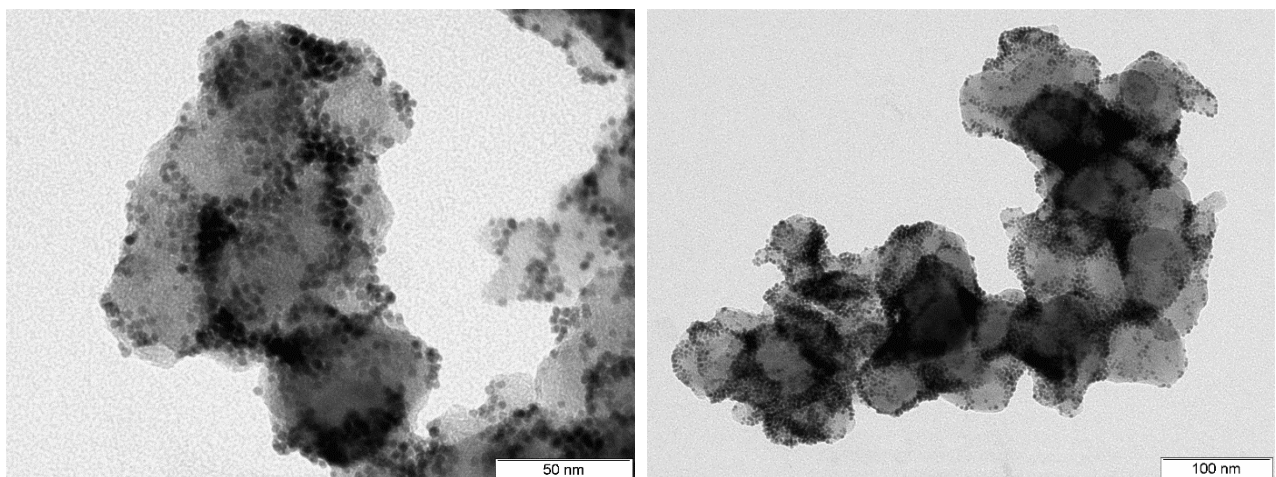


**Fig. 10.20:** TEM images of PtNi on *Vulcan XC72R*, oxidised for two hours and triethylenetetramine-functionalised.

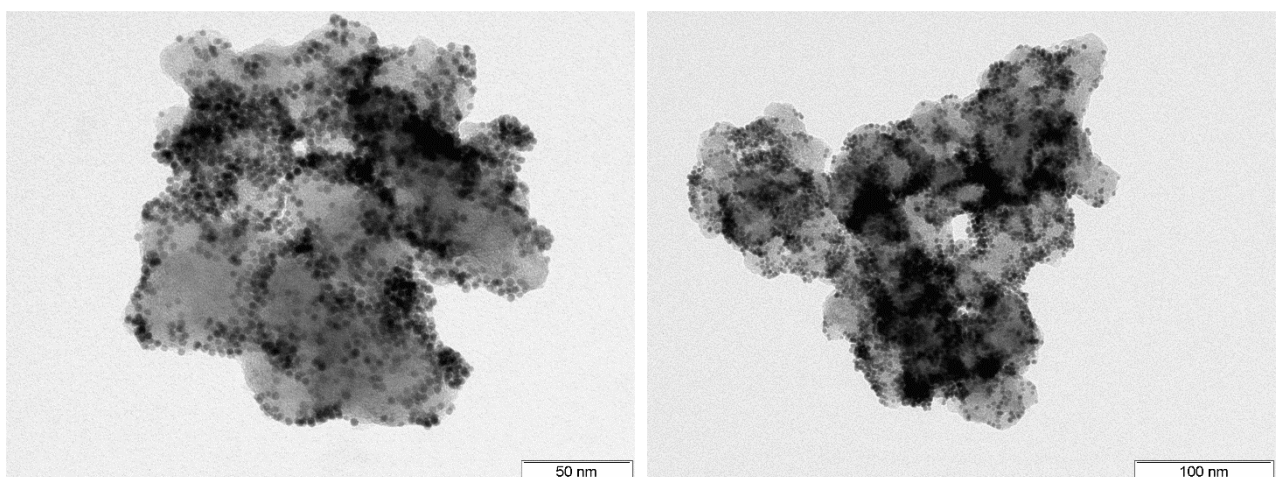


**Fig. 10.21:** TEM images of PtNi on *Vulcan XC72R*, oxidised for four hours.

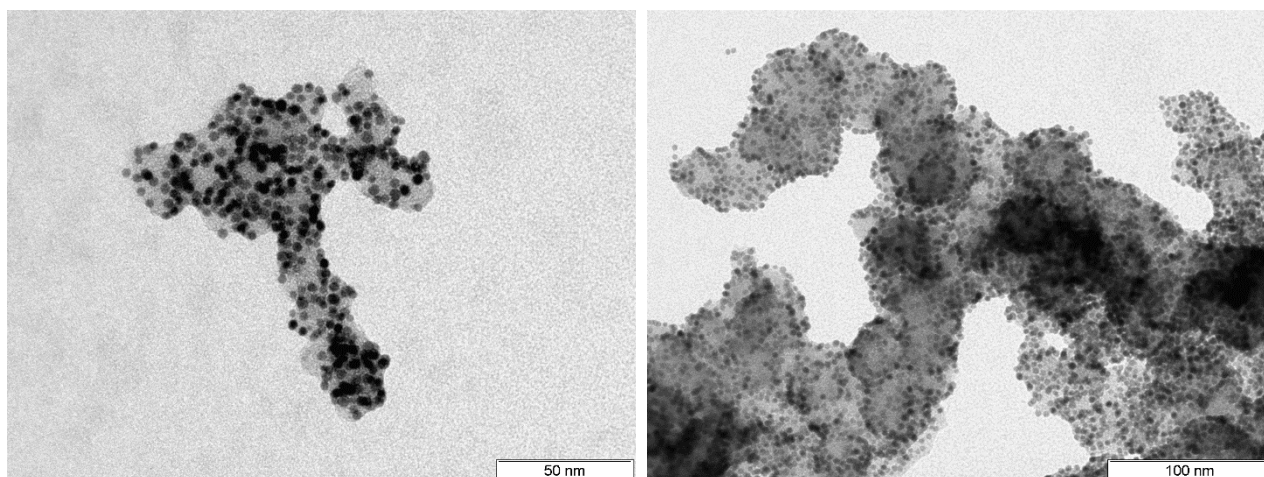


**Fig. 10.22:** TEM images of PtNi on *Vulcan XC72R*, oxidised for four hours and ethylenediamine-functionalised.

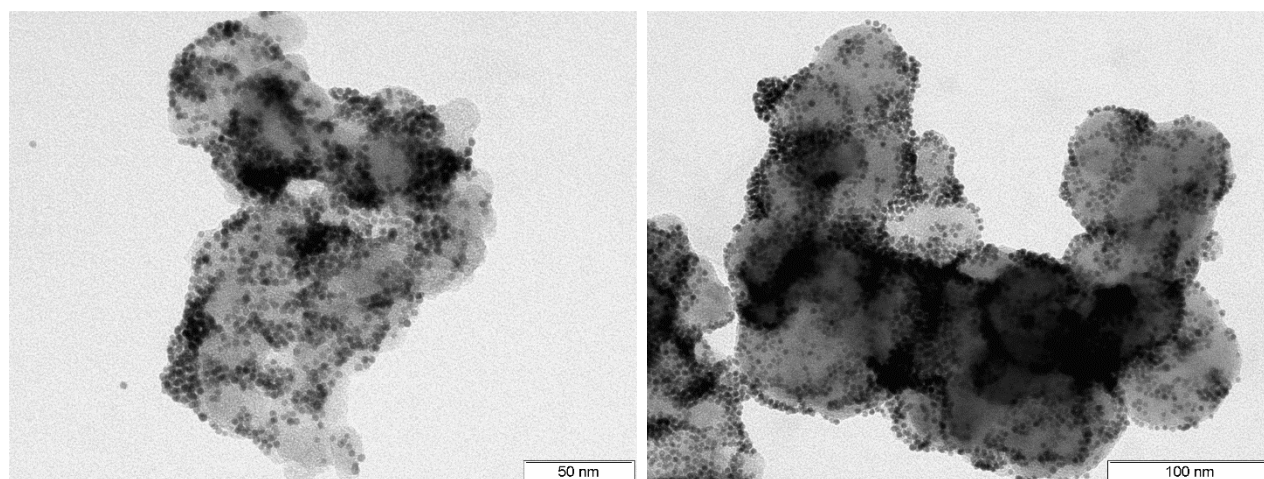


**Fig. 10.23:** TEM images of PtNi on *Vulcan XC72R*, oxidised for four hours and triethylenetetramine-functionalised.

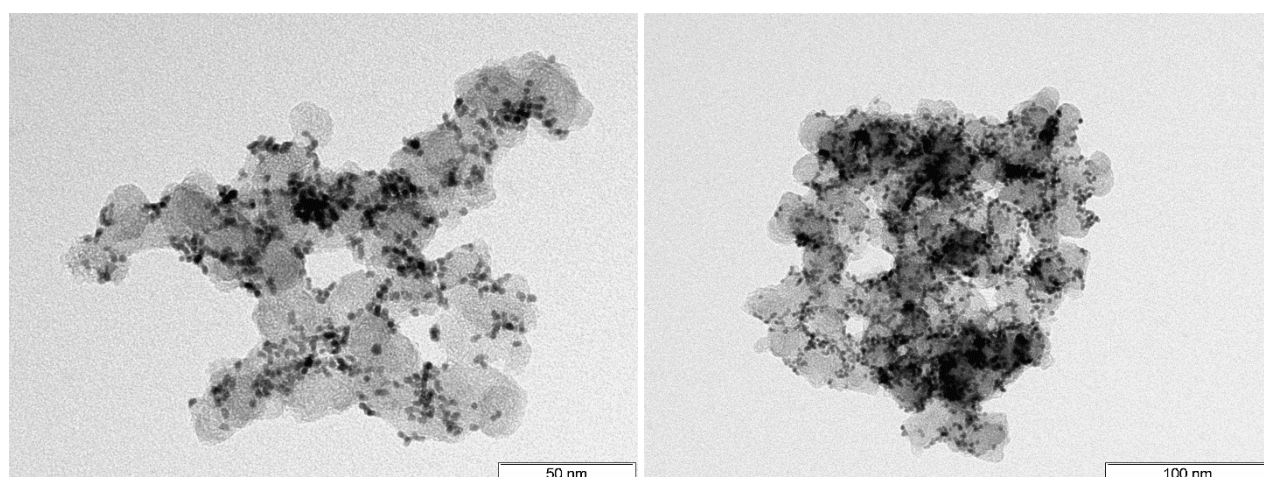


**Fig. 10.24:** TEM images of Pt on *Vulcan XC72R*.

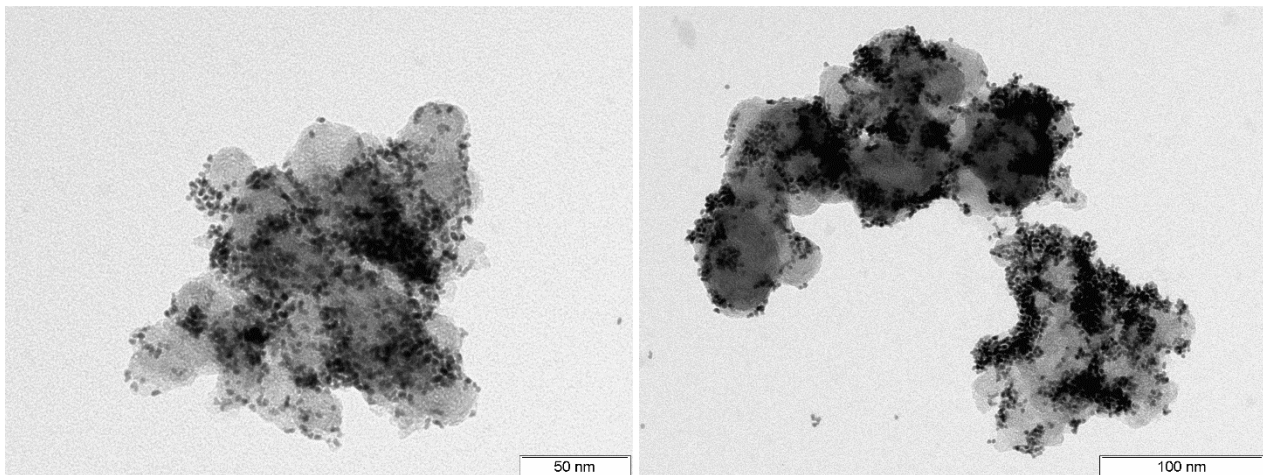


**Fig. 10.25:** TEM images of Pt on *Vulcan XC72R*, oxidised for four hours.

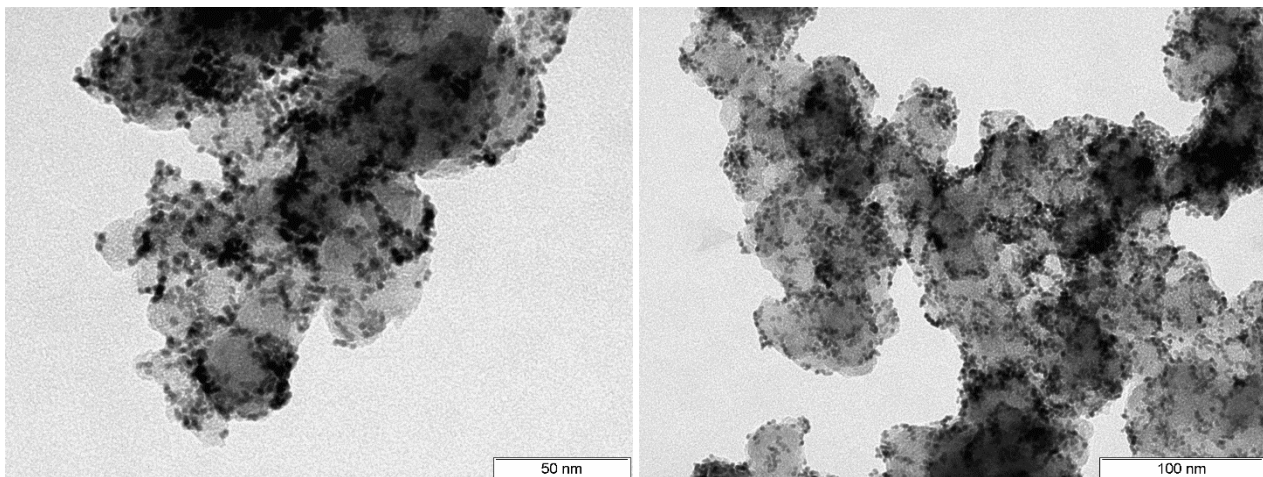


**Fig. 10.26:** TEM images of Pt on *Vulcan XC72R*, oxidised for four hours and ethylenediamine-functionalised.

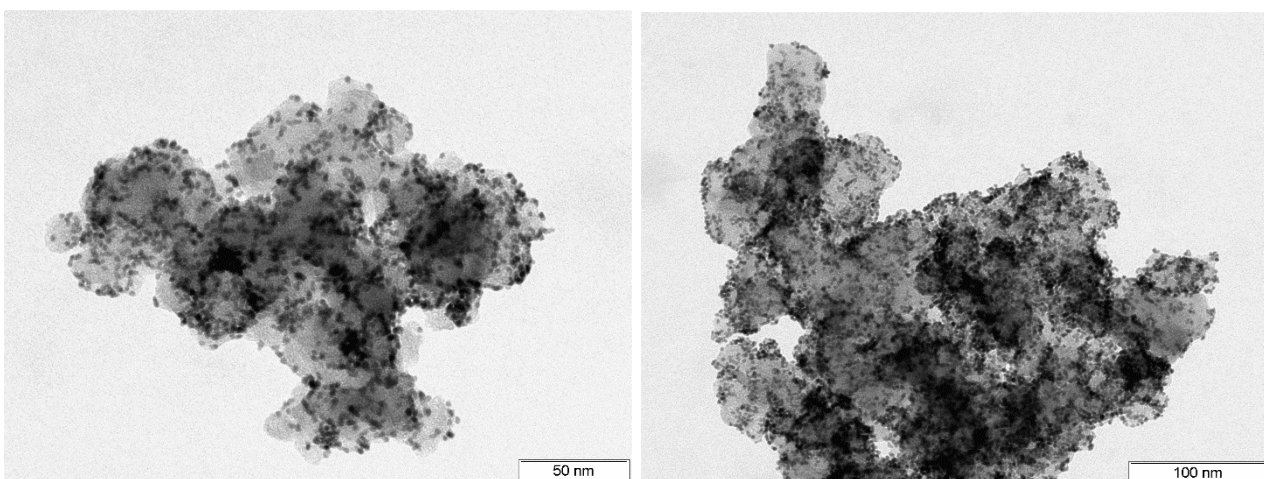


**Fig. 10.27:** TEM images of Pt on *Vulcan XC72R*, oxidised for four hours and triethylenetetramine-functionalised.

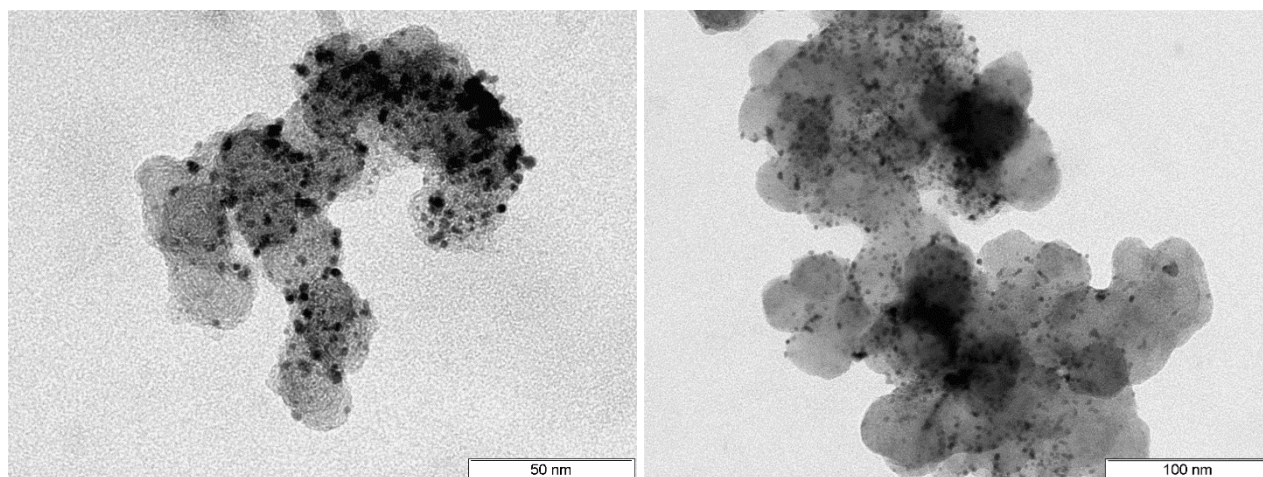


**Fig. 10.28:** TEM-images of *HiSPEC*<sup>®</sup> 3000 (Platinum, nominally 20% on carbon black; *Alfa Aesar*; Lot: 61601012).

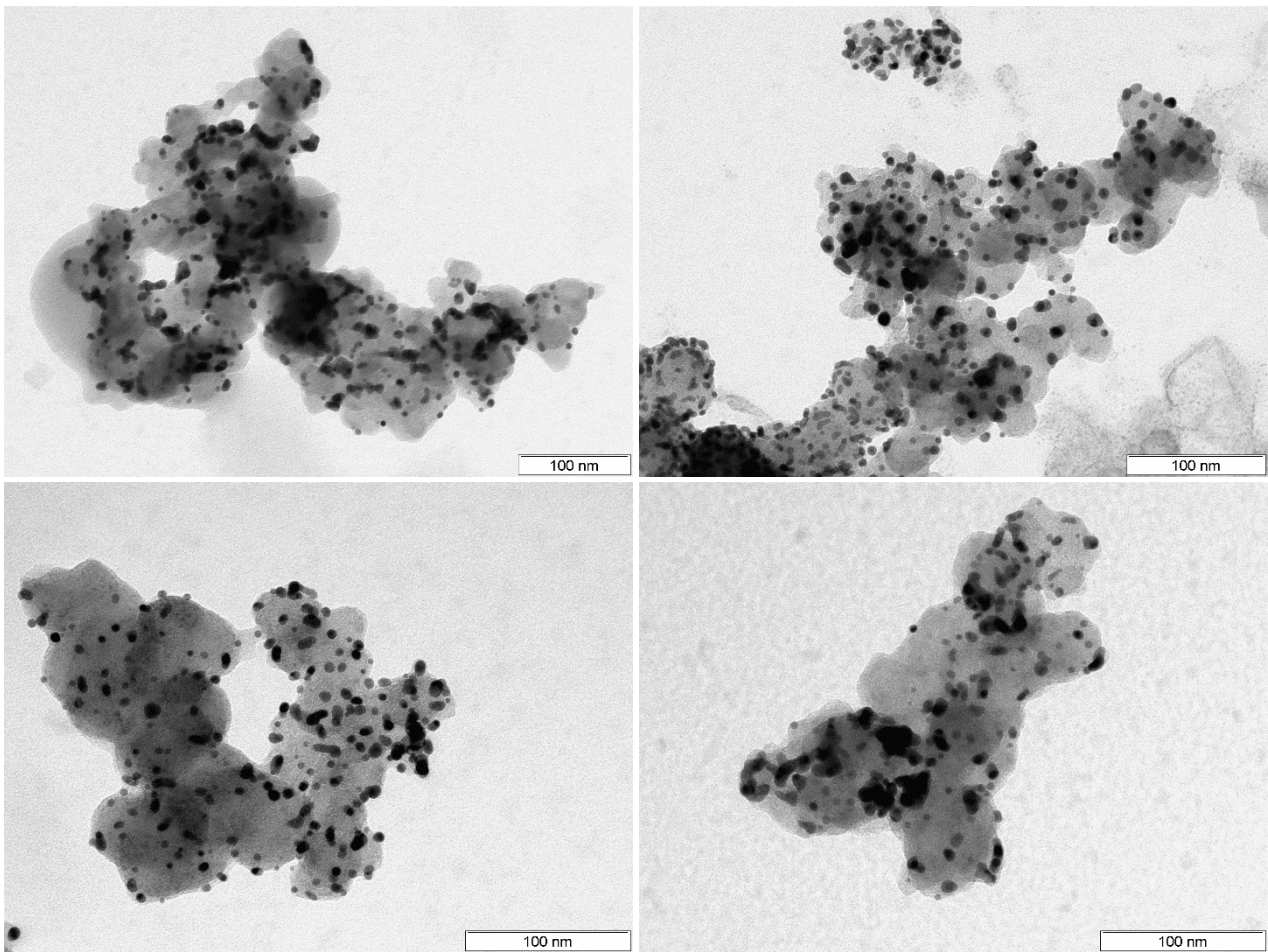


**Fig. 10.29:** TEM images of PtNi on *Vulcan XC72R*, after 30000 AST cycles.

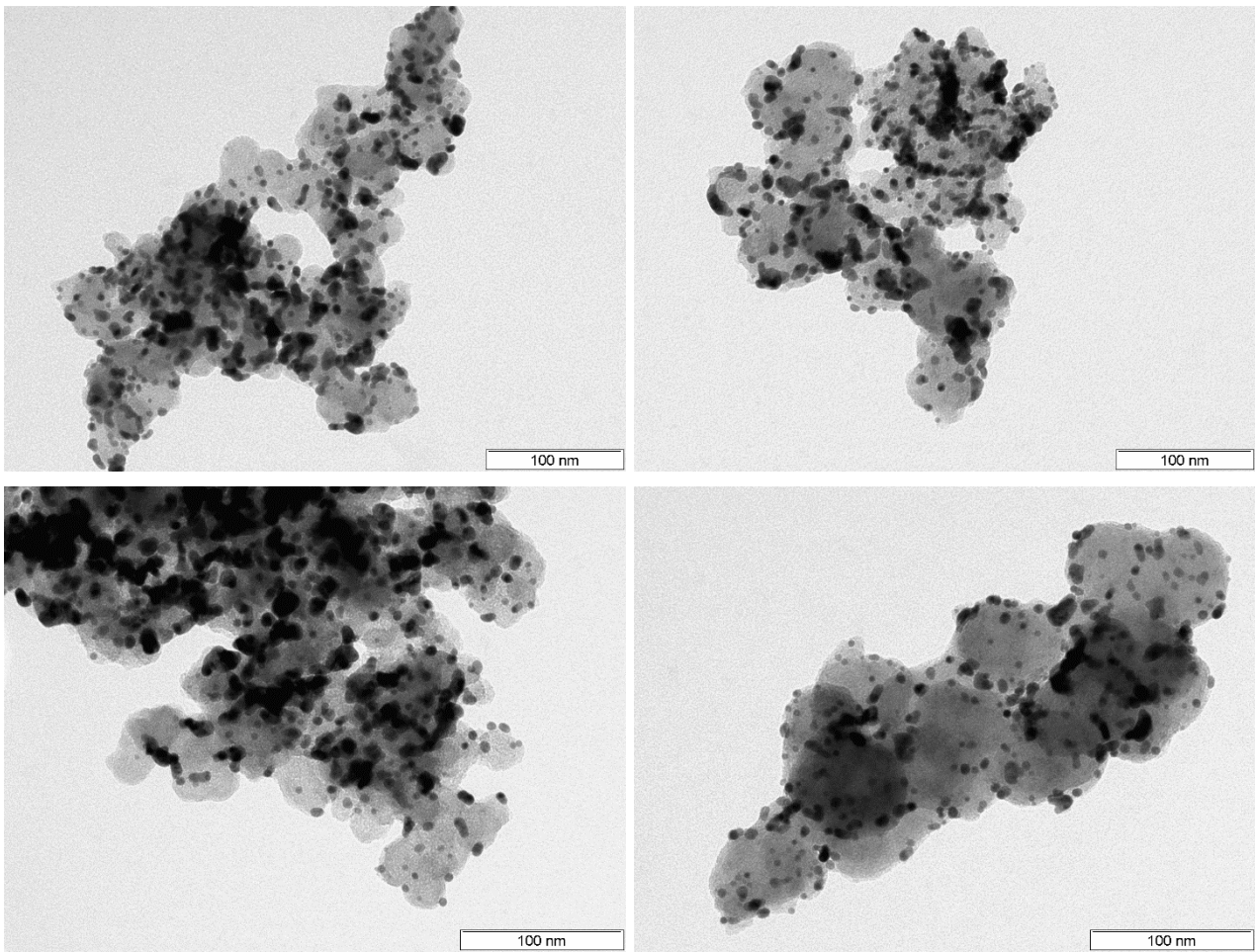


**Fig. 10.30:** TEM images of PtNi on *Vulcan XC72R*, oxidised for four hours and ethylenediamine-functionalised, after 30000 AST cycles.

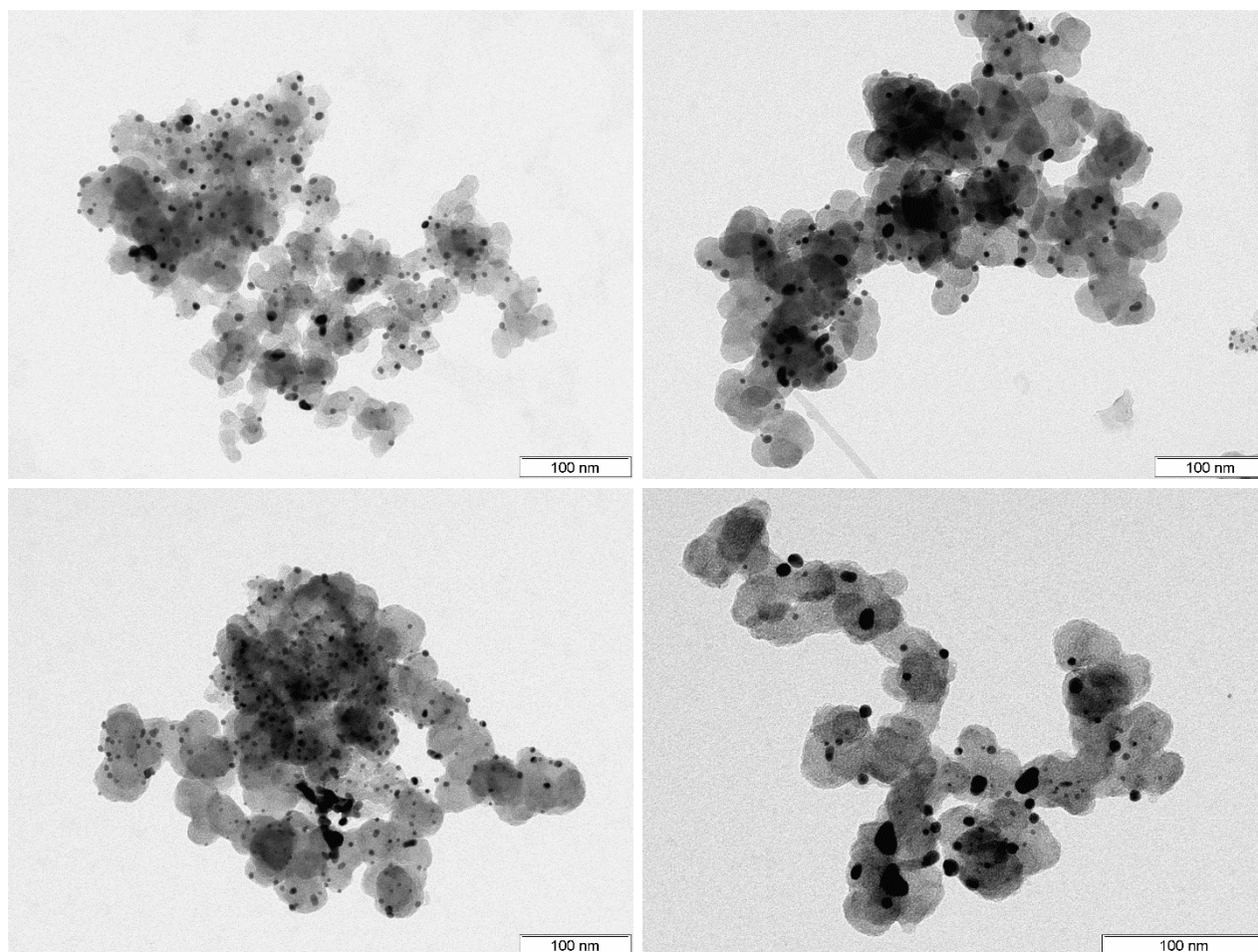


**Fig. 10.31:** TEM-images of *HiSPEC*<sup>®</sup> 3000 (Platinum, nominally 20% on carbon black; *Alfa Aesar*; Lot: 61601012), after 30000 AST cycles.

## 11. Danksagung

Jede große wissenschaftliche Reise erfordert die Unterstützung von vielen. In dieser Danksagung möchte ich den Menschen meinen Dank aussprechen, die mir während dieser langen Reise zur Seite standen.

Zunächst einmal möchte ich meinen Betreuern Horst Weller und Hauke Heller für die hilfreiche fachliche Unterstützung bei der Anfertigung meiner Arbeit danken. Ich bin sehr dankbar dafür, dass Ihr Euch trotz voller Terminkalender immer wieder die Zeit genommen habt, mir zuzuhören und mit Rat zur Seite zu stehen. Insbesondere möchte ich mich bei Hauke für die teilweise nächtlichen Korrekturen an meiner Dissertation bedanken.

Des Weiteren danke ich Alf Mews für die Begutachtung meiner Arbeit und Mehtap Özaslan und Jakob Albert für die Teilnahme in meiner Prüfungskommission. Zudem danke ich Mehtap für die herzliche Aufnahme in ihren Arbeitskreis, auch wenn es nur für eine kurze Zeit war.

Außerdem danke ich Tobias Vossmeier für die fachlichen Ratschläge und das offene Ohr, insbesondere zu einer Zeit, als meine beiden Betreuer nicht anwesend waren.

Auch danke ich allen Kollegen aus dem Arbeitskreis Weller: Steffen Woderich, Jana Struck, Ahir Bose, Finn Dobschall, Sebastian Graf, Sönke Wengler-Rust, Julia Funk, Lea Klauke, Nancy Liu, Bendix Ketelsen, Arthur Feld, Agnes Weimer, Hauke Hartmann, Felix Thiel, Jil Rüter, Clemens Schröter, Kathrin Hoppe, Nina Schober und Marion Manin, sowie den neuen Kollegen aus dem AK Bigall: Jan-Niklas Beyer, Christoph Tioka, Larissa Schoske, Pia Thomsen, Fahima Islam, Ole Krüger, Suvadip Saha, Thorben Stoebeke, Daniel Limouchi und vielen mehr. Vielen Dank für Eure Unterstützung, für die netten Gespräche beim Mittagessen, die gemeinsamen AK Aktivitäten und generell für die gemeinsame Zeit.

Des Weiteren danke ich meinen beiden Bachelorantinnen, Tzu-Ying Yu und Johanna Rübült, und meinen Praktikanten, für ihren Beitrag zu meiner Doktorarbeit im Zuge ihrer Projekte.

Zudem möchte ich mich bei allen Serviceeinrichtungen, die mir im Laufe meiner Doktorarbeit geholfen haben, bedanken. Eure Arbeit hat meine Doktorarbeit erheblich erleichtert und teilweise auch erst möglich gemacht. Insbesondere danke ich der Elektronenmikroskopie-Abteilung von Charlotte Ruhmlieb, Stefan Werner und Robert Schön, die die meisten TEM und SEM-Bilder aufgenommen haben. Auch danke ich der zentralen Elementanalytik für die durchgeführten Messungen und ich danke Sandra König für die Hilfe bei den BET-Messungen. Weiterhin möchte ich mich bei der Forschungswerkstatt und den Glasbläsern für die Hergestellten Geräte und

Reparaturen bedanken. Auch danke ich den Kollegen aus dem Fraunhofer Institut, die die unkomplizierte Mitbenutzung von Geräten ermöglichten.

Weiterhin danke ich Skadi Kull für die schöne Zeit im Molecules and Schools Team und auch für die vielen hilfreichen Gespräche über meine Doktorarbeit. Und ich möchte mich bei allen Beteiligten von DynaMent für die sehr hilfreiche Zeit in dem Programm und die tolle Gemeinschaft bedanken.

Zu guter Letzt möchte ich mich bei meiner Familie und meinen Freunden bedanken, die mir die ganze Zeit zur Seite standen. Vielen Dank für Eure Unterstützung, die Geduld und das Verständnis. Im Speziellen danke ich meinem Vater Dirk von Ahlften für die Hilfe und den Rat, auf die ich mich immer verlassen konnte. Meiner Großmutter Clara von Ahlften und meinem Bruder Ruben Felgenhauer danke ich dafür, dass sie mir immer zur Seite standen. Und meiner Mutter Marion Felgenhauer danke ich dafür, dass sie mich dazu inspiriert hat, meinen Doktor zu machen. Ich werde meine Mutter unter anderem auf diese Weise immer im Herzen tragen.

## 12. Eidesstattliche Versicherung

Hiermit versichere ich an Eides statt, die vorliegende Dissertationsschrift selbst verfasst und keine anderen als die angegebenen Quellen und Hilfsmittel benutzt zu haben. Sofern im Zuge der Erstellung der vorliegenden Dissertationsschrift generative Künstliche Intelligenz (gKI) basierte elektronische Hilfsmittel verwendet wurden, versichere ich, dass meine eigene Leistung im Vordergrund stand und dass eine vollständige Dokumentation aller verwendeten Hilfsmittel gemäß der Guten wissenschaftlichen Praxis vorliegt. Ich trage die Verantwortung für eventuell durch die gKI generierte fehlerhafte oder verzerrte Inhalte, fehlerhafte Referenzen, Verstöße gegen das Datenschutz- und Urheberrecht oder Plagiate

Hamburg, 19. Dezember 2024

A handwritten signature in blue ink, appearing to read 'E. Felgenhauer', with a stylized flourish extending to the right.